Modelling active galactic nuclei in cosmological simulations: how sub-grid models help to reveal the driving mechanisms of nuclear activity

Lisa Karin Steinborn

München 2018

Modelling active galactic nuclei in cosmological simulations: how sub-grid models help to reveal the driving mechanisms of nuclear activity

Lisa Karin Steinborn

Dissertation
an der Fakultät für Physik
der Ludwig–Maximilians–Universität
München

vorgelegt von
Lisa Karin Steinborn
aus Erlenbach am Main

München, den 25.05.2018

Erstgutachter: PD Dr. Klaus Dolag
Zweitgutachter: Prof. Dr. Harald Lesch
Tag der mündlichen Prüfung: 09.07.2018

To Daniel and

my little sunshine Lily

Contents

Zusammenfassung

Aktive Galaxienkerne (AGNs) werden schon seit über einem Jahrhundert beobachtet und sind immer noch Gegenstand aktueller Forschung. Es ist zwar weitestgehend akzeptiert, dass AGNs von supermassiven Schwarzen Löchern angetrieben werden, die in Zentren von Galaxien angesiedelt sind, doch deren genaue Antriebsmechanismen sind noch nicht vollständig verstanden. Vermutlich liegt das daran, dass eine nur winzig kleine Region um das Schwarze Loch herum die gesamte restliche Galaxie um mehrere Größenordnungen überstrahlen kann. Diese Region kann außerdem gigantische Radio-Emissionsgebiete entstehen lassen, die größer als die gesamte sichtbare Galaxie sein können. Somit ist es zwar möglich, die Helligkeit von AGNs über extrem große Entfernungen hinweg zu messen, die innere Region um das Schwarze Loch herum bleibt dem Beobachter jedoch weitgehend verborgen. Natürlich implizieren diese großen Skalen, dass AGN Aktivität sehr wichtig für die Entstehungsgeschichte von Galaxien sein muss.

In den letzten Jahrzehnten wurden hydrodynamische Simulationen entwickelt, die innerhalb eines kosmologischen Modells nachstellen, wie sich baryonische Strukturen im Universum bilden. In der vorliegenden Arbeit verwenden wir die Magneticum Pathfinder Simulationen, eine Reihe kosmologischer, hydrodynamischer Simulationen mit unterschiedlichen Auflösungen und Volumina. Diese Simulationen haben räumliche Auflösungen von bis zu etwa 2kpc, so dass selbst morphologische Strukturen innerhalb von Galaxien sichtbar werden. Um die Entstehungsgeschichte von Galaxien so wirklichkeitsgetreu wie nur möglich nachzustellen, muss auch der Effekt von AGNs berücksichtigt werden. Weil die Region, in der sich die Akkretion auf das Schwarze Loch abspielt, in kosmologischen Simulationen nicht aufgelöst wird, wurden sogenannte Subgrid-Modelle entwickelt, die das Anwachsen Schwarzer Löcher so selbstkonsistent wie nur möglich widerspiegeln sollen. Dazu nimmt man an, dass die Akkretionsrate auf das Schwarze Loch und der damit verbundene Energierückstoß von den grundlegenden Eigenschaften des Gases abhängen, welches sich in der inneren aufgelösten Region um das Schwarze Loch herum befindet. Ein Teil der vorliegenden Arbeit ist es, Subgrid-Modelle für AGNs zu verbessern und aufzuzeigen, welchen Effekt diese auf die Entwicklung Schwarzer Löcher und derer Heimatgalaxien haben.

Kosmologische Simulationen, die beobachtete Eigenschaften von Galaxien und deren Schwarzen Löchern weiterstgehend reproduzieren, bieten somit nicht nur eine optimale Testumgebung, um die Entstehungsgeschichte von Galaxien zu studieren, sondern auch, um eine bessere Einsicht in die Antriebsmechanismen von AGNs zu gewinnen. In den Magneticum Pathfinder Simulationen wird die Dynamik Schwarzer Löcher während der

Verschmelzung zweier Galaxien soweit verfolgt, bis das Auflösungslimit erreicht ist. Somit bieten die Simulationen eine optimale Grundlage, um zu untersuchen, inwieweit Verschmelzungen von Galaxien zu AGN Aktivität beitragen. Unsere Simulationen erzeugen sogar eine Reihe von Paaren Schwarzer Löcher, die nur weniger als 10kpc voneinander entfernt sind, darunter auch AGN Paare. Im Rahmen dieser Arbeit analysieren wir diese Paare im Detail, mit besonderem Augenmerk auf den Unterschieden zwischen aktiven und inaktiven Paaren. Weil die Wahrscheinlichkeit für AGN Aktivität größer ist, je kleiner der Abstand zwischen den beiden Schwarzen Löcher ist, liegt die Vermutung nahe, dass Verschmelzungen von Galaxien einen wichtigen Antriebsmechanismus für AGN Aktivität darstellen. Wirft man jedoch einen Blick auf die gesamte AGN-Population, erweist sich dies als ein Trugschluss, da nur ein geringer Anteil aller AGNs auf eine Galaxienverschmelzung zurückzuführen ist.

Im letzten Teil der vorliegenden Arbeit verwenden wir schließlich Simulationen mit Volumina bis hin zu $(909\text{Mpc})^3$, die so viele AGNs enthalten, dass es möglich ist, präzise Aussagen über deren großräumige Verteilung zu treffen. Dabei stellt sich heraus, dass die Verteilung von AGNs deutlich komplexer ist als Verteilung von Galaxien im Allgemeinen. Insbesondere sind verschiedene AGN-Typen in sehr unterschiedliche großräumige Strukturen eingebettet, was darauf hinweist, dass diese unterschiedliche Stadien in der Entstehungsgeschichte von Galaxien darstellen.

Abstract

Active Galactic Nuclei (AGN) have been observed for more than a century and are still a major research topic. While it is generally accepted that AGN are driven by supermassive black holes (SMBHs) which reside in the centres of galaxies, their detailed physical driving mechanisms are not yet fully understood. The reason is probably that a very small region around the black hole (BH) can outshine the rest of the galaxy by several orders of magnitude and produce outflows which are observed as enormous radio-lobes, which can be larger than the size of the galaxy. Therefore, it is possible to measure the luminosity of AGN over very large distances. These extreme scales naturally imply that AGN activity must have important implications for the evolution of galaxies. However, the innermost region around the central SMBH remains hidden.

In the recent decades hydrodynamic simulations have been developed which mimic the baryonic structure formation of the Universe in a cosmological context. In this thesis we make use of the Magneticum Pathfinder simulation set, which is a set of cosmological hydrodynamic simulations with different resolutions and volumes. Since these simulations reach resolutions large enough to resolve the morphological structure of galaxies down to kiloparsec scales, models which mimic the effect of AGN activity onto their host galaxies are absolutely necessary to simulate the evolution of galaxies as realistically as possible. Since the actual accretion region around the BH is not resolved in cosmological simuations, sub-grid models have been developed to mimic the growth of BHs as self-consistently as possible, assuming that the accretion rate onto the BH and the associated AGN feedback depend on the properties of the surrounding gas. It is a major goal of this thesis to improve the sub-grid model for AGN and to investigate its effect onto BH growth as well as onto the evolution of their host galaxies.

Cosmological simulations, which reproduce observed properties of BHs and their host galaxies, are not only an ideal testbed to study the formation and evolution of galaxies, but also to get insights into the driving mechanisms of AGN activity. The Magneticum Pathfinder simulations follow the dynamical evolution of BHs during galaxy mergers down to the resolution limit and, thus, they enable to investigate in detail the role of mergers for driving nuclear activity. Thereby, they do even produce a number of SMBH pairs with separations of only a few kpc, including dual AGN. Within the scope of this thesis, we analyse these SMBH pairs in detail, particularly focusing on the differences between active and inactive SMBH pairs. Since the probability for AGN activity in our simulations increases with decreasing separation between the SMBHs, one might expect that galaxy

mergers play a major role for driving AGN activity. However, turning towards the overall AGN population, we find that only a small fraction of AGN is driven by recent galaxy mergers.

Finally, we use large simulation runs with volumes up to $(909\mathrm{Mpc})^3$, which provide a large sample of simulated AGN. Relating the AGN to their host dark matter haloes reveals their large scale distribution, which turns out to be far more complex than that of the overall simulated galaxy sample. Particularly, we find that different AGN types reside in different environments. This points towards a picture in which different AGN types represent different evolutionary stages of galaxies and, thus, helps to better understand what makes AGN so special.

Chapter 1

Introduction

1.1 What is an Active Galactic Nucleus?

AGN are one of the most fascinating objects in the Universe. Although astronomers have studied AGN for many years they are still a major research topic. Not only their detailed structure, but also their driving mechanisms, are still highly debated. In this section I will briefly give an overview about AGN in general, focusing on their history and the current research status.

1.1.1 How the story begins

More than a century ago Fath (1909) observed the spectra of 'spiral nebulae', among them NGC 1068. In contrast to the spectra of inactive galaxies, which do generally not have emission lines, he observed a composite spectrum with both emission lines and absorption lines in the centre of NGC 1068. By that time Fath of course did not know that he observed the first AGN, nor did he realise the importance of his discovery, opening a completely new field in astronomy. His observation was confirmed by Slipher (1917), who found that the central emission lines are broadened at the centre peculiar to the galactic plane. This was very surprising, being *'the first striking observation of this kind'* (Slipher, 1917). The observation of broad emission lines in NGC 1068 was confirmed by Campbell & Moore (1918), who also observed broad emission lines in NGC 4151.[1] In the following years more galaxies with central emission lines have been reported (Seyfert, 1943, and references therein). Seyfert (1943) observed high excitation nuclear emission lines in six spiral galaxies. He found that all emission lines in these galaxies are broadened, similar to NGC 1068. Assuming that the lines are broadened by Doppler motion, he found velocities up to 8500 km/s for hydrogen atoms. The work from Seyfert (1943) is often seen as the starting point of the systematic search for AGN (e.g. Shields, 1999; Schneider, 2006). Until today, AGN with broad emission lines are called Seyfert galaxies. Weedman

[1] Although Campbell & Moore (1918) thought that NGC 4151 was a planetary nebula they stated that the spectrum was similar to that of NGC 1068.

(1970) realized that there are two different types of Seyfert galaxies: in one of four Seyfert galaxies he observed forbidden lines which are significantly broader than in the others. Khachikyan & Weedman (1971) distinguished between dense nuclei with low gas velocities and larger, less dense nuclei with higher gas velocities. Finally, Khachikian & Weedman (1974) defined these different types as follows: *'The Seyfert galaxies are either class 1, in which the Balmer lines are broader than the forbidden lines, or class 2, in which the forbidden lines and Balmer lines are the same width'* (Khachikian & Weedman, 1974). The simplest interpretation is that, for a given element, different line widths originate from different regions: *'So in the case of Seyfert 2s, we are left with the impression that both forbidden and permitted lines are formed in the same region of the nucleus, whilst for Seyfert 1s, the permitted lines and forbidden lines originate from distinctly differing regions'* (Robson, 1996). Later, these regions were named the narrow-line region (NLR) and the broad-line region (BLR). Accordingly, Seyfert 1 galaxies have both broad and narrow[2] emission lines (FWHM $>$ 1000km/s)[3], whereas Seyfert 2 galaxies have only narrow emission lines (FWHM $<$ 1000km/s, e.g. Robson, 1996; Schneider, 2006; Padovani et al., 2017). Since the work of Seyfert (1943), more than two decades had passed until the number of known Seyfert galaxies increased significantly with the release of the Markarian survey and observations of compact galaxies from Zwicky (Weedman, 1977, and references therein).

In addition to optical observations, the progress in radio astronomy in the 1950s led to the first observations of radio-loud AGN[4]. Although the number of observed extragalactic radio sources grew rapidly, their origin at that time was of course not understood (e.g. Hanbury Brown et al. 1952 and references therein). In particular, a radio source in Cygnus A (Cyg A) had been observed by Smith (1951), having a larger radio luminosity than its optical counterpart (Baade & Minkowski, 1954). Just two years later Jennison & Das Gupta (1953) reported that Cyg A *'must have at least two distinct centres of emission'*. This was the first observation of radio lobes, which could later be explained with models of relativistic jets (Scheuer, 1974; Blandford & Rees, 1974), which transport energy from the nucleus to the outskirts of the galaxy. The radio emission is produced by *'interactions between large-scale jets and the hot, diffuse gas that surrounds elliptical galaxies'* (Hughes, 1991) and also, to a much smaller extent, spiral galaxies. In the same year in which Scheuer (1974) and Blandford & Rees (1974) published their models, Fanaroff & Riley (1974) classified radio galaxies depending on whether the core (FR I) or the edge (FR II) is brighter[5] (e.g. review from Padovani et al., 2017).

[2]Note that, although 'narrow' emission lines are clearly narrower than the so-called 'broad' emission lines, they are still relatively broad with velocities up to a few hundred km/s (Schneider, 2006).

[3]FWHM = full width at half maximum

[4]For further details on the history of radio-loud AGN I refer the reader e.g. to the review from Shields (1999).

[5]The classification was made *'using the ratio of the distance between the regions of highest brightness on opposite sides of the central galaxy or quasar, to the total extent of the source measured from the lowest contour'* (Fanaroff & Riley, 1974), excluding any compact central component. In FR (Fanaroff Riley) I/ II objects this ratio is below/above 0.5.

Independent of observations of Seyfert galaxies and extragalactic radio sources, several 'star-like' objects with broad emission lines at unfamiliar wavelengths were observed in the 1960s, among them the radio sources 3C 48 and 3C 273. Schmidt (1963) and Oke (1963) observed the spectrum of 3C 273 and realized that the spectral lines were in agreement with the Balmer emission lines of hydrogen, corresponding to a redshift of $z = 0.16$. Similarly, Greenstein & Matthews (1963) concluded that 3C 48 had a redshift of $z = 0.37$. At first these quasi-stellar objects (QSOs), also called quasars (quasi-stellar radio sources), were believed to be very dense Galactic stars. However, due to their spectral properties, the most likely explanation was that the high redshifts were cosmological redshifts due to the expansion of the Universe. In the next years more quasar redshifts were reported (Schmidt & Matthews, 1964; Schmidt, 1965). With the discovery of the ultraviolet excess (Matthews & Sandage, 1963) methods were developed to systematically search for quasars (Ryle & Sandage, 1964). Finally, Sandage (1965) published a large sample of quasars, most of them being radio-quiet.

1.1.2 Spectral energy distribution of AGN and the unified model

In the late 1970s, first ideas came up about a unification of different AGN types. In 1977, Rowan-Robinson presented for the first time a scheme *'which unites quasars, radio galaxies, N galaxies*[6]*, and Seyfert galaxies into a single picture'* (Rowan-Robinson, 1977). He came also up with the idea that *'dust surrounding the optical core ... attenuates the broad ... wings of the permitted lines and causes the distinction between Type 1 and Type 2 spectra'* (Rowan-Robinson, 1977).

16 years later, Antonucci published a review about *'unified models for active galactic nuclei and quasars'* (Antonucci, 1993). He argued that there are only two intrinsic AGN types: radio-quiet and radio-loud AGN. The many different observed AGN types, for a given intrinsic luminosity, result from different viewing angles onto intrinsically very similar objects. With the review from Urry & Padovani (1995) the unified model of AGN became broadly accepted in the AGN community.

However, the many different spectral features and the different wavelength bands in which AGN had been observed led to an unprecedented amount of different AGN types in the literature, making it more and more difficult to get an overview of the big picture of AGN. Padovani et al. (2017), for example, list 51 different AGN types, all having very specific features: BLRGs (broad line radio galaxies), HEGs (high-excitation galaxies), LEGs (low-excitation galaxies), and LINERs (low-excitation nuclear emission-line regions) are only a few examples. To bring order to chaos, Padovani et al. (2017) made an effort to order AGN by just two criteria: *the efficiency of the radiation* and *the presence of a jet*. Since this is the most relevant AGN classification scheme for this thesis I will not go further into the details of the many AGN types defined in literature.

The sketch (adopted from Urry & Padovani, 1995) on the left-hand side in Fig. 1.1

[6]Galaxies which had both signatures of an elliptical galaxy, as well as of a central quasar were named N galaxies (Sandage, 1973).

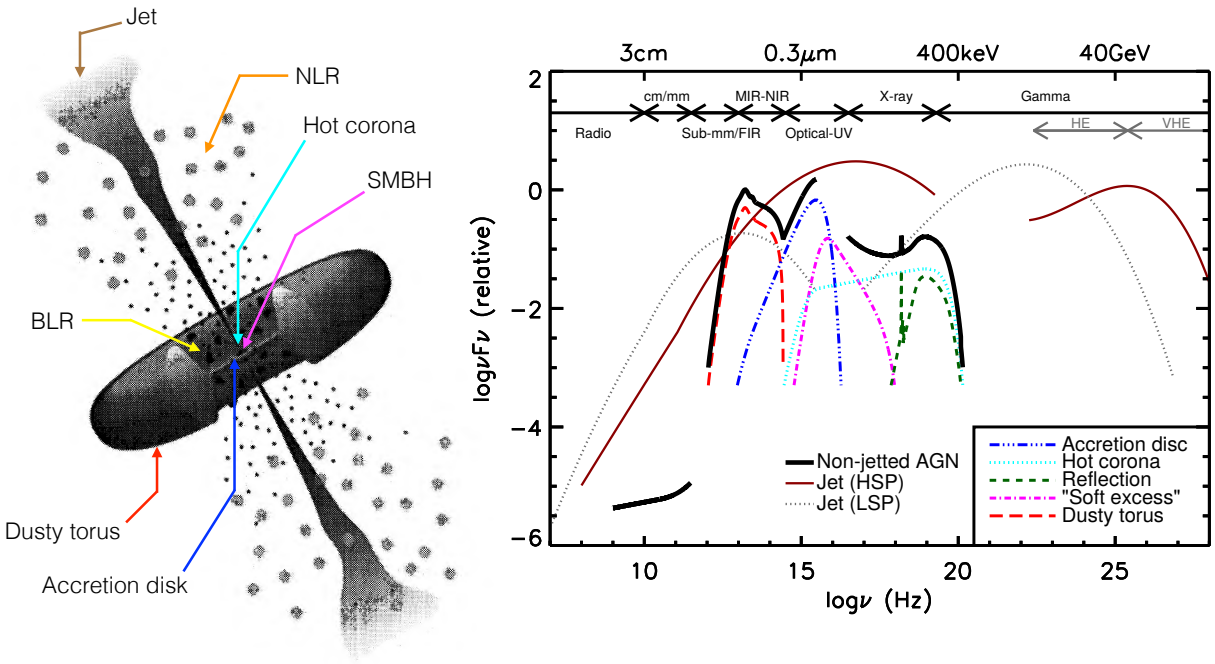

Figure 1.1: *left:* This figure is taken from the original work by Urry & Padovani (1995), demonstrating the unified model for radio-loud AGN. The SMBH in the centre is surrounded by an accretion disk. Above the accretion disk, the X-ray continuum is produced by a hot corona. While the narrow-line region (NLR) is farther away from the centre, the broad-line region (BLR) are gas clouds which are located between the accretion disk and the SMBH. These clouds are obscured by a dusty torus. Thus, it depends on the line of sight whether the BLR is visible or not. Furthermore, radio-jets perpendicular to the accretion disk are produced near the BH. These jets are characteristic for radio-loud AGN, while the other components are also present in radio-quiet AGN. *right:* Schematic representation of a typical spectral energy distribution (SED) of a non-jetted AGN (black solid line), a high synchrotron peaked (HSP) quasar (brown solid line), and a low synchrotron peaked (LSP) quasar (grey dotted line), taken from Padovani et al. (2017). The coloured lines (shifted downwards for clarity) show the different components of a non-jetted AGN.

shows the intrinsic structure of radio-loud AGN. The graph on the right-hand side of Fig. 1.1 is adapted from Padovani et al. (2017)[7], showing a typical spectral energy distribution (SED) of a non-jetted AGN (black solid line), a high synchrotron peaked (HSP) quasar (brown solid line), and a low synchrotron peaked (LSP) quasar (grey dotted line). The coloured lines (shifted downwards for clarity) show how different components contribute to the SED of a non-jetted AGN. The radiation of an AGN is believed to originate from the accretion disk surrounding the central SMBH. The SED of the accretion disk (blue dotted-dashed line) peaks in the optical light, producing the so-called 'big blue bump'. A fraction of the radiation from the accretion disk is believed to be scattered via inverse Compton scattering in the so-called hot corona, which is supposed to be located above the accretion disk. This results in the X-ray continuum (light blue dotted line), which can be described very well with a power law. Part of this X-ray radiation is reflected from the torus or the accretion disk, producing an additional X-ray component (green dashed line, see George & Fabian 1991 for further details)[8]. In the soft X-ray regime, the X-ray continuum is overlaid by the so-called 'soft excess' (magenta dotted-dashed line), a component which can be fitted by cool, optically thick thermal Comptonization emission, in contrast to the hot, optically thin Compton emission from the corona (Done et al., 2013). However, the origin of the soft excess is still a matter of debate. Done et al. (2013) argue that it is most likely additional direct radiation from the accretion disk, rather than a reflection component. Interestingly, it can be used as a tracer of the BH spin (Done et al., 2013). Another component of the SED is infrared radiation produced in the dusty torus, which is heated by the accretion disk photons, thus producing thermal radiation (red dashed line). In contrast to radio-quiet AGN (characterized by the low radio intensity, black solid line on the left), the radio-emission in radio-loud AGN can be several orders of magnitude larger. Characteristic for radio-loud AGN are enormous radio jets perpendicular to the accretion disk, which can be much larger than the visible part of the galaxy. For radio-quiet AGN the jets are much smaller or not present at all. Narrow emission lines are produced in gas clouds far away from the SMBH, in the NLR. Closer to the SMBH, where the gas velocity is higher, broad lines are produced in the BLR. Since this region is surrounded by the torus, broad lines are not visible from all viewing angles, thus separating AGN into unobscured (Type 1) and obscured (Type 2) AGN. Thereby, Type 1 AGN include both Seyfert 1 galaxies and quasars, which are simply separated by their luminosity: quasars are generally more luminous than Seyfert 1 galaxies and can thus be observed over much larger distances. Type 2 AGN are in principal Seyfert 2 galaxies, including both low and high luminosity Seyfert 2 galaxies.

[7]I follow this review for the description of the figure, as well as the original work from Harrison (2014).

[8]The vertical green dashed line represents an emission feature produced by fluorescence by iron (George & Fabian, 1991).

1.1.3 Evolutionary sequence

At the same time the first ideas about the unified model of AGN came up, it was also debated whether Seyfert 1 and Seyfert 2 galaxies represented different evolutionary stages of the same type of objects. However, with the establishment of the unified model, these ideas were not followed much further for decades. A proceeding from Osterbrock (1977) went fairly unnoticed, where he already suggested at an IAU symposium, what is a rigorous matter of debate in the current AGN community:

> *'... several Seyfert-galaxy nuclei are known to vary in light in time scales as short as a month (see e.g. Selmes et al. 1975). All of them are Seyfert 1 galaxies. It appears that the optical activity is connected with the presence of high-velocity ionized gas, but that radio emission, though sometimes present in this phase, is more often observed in the "quiescent" phase in which the ionized gas has velocities of order 500 km s^{-1}. The similarity of both radio and narrow-line optical properties suggests that narrow- and broad-line galaxies are different stages in the evolution of one and the same type of objects.'*

This quotation clearly shows that, already in 1977, Osterbrock had an impressive overview of the big picture of AGN, going beyond the classical unified model. In fact, he already distinguished between an active phase and a quiescent phase. The active phase is characterized by broad emission lines from high-velocity ionized gas and a high variability of the optical AGN luminosity. The quiescent phase is associated with radio emission and lower gas velocities. Later, the radio emission has been associated with gigantic radio jets. Today, active and quiescent phase are often called quasar-mode and radio-mode, or, more descriptively, radiative mode and jet-mode (e.g. Padovani et al., 2017).

Sanders et al. (1988) proposed that quasars are an evolutionary stage of galaxies. They observed ten ultraluminous infrared galaxies (ULIRGs) and found that all of them are interacting systems. They concluded that ULIRGs are young quasars which are still surrounded by dust. When the dust has been removed by the quasar, it appears as an optical quasar.

Two decades later Hopkins et al. (2008) revisited and refined this idea by developing a model for following the growth of BHs in simulations of galaxy mergers. They named different evolutionary phases of galaxies, beginning with an isolated disk appearing as a Seyfert galaxy. With time such disk galaxies build up galaxy groups. The member galaxies of a group interact and merge with each other, resulting in the so-called coalescence phase, in which the buried AGN appears as an (ultra-)luminous infrared galaxy (ULIRG/LIRG). During the blowout-phase the gas is removed and the BH grows rapidly until the AGN appears as quasar. Afterwards, in the decay phase, the AGN luminosity decreases again, resulting in a red elliptical galaxy. In this scenario the quasar represents the transition phase between blue disks and red elliptical galaxies. From observations of the colour-magnitude diagram or, equivalently, the star formation rate (SFR) stellar mass plane, this is also known as the so-called green valley (e.g Goulding et al., 2014; Leslie et al., 2016). The evolutionary sequence has also been constrained by observations from Hickox et al.

(2009), who, for example, compared the host galaxies of AGN selected in the radio, X-ray, and infrared (IR) wavebands. They found that X-ray selected AGN are mostly located in the green valley, radio AGN are preferably located in luminous red galaxies (LRGs), and IR AGN are hosted by bluer, less luminous galaxies, being consistent with the evolutionary sequence. Goulding et al. (2014) found a similar distinction, but only between the host galaxies of radio AGN and X-ray/IR AGN.

1.1.4 Is the unified model of AGN still valid?

Although the unified model of AGN has been broadly accepted, it seems to be outdated and has to be refined to furthermore explain recent observations. In particular that AGN evolve over time challenges the unified model of AGN, since the origin of the different observed AGN types are not just different viewing angles, but also different evolutionary stages of AGN and their host galaxies.

Furthermore, not all different components in Fig. 1.1 are directly observed. While it is relatively easy to observe large radio jets, the existence of the corona is not clear at all. The shape of the torus and whether it is present in all AGN is also highly debated, since it is feasible only indirectly with models. Direct observations of dust around AGN are very challenging and became possible only recently. Tristram et al. (2014), for example, resolve the structure of the dust around the central AGN of the Circinus galaxy using infrared interferometry. Indeed, the shape of the dust constrains the classical torus model. In contrast, other observations from Prieto et al. (2014) indicate that a torus is not always necessary to explain the observed spectra, in particular not in nearby low-luminosity AGN. They find that the obscuration can be explained by dust lanes in front of the AGN, which are not shaped like a classical torus. These findings strongly indicate that not all components in the unified model are necessary to explain AGN activity. It also implies that the observed AGN spectra can be strongly driven by external factors.

The observed spectrum of an AGN is influenced not only by dust lanes in the direct vicinity of the AGN, but also by the gas in the whole host galaxy. Buchner & Bauer (2017), for example, find that the gas of the host galaxy can produce a large fraction of all Compton-thin AGN. In particular, the obscured fraction of the most luminous AGN can be explained just by obscuration from the host galaxy.

Another, relatively new method to test the unified model is AGN clustering. In particular, measuring the clustering properties of different AGN types reveals their different spatial distributions and, thus, gives insights into their different origin. AGN clustering is a major part of this thesis (Chapter 6) and is described in the following section in detail.

1.2 AGN clustering: a method to show that AGN are special

The content of this section is part of an upcoming paper (Steinborn & Krumpe et al., in prep.), which will soon be submitted.

All galaxies are believed to host a super-massive black hole (SMBH) in their centres. However, only a small fraction of them are active, i.e., accrete material in considerable amounts and thus turn into an AGN. AGN are among the most powerful and persistent energy sources in the Universe. The high energy output allows their observation over a large fraction of cosmic time. AGN phases in the life time of a galaxy are believed to be episodic and impact the evolution of the host galaxy. Despite several decades of observational and theoretical research the triggering mechanisms of AGN are still not well understood. A fundamental question is whether AGN activity happens randomly in galaxies over their life time or in certain environments?

AGN clustering measurements, i.e., the distribution of AGN in the Universe, can be used to reveal the typical dark matter halo (DMH) mass in which AGN reside in (see review by Krumpe et al. 2014). Observationally, the clustering is most commonly derived by using the two-point correlation function. The clustering strength of an object class is described by the large-scale bias parameter b. The typical DMH mass is estimated by comparing this observed bias value to the bias parameter predictions from dark matter simulations (e.g. Sheth & Tormen, 1999; Sheth et al., 2001; Tinker et al., 2005). Although AGN clustering studies have been derived for all different wavelength ranges, most frequently optical (e.g. Croom et al., 2005; Myers et al., 2006; Coil et al., 2007; Porciani et al., 2004) and X-ray selected AGN samples (e.g. Coil et al., 2009; Hickox et al., 2009; Cappelluti et al., 2010; Allevato et al., 2014) are used. In recent years, halo occupation distribution (HOD) modelling (e.g. Peacock & Smith, 2000; Seljak, 2000; Cooray & Sheth, 2002) of the AGN two-point correlation function has been used to derive the full distribution of AGN as a function of DMH mass instead of only deriving a mean DMH mass (e.g. Shen et al., 2010; Miyaji et al., 2011; Krumpe et al., 2018).

Galaxies outnumber AGN detections at low and median redshifts. However, AGN can also be observed in sufficient numbers at high redshifts. Consequently, at low and median redshifts the clustering properties of galaxies, i.e. the large scale bias parameter and the HOD, is very accurately known as a function of different galaxy properties such as stellar mass and luminosity (e.g. Zehavi et al., 2011; de la Torre et al., 2013; Guo et al., 2013). AGN clustering studies with several thousand AGN have been carried out up to $z \sim 5$ (e.g. Shen et al., 2007, 2009).

To overcome the limitation of low signal-to-noise AGN clustering studies, one can perform cross-correlation measurements between AGN and a large tracer set of galaxies. Large area surveys such as the Sloan Digital Sky Survey (SDSS) target different object classes. Computing the distances between galaxies and AGN results in many more pairs and, thus, much lower statistical uncertainties than only measuring the distances between AGN

(auto-correlation functions). Various studies used this approach to compute the clustering properties of AGN (e.g. Li et al., 2006; Coil et al., 2007, 2009; Hickox et al., 2009; Mountrichas et al., 2009; Krumpe et al., 2010; Shen et al., 2013).

The key idea of Chapter 6 and follow-up studies is to use not only galaxy luminosity functions to test cosmological simulations, but also to utilize the observed HOD for galaxies and AGN as additional constraints that have to be reproduced by any cosmological simulation. Therefore, observations and simulations have to be compared as directly as possible (i) by including observational selection effects in the simulated data and (ii) by clearly stating the limits of the simulations. This approach of merging the efforts of observational and theoretical work can be the key to identifying missing links in the physics of AGN activity and the co-evolution with their host galaxies in simulations. Improving cosmological simulations with these new and additional constraints will therefore be a crucial test of our theoretical understanding of the co-evolution between AGN and their host galaxies.

Observed galaxy and AGN samples are affected by observational biases, such as flux/ magnitude cuts and obscuration effects. Each survey and clustering study might have different limitations and thus one should compare results from different studies with caution. Cosmological simulations have to mimic all involved observational biases as accurately as possible to enable a direct comparison between observations and simulations. Even in the case of the underlying physics being *incorrect*, simulations can be used to test the impact of observational biases on clustering properties and the HOD for galaxies and AGN.

Until now, a few authors have investigated clustering properties of AGN using semi-analytical simulations (SAMs, Fanidakis et al., 2013; Altamirano-Dévora et al., 2016; Gatti et al., 2016; Oogi et al., 2016). For example, both Gatti et al. (2016) and Oogi et al. (2016) find a lower AGN bias than in observations, especially at high redshifts. Gatti et al. (2016) point out that the bias strongly depends on selection criteria like the redshift or the luminosity range. Furthermore, Fanidakis et al. (2013) find a dependence on the BH fuelling modes, which are related to the different observed types of AGN. Krumpe et al. (2015) use semi-analytical simulations (Fanidakis et al., 2012, 2013) to mimic an X-ray selected AGN sample. They show that an AGN sample without observational biases and an observed flux-limited AGN sample show moderate differences in their clustering properties. Such findings have to be included in a proper interpretation of the observed clustering. In particular future galaxy and AGN samples will lead to clustering measurements with statistical uncertainties of up to only a few percent. Ignoring the impact of selection effects or systematic uncertainties will lead to severe misinterpretations of clustering studies.

Although SAMs can capture an extremely large volume and thus minimize statistical errors, the outcome is directly related to the input model. Thus, their numerous free parameters can be fine-tuned such that the outcome of the model agrees well with observations but the underlying physics might be not correctly represented. In contrast, fully hydrodynamic simulations (e.g. Magneticum: Hirschmann et al. 2014; Illustris: Vogelsberger et al. 2014; EAGLE: Schaye et al. 2015; MassiveBlack: Khandai et al. 2015; MUFASA: Davé et al. 2016; Horizon-AGN:Kaviraj et al. 2017; Romulus: Tremmel et al. 2017; IllustrisTNG: Springel et al. 2018) have far fewer free parameters and predict different

aspects of galaxy evolution self-consistently. Particularly in the case of incorporating AGN in the simulations, they do not require any assumptions about AGN trigger mechanisms, but automatically consider all possible scenarios within the resolution limits, ranging from galaxy mergers to smooth gas accretion. However, we remark that current state-of-the-art hydrodynamic cosmological simulations are not able to resolve in detail how the gas within the central kpc feeds the BH. Instead, the Bondi model (Hoyle & Lyttleton, 1939; Bondi, 1952; Bondi & Hoyle, 1944) is generally used to make an estimate for the accretion rate based on the properties (density, velocity, and temperature) of a specific number of gas particles surrounding the SMBH (Springel et al., 2005). In that way the accretion is smoothed out, not considering any gas clumps (e.g. G2) or star clusters which might lead to AGN flares. Furthermore, other possible AGN triggering mechanisms requiring very detailed information about the internal morphology of galaxies as well as a sufficient time resolution (e.g. disk instabilities, violent relaxation) are not resolved within cosmological simulations. Generally speaking, since hydrodynamic cosmological simulations are computationally very expensive and time consuming, the limited number of resolution elements restricts either the simulated volume or the resolution. Since most of current state-of-the-art hydrodynamic cosmological simulations focus on the formation and evolution of galaxies, they require resolutions large enough to resolve the internal structure of galaxies and, in turn, have relatively small volumes. Therefore, the clustering in these simulations can be studied only for the overall BH sample (Degraf et al., 2011) or for AGN with relatively low luminosities (Chatterjee et al., 2012; DeGraf & Sijacki, 2017), which makes a comparison with large AGN surveys like the ROSAT All Sky Survey (RASS) difficult, which, for example, detects only AGN above $L_{SXR} > 10^{43}$erg/s. However, similar to observations, where luminous quasars generally outshine their host galaxy, thus revealing no insight into their morphological structure, it is not necessary to resolve the morphology of galaxies to study the clustering of AGN. Instead, it is more important to have a large sample of AGN, also capturing the most luminous ones. For the study in Chapter 6 we use a simulation run from the Magneticum Pathfinder simulation set with a volume of (909 Mpc)^3 and a resolution which is still high enough to resolve SMBH growth sufficiently well. This simulation ran until $z = 0.25$, enabling us to compare our results for example with observed AGN from RASS.

1.3 The interplay between AGN and their host galaxies

Looking up the word 'active' in the Cambrige Dictionary[9] gives, for example, the following results: energetic or lively, involved, causing an effect or effects, in force. Thus, already the expression 'active galactic nucleus' implies that an AGN must significantly change its environment.

Fig. 1.2 shows two examples of very different active galaxies. The picture on the

[9]https://dictionary.cambridge.org/ (accessed: 01-04-2018)

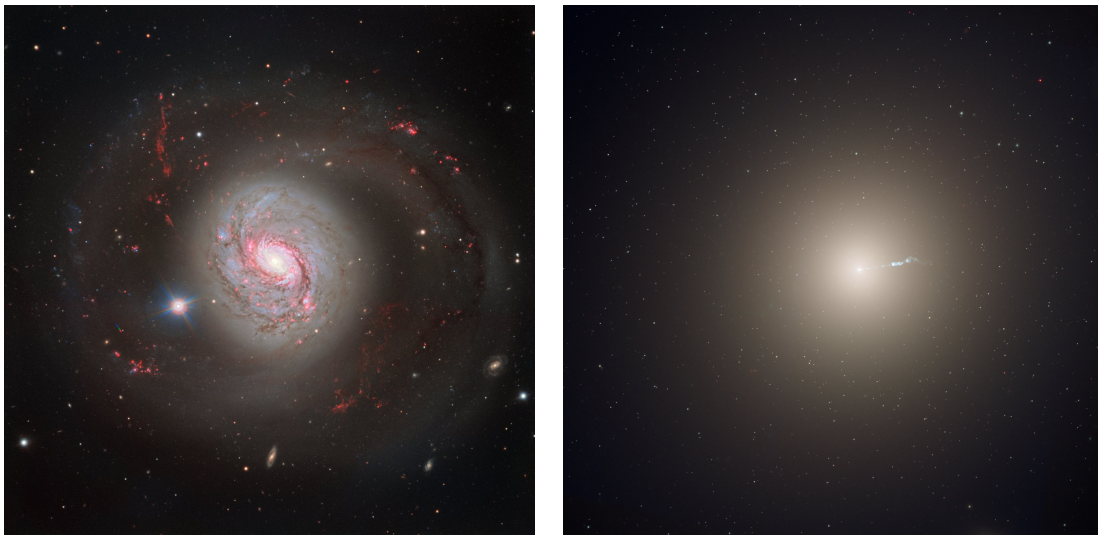

Figure 1.2: *left:* VLT image of NGC 1068. Image credit: ESO. *right:* HST image of M87. Image credit: NASA, ESA, and the Hubble Heritage Team (STScI/AURA).

left-hand side shows a VLT (Very Large Telescope) image[10] of the spiral galaxy NGC 1068, the Seyfert galaxy, which was already observed by Fath (1909). The picture on the right-hand side shows an HST (Hubble Space Telescope) image[11] of M87, a very massive elliptical galaxy, hosting a radio-loud AGN. Just by looking at the pictures in Fig. 1.2 it is intuitively clear that the AGN must enormously affect their host galaxies and vice versa.

Before I will describe the co-evolution between SMBHs and their host galaxies as well as the link between AGN activity and galaxy mergers, I will give a brief overview about galaxies in general, particularly focusing on aspects which are relevant for this thesis.

1.3.1 Galaxy morphology and scaling relations

Basically, there are four different classes of galaxies: elliptical galaxies, spiral galaxies, lenticular galaxies, and irregular galaxies[12]. Fig. 1.2 shows an example for a spiral galaxy (NGC 1068, left-hand side) and an elliptical galaxy (M87, right-hand side), both hosting an AGN. The most prominent characteristic of spiral galaxies is the galactic disk, which is typically built up of gas, dust, and young stars. In addition, most spiral galaxies have a central spheroidal component, the so-called bulge, which I will describe later in detail. Lenticular galaxies, also known as S0 galaxies, also have a galactic disk and a bulge. However, the disk is composed of relatively old stars and has no spiral arms, gas, or dust. In contrast, elliptical galaxies *'are smooth, featureless ... systems containing little or no gas*

[10]Image credit: ESO; adopted from the website https://www.eso.org/public/images/eso1720a/ (accessed: 30-03-2018)

[11]Image credit: NASA, ESA, and the Hubble Heritage Team (STScI/AURA); adopted from the website http://hubblesite.org/image/2391/gallery (accessed: 30-03-2018)

[12]see, e.g. Binney & Tremaine (2008) for a detailed description of the different galaxy types

and dust' (Binney & Tremaine, 2008). Traditionally, elliptical galaxies and S0 galaxies are also called early-type galaxies, whereas spiral galaxies and irregular galaxies are called late-type galaxies. More detailed classifications are typically made according to the so-called 'Hubble fork'[13] (Hubble, 1926), which additionally divides elliptical and spiral galaxies into sub-classes. Elliptical galaxies are classified according to their ellipticity and spiral galaxies are classified according to the size of the bulge, the structure of the spiral arms, and the presence (or not) of a bar.

Spiral and lenticular galaxies can have two different types of bulges, which have very different formation histories: classical bulges and pseudobulges (see, for example, review from Kormendy & Ho 2013. Classical bulges (e.g. Renzini, 1999) are in principle identical to elliptical galaxies. Traditionally, both are believed to form during galaxy mergers (e.g. Barnes, 1992). Following such a hierarchical structure formation scenario, massive elliptical galaxies are typically located at the centres of galaxy clusters and, thus, they have a denser environment than spiral galaxies, which are distributed more uniformly (e.g. Dressler, 1980; Strauss & Willick, 1995). Furthermore, both elliptical galaxies and classical bulges consist of relatively old stars which have in general high velocity dispersions. When an elliptical galaxy builds up a disk with time, it is classified as a spiral or lenticular galaxy as soon as the disk dominates (e.g. Steinmetz & Navarro, 2002). In contrast, during the formation of pseudobulges the disk is already present. The pseudobulge then forms out of the disk via so-called 'secular evolution', which is the redistribution of energy and mass due to interactions (e.g. review from Kormendy & Kennicutt, 2004). Consequently, in contrast to classical bulges, pseudobulges still have imprints of the disk: many pseudobulges have a flatter, more 'disk-like' morphology than classical bulges. Sometimes they even have a spiral structure and bars within the bulge. Furthermore, they consist of relatively young stars with smaller velocity dispersions than in classical bulges (Kormendy, 1993; Kormendy & Kennicutt, 2004).

It has been shown extensively that galaxies follow some fundamental scaling relations. For rotation dominated systems (spiral galaxies and irregular galaxies) the Tully-Fisher relation, a relation between the luminosity L of the galaxy and the rotational velocity v_{rot}^4 of the stars, is the tightest known correlation (Tully & Fisher 1977, see e.g. Strauss & Willick 1995 for a detailed description): $L \propto v_{\mathrm{rot}}^4$. Because v_{rot}^4 is independent of the distance, the Tully-Fisher relation can be used to estimate the distance of galaxies. Analogous to the Tully-Fisher relation, the most important scaling relation for dispersion dominated systems is the so-called Faber-Jackson relation (Faber & Jackson, 1976), which is a tight correlation between the velocity dispersion σ and the luminosity of elliptical galaxies and classical bulges: $L \propto \sigma^4$. Pseudobulges lie systematically below the Faber-Jackson relation due do their smaller velocity dispersions and higher star formation rates (e.g. Kormendy & Kennicutt, 2004). Since the Faber-Jackson relation still has a considerable amount of scatter, Djorgovski & Davis (1987) introduced the so-called fundamental plane of elliptical galaxies, a *'remarkably thin'* (Djorgovski & Davis, 1987) plane given by the logarithmic effective radius $\log R_{\mathrm{e}}$ (or the logarithmic luminosity $\log L$ within R_{e}), σ, and the logarithmic

[13] See for example Remus (2015) and references therein for details.

mean surface brightness $< I_e >$ within R_e: $R_e \propto \sigma^{1.4} < I_e >^{-0.9}$ (e.g. Kormendy & Djorgovski, 1989). Like the Tully-Fisher relation, the fundamental plane is also used to measure the distance of galaxies.

1.3.2 Co-evolution between SMBHs and their host galaxies: Scaling relations and the BH fundamental plane

Magorrian et al. (1998) discovered a correlation between the mass of SMBHs, $M_\bullet$, and the stellar mass of their host galaxies bulge, $M_{\rm bulge}$, which had been predicted theoretically by Silk & Rees (1998). Since then this relation has been constrained and revisited by many authors (e.g. Häring & Rix, 2004; Gültekin et al., 2009; McConnell & Ma, 2013; Scott et al., 2013; Kormendy & Ho, 2013). Fig. 1.3 summarizes some of these observations. Ferrarese & Merritt (2000) found an even tighter correlation between $M_\bullet$ and the velocity dispersion σ of the host galaxies' bulge, which has also been constrained by many authors (e.g. Tremaine et al., 2002; McConnell & Ma, 2013; Kormendy & Ho, 2013). Analogous to the Faber-Jackson relation, the $M_\bullet$-σ relation and thus also the $M_\bullet$-M_* relation seems to hold only for elliptical galaxies and classical bulges. Pseudobulges, however, are mostly located below the $M_\bullet$-σ relation (Kormendy & Ho, 2013). Another interpretation is that early-type and late-type galaxies follow different scaling laws. McConnell & Ma (2013), for example, find a lower normalization for late-type galaxies than for early-type galaxies, but a nearly identical slope. Similarly, Scott et al. (2013) revisited the $M_\bullet$-$M_{\rm bulge}$ relation and find very different slopes for Sérsic and core-Sérsic galaxies[14] (see Fig. 1.3): $M_\bullet \propto M_{\rm bulge}^{0.97\pm0.14}$ and $M_\bullet \propto M_{\rm bulge}^{2.22\pm0.58}$. Interestingly, the steep $M_\bullet$-$M_{\rm bulge}$ relation for Sérsic galaxies is in agreement with the intermediate mass BH in LEDA 87300, having a mass of $M_\bullet = 5{\cdot}10^4 M_\odot$ (Graham et al., 2016), and it can also explain 'over-massive' BHs like the one in NGC 1271 (Graham et al., 2016).

Combining the $M_\bullet$-σ relation with the fundamental plane of elliptical galaxies naturally implies a so-called BH fundamental plane: a tight correlation between BH mass, velocity dispersion, and either the size of the galaxy or its stellar mass. The BH fundamental plane was firstly identified by Hopkins et al. (2007b) using observations. In the same year it was constrained theoretically by Hopkins et al. (2007a). In a more recent study van den Bosch (2016) includes also spiral and lenticular galaxies, arguing that the SMBH mass scales not necessarily just with the host galaxies' bulge mass, but with the total galaxy mass, when the size of the galaxy is taken into account.

The scaling relations between BHs and their host galaxies imply a fundamental link between the growth of the central SMBH and the growth of the host galaxy, which is, however, still not fully understood. Churazov et al. (2005) shows theoretically that the $M_\bullet$-σ relation and, thus, following the Faber-Jackson relation, also the $M_\bullet$-M_* relation, reflects an equilibrium between the heating from the AGN feedback and the cooling of the gas of the host galaxy. This model predicts the slope of the $M_\bullet$-σ relation, while the

[14]The bulge of a Sérsic galaxy can be described with a single Sérsic profile, while the profile of a core-Sérsic galaxy has a partially depleted core.

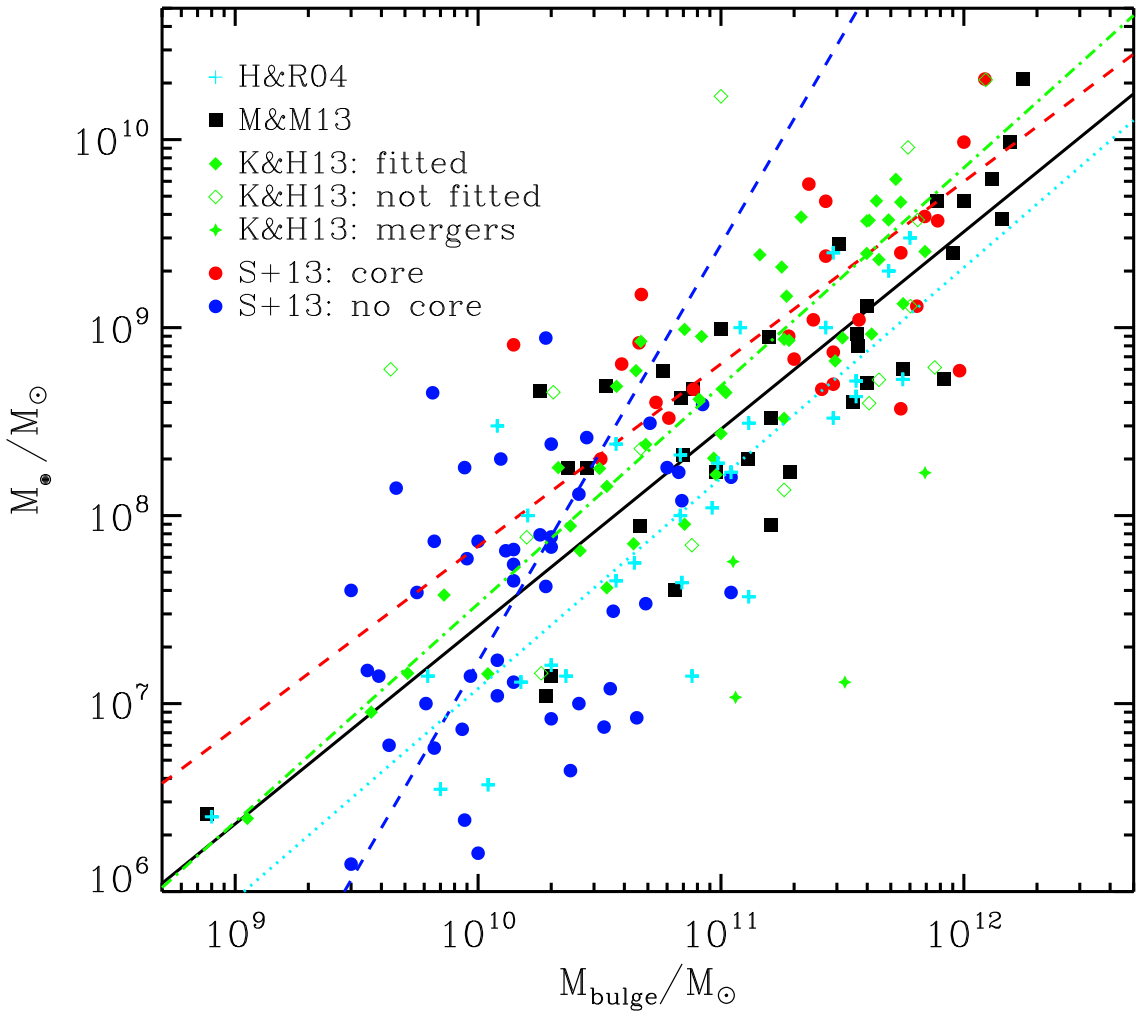

Figure 1.3: Observed relation between the stellar mass of the bulge $M_{\rm bulge}$ and the BH mass $M_\bullet$. Differently coloured symbols correspond to different observations. The lines (in the same colours) are the corresponding fits. (1) Häring & Rix (2004): light blue crosses and dotted line; (2) McConnell & Ma (2013): black squares and solid line; (3) Kormendy & Ho (2013): green symbols and dotted-dashed line (only filled green diamonds are included in the fit, open green diamonds are not included, green stars are mergers in progress, which are also not included in the fit; (4) Scott et al. (2013): red/ blue filled circles and dashed lines are core-Sérsic/ Sérsic galaxies, respectively.

normalization depends on the efficiency of the AGN feedback. In cosmological simulations (e.g. Vogelsberger et al., 2014; Khandai et al., 2015; Schaye et al., 2015; Hirschmann et al., 2014), the $M_\bullet$-$M_{\rm bulge}$ relation is often used to calibrate the AGN feedback efficiency $\epsilon_f \epsilon_r$, where ϵ_f is the fraction of the feedback energy coupling to the surrounding gas and ϵ_r is the radiative efficiency. The more efficient the AGN feedback, the less BHs grow, leading to a smaller value of the normalization for the $M_\bullet$-$M_{\rm bulge}$ relation. It is a major goal of this thesis (Chapter 3) to develop a model based on Churazov et al. (2005), which predicts the slope of the observed $M_\bullet$-M_* relation self-consistently. In this model only one free feedback parameter remains, namely ϵ_f, which is, however, barely understood both from the observational and theoretical side. A first simulation run using this model is analysed in detail in section 3, showing that not only the properties of the BHs, but also the properties of their host galaxies (e.g. SFR, stellar mass) could be improved with respect to the generally used model with constant feedback efficiencies.

1.3.3 Dual and offset AGN as tracers for AGN activity in galaxy mergers

The content of this section has been published in Steinborn et al. (2016).

When two galaxies merge with each other, a close SMBH pair can form. At the stage at which these BHs are separated by a few kpc, they can be observed as dual or offset AGN, which are also called proto super-massive binary BHs in the literature (Hudson et al., 2015). In dual AGN, both BHs are observed as AGN, whereas in offset AGN only one BH is active. Note that the expression 'offset AGN' is also used in literature for single AGN which are offset from the galaxy centre. In these cases, the offsets are thought to be caused by recoiling BHs after BH mergers (e.g. Sijacki et al. 2011, Volonteri & Madau 2008, Blecha et al. 2016). In contrast to BH pairs, recoiling BHs are not self-consistently produced by cosmological simulations. Following Comerford et al. (2015), dual and offset AGN are BH pairs with a spatial separation of less than 10kpc. However, other maximum separations up to 100kpc exist in the literature (Koss et al., 2012).

In the local Universe, offset AGN may be quite common (Comerford & Greene 2014, Comerford et al. 2009, Comerford et al. 2013), while dual AGN might be more rare (e.g. Rosario et al. 2011, Fu et al. 2011). In addition, they are still difficult to observe due to the small spatial separations. Although first evidence for the existence of dual AGN was already found by Owen et al. (1985), who observed two distinct radio jets in the radio source 3C 75 in Abell 400, only a few dual AGN have been confirmed so far. To confirm dual AGN observationally, both nuclei need to be spatially resolved (Komossa et al. 2003, Hudson et al. 2015, Bianchi et al. 2008, Koss et al. 2011, Koss et al. 2012, Mazzarella et al. 2012, Shields et al. 2012). One possibility to find dual AGN is to search for double-peaked narrow AGN emission lines. However, a double-peak alone can also be produced by the kinematics of the narrow line region of a single AGN (Müller-Sánchez et al., 2015) and hence this method can only be used to select dual AGN candidates (e.g. Comerford et al. 2009, Comerford et al. 2011, Barrows et al. 2013). Using this method, Fu et al. (2011),

Liu et al. (2013), Comerford et al. (2015) and Müller-Sánchez et al. (2015) recently found seven dual AGN systems, in which the existence of dual AGN was subsequently confirmed by spatially resolving two distinct nuclei with separations less than 10kpc.

These detections indicate that galaxy mergers might trigger AGN activity, but since observations only capture "one moment in time", it is still unclear whether the AGN are actually triggered by the gas inflow due to merger events or whether they have already been luminous before the merger event, i.e., whether their nuclear activity is driven by internal processes or due to their location in the large-scale cosmic web. Related to that, it is also a matter of vigorous debate why in some BH pairs both BHs are active and in others only one of them or even none is active.

In Steinborn et al. (2016) we investigate the origin of the differences between dual AGN, offset AGN, and inactive BH pairs. To explore the underlying driving mechanisms for AGN activity during galaxy mergers, we employ a large-scale cosmological simulation at redshift $z = 2$ with both a large volume of $(182\text{Mpc})^3$ and sufficiently high resolution to properly resolve the morphology of galaxies. In this simulation, we do not artificially keep BHs in the galaxy centre, providing a first attempt to study BH pairs in a fully cosmological context, as suggested by Volonteri et al. (2016). To get a representative sample of BH pairs, we performed a large cosmological simulation with a volume of $(182\text{Mpc})^3$ and an initial particle number of 7.2 billion particles down to redshift $z = 2$, where we find many BH pairs due to the rather high merger rate at that time. The results from Steinborn et al. (2016) are presented in Chapter 4.

1.3.4 The role of galaxy mergers for the overall AGN population

The content of this section has been published in Steinborn et al. (2018).

Most, if not all, massive galaxies are nowadays believed to contain a supermassive black hole (BH) in their centers (see e.g. Kormendy & Ho, 2013). During specific, highly variable episodes in the life of a BH, lasting up to $\sim 10^7$ yr, the BH can grow via heavy gas accretion events. Due to resultant gravitational losses, huge amounts of energy can be released, (partly) converted into radiation, causing the BH to shine as an active galactic nucleus (AGN). The required high levels of gas accretion onto a BH demand the supply of gas in the central kpc of a BH's host galaxy (fuelling) together with one or more process(es) that make the gas lose its angular momentum, enabling it to move towards the galactic center, i.e. the BH (triggering). In general, various processes are believed to be capable of generating the above prerequisites for nuclear activity, such as: secular evolution bar/disk instabilities (Shlosman et al., 1989); violently unstable disks (Dekel et al., 2009; Bournaud et al., 2011); gas cooling from the hot halo (Croton et al., 2006); galaxy merger events (Silk & Rees, 1998; Springel et al., 2005); fly-bys (Hopkins et al., 2008); mass loss from stellar winds (Davies et al., 2012); and smooth gas accretion from the halo (King & Pringle, 2007) – in part demonstrated by idealised hydrodynamic simulations of isolated galaxies. However, which of the physical mechanisms are the most efficient and most common drivers for nuclear activity, still remains a heavily debated issue.

Traditionally, merger events have been thought to be the *main* process for igniting nuclear activity, simultaneously generating a starburst and forming a stellar bulge in a galaxy. This conventional picture has been historically motivated by the observed relation between the BH and stellar bulge mass (Magorrian et al., 1998; Häring & Rix, 2004), by direct observations of merger signatures in AGN host galaxies (e.g. Sanders et al., 1988), and pushed forward by a number of binary merger simulations (e.g. Di Matteo et al., 2005; Hopkins et al., 2006, 2008). As a consequence, in many modern semi-analytic galaxy formation models (SAMs), AGN activity is (still) assumed to be mostly driven by major and minor mergers (e.g. De Lucia et al., 2006; Somerville et al., 2008; Henriques et al., 2015; Hirschmann et al., 2016).

Some theoretical studies, employing either idealised simulations as outlined above, phenomenological models or SAMs, started to challenge this traditional "merger paradigm". Specifically the latter model predictions indicated the necessity to add other processes as drivers for nuclear activity, in order to reproduce the observed evolution of the AGN luminosity function, in particular the faint end (e.g. Hirschmann et al., 2012; Fanidakis et al., 2012). Nevertheless, both refined SAMs as well as phenomenological models point towards an increasing relevance of mergers for driving AGN activity with increasing luminosity (e.g., Menci et al., 2014; Hickox et al., 2014; Weigel et al., 2018).

In addition to theoretical studies, during the last couple of years, an increasingly large amount of observations further severely questioned our traditional merger paradigm: specifically, Grogin et al. (2005); Cisternas et al. (2011); Kocevski et al. (2012); Villforth et al. (2014); Rosario et al. (2015); Mechtley et al. (2016); Villforth et al. (2017) find no statistically relevant evidence for an enhanced fraction of mergers in active galaxies, compared to a control sample of inactive galaxies (see, however, Cotini et al., 2013; Hong et al., 2015). Even if the majority of modern observational studies agree that for low- and intermediate-luminosity AGN merger events play only a minor role (see also Del Moro et al., 2016), some observations indicate that for luminous AGN, mergers may still be a statistically relevant driving mechanism, due to measured merger fractions of up to 80 per cent (Fan et al., 2016; Urrutia et al., 2008; Glikman et al., 2015; Treister et al., 2012; Hopkins & Hernquist, 2009). In contrast, observations from Villforth et al. (2017) and Hewlett et al. (2017) question such a relation: they find no signs for major mergers being the dominant mechanism for triggering luminous AGN at $z \sim 0.6$, as their major merger fractions stay fairly low ($\leq 20\%$); moreover, up to $z = 2$, the AGN merger fractions of a given AGN luminosity are only marginally enhanced with respect to those of inactive galaxies.

These rather controversial observational results are likely a consequence of a combination of various limitations and complications of AGN surveys: dust obscured AGN/merger signatures; the difficulty in detecting AGN activity delayed relative to the actual merger event; the visibility of signatures for (minor) mergers; or other selection effects. As an example, Kocevski et al. (2015), Weston et al. (2017), Urrutia et al. (2008), Fan et al. (2016), and Ricci et al. (2017) find that heavily obscured or reddened AGN have very high incidences of merger features. Furthermore, Juneau et al. (2013) find that galaxies with enhanced specific star formation rates have a higher obscured AGN fraction, which could be linked to an evolutionary phase in gas-rich mergers. Schawinski et al. (2010),

investigating a sample of early-type galaxies in different evolutionary phases, show that merger signatures are often hardly visible anymore due to a potentially large time delay between the merger event and the peak of AGN activity. Studies analysing the incidence of nuclear activity with respect to the nearest neighbour separation (Koss et al., 2010; Ellison et al., 2011, 2013; Satyapal et al., 2014) find enhanced fractions of AGN the smaller the distance to the nearby neighbours (merging galaxy) and a particularly high AGN fraction in post-mergers, supporting the time-delay scenario. But again, despite this observational evidence that merger events are *principally* capable of driving nuclear activity, most modern studies agree that *statistically*, the majority of nuclear activity in AGN populations (dominated by faint and moderately luminous AGN) is likely driven by mechanisms other than mergers – even though many details remain hardly understood.

To overcome these observational limitations, we can take advantage of hydrodynamic simulations, which self-consistently capture all stages of a merger process and corresponding gas fuelling onto the BH. Up to now, many numerical studies, focusing on AGN driving mechanisms, employed idealised hydrodynamic simulations of isolated galaxies or isolated binary mergers (e.g. Di Matteo et al., 2005; Hopkins et al., 2006; Hopkins & Quataert, 2010; Capelo et al., 2015), neglecting any cosmological context and, thus, not following merger rates and AGN populations over cosmic time. However, recent large-scale *cosmological* hydrodynamic simulations (e.g. Magneticum: Hirschmann et al., 2014; EAGLE: Schaye et al., 2015; IllustrisTNG: Pillepich et al., 2018; MassiveBlack: Khandai et al., 2015; Horizon-AGN: Dubois et al., 2016; ROMULUS: Tremmel et al., 2017; IllustrisTNG: Springel et al., 2018), providing statistically relevant and fairly realistic AGN and BH populations (e.g. Hirschmann et al., 2014; Sijacki et al., 2015; Volonteri et al., 2016; Rosas-Guevara et al., 2016; Weinberger et al., 2017), allow us to investigate the *statistical significance* of mergers for nuclear activity *at different cosmic epochs*, with respect to other processes, such as smooth gas accretion (Martin et al., 2018)[15]. To date, however, a statistical analysis directly linking AGN activity to the merger history and the merger rates of the host galaxy is still widely lacking.

In Section 5, we close this gap: we take advantage of the Magneticum Pathfinder simulation set[16] (Dolag et al. in prep., Hirschmann et al. 2014) to statistically investigate the role of merger events for driving nuclear activity in a galaxy. Due to limited resolution in a cosmological set-up, our analysis is restricted to explore *the impact of mergers on fuelling gas onto the central few kpc* of a galaxy. Specifically, our analysis evolves around two related questions:

- To what extent does the merger history affect the incidence for nuclear activity in galaxies, as well as the ISM properties in the central few kpc of a galaxy, which are controlling the accretion luminosities?

- What is the probability that an AGN host galaxy of a given luminosity has experi-

[15]Note that the resolution in large-scale cosmological simulations is not high enough to study the role of secular evolution disk instabilities and/or violently unstable disks for nuclear activity or to examine processes driving the gas from the central few kpc to the innermost regions close to the BH.

[16]www.magneticum.org

enced a recent merger event, and to what extent do these merger fractions reflect an intrinsic AGN-merger connection?

The results of Steinborn et al. (2018), which is the second in a series focusing on BH growth and AGN populations using the Magneticum set, are presented in Chapter 5 In Paper I (Hirschmann et al., 2014) we demonstrated that AGN luminosities together with their anti-hierarchical trend are consistent with observations over cosmic time. In addition, our simulations can successfully reproduce various other observed galaxy and BH properties (e.g., Teklu et al., 2015; Steinborn et al., 2015; Remus et al., 2017; Teklu et al., 2017; Remus et al., 2017; Teklu et al., 2018; Schulze et al., 2018) providing an ideal testbed for our study. We emphasize that thanks to the uniquely large simulated volume of $(500\ \mathrm{Mpc})^3$, we are able to study the AGN-merger connection for the rarest very luminous quasars, which are not accessible in most other state-of-art simulations (like EAGLE, Illustris).

1.4 Modelling the physics of AGN within cosmological simulations

Although the number of resolution elements in cosmological hydrodynamic simulations increases continuously, current state-of-the-art cosmological simulations are still far away from resolving the actual physics of SMBHs and their related AGN activity. Nonetheless, it is without doubt that AGN feedback is essential for the formation and evolution of galaxies. Therefore, it is absolutely necessary to mimic the effect of AGN feedback as closely as possible in simulations of galaxy formation. In this chapter I will describe the physical mechanisms related to the growth of SMBHs which need to be considered in such simulations and summarize the various methods used to model them within a cosmological context.

1.4.1 Simulations of SMBH growth: a general overview

During the last few years, large-scale hydrodynamic cosmological simulations have established themselves as one of the most powerful tools to make predictions for the evolution of the baryonic structures in the Universe. Thanks to the increasing power of modern supercomputers, the resolution in these simulations has been increased, helping to resolve the morphological structures of galaxies, even producing disk galaxies (Vogelsberger et al. 2014, Schaye et al. 2015, Remus et al. 2015, Teklu et al. 2015), which was a long-standing problem in the past. Such simulations (e.g. Magneticum: Hirschmann et al. 2014; Illustris: Vogelsberger et al. 2014; EAGLE: Schaye et al. 2015; MassiveBlack: Khandai et al. 2015; MUFASA: Davé et al. 2016; Horizon-AGN:Kaviraj et al. 2017; Romulus: Tremmel et al. 2017; IllustrisTNG: Springel et al. 2018) produce larger and larger samples of simulated galaxies, including more and more detailed physical sub-grid models, for instance for star formation (e.g. Springel & Hernquist, 2002; Schaye & Dalla Vecchia, 2008), stellar evolution, supernova feedback, chemical enrichment (e.g. Tornatore et al., 2003, 2007; Pillepich

et al., 2018), magnetic fields (e.g. Pakmor et al., 2011; Pakmor & Springel, 2013), and the evolution of SMBHs and their associated AGN feedback (Springel et al., 2005; Fabjan et al., 2010; Rosas-Guevara et al., 2015; Steinborn et al., 2015; Weinberger et al., 2017, e.g.). The overall properties of these simulated galaxy samples (e.g. the stellar mass function, the star formation main sequence, the mass-size relation, and the mass-metallicity relation) do in general agree surprisingly well with observations, given the fact that they are produced self-consistently (e.g. Hirschmann et al., 2014; Steinborn et al., 2015; Remus et al., 2017; Dolag et al., 2017; Weinberger et al., 2017).

Simulations including SMBHs do also reproduce the observed BH mass function as well as the observed scaling relations between BHs and their host galaxies relatively well, for example the $M_\bullet$-M_* relation and the stellar mass M_*, or the $M_\bullet$-σ relation (e.g. Sijacki et al., 2015; Hirschmann et al., 2014; Steinborn et al., 2015; Weinberger et al., 2017).

1.4.2 Sub-grid models for SMBHs

The content of this section has been published in Steinborn et al. (2015).

Black holes play an essential role in the formation and evolution of galaxies. They can even influence galaxy clusters and the intra cluster medium (ICM). However, observations of active galactic nuclei (AGN) indicate that gas accretion onto black holes and AGN feedback are complex processes, which are not yet fully understood (e.g. Merloni & Heinz 2007, McNamara et al. 2011, Ma et al. 2013). There is evidence for two distinct phases of AGN activity and feedback: the radio-mode and the quasar-mode. The radio-mode is characterized by large radio jets generating hot X-ray cavities (Russell et al. 2013, Mezcua & Prieto 2014), whereas in the quasar-mode the emission is dominated by the accretion disk, which is visible as the so-called blue bump in the spectrum of quasars and Seyfert galaxies (e.g. Elvis et al. 1994, Prieto et al. 2010).

Churazov et al. (2005) characterized this distinction in a theoretical model by describing AGN feedback with two components: radiation and mechanical outflow. In their model the amount of energy associated with each component depends on the Eddington ratio $f_{\mathrm{Edd}} = \dot{M}_\bullet / \dot{M}_{\mathrm{Edd}}$. When a black hole accretes with the Eddington accretion rate $\dot{M}_{\mathrm{Edd}}$, gas cooling and AGN feedback are in equilibrium. Churazov et al. (2005) also took advection-dominated accretion flows (ADAFs) into account, although a jet contribution can successfully replace an ADAF (Falcke et al. 2004, Fernández-Ontiveros et al. 2011).

To constrain this model and to really understand the origin of different types of AGN and how they influence their environment, large cosmological simulations play a key role. They have two major advantages: firstly, they provide a statistically large sample of black holes. This allows to compare the simulations to the newest and currently most complete observations of the $M_\bullet$-M_* relation (e.g. McConnell & Ma 2013) or black hole mass functions (e.g. Marconi et al. 2004, Shankar et al. 2004, Shankar et al. 2009) and stellar mass functions (e.g. Muzzin et al. 2013, Bernardi et al. 2013), in particular the very massive end. Secondly, having large enough cosmological boxes where also massive galaxy clusters form, allows to probe the influence of black holes across all scales of cosmic environment.

There already exist a number of studies discussing large cosmological simulations that include black holes (e.g. Di Matteo et al. 2005, Di Matteo et al. 2008, Robertson et al. 2006, Teyssier et al. 2011, Degraf et al. 2011, Booth & Schaye 2009, Khandai et al. 2015, Rosas-Guevara et al. 2015, Hirschmann et al. 2014, Vogelsberger et al. 2014, Schaye et al. 2015). Those simulations mostly use the black hole model implemented by Springel et al. (2005) or are based on it. In these models – in contrast to some more simplified black hole models (e.g. Battaglia et al. 2010) – black holes are typically described as sink particles which have fundamental properties like mass and accretion rate, which can be linked directly to observables. Hence, we can study black hole growth and the co-evolution between black holes and their host galaxies to constrain and improve the parametrization of the underlying model. In the model from Springel et al. (2005) the gas accretion onto black holes is calculated according to the Bondi formula (Hoyle & Lyttleton 1939, Bondi 1952, Bondi & Hoyle 1944), multiplied by a so-called boost factor α. This factor was introduced to account for the limited resolution in simulations leading to smaller densities and larger temperatures near the black hole (Booth & Schaye, 2009). To estimate the AGN feedback, a constant value for the radiative efficiency is typically used (Shakura & Sunyaev 1973).

For low resolutions this model works reasonably well. However, to study not only the origin of the observed fundamental relations between black holes and their host galaxies (Häring & Rix 2004, Tremaine et al. 2002, McConnell & Ma 2013), but also the impact of gas accretion and AGN feedback on the morphology of the galaxy, simulations with higher resolution are needed. Until now, this was only studied in simulations of isolated galaxies and mergers of galaxies (e.g. by Hopkins et al. 2008, Debuhr et al. 2011, Van Wassenhove et al. 2014, Capelo et al. 2015) as well as in cosmological zoom simulations (e.g. by Anglés-Alcázar et al. 2013, Marinacci et al. 2014, Dubois et al. 2013, Choi et al. 2014). To reproduce both statistical black hole and galaxy properties within a fully cosmological context and across various environments in a statistically relevant sample size, large cosmological boxes with high resolution are needed. This is still a challenge, but thanks to increasing computational power it now becomes feasible. However, despite of this success, new challenges arise as simulations typically over-estimate the high-mass end of the black hole and stellar mass function (e.g. Sijacki et al. 2015, Khandai et al. 2015, Vogelsberger et al. 2014, Genel et al. 2014, Hirschmann et al. 2014). Therefore, a more detailed black hole model is necessary.

In Chapter 3 (Steinborn et al., 2015) we extend the model by Springel et al. (2005) by improving the treatment of the two modes of AGN feedback: radiation and mechanical outflows. Following theoretical predictions (Churazov et al. 2005, White & Frenk 1991, Narayan & Yi 1995) as well as recent observational results (Davis & Laor 2011, Chelouche 2013, Russell et al. 2013) gives us estimates for the corresponding two efficiencies depending on the black hole mass and the accretion rate, which outreaches the simplified black hole model commonly used in simulations.

Following Sijacki et al. (2007), a steep transition between radio-mode and quasar-mode is often used in current simulations (e.g. Fabjan et al. 2010, Hirschmann et al. 2014). This is only a rough approximation to the smooth transition which is observed and also theoretically expected. Adopting the model by Churazov et al. (2005) - which was

already constrained by observations, e.g. Russell et al. 2013 - allows us to get a smooth transition between the two modes. This was used by Hirschmann et al. (2014) to calculate AGN luminosities, but it was never implemented into simulations. Such modifications were also suggested by a recent paper of Sijacki et al. (2015), who studied the AGN luminosity function within a cosmological simulation using a constant radiative efficiency. They concluded that in the radio-mode radiative efficiencies might depend on the accretion rate and on average should be lower than the value 0.1 used in the original black hole model from Springel et al. (2005). Furthermore, Davis & Laor (2011) and Chelouche (2013) found that the radiative efficiency not only correlates with the accretion rate, but also with the black hole mass.

Another deficiency in current implementations of black holes in cosmological simulations is that the (original) Bondi model predicts far too low accretion rates during the quasar-mode so that black holes do not reach the observed masses for a given bulge mass. Therefore, a so-called boost factor is commonly used to artificially raise the accretion rates. This results in realistic accretion rates for the accretion of cold gas. However, it has the disadvantage that it also raises the accretion rate when the hot gas content is large enough to fulfill the assumptions of the Bondi model, namely when the gas is distributed in an isotropic sphere. This typically is the case in old quiescent galaxies. Consequently, black holes become too massive at low redshifts. Hence, accretion rates have to be lower in the radio-mode (Li et al., 2013).

Indeed, several studies adapt the black hole model for higher resolution simulations by using a boost factor which depends on the resolution (Choi et al. 2012, Choi et al. 2014), density (Booth & Schaye 2009), pressure (Vogelsberger et al. 2013) or angular momentum (Rosas-Guevara et al., 2015), although none of them contains a direct distinction between the accretion of cold and hot gas, even if the existence of such two distinct accretion modes has been shown by observations (e.g. Hlavacek-Larrondo et al. 2013) and predicted by high-resolution simulations of black hole accretion on sub-kpc scales (Gaspari et al. 2013, Bourne et al. 2014) as well as semi-analytical models (e.g. Somerville et al. 2008, Hirschmann et al. 2012, Fanidakis et al. 2011, Fanidakis et al. 2013). A distinction between accretion of cold and hot gas based on the multi-phase model from Springel & Hernquist (2003) was implemented in the simulations from Pelupessy et al. (2007). In their study, the molecular gas of the star forming particles was evaluated from a multi-phase model, in which the accretion of this cold gas was evaluated separately without any boost factor, assuming the corresponding temperature as fixed in the underlying multi-phase model.

A black hole mainly grows in the quasar-mode, where cold gas forms an accretion disk around the black hole which leads to higher accretion rates. During that period, black holes grow until the AGN feedback and gas cooling are in equilibrium. At that point, they reach the $M_\bullet$-σ relation (Churazov et al., 2005) and thus, the $M_\bullet$-M_* relation. Consequently, the accretion rate drops until the black hole crosses the threshold towards the radio-mode. As reviewed by several authors (e.g. Yuan & Narayan 2014, Heckman & Best 2014), the accretion in the radio-mode, sometimes also called jet-mode, can be described with ADAFs containing hot gas (Yuan et al., 2009). Alternatively, the accretion of hot adiabatic gas can be described with the Bondi model (Gaspari et al., 2013). Therefore, we distinguish

between hot and cold gas and estimate the accretion rate separately for both gas phases. This allows us to use different boost factors for hot and cold gas and thus, to account for both observed accretion modes. Our refined model for BH accretion and AGN feedback has been published in Steinborn et al. (2015) and is presented in Chapter 3 of this thesis.

1.4.3 Accretion onto BHs: the Bondi model and beyond

The huge amount of energy released by an AGN could relatively early be explained by accretion onto a very massive, compact central object, possibly a neutron star or a SMBH (e.g. Novikov & Thorne, 1973; Weedman, 1977, and references therein). Most cosmological simulations including BH growth use the model from Springel et al. (2005) or are based on it. To estimate the accretion rate onto BHs, Springel et al. (2005) use the Bondi-Hoyle-Lyttleton approach (Hoyle & Lyttleton 1939, Bondi & Hoyle 1944, Bondi 1952).

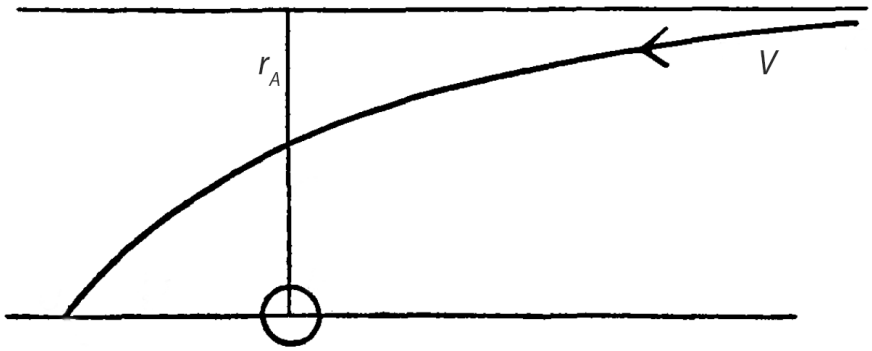

Figure 1.4: Sketch of the accretion model. The sketch is taken from Hoyle and Lyttleton (1939) and has been slightly modified.

Figure 1.4 shows a sketch[17] from Hoyle & Lyttleton (1939), who calculated the accretion rate $\dot{M}$ of a star. They argued that the number of accreted particles per second is the number of particles crossing an area bound by a circle of radius r_A. This accretion radius is perpendicular to the velocity v of the test particles and can be expressed by

$$r_\mathrm{A} = \frac{2GM}{v^2}. \tag{1.1}$$

Thus, Hoyle & Lyttleton (1939) concluded

$$\dot{M} = \pi r_\mathrm{A}^2 \rho v = \frac{4\pi G^2 M^2 \rho}{v^3}, \tag{1.2}$$

where ρ is the gas density.
A few years later Bondi & Hoyle (1944) noticed that forces due to gas pressure have to be

[17]Note that the notation has been changed according to the notation used in this thesis.

considered, given by the factor $\alpha_{\rm HL}$. With numerical calculations they found $\alpha_{\rm HL} = 1.25$ and concluded

$$\dot{M} = \pi \alpha_{\rm HL} r_{\rm A}^2 \rho v = \frac{2.5\pi G^2 M^2 \rho}{v^3}. \tag{1.3}$$

Later Bondi (1952) derived the accretion rate considering the effects of pressure analytically, assuming that the gas is ideal and adiabatic. The calculation is based on the equation of continuity

$$4\pi r^2 \rho v = \text{const} = \dot{M} \tag{1.4}$$

and on Bernoulli's equation

$$\frac{v^2}{2} + \int_{p_\infty}^{p} \frac{\mathrm{d}p}{\rho} - \frac{GM}{r} = \text{const}(= 0). \tag{1.5}$$

The constant equals zero if the boundary conditions are at infinity. With

$$\frac{p}{p_\infty} = \left(\frac{\rho}{\rho_\infty}\right)^\gamma \tag{1.6}$$

one can write equation (1.5) as

$$\frac{v^2}{2} + \frac{\gamma}{\gamma - 1}\frac{p_\infty}{\rho_\infty}\left[\left(\frac{\rho}{\rho_\infty}\right)^{\gamma-1} - 1\right] = \frac{GM}{r}, \tag{1.7}$$

where γ is the adiabatic index. At that point Bondi (1952) introduces three non-dimensional variables x, y and z to replace r, v and ρ:

$$r = \frac{xGM}{c_{\rm s}^2}, \tag{1.8}$$

$$v = yc_{\rm s}, \tag{1.9}$$

$$\rho = z\rho_\infty. \tag{1.10}$$

$c_{\rm s}$ is the sound speed and ρ_∞ the density at infinity. Then one can write equation (1.4) as

$$\dot{M} = \frac{4\pi\lambda G^2 M^2 \rho_\infty}{c_{\rm s}^3} \tag{1.11}$$

with $x^2 yz = \lambda$. Using

$$c_{\rm s}^2 = \gamma \frac{p_\infty}{\rho_\infty} \tag{1.12}$$

equation(1.7) can be written as

$$\frac{1}{2}y^2 + \frac{z^{\gamma-1} - 1}{\gamma - 1} = \frac{1}{x}. \tag{1.13}$$

From equation (1.11) and (1.13) Bondi (1952) calculated the maximum value of λ:

$$\lambda_c = \left(\frac{1}{2}\right)^{\frac{\gamma+1}{2(\gamma-1)}} \left(\frac{5-3\gamma}{4}\right)^{-\frac{5-3\gamma}{2(\gamma-1)}}. \tag{1.14}$$

Thus, the accretion rate depends on γ. Setting $\gamma = 5/3$ we get

$$\dot{M} = \pi G^2 M^2 \frac{\rho_\infty}{c_\mathrm{s}^3}. \tag{1.15}$$

This defines the Bondi-Hoyle radius as it is mentioned for example by Booth & Schaye (2009) and Edgar (2004):

$$r_\mathrm{B} = \frac{GM_\bullet}{c_\mathrm{s}^2}. \tag{1.16}$$

In the literature different values for γ have been used. For the interstellar medium with $\gamma = 1.4$ (Frank et al. 1992), for example, equation (1.11) becomes $\dot{M} = 2.5\pi G^2 M^2 \frac{\rho_\infty}{c_\mathrm{s}^3}$. In contrast, Bondi (1952) used the value $\gamma = 3/2$ and concluded

$$\dot{M} = 2\pi G^2 M^2 \frac{\rho_\infty}{c_\mathrm{s}^3}. \tag{1.17}$$

In contrast to the velocity-limited case given by equation (1.3), equation (1.17) describes the temperature-limited case. Bondi (1952) concluded that the real accretion rate is an interpolation between these two cases, containing dynamical effects as well as the effects of pressure:

$$\dot{M} = \frac{2\pi G^2 M^2 \rho_\infty}{(v^2 + c_\mathrm{s}^2)^{3/2}}. \tag{1.18}$$

Later, Shima et al. (1985) showed that the best interpolation is differs by the factor 2 from the estimation from Bondi (1952):

$$\dot{M} = \frac{4\pi G^2 M^2 \rho_\infty}{(v^2 + c_\mathrm{s}^2)^{3/2}}. \tag{1.19}$$

Shima et al. (1985) introduced an effective accretion radius r_Ae. Accordingly, the accretion rate is given by

$$\dot{M} = \pi r_\mathrm{Ae} \rho_\infty v. \tag{1.20}$$

Combining equation (1.20) with equation (1.18) gives

$$r_\mathrm{Ae} = \frac{2^{1/2} \cdot GM}{(v^2 + c_\mathrm{s}^2)^{3/4} \cdot v^{1/2}}. \tag{1.21}$$

Shima et al. (1985) argued that $r_\mathrm{Ae}/r_\mathrm{A}$ had to approach unity for large Mach numbers M_∞ at infinity. From the equations (1.1) and (1.21) one gets

$$\frac{r_\mathrm{Ae}}{r_\mathrm{A}} = 2^{-1/2} \left(\frac{M_\infty^2}{M_\infty^2 + 1}\right)^{3/4}. \tag{1.22}$$

Thus, Shima et al. (1985) concluded that equation (1.22) had to be multiplied by $2^{1/2}$. This explains equation (3.1). For $v = c_\mathrm{s}$ equation (1.21) becomes the Bondi radius (e.g. Choi et al., 2012)

$$r_\mathrm{B} = \frac{2GM_\bullet}{c_\mathrm{s}^2 + v^2}, \tag{1.23}$$

which implies that the Bondi radius is the threshold between subsonic and supersonic flows.

In Springel et al. (2005), equation (3.1) is multiplied by a so-called boost factor α:

$$\dot{M}_\mathrm{B} = \frac{4\pi\alpha G^2 M_\bullet^2 \rho}{(c_\mathrm{s}^2 + v^2)^{3/2}}. \tag{1.24}$$

The factor α is generally estimated empirically and is typically set to a constant value of $\alpha = 100$ following Springel et al. (2005). Before we summarize methods to estimate α more physically, we describe how equation (1.24) is realized in hydrodynamic simulations. There are two different approaches in literature to estimate $\dot{M}_\mathrm{B}$ based on the properties of the surrounding gas particles. In most simulations (also in the Magneticum Simulations) $\dot{M}_\mathrm{B}$ is computed using the mean values of ρ, c_s and v of a specific number of surrounding gas particles:

$$\dot{M}_\mathrm{B} = \frac{4\pi\alpha G^2 M_\bullet^2 \langle\rho\rangle}{(\langle c_\mathrm{s}\rangle^2 + \langle v\rangle^2)^{3/2}}. \tag{1.25}$$

In contrast, Choi et al. (2012) use an alternative method, averaging $\dot{M}_\mathrm{B}$ for all single gas particles over the SPH kernel:

$$\dot{M}_{\mathrm{B,\ AA}} = \left\langle \frac{4\pi\alpha G^2 M_\bullet^2 \rho}{(c_\mathrm{s}^2 + v^2)^{3/2}} \right\rangle \tag{1.26}$$

That way the dependency on the chosen number of neighbouring gas particles is reduced, since outer particles contribute less to the overall accretion rate.

Generally, the black hole accretion rate $\dot{M}_\bullet$ is limited by the Eddington accretion rate. In other words: matter can only be radiated if the radiation force is smaller than the gravitational force for an electron proton pair:

$$\frac{\sigma_\mathrm{T} L}{4\pi r^2 c} < \frac{GM_\bullet(m_\mathrm{p} + m_\mathrm{e})}{r^2}, \tag{1.27}$$

where m_p is the proton mass, m_e the electron mass, and σ_T the Thompson scattering cross section. Using the approximation $m_\mathrm{p} + m_\mathrm{e} \approx m_\mathrm{p}$ and solving equation (1.27) for L defines the Eddington luminosity:

$$L_\mathrm{Edd} := \frac{4\pi G c m_\mathrm{p} M_\bullet}{\sigma_\mathrm{T}}. \tag{1.28}$$

With $L = \epsilon_\mathrm{r}\dot{M}c^2$, the Eddington accretion rate is given by:

$$\dot{M}_\mathrm{Edd} = \frac{L_\mathrm{Edd}}{\epsilon_\mathrm{r} c^2} = \frac{4\pi G M_\bullet m_\mathrm{p}}{\epsilon_\mathrm{r}\sigma_\mathrm{T} c}, \tag{1.29}$$

where

$$\epsilon_{\mathrm{r}} = \frac{L}{\dot{M}c^2} \tag{1.30}$$

(Springel et al. 2005) is the radiative efficiency. Thus, the black hole accretion rate $\dot{M}_\bullet$ is given by

$$\dot{M}_\bullet = \min(\dot{M}_{\mathrm{B}}, \dot{M}_{\mathrm{Edd}}). \tag{1.31}$$

Let us now have a closer look onto the boost factor α: Booth & Schaye (2009) verify this parameter by two arguments. The first is the uncertainty in the estimation of the temperature of the accreted gas and thus of the sound speed c_{s} of the interstellar medium (ISM). The reason for that is the limited resolution but also the uncertainty in the physics of the cold-phase of the ISM. Booth & Schaye (2009) argue that the temperature might be overestimated, which justifies large values of α. Their second argument for introducing α is that the Jeans length is not resolved in low-resolution simulations. The Jeans length λ_{J} is the length at which pressure and gravitational forces are in equilibrium (Peebles 1993). Thus, the gravitational growth time $t_{\mathrm{g}} \sim (G\rho_0)^{-1/2}$ is comparable to the time $t_{\mathrm{J}} \sim \lambda_{\mathrm{J}}/c_{\mathrm{s}}$ for a pressure wave to move across the Jeans length (Peebles 1993). The Jeans mass M_{J} is the mass within a sphere of diameter λ_{J} and density ρ_0:

$$M_{\mathrm{J}} = \frac{4\pi}{3}\rho_0 \left(\frac{1}{2}\lambda_{\mathrm{J}}\right)^3 \tag{1.32}$$

(Binney & Tremaine 2008). Thus, the Jeans length can be expressed as

$$\lambda_{\mathrm{J}} \sim \sqrt{\frac{c_{\mathrm{s}}^2}{G\rho}} \sim \frac{GM_{\mathrm{J}}}{c_{\mathrm{s}}^2}. \tag{1.33}$$

The equations (1.16) and (1.33) show that for $M_\bullet > M_{\mathrm{J}}$ the Bondi radius is resolved if the Jeans length is resolved. Thus, the above argument that the Jeans length is not resolved at low resolutions leads to an underestimation of the density at the Bondi radius.

Booth & Schaye (2009) concluded from the above arguments that α should be a function of the density rather than being constant:

$$\alpha = f(n) = \begin{cases} 1, & \text{if } n_{\mathrm{H}} < n_{\mathrm{H}}^*, \\ \left(\frac{n_{\mathrm{H}}}{n_{\mathrm{H}}^*}\right)^\beta, & \text{otherwise} \end{cases} \tag{1.34}$$

where $n_H^* = 0.1\mathrm{cm}^{-3}$. n_{H}^* is the threshold density above which a cold interstellar gas phase forms. This guarantees that the accretion is described correctly when the resolution allows it and that the accretion rate is increased artificially by α when not. Although this makes the accretion more realistic rather than using a constant α there is still one free parameter β. Thereby, the values of both α and β are not motivated physically. In Chapter 3 (Steinborn et al., 2015) we introduce a similar method to overcome the problem that $\alpha = 100$ is not valid for hot gas, by distinguishing between hot and cold gas accretion.

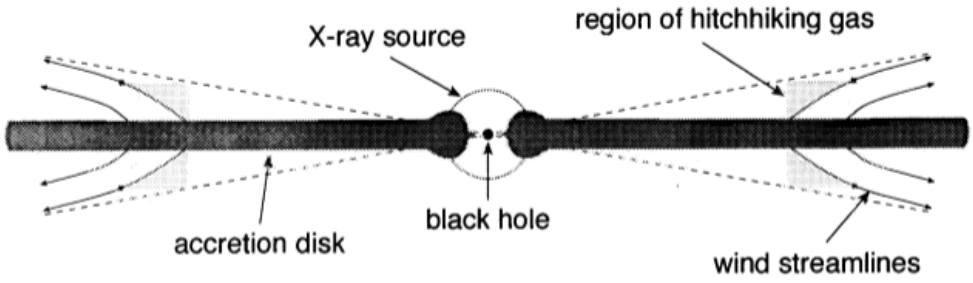

Figure 1.5: This sketch from Murray et al. (1995) is a schematic representation of disk winds. Wind streamlines are shown as curved solid lines. Between the wind and the central X-ray source shielding gas ('hitchhiking gas') blocks the line of sight from the central BH to the critical point (marked with little crosses on the solid lines) on the innermost streamline.

Another approach (Vogelsberger et al., 2013) to account for the different gas phases is to compare the external pressure $P_{\rm ext}$ with a reference pressure $P_{\rm ref} = (\gamma - 1)\rho_{\rm sfr} u_{\rm eq}$, where $\rho_{\rm sfr}$ is the star formation threshold and $u_{\rm eq}$ is the equilibrium thermal energy per unit mass. If $P_{\rm ext} < P_{\rm ref}$, Vogelsberger et al. (2013) lower the accretion rate by a factor $(P_{\rm ext}/P_{\rm ref})^2$.

1.4.4 AGN feedback

The BH accretion rate (equation 1.31) gives not the amount of gas which actually passes the BH's radius of influence, but the amount of gas which is stored in the accretion disk around the BH. Indeed, a major part of the accretion rate contributes to the BH growth. However, a fraction of the stored energy is emitted back into the surrounding medium via AGN feedback. There are basically two different forms of AGN feedback: radiative feedback and mechanical/kinetic feedback. Radiative feedback and also unresolved mechanical feedback can be realized in the simulations as thermal feedback by increasing the temperature of the gas particles surrounding the BH (Springel et al., 2005).

Mechanical feedback can be either in the form of AGN driven winds or jets. Due to Murray et al. (1995) AGN driven winds originate in the accretion disk and are driven out by a combination of radiation pressure and gas pressure. The winds, which are almost in the plane of the disk, are believed to produce emission lines at almost all viewing angles, thus contributing significantly to the characteristic broad emission lines of AGN. Fig. 1.5 is taken from Murray et al. (1995), showing schematically how the disk winds are driven out.

Although jets exist in the majority of AGN (often on relatively small scales), they are commonly associated to large radio lobes which can be even larger than the stellar component of the host galaxy. Scheuer (1974) and Blandford & Rees (1974) came up with theoretical models postulating that the radio lobes were fed by narrow jets which transport energy from the nucleus to the outer regions of the galaxy (Robson, 1996). That way, Blandford & Rees (1974) could explain the size and luminosity of the prominent radio lobes in Centaurs A, which have been observed by Hargrave & Ryle (1974). Fig.

1.6 shows a more recent decomposition of Centaurus A from different wavelength bands: X-rays (blue), optical (yellow), radio continuum (green), and a radio image at the 21cm line (red). While the optical image and also the image at the 21cm line reveal no hints for a jet, its structure is clearly visible in the X-ray image and in the radio continuum. The jet itself is very bright in the X-ray image, but it is also faintly visible in the radio continuum image. The corresponding radio lobes are clearly visible in the radio continuum. A closer look onto the X-ray image reveals 'blobs' within the jet, indicating specific outburst events. Generally speaking, jets are produced by magnetic fields which are generated by moving charges within the accretion disk and/ or by the rotating BH. For the purpose of this thesis I will not go into further details on the formation of jets and refer the reader to the reviews from Rees (1984), Begelman et al. (1984), and Ferrari (1998), as well as to the book from Hughes (1991).

In the scope of this thesis, let me just briefly mention that there are two basic types of accretion disks, thin disks and thick disks (e.g Hughes, 1991). In thin disks the disk's magnetic field, which is perpendicular to the accretion disk, is used to collimate and accelerate particles. In thick disks the magnetic field lines build up a vortex funnel, in which particles from an ionized collisionless synchrotron plasma are collimated and accelerated (ion-supported tori, Rees et al. 1982). Generally thin disks are associated with the radiatively efficient quasar-mode (radiative mode), whereas thick disks are associated with the radiatively inefficient radio-mode (jet-mode), which is mostly dominated by jets (Heckman & Best, 2014; Padovani et al., 2017, e.g.).

Although AGN driven winds and jets have a very different origin, they are technically implemented in current state-of-the-art simulations in very similar ways. Both forms of mechanical feedback play a role only when the resolution is high enough to resolve the scales on which they act.[18] Since the actual physics driving mechanical feedback is neither resolved nor completely understood, there are several different approaches in the literature, all with the aim of modelling the effect of mechanical feedback as close as possible to observations. Sijacki et al. (2007), for example, inject thermal energy into bubbles which are randomly placed in a sphere around the BH, as long as the BH accretes in the radio-mode. This method has been used in the Illustris simulation (Sijacki et al., 2015). However, it has not only the caveat that the bubbles are injected completely randomly, but also that it leads to substantial overheating. Therefore, Weinberger et al. (2017) model the effect of mechanical jets by injecting momentum in a random direction, which changes for every injection event. This model has been implemented in the IllustrisTNG simulation (Weinberger et al., 2017). Very similar is the model from Barai et al. (2016), who inject momentum within a bi-cone. In this model, the efficiency of the mechanical feedback is estimated using the model from Steinborn et al. (2015, Chapter 3). In contrast to jets, which are most relevant for inefficiently accreting AGN, AGN driven winds (e.g. Choi et al., 2012; Negri & Volonteri, 2017) are expected to scale with luminosity (Hopkins et al., 2016).

[18]Note that this is not the case in the Magneticum Pathfinder Simulations. Nevertheless, it is worth mentioning it since it will be necessary to implement mechanical feedback, based on Steinborn et al. (2015, Chapter 3 of this thesis), in future simulation runs with higher resolutions.

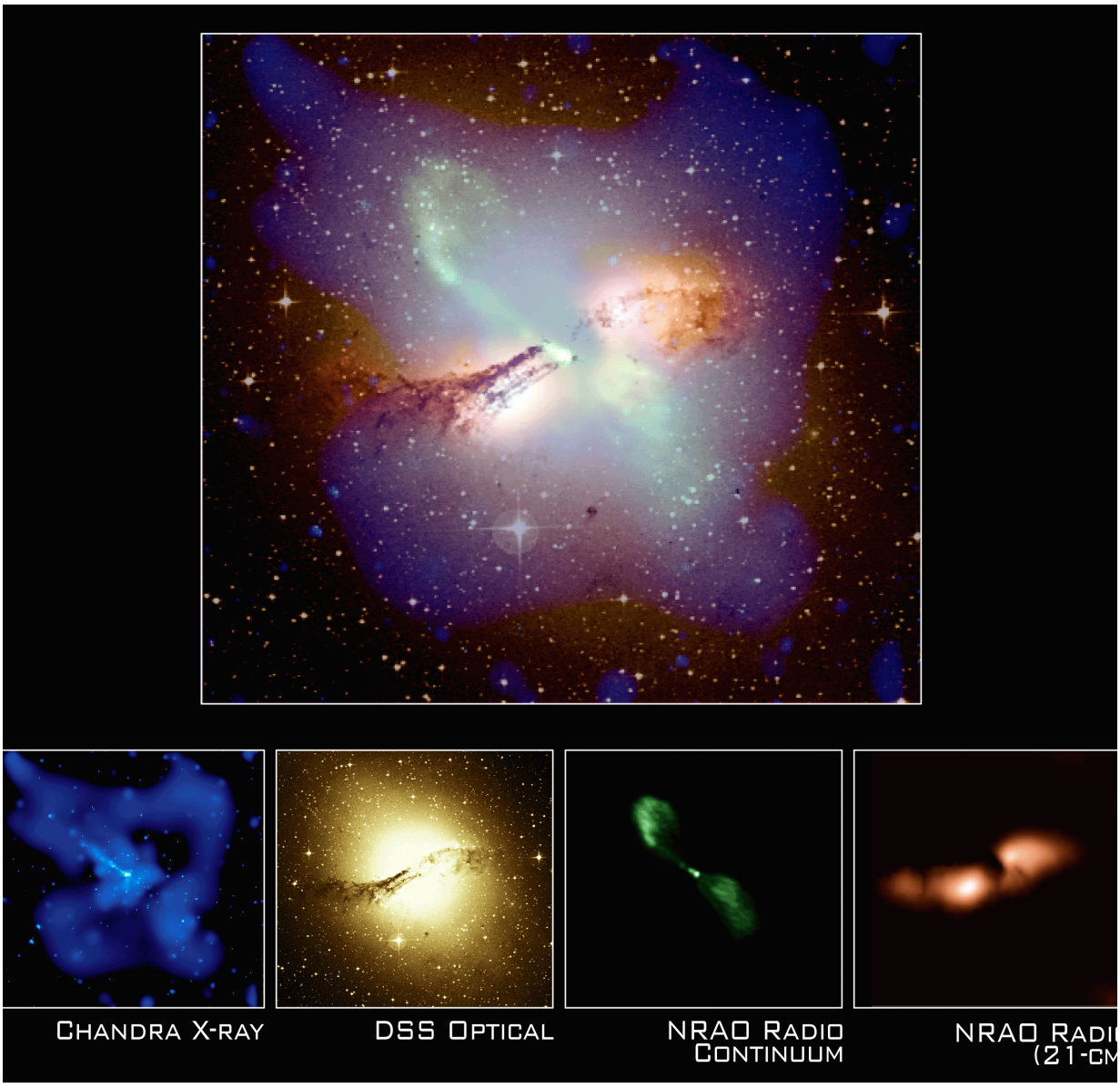

Figure 1.6: Decomposition of Centaurus A in different wavelength bands. Blue shows an X-ray image from the *Chandra X-ray Observatory* and yellow is an optical image from the *Digitized Sky Survey* (DSS). The radio continuum is shown in green and the radio image at the 21cm line is shown in red, both observed at the *National Radio Astronomy Observatory* (NRAO). The image is taken from https://apod.nasa.gov/apod/ap020812.html (accessed: 09-04-2018)

1.4.5 The dynamics of SMBHs

Despite the variety of existing hydrodynamic cosmological simulations, only a few of the currently used BH models are capable of producing AGN pairs with separations down to kpc scales within a cosmological simulation. One reason is that very large volumes are required at relatively high resolutions, making such simulations computationally very expensive. Another reason is that most of the currently used BH models are not capable of tracing BHs down to the resolution limit during a galaxy merger. Specifically, in most cosmological simulations BHs are pinned to the gravitational potential minimum (Blecha et al., 2016; Springel et al., 2005) to avoid BHs becoming artificially dislocated from the galaxy centre. Consequently, during a galaxy merger, the two central BHs merge instantaneously as soon as the two merging galaxies are identified as only one galaxy by the halo finder. Since this occurs relatively early during the merger, it is not possible to directly trace the two BHs during the merger. Making predictions about the number density of SMBH pairs using such simulations is only possible indirectly, for example using models like in Blecha et al. (2016), who studied recoiling BHs in Illustris, or like in Salcido et al. (2016), making predictions about gravitational waves from SMBH mergers using the EAGLE simulations.

However, some authors developed methods to avoid that the BHs have to be pinned to the potential minimum. In the cosmological zoom-in simulations from Bellovary et al. (2010), for example, dark matter particle masses are set similar to the gas particle masses in the high resolution region. Okamoto et al. (2008) artificially drag the BHs along the local density gradients. Hirschmann et al. (2014), Dubois et al. (2014), Tremmel et al. (2015) and Volonteri et al. (2016) use a similar approach by accounting for a dynamical friction force caused by small and large scale perturbations of the surrounding particles (see e.g. Tremmel et al. 2015 and references therein for a detailed description). Due to these perturbations BHs are, equivalently to stars, decelerated in the direction of their motion: (Chandrasekhar, 1943):

$$\Delta\vec{v} = \delta\vec{v}(\Delta t) - \eta\vec{v}\Delta t. \tag{1.35}$$

Following (Chandrasekhar, 1943), and assuming that $M_\bullet$ is much larger than the masses of the surrounding particles m_i, the dynamical friction coefficient η is given by

$$\eta = 4\pi m_i M_\bullet G^2 \frac{\vec{v_\bullet}}{v_\bullet^3} \ln\left(\frac{D_0 < v^2 >}{GM_\bullet}\right) \int_0^{v_\bullet} N(v_i)\mathrm{d}v_i, \tag{1.36}$$

where D_0 is the average distance between the BH and the surrounding particles, $\vec{v_\bullet}$ is the velocity of the BH, $\vec{v_\mathrm{i}}$ are the velocities of the neighbouring particles, $< v^2 >$ is the mean square of these velocities, and $N(v_i)$ is the according velocity distribution. Note that only particles with $v < v_\bullet$ are considered in this formula.

Chapter 2

The Magneticum Pathfinder Simulations

The Magneticum (Pathfinder) Simulations are a set of cosmological simulations [1] (Dolag et al. in prep.), which have been performed with an updated version of the TreePM-SPH code P-GADGET3 (Springel, 2005). Before I describe the simulations in detail I will give a brief overview about the history of cosmological simulations and the various methods used to carry out such simulations in general, particularly concentrating on the smoothed particle hydrodynamics (SPH) method.

2.1 From light bulbs to modern SPH: A brief history

Considering only gravity, it is already for just three point sources impossible to solve their equations of motion analytically. However, an N-body problem (with $N \geq 3$) can be approximated numerically by discretizing continuous quantities. Generally speaking, there are two different discretization paradigms: Lagrangian, particle-based methods discretize mass, whereas Eulerian, mesh-based methods discretize space. The first N-body simulations were of Lagrangian nature. Already before the first computer simulations, Holmberg (1941) developed a method to simulate an encounter of two galaxies. He used 37 mass elements per galaxy, which were represented by light-bulbs with candle brightnesses proportional to the mass of each element. The net gravitational force of each mass element could then be estimated by measuring the total light intensity at the position of every light bulb. With the development of the first computers, N-body simulations have been used to compute the dynamics of stars in star clusters (von Hoerner, 1963), the dynamics of galaxies in galaxy clusters (Aarseth, 1963; Peebles, 1970), or to simulate gravitational interactions between galaxies (review from Toomre 1974 and references therein). Press & Schechter (1974) finally followed the formation of galaxies and galaxy clusters within a cosmological context using N=1000 particles. Since then the size of cosmological N-body simulations continuously grew with increasing computational power.

[1] www.magneticum.org

However, when the gravitational forces are computed by direct integration, the number of operations increases rapidly with $\mathcal{O}(N^2)$. Therefore, methods have been developed to compute the gravitational forces more effectively.

The particle-mesh (PM) technique (e.g. Hockney & Eastwood, 1981; Efstathiou et al., 1985) combines Lagrangian and Eulerian methods by discretizing the density distribution of the particles on a grid. The Poisson equation

$$\nabla^2\Phi = 4\pi G\rho \tag{2.1}$$

is than solved numerically by applying a discrete Fourier transform (e.g. Klypin & Shandarin, 1983), where Φ is the gravitational potential, G is the gravitational constant, and ρ is the density. With the fast Fourier transformation (FFT, Danielson & Lanczos 1942) the number of operations is reduced to $\mathcal{O}(N\log N)$. Another prominent method is to construct a hierarchical 'tree', for example by dividing the volume *'into cubic cells, each of which is recursively divided into eight sub-cells whenever more than one particle is found to occupy the same cell'* (Barnes & Hut, 1986). That way the number of operations can also be decreased to $\mathcal{O}(N\log N)$. Tree and PM methods were later combined (TPM or TreePM, Xu 1995) *'by restricting the tree algorithm to short-range scales, while computing the long-range gravitational force by means of a PM algorithm'* (Springel, 2005). In 2005 a major break-through of (Lagrangian) N-body simulations came with the Millennium simulation (Springel et al., 2005), following $N = 2160^3$ dark matter particles in a volume of $(500\mathrm{Mpc}/h)^3$.

Another, purely Eulerian method to compute gravity is to solve the Poisson equation with the adaptive mesh refinement (AMR) technique (Berger & Oliger, 1984), in which the computing time is optimized by continuously refining and removing grid cells. One advantage of this method is that it is possible to increase the spatial resolution locally by recursively defining an even finer grid within a grid. Kravtsov et al. (1997) further optimized the AMR method by defining the mesh with a recursive tree (adaptive refinement tree, ART).

So far, I mentioned only simulation techniques used to compute gravitational forces, for example between dark matter particles. A computationally not very expensive way to mimic baryonic physics is to use dark matter only simulations, for example, to apply semi-analytic models (SAMs, e.g. Springel et al., 2005; Monaco & Fontanot, 2005; Bower et al., 2006; De Lucia & Blaizot, 2007). SAMs, however, have the caveat that they model the formation and evolution of galaxies not self-consistently, but based on several assumptions, for example for the trigger mechanisms of AGN activity. Therefore, simulating the baryonic physics directly is a much more accurate approach.

Eulerian methods use either fixed or adaptive meshes to solve the hydrodynamic con-

servation equations in their Eulerian form:

$$\frac{\partial \rho}{\partial t} = -\nabla \cdot (\rho \vec{v}) \quad \text{(mass conservation)} \tag{2.2}$$

$$\frac{\partial (\rho \vec{v})}{\partial t} = -\nabla \cdot (\rho \vec{v} \vec{v}) - \nabla P - \rho \nabla \Phi \quad \text{(momentum conservation)} \tag{2.3}$$

$$\frac{\partial (\rho u)}{\partial t} = -\nabla \cdot (\rho u \vec{v}) - \nabla \cdot (P \vec{v}) \quad \text{(energy conservation)}, \tag{2.4}$$

where $\vec{v}$ is the velocity, P is the pressure, and u is the specific internal energy. One famous example for a purely Eulerian scheme including baryonic physics is the grid code RAMSES (Teyssier, 2002), which is based on the AMR technique. The RAMSES code has for example been used for the cosmological simulation HORIZON-AGN (Dubois et al., 2014).

In contrast to Eulerian methods, Lagrangian methods simulate a fixed number of mass elements. Making use of the identity

$$\frac{\mathrm{d}}{\mathrm{d}t} = \frac{\partial}{\partial t} + \vec{v} \cdot \nabla, \tag{2.5}$$

equations 2.2-2.4 can be written in their Lagrangian form:

$$\frac{\mathrm{d}\rho}{\mathrm{d}t} = -\rho \nabla \cdot \vec{v} \quad \text{(mass conservation)} \tag{2.6}$$

$$\rho \frac{\mathrm{d}\vec{v}}{\mathrm{d}t} = -\nabla P - \rho \nabla \Phi \quad \text{(momentum conservation)} \tag{2.7}$$

$$\rho \frac{\mathrm{d}u}{\mathrm{d}t} = -P \nabla \cdot \vec{v} \quad \text{(energy conservation)}. \tag{2.8}$$

Thereby, mass conservation is implicitly given using a particle based simulation technique.

Gingold & Monaghan (1977) and Lucy (1977) presented a method based on a Lagrangian scheme, in which fluids are represented by discrete fluid particles with random positions according to the density. Using the Monte Carlo method, the underlying continuous density distribution can be obtained from the probability distributions of the fluid particles. Gingold & Monaghan (1977) used an approximation of the Monte Carlo method, the so-called smoothing kernel method (Parzen, 1962; Bartlett, 1963), and therefore, they called their method smoothed particle hydrodynamics (SPH). The principle idea (following Gingold & Monaghan 1977) is that the density of each fluid particle is smoothed:

$$\rho(\vec{x}) = \int W(|\vec{x} - \vec{x'}|, h) \rho(\vec{x'}) \mathrm{d}V. \tag{2.9}$$

The smoothing kernel function $W(r, h)$ depends on the distance $r = |\vec{x} - \vec{x'}|$ to the 'particle centre' and on the smoothing length h. It has to fulfill the condition

$$\int W(r, h) \mathrm{d}V = 1. \tag{2.10}$$

Practically, the density of an SPH particle with index i is computed by summing over a specified number N of neighbouring particles j:

$$\rho_i = \sum_{j=1}^{N} m_j W(|r_{ij}|, h_i), \tag{2.11}$$

where m_j is the particle mass. Hernquist & Katz (1989) combined SPH with a tree method (TREESPH). The same approach has been followed by (Springel et al., 2001) in the GADGET (**GA**laxies with **D**ark matter and **G**as int**E**rac**T**) code, which follows an N-body approach for collisionless fluids (dark matter and stars) and a hydrodynamic approach for collisional gas. The 'traditional' SPH code GADGET and its follow-up version GADGET2 (Springel, 2005) use the spline kernel function from Monaghan & Lattanzio (1985). However, traditional SPH schemes naturally also smooth out features like shocks and generally suppress fluid mixing (e.g. Price, 2012; Dehnen & Aly, 2012). Therefore, 'modern' SPH schemes have been developed which solve these issues, for example by using higher order Wendland kernel functions (e.g. Read et al., 2010; Dehnen & Aly, 2012; Donnert et al., 2013; Beck et al., 2016) and improved treatments of artificial viscosity (Dolag et al., 2005; Donnert et al., 2013; Beck et al., 2016). The Magneticum Pathfinder Simulations (see Section 2.3 for further details) have been performed with a 'modern' state-of-the-art version of P-GADGET3, the follow-up version of GADGET2.

Despite recent improvements in SPH schemes, other methods have been developed in recent years to overcome the problems of both SPH and grid-based methods by combining both techniques. Probably the most prominent example is the moving mesh method (e.g. AREPO from Springel 2010), in which discrete, arbitrarily moving points define an unstructured, moving mesh using Voronoi tessellation. This mesh is then used to solve the hydrodynamic conservation equations. Another, similar way to combine Lagrangian and Eulerian methods are meshfree finite-volume techniques like in GIZMO (Hopkins, 2015). A detailed description of these methods is, however, beyond the scope of this thesis and I refer the reader to the overview papers from Springel (2010) and Hopkins (2015) and the references therein.

2.2 The cosmological framework

2.2.1 The Cosmological model

The Magneticum simulations follow a ΛCDM (Λ cold dark matter) cosmology. In the scope of this thesis I will only briefly describe the cosmological model and refer the reader for example to the book from Peebles (1993) for a detailed description of the standard model of cosmology. The cosmological constant Λ was introduced by Einstein to modify the field equations to avoid a negative pressure of the world matter:

$$R_{\mu\nu} - \frac{1}{2} g_{\mu\nu} R - \Lambda g_{\mu\nu} = -\frac{8\pi G}{c^2} T_{\mu\nu}. \tag{2.12}$$

Thereby, the metric tensor $g_{\mu\nu}$ represents the gravitational field and

$$R_{\mu\nu} = \Gamma^{\alpha}_{\mu\alpha,\nu} - \Gamma^{\alpha}_{\mu\nu,\alpha} - \Gamma^{\alpha}_{\mu\nu}\Gamma^{\beta}_{\alpha\beta} + \Gamma^{\alpha}_{\mu\beta}\Gamma^{\beta}_{\nu\alpha} \tag{2.13}$$

is the Ricci tensor, which is given by the Christoffel symbols

$$\Gamma^{\mu}_{\nu\sigma} = \frac{1}{2}g^{\mu\lambda} = (g_{\lambda\nu,\sigma} + g_{\lambda\sigma,\nu} - g_{\nu\sigma,\lambda}). \tag{2.14}$$

The equations of motion for the accelerated expansion of the universe are

$$\frac{\ddot{a}}{a} = -\frac{4}{3}\pi G(\rho_{\mathrm{b}} + 3p_{\mathrm{b}}) + \frac{\Lambda}{3} \tag{2.15}$$

and

$$\left(\frac{\dot{a}}{a}\right)^2 = \frac{8}{3}\pi G\rho_{\mathrm{b}} \pm \frac{1}{a^2R^2} + \frac{\Lambda}{3}, \tag{2.16}$$

where $a = (1+z)^{-1}$ is the scale factor, R is a constant corresponding to the curvature, and ρ_{b} and p_{b} are the density and the pressure of baryonic matter, respectively. Furthermore we use $c = 1$ for simplicity. The Hubble parameter H is defined as the expansion rate of the Universe:

$$H(t) = \frac{\dot{a}(t)}{a(t)}. \tag{2.17}$$

Due to the expansion of the Universe, the wavelengths of photons are also expanded, leading to a cosmological redshift:

$$z = \frac{1}{a} - 1. \tag{2.18}$$

The Hubble parameter at $z = 0$ is defined as the Hubble constant H_0. It is often given in terms of h: $H_0 = 100h$ km s^{-1} Mpc^{-1}. In simulations the calculations are made in co-moving units. Thus the box size is constant.

Equation (2.16) can also be written by using the three cosmological parameters Ω_{m}, Ω_R and Ω_Λ. The first one is the density parameter, representing both (cold) dark matter (Ω_{dm}) and baryons (Ω_{b}):

$$\Omega_{\mathrm{m}} = \Omega_{\mathrm{dm}} + \Omega_{\mathrm{b}} = \frac{8\pi G\rho_0}{3H_0^2}. \tag{2.19}$$

The second parameter describes the curvature:

$$\Omega_R = \frac{1}{(a_0H_0R)^2}, \tag{2.20}$$

which is set $\Omega_R = 0$ assuming a flat universe, and the third parameter represents dark energy:

$$\Omega_\Lambda = \frac{1}{3H_0^2}. \tag{2.21}$$

With equations (2.17) - (2.21) one can write equation (2.16) as:

$$H^2 = H_0^2[\Omega_{\mathrm{m}}(1+z)^3 + \Omega_R(1+z)^2 + \Omega_\Lambda]. \tag{2.22}$$

2.2.2 SPH in a ΛCDM universe

Generally, cosmological simulations are run in comoving coordinates. In contrast to the proper length x, the comoving length x' does not change with cosmological time and can easily be converted into proper units[2]:

$$x = a(t) \cdot x'. \tag{2.23}$$

Thus, the comoving size of a cosmological box does not change during the simulation run. This has the advantage that the enormous expansion of the length scales, in particular at early times, is avoided. Furthermore, no dark energy term is required in the energy equation. The SPH kernel function (equation 2.9) is then generally computed in a comoving framework. However, it is often suitable to introduce a redshift dependent smoothing length, at least at very high redshifts (e.g. Dolag et al., 2008).

Since the conversion from proper to comoving length (equation 2.23) is time dependent, the hydrodynamic conservation laws (equations 2.6 - 2.8) need to be adjusted in a comoving framework. From equation (2.23), we obtain the proper velocity

$$\vec{v} = \dot{a}(t) \cdot \vec{x}' + \vec{v}_\mathrm{p}, \tag{2.24}$$

where the proper peculiar velocity is defined as $\vec{v}_\mathrm{p} = a(t) \cdot \vec{v}'$. In addition to the peculiar motion, particles move away from the origin of the coordinate system due to the expansion of the Universe (e.g. Peebles, 1993). The time derivative of the comoving velocity is

$$\frac{\mathrm{d}\vec{v}'}{\mathrm{d}t} = \frac{\dot{a}}{a}\vec{v}_\mathrm{p} + \frac{\mathrm{d}\vec{v}_\mathrm{p}}{\mathrm{d}t}. \tag{2.25}$$

According to equation (2.23), also the gradient is modified in a comoving framework:

$$\nabla' = a\nabla. \tag{2.26}$$

Inserting the above equations into equation 2.7 and 2.8 gives the momentum and energy conservation equations in an expanding ΛCDM universe in their Lagrangian form:

$$\rho\left(\frac{\mathrm{d}\vec{v}_\mathrm{p}}{\mathrm{d}t} + \frac{\dot{a}}{a}\vec{v}_\mathrm{p}\right) = -\frac{1}{a}\nabla' P - \frac{1}{a}\rho\nabla'\Phi \quad \text{(momentum conservation)} \tag{2.27}$$

$$\rho\frac{\mathrm{d}u}{\mathrm{d}t} = -P\left(\frac{1}{a}\nabla' \cdot \vec{v}_\mathrm{p} + 3\frac{\dot{a}}{a}\right) \quad \text{(energy conservation)}. \tag{2.28}$$

where the Hubble parameter $H(t) = \dot{a}/a$ is given by equation (2.22).

In a similar fashion, the Poisson equation is adjusted to the cosmological model (see, e.g., Peebles 1993 for details):

$$\nabla^2\Phi = 4\pi G a^2(\rho - \rho_\mathrm{b}), \tag{2.29}$$

where ρ_b is the density of the baryons.

[2]In the following equations comoving properties will be denoted as primed symbols, in contrast to proper units (unprimed).

2.3 General settings

This section is based on Hirschmann et al. (2014), Steinborn et al. (2015), Steinborn et al. (2016), and Steinborn et al. (2018).

The Magneticum (Pathfinder) Simulations are a set of cosmological simulations[3] (Dolag et al. in prep.), which have been performed with an updated version of the TreePM-SPH code P-GADGET3 (Springel, 2005). The cosmological simulation runs start from an isotropic particle distribution, in which initial density fluctuations are imprinted. These fluctuations are obtained theoretically from the underlying cosmological model. We adopt a ΛCDM-cosmology with parameters according to the seven year results of the Wilkinson Microwave Anisotropy Probe with $\Omega_m = 0.272$, $\Omega_\Lambda = 0.728$, $\Omega_\mathrm{b} = 0.0456$ and $h = 0.704$ (Komatsu et al., 2011). We follow the hydrodynamics of the gas using the smoothed particle hydrodynamics method (see Price 2012 for a review on the SPH method). We use an entropy conserving formulation (Springel & Hernquist, 2002), where star formation is based on a multi-phase sub-resolution model by Springel & Hernquist (2003). Additionally, we include complex treatment for a wide range of physical processes such as isotropic thermal conduction (Dolag et al., 2004) with an efficiency of $\kappa = 1/20$ of the classical *Spitzer* value (Arth et al., 2014), stellar evolution, metal enrichment and supernova feedback (Tornatore et al. 2003, Tornatore et al. 2007), a cooling function which depends on the individual metal species following Wiersma et al. (2009). We improve the accuracy, stability and reliability of our hydrodynamical method with several state-of-the-art improvements of the SPH method. This includes the higher-order Wendland kernel functions (Dehnen & Aly 2012, see Donnert et al. 2013 and Beck et al. 2016) as well as time dependent artificial viscosity to properly track turbulence within galaxy clusters (Dolag et al., 2005; Donnert et al., 2013; Beck et al., 2016).

The Magneticum simulation set contains several simulation runs with different volumes and resolutions ranging from large boxes with medium resolution (mr) down to small boxes with an extremely high resolution (xhr). The initial particle numbers of the different simulation runs are summarized in Table 2.1. The volumes corresponding to the different boxes are given in the second/ third row. Simulation runs marked in grey are not published. Blue shows the simulations which are used for this thesis. Two of these runs (Box3/uhr and Box2b/hr, light blue) did not run until $z = 0$. Box3/uhr ran until $z = 2$ and Box2b/hr ran until $z = 0.25$.

The initial masses for dark matter and gas particles for the different resolution levels are listed in Table 2.2. During the simulation run gas particles are converted into star particles. To increase the resolution, out of one gas particle 4 star particles can form, which have 1/4 of the initial mass of the gas particle. When a star particle is formed the mass of the gas particle is decreased by the mass of the star particle. The softening lengths of dark matter (ϵ_dm), gas (ϵ_gas), and stars (ϵ_*) are also given in Table 2.2.

While the softening length for gas and star particles was constant during time, the gravitational softening length for dark matter particles was kept fixed at $4.2\mathrm{kpc}/h$ comoving

[3] www.magneticum.org

	Box0	Box1	Box2b	Box2	Box3	Box4	Box5
V [(Mpc/h)^3]	2688^3	896^3	640^3	352^3	128^3	48^3	18^3
V [Mpc^3]	3818^3	1273^3	909^3	500^3	182^3	68^3	26^3
mr	$2 \cdot 4536^3$	$2 \cdot 1526^3$		$2 \cdot 594^3$	$2 \cdot 216^3$	$2 \cdot 81^3$	
hr			$2 \cdot 2880^3$	$2 \cdot 1584^3$	$2 \cdot 576^3$	$2 \cdot 216^3$	$2 \cdot 81^3$
uhr					$2 \cdot 1536^3$	$2 \cdot 576^3$	$2 \cdot 216^3$
xhr							$2 \cdot 576^3$

Table 2.1: Initial particle numbers of the different Magneticum Pathfinder simulation runs. The simulations have different resolution levels: medium (mr), high (hr), ultra-high (uhr), and extremely high (xhr) resolution. The different boxes from Box0 to Box5 have different volumes V from 2688^3(Mpc/h)^3 down to 18^3(Mpc/h)^3. The box lengths are stated in the second/third row. Blue are the simulation runs which have been used for this thesis. Box3/uhr and Box2b/hr (light blue) did not run until $z = 0$, but only until $z = 2$ and $z = 0.25$, respectively. Unpublished simulations are written in grey.

	$m_{\rm dm}/(M_\odot/h)$	$m_{\rm gas}/(M_\odot/h)$	$\epsilon_{\rm dm}/({\rm kpc}/h)$	$\epsilon_{\rm gas}/({\rm kpc}/h)$	$\epsilon_*/({\rm kpc}/h)$
mr	$1.3 \cdot 10^{10}$	$2.6 \cdot 10^9$	10	10	5
hr	$6.9 \cdot 10^8$	$1.4 \cdot 10^8$	3.75	3.75	2
uhr	$3.6 \cdot 10^7$	$7.3 \cdot 10^6$	1.4	1.4	0.7
xhr	$1.9 \cdot 10^6$	$3.9 \cdot 10^5$	0.45	0.45	0.25

Table 2.2: Initial particle masses and softening lengths for the different resolution levels of the Magneticum Simulations.

Plummer-equivalent and was switched to a physical softening length of 1.4kpc/h at $z = 2$. The black hole sink particles are treated with the same softening as star particles and we did not apply any restriction to the SPH smoothing length of the gas particles. This allows us, for example, to resolve BH pairs in the uhr resolution level roughly down to 2kpc, which is twice as large as the softening length of the stars (see, e.g., Teklu et al. 2015 and Remus et al. 2017 for a detailed study of galaxy properties at this resolution level). We remark that this is a very conservative assumption for the resolution and hence, although we cannot give a prediction for the number of BH pairs with distances below 2kpc, the simulations can still contain BH pairs with smaller spatial separations.

Figure 2.1 visualizes the baryonic matter distribution in 70 Mpc thick slices through the 500Mpc/hr simulation run, which has been used in Section 5 of this thesis. Each panel also shows a zoom onto the most massive cluster. Furthermore, white, blue, and red circles mark the positions of the 20 BHs with the highest masses, Eddington-ratios, and accretion rates within the shown slice, respectively. Already from visual inspection it appears that the most massive BHs (white circles) reside in very dense regions, at least above $z = 2$. In contrast, BHs with high Eddington ratios $\dot{M}/\dot{M}_{\rm Edd}$ and high accretion rates also reside in less dense regions. The detailed distribution of AGN with different BH masses, Eddington ratios, and AGN luminosities will be addressed in detail in Chapter 6.

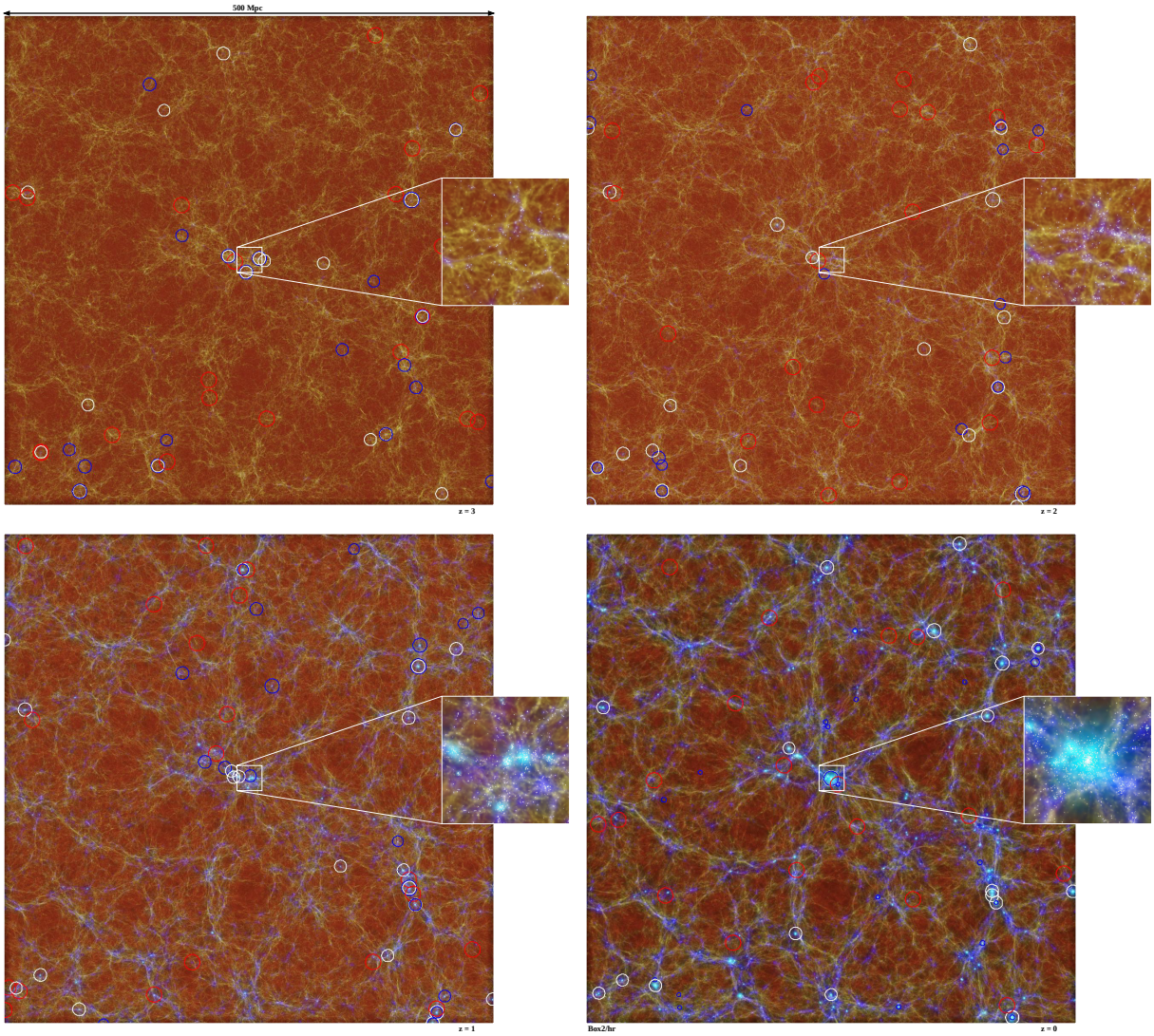

Figure 2.1: Time evolution of the 500Mpc/hr simulation run from the Magneticum Simulation set. The four panels of the figure, which is taken from Hirschmann et al. (2014), show visualizations of 500 Mpc wide, 70 Mpc thick slices through the cosmological baryonic mass distribution (stellar and gaseous density) at $z = 3, 2, 1$, and 0 (upper left, upper right, bottom left, and bottom right panel, respectively), performed with the ray tracing program SPLOTCH (Dolag et al., 2008). White, blue, and red circles indicate the 20 BHs within these slices which have the highest masses, the highest Eddington-ratios and the highest accretion rates, respectively. The sizes of the circles are scaled logarithmically with the according values and are normalised to the maximum value of each quantity. Furthermore, a zoom onto the region where the most massive cluster forms is shown in each panel.

2.4 Model for BH growth

The implementation of SMBHs in the Magneticum simulations is based on Springel et al. (2005). However, the model has been modified strongly, especially regarding the dynamical treatment of BHs. The accretion model and the feedback model have also been refined. In this section I will specify all relevant settings and implementations regarding the SMBH model used in the Magneticum Simulations.

2.4.1 BH seeding

BHs are treated as collision-less sink particles. We evaluate on the fly friends-of-friends (FoF) groups of star particles with a seven times smaller than usual linking-length to identify stellar objects (e.g. galaxies) which do not yet contain BHs.

If the mass of such stellar objects is larger than $M_{*,thresh}$, the star particle with the highest binding energy is replaced by a BH sink particle. For the initial true mass of the BH particles $M_{\bullet,\mathrm{seed}}$ we choose a BH mass which is clearly below the mass expected from the observed relation between the BH mass and the stellar mass (e.g. McConnell & Ma 2013). In that way, we avoid an overheating of the surrounding gas, since the effect of the AGN feedback is less abrupt. For the dynamical mass of the BH sink particle we choose the mass of a single dark matter particle. The dynamical mass of the sink particle is only used as mass when computing the gravitational forces and it only starts to increase when the true mass of the BH particle starts to grow and exceeds the dynamical mass. The values of $M_{*,thresh}$ and $M_{\bullet,\mathrm{seed}}$ for the hr and uhr resolution level are given in Table 2.3.

	$M_{*,thresh}/M_\odot$	$M_{\bullet,\mathrm{seed}}/M_\odot$
hr	$2.3 \cdot 10^{10}$	$4.6 \cdot 10^5$
uhr	$5.7 \cdot 10^9$	$7.1 \cdot 10^5$

Table 2.3: Stellar mass above which a BH is seeded within a halo and the seeding mass of BHs, both for the hr and uhr resolution level.

2.4.2 Gas accretion and AGN feedback

Since the different Magneticum Simulation runs had been performed with state-of the art code versions, they had been run with two different models for gas accretion and AGN feedback, which we call 'fiducial model' and 'new feedback and accretion model' (NFAM). In contrast to the original implementation from Springel et al. (2005), the fiducial model contains the feedback prescription as described by Fabjan et al. (2010), where we switch from quasar- to radio-mode feedback (Sijacki et al., 2007) whenever the Eddington ratio $f_{\mathrm{Edd}} = \dot{M}_\bullet / \dot{M}_{\mathrm{Edd}}$ falls below 10^{-2}. The fiducial model considers only radiative feedback with an efficiency $\epsilon_r = 0.2$ and is realized as thermal feedback. In the NFAM model we account for both radiation and mechanical outflows, which are also both implemented as

thermal feedback since the scales on which mechanical feedback would act are not resolved. The radiative efficiency ϵ_r as well as the efficiency of mechanical outflows ϵ_o are variable and depend on the accretion rate onto the BH $\dot{M}_\bullet$ and on the BH mass $M_\bullet$, as deduced from observations (Davis & Laor 2011, Chelouche 2013). The coupling factor ϵ_f of the radiation to the surrounding medium depends strongly on the feedback model and for the NFAM model also on the resolution. Its value is chosen such that the simulation reproduces the normalization of the observed $M_\bullet$-M_* relation from McConnell & Ma (2013). Our choices of ϵ_f and the model for the specific simulation runs used for this thesis are summarized in Table 2.4.

	model	ϵ_f
Box2b/hr	fiducial	0.15
Box2/hr	fiducial	0.15
Box3/uhr	NFAM	0.03
Box4/uhr	fiducial	0.15

Table 2.4: SMBH models and values of the coupling factor ϵ_f of the radiation to the surrounding medium for the different simulation runs used for this thesis. In this table we excluded the test-runs which are listed in Table 3.1.

In the fiducial model the accretion rate is estimated according to equations (3.2 and 3.1) with a boost factor $\alpha = 100$. The accretion rate is limited to $\dot{M}_\mathrm{Edd}$. In the NFAM model we compute the Bondi accretion rate separately for hot and cold gas. To account for turbulence (following Gaspari et al. 2013), we multiply the cold gas accretion rate by the boost factor $\alpha = 100$ and the hot gas accretion rate by $\alpha = 10$. For further details regarding the sub-grid model for BH accretion and AGN feedback, see Section 3.1 (Steinborn et al., 2015).

2.4.3 Dynamical prescription of BHs and BH mergers

We do not perform any pinning of the BHs to the deepest potential in their surrounding, but let them evolve self-consistently. This prevents the BH sink particles from merging too early and is only possible due to an improved numerical handling of the BH sink particles, which effectively avoids artificial drifting of such BH sink particles due to numerical inaccuracies as observed in the past. Thereby, the BH sink particles evolve self-consistently during a merger event. In particular, seeding on the star particle with the highest binding energy (compared to choosing the dark matter particle with the largest density as originally done in Springel et al. 2005) already leads to a very precisely centered BH sink particle from the beginning. Additionally, by setting the dynamical mass of the BH sink particle to the mass of a dark matter particle, by carefully choosing the softening, and by seeding only in galaxies which are resolved by the order of thousands of star particles, we guarantee that the code naturally captures dynamical friction and no additional friction term has to be used at the uhr resolution level. At lower resolutions, we adopt an artificial dynamical

friction force following Chandrasekhar (1943, see also Section 1.4.5):

$$F_{\mathrm{df}} = -4\pi \left(\frac{GM_{\bullet}}{v}\right)^2 \rho \ln(\Lambda) \left(err(x) - \frac{2x}{\sqrt{\pi}} e^{-x^2}\right) \frac{\vec{v}}{v}, \tag{2.30}$$

Finally, we modified the conditions under which two BH sink particles will merge. Close pairs of BH sink particles will not be merged as long as they fulfill one of the following conditions: (i) the relative velocity of the BHs to each other is larger than $0.5 c_{\mathrm{s}}$, where c_{s} is the sound-speed of the surrounding gas; (ii) the distance is larger than five times the softening length and none of the two BHs is gravitationally bound to the other one. For too large separations between the BHs the second argument prevents a too early merging of the two BH sink particles. This approach still ignores any additional time the BHs need for the final merging, assuming that this timescale is still smaller than the dynamical time-steps of the cosmological simulation. Nevertheless, due to our novel approach in handling the BH sink particles, the final merging of the BHs in the simulation happens only in the very late state of the merger event, allowing us to study, for the first time, close BH pairs in cosmological simulations.

2.5 Results from the Magneticum Pathfinder Simulations

In recent years several authors used the Magneticum Pathfinder Simulations to study physical processes on different scales, ranging from the inner properties of galaxies up to cosmic voids (Dolag et al., 2017). With a very large initial particle number of almost 200 billion particles, Box0/mr is the largest cosmological simulation up to date including baryonic physics (Bocquet et al., 2016). This simulation run has a very large volume of $(3818\mathrm{Mpc})^3$. Combining Box0/mr with Box2(b)/hr and Box4/uhr allows for a precise determination of the halo mass function ranging from halo masses below $M_{\mathrm{h}} = 10^{12} M_{\odot}$ up to almost $M_{\mathrm{h}} = 10^{16} M_{\odot}$ at $z = 0$. Pollina et al. (2017) concentrate on structures, which are even larger than galaxy clusters: cosmic voids. Using different tracers (galaxies, galaxy clusters, AGN) they find that the bias of cosmic voids is linear with respect to the underlying dark matter distribution. Another application of the Magneticum Simulations are predictions for measurements of Sunyaev-Zeldovich (SZ) effects. Dolag et al. (2016) for example find an overall good agreement of the probability density distribution functions and power spectra of the thermal and, in particular, the kinematic SZ effect using Box1/mr (the largest Magneticum simulation run by that time). Soergel et al. (2017) produce SZ maps from Box0/mr and find a relation between the Compton-Y parameter and optical depth, which can be used to estimate the parameter combination $Hf\sigma_8$ as an independent probe of the underlying cosmological model using the kinematic SZ effect. Gupta et al. (2017) have a closer look at the thermal SZ effect, finding a dependence of the pressure profiles on the halo mass and redshift.

At the uhr resolution level the Magneticum Simulations produce a realistic population of galaxies, including different morphological and kinematical types (Teklu et al., 2015;

Schulze et al., 2018). Thereby, the galaxy properties are in overall good agreement with observations. Remus et al. (2017) for example show that the mass-size relation of the simulated early-type galaxies is in agreement with observations from the GAMA survey. Teklu et al. (2015) have shown that the different galaxy types are distributed on the M_*-J_* plane similar to observations, where M_* and J_* are the stellar mass and the total angular momentum of the stars, respectively. Thereby, elliptical galaxies and disk galaxies follow different relations with the same slope, but a different normalization. Thus, the position on the M_*-J_* plane is used to classify the simulated galaxies. Comparing a dark matter only simulation with the baryonic run, Teklu et al. (2015) find that the galaxy morphology is already imprinted in the dark matter, suggesting that the morphology of galaxies is strongly connected to their formation history and environment. Furthermore, Teklu et al. (2017) find that at a fixed stellar mass the satellite fraction of central galaxies is nearly independent of the morphology. At first sight this seems to contradict with observations of a relation between the quiescent fraction of satellite galaxies and their environmental density. However, Teklu et al. (2017) show that this relation is produced because massive satellite galaxies are identified as central galaxies in observations. Including these companion galaxies, Teklu et al. (2017) reproduce the observed morphology-density-relation. In addition to the morphological variety, the simulated galaxies also have different kinematical features. Schulze et al. (2018) for example show that part of the simulated early-type galaxies have kinematically distinct cores. In addition, Remus et al. (2017) could constrain recent observations of a diffuse stellar component (DSC) around brightest cluster galaxies (BCGs).

The different resolutions and volumes make the Magneticum simulations an ideal tool to study AGN activity, since AGN trigger mechanisms on galaxy scales can be studied as well as the large scale distribution of AGN. Box3/uhr, for example, has been used to study dual and offset AGN at $z = 2$ for the first time within a cosmological simulation (Steinborn et al., 2016, Chapter 4). For studying statistical properties of galactic nuclei like the BH mass function, the AGN luminosity function, or scaling relations between BHs and their host galaxies, it is most suitable to use the hr resolution level. This resolution is still high enough to resolve BH growth, but not the morphology of galaxies. Due to the very large box sizes of Box2/hr and Box2b/hr the simulations produce enormous amounts of AGN, even allowing AGN clustering studies. This thesis contains a detailed analysis of the clustering properties of AGN within the Magneticum Simulations (Steinborn 2018 in prep., Chapter 6), particularly concentrating on the halo occupation distribution (HOD) of AGN. Hirschmann et al. (2014) used Box2/hr to investigate BH growth in detail. In particular, the observed down-sizing trend is reproduced in the Magneticum Simulations and they are in overall good agreement with observed AGN luminosity functions (see also Biffi et al., 2018). In a follow-up study we analyze the relation between galaxy mergers and AGN activity in detail (Steinborn et al., 2018, Chapter 5).

Chapter 3

A refined sub-grid model for black hole accretion and AGN feedback in large cosmological simulations

The content of this chapter has been published in Steinborn et al. (2015):

> **Lisa K. Steinborn**, Klaus Dolag, Michaela Hirschmann, M. Almudena Prieto, Rhea-Silvia Remus: *A refined sub-grid model for black hole accretion and AGN feedback in large cosmological simulations*, 2015, MNRAS, 448, 1504

Abstract

In large scale cosmological hydrodynamic simulations simplified sub-grid models for gas accretion onto black holes and AGN feedback are commonly used. Such models typically depend on various free parameters, which are not well constrained. We present a new advanced model containing a more detailed description of AGN feedback, where those parameters reflect the results of recent observations. The model takes the dependency of these parameters on the black hole properties into account and describes a continuous transition between the feedback processes acting in the so-called radio-mode and quasar-mode. In addition, we implement a more detailed description of the accretion of gas onto black holes by distinguishing between hot and cold gas accretion. Our new implementations prevent black holes from gaining too much mass, particularly at low redshifts, so that our simulations are successful in reproducing the observed present-day black hole mass function. Our new model also suppresses star formation in massive galaxies slightly more efficiently than many state-of-the-art models. Therefore, the simulations that include our new implementations produce a more realistic population of quiescent and star-forming galaxies compared to recent observations, even if some discrepancies remain. In addition, the baryon conversion efficiencies in our simulation are – except for the high mass end

– consistent with observations presented in literature over the mass range resolved by our simulations. Finally, we discuss the significant impact of the feedback model on the low-luminous end of the AGN luminosity function.

3.1 Theoretical Model

3.1.1 Black hole accretion

The Bondi model is commonly used in simulations to estimate the black hole accretion rate. The Bondi accretion rate $\dot{M}_{\rm B}$ (Bondi 1952, Shima et al. 1985) is given by

$$\dot{M}_{\rm B} = \frac{4\pi G^2 M_\bullet^2 \rho_\infty}{(v^2 + c_{\rm s}^2)^{3/2}}, \tag{3.1}$$

where $M_\bullet$ is the black hole mass, ρ is the density, c_s is the sound speed of the accreted gas and v is the velocity of the gas relative to that of the black hole. Since Bondi (1952) assumed an isotropic and isothermal sphere of gas for his estimation, it is not straight forward to adopt this Bondi accretion model for hydrodynamic, cosmological simulations aiming to follow a self consistent accretion history of black holes. For the implementations based on Springel et al. (2005), the accretion rate of the black hole is estimated by

$$\dot{M}_{\rm B} = \frac{4\pi\alpha G^2 M_\bullet^2 \langle\rho\rangle}{(\langle c_{\rm s}\rangle^2 + \langle v\rangle^2)^{3/2}}, \tag{3.2}$$

where $\langle\rho\rangle$, $\langle v\rangle$ and $\langle c_s\rangle$ are computed using kernel weighted SPH estimations. Due to limited numerical resolution in such simulations, the original equation (3.1) is multiplied by a boost factor α, which in Springel et al. (2005) is set to a value of $\alpha = 100$. Note that the SPH estimates also depend on the type of SPH kernel and the number of neighbours. To make this estimation less sensitive to the actual structure of the multi phase media in the vicinity of the black hole and therefore the algorithm less dependent on resolution and on the actual choice of numerical parameters for the kernel weighted interpolation, Choi et al. (2012) suggested to use a different way of building the averages:

$$\dot{M}_{\rm B} = \left\langle \frac{4\pi\alpha G^2 M_\bullet^2 \rho}{(c_{\rm s}^2 + v^2)^{3/2}} \right\rangle. \tag{3.3}$$

Still, choosing the correct value for the boost factor α is not trivial. Since due to the limited resolution the density in the not resolved vicinity of black holes is large, it will be underestimated and – in turn – the temperature (and thus the sound speed) will be overestimated. Following this argument, Booth & Schaye (2009) parametrize α, which is chosen to be $\alpha = 1$ as long as the density is below the critical value where one can assume the gas to be in the hot phase. For larger densities, when gas is accreted mainly in a cold phase, α increases with density. Alternatively, Vogelsberger et al. (2013) have presented a recipe for modelling α based on the equilibrium between cooling losses and AGN feedback.

However, both models do not directly account for the different accretion modes of hot and cold gas phase, where cold gas usually is accreted in turbulent streams, whereas hot gas indeed can be assumed to be isotropic and isothermal.

In our model, we use a sixth-order Wendland kernel (Dehnen & Aly, 2012) with 295 neighbours, building the mean values according to equation (3.2) and directly distinguishing between the accretion of hot and cold gas. In this way, we can safely use the original estimate of building the averages, which has the advantage to be more sensitive to density structures close to the black hole. In general, we assume hot gas has temperatures above $T \approx 10^6 K$, whereas cold gas has temperatures below $T \approx 10^5 K$ (Gaspari et al., 2013). Since we do not account for a third warm phase, we choose $T = 5 \cdot 10^5$K as threshold between hot and cold gas. In contrast to Pelupessy et al. (2007), who use the molecular fraction of the gas for star-forming particles from the multi-phase model (Springel & Hernquist, 2003) to account for cold gas accretion, we also assign gas with a temperature below our threshold in addition to the star forming gas to the cold phase. For both gas phases the accretion rate is calculated separately according to equation 3.2, but with different values for α according to the result by Gaspari et al. (2013), who argue that due to turbulence the assumptions of the Bondi model are not fulfilled for the cold gas. When they include cooling and turbulence in their simulation, they find an accretion rate which is around 100 times larger than the Bondi accretion rate. Interestingly, this is the same value which is used as boost factor α in the original model from Springel et al. (2005). But for adiabatic accretion, the difference, Gaspari et al. (2013) find, is about one order of magnitude smaller. Hence, we use $\alpha = 10$ for hot gas and $\alpha = 100$ for cold gas.

Furthermore, the black hole accretion rate $\dot{M}_\bullet$ is limited to the Eddington accretion rate

$$\dot{M}_{\mathrm{Edd}} = \frac{4\pi G M_\bullet m_{\mathrm{p}}}{\eta_{\mathrm{Edd}} \sigma_{\mathrm{T}} c}, \tag{3.4}$$

where m_{p} is the proton mass, σ_{T} the Thompson scattering cross section and η_{Edd} the feedback efficiency if the black hole would accrete with $\dot{M}_{\mathrm{Edd}}$. Then the accretion rate is given by:

$$\dot{M}_\bullet = \min(\dot{M}_{\mathrm{B,hot}} + \dot{M}_{\mathrm{B,cold}}, \dot{M}_{\mathrm{Edd}}). \tag{3.5}$$

The distinction between hot and cold gas accretion leads to a faster black hole growth in the quasar-mode, because when calculating the mean value of the sound speed $\langle c_s \rangle$ and the gas velocity $\langle v \rangle$ only for cold gas, the accretion rate estimated with equation (3.2) is higher than calculating the mean values of both cold and hot gas together. This solves the well known problem of too low gas accretion, which was addressed in other simulations by increasing the maximum accretion rate to a few times $\dot{M}_{\mathrm{Edd}}$ (e.g. Di Matteo et al. 2012), which is not needed in our simulations.

3.1.2 AGN feedback

In the commonly used black hole model by Springel et al. (2005), the feedback energy per unit time is calculated as

$$\dot{E} = \epsilon_{\mathrm{f}} \epsilon_{\mathrm{r}} \dot{M}_\bullet c^2, \tag{3.6}$$

where ϵ_f is the efficiency with which the energy radiated from the black hole is coupled to the ISM (Springel et al. 2005, Booth & Schaye 2009) and ϵ_r is the radiative efficiency.

The original model as used in Hirschmann et al. (2014) is simplified, since it uses a constant radiative efficiency and thus does not allow for a smooth transition between quasar- and radio-mode. Furthermore, it neglects mechanical feedback, which was already implemented in other simulations as AGN driven winds (i.e. Choi et al. 2014). To account for both mechanical and radiative feedback, we adopt a new feedback scheme based on Churazov et al. (2005). In this study, they propose that AGN feedback can be split up into two components:

1. **Outflow:** The outflow component is a mechanical feedback which dominates at accretion rates below $\sim 0.01\dot{M}_\mathrm{Edd}$ and diminishes at accretion rates above $\sim 0.1\dot{M}_\mathrm{Edd}$. The corresponding gas heating power is given by:
$$P_\mathrm{o} = \epsilon_\mathrm{o}\dot{M}_\bullet c^2, \tag{3.7}$$
where ϵ_o is the outflow efficiency.

2. **Radiation:** The radiative component dominates near the Eddington limit ($f_\mathrm{Edd} > 0.1$) and has the luminosity
$$L = \epsilon_\mathrm{r}\dot{M}_\bullet c^2. \tag{3.8}$$

We implement both radiative and mechanical AGN feedback as thermal feedback due to the inability to resolve the sub-kpc scales, where the jets provide the mechanical feedback. The feedback energy per unit time in this model is then the sum of P_o and the fraction ϵ_f of the luminosity:
$$\dot{E} = (\epsilon_\mathrm{o} + \epsilon_\mathrm{f}\epsilon_\mathrm{r})\dot{M}_\bullet c^2. \tag{3.9}$$
The effect of accreted matter can be split into outflow and radiation components:
$$\frac{\dot{M}_\bullet}{\dot{M}_\mathrm{Edd}} = \frac{P_\mathrm{o}}{L_\mathrm{Edd}} + \frac{L}{L_\mathrm{Edd}}, \tag{3.10}$$
where the Eddington accretion rate
$$\dot{M}_\mathrm{Edd} = \frac{L_\mathrm{Edd}}{\eta_\mathrm{Edd}c^2} \tag{3.11}$$
depends on the total efficiency
$$\eta := \epsilon_\mathrm{o} + \epsilon_\mathrm{r}. \tag{3.12}$$
This model is shown as solid lines (blue corresponds to mechanical outflow and red to radiation) in Fig. 3.1, which were adopted from Churazov et al. (2005). For the outflow-dominated regime they assume
$$\frac{L}{L_\mathrm{Edd}} = 10 \cdot \left(\frac{\dot{M}_\bullet}{\dot{M}_\mathrm{Edd}}\right)^2 \tag{3.13}$$

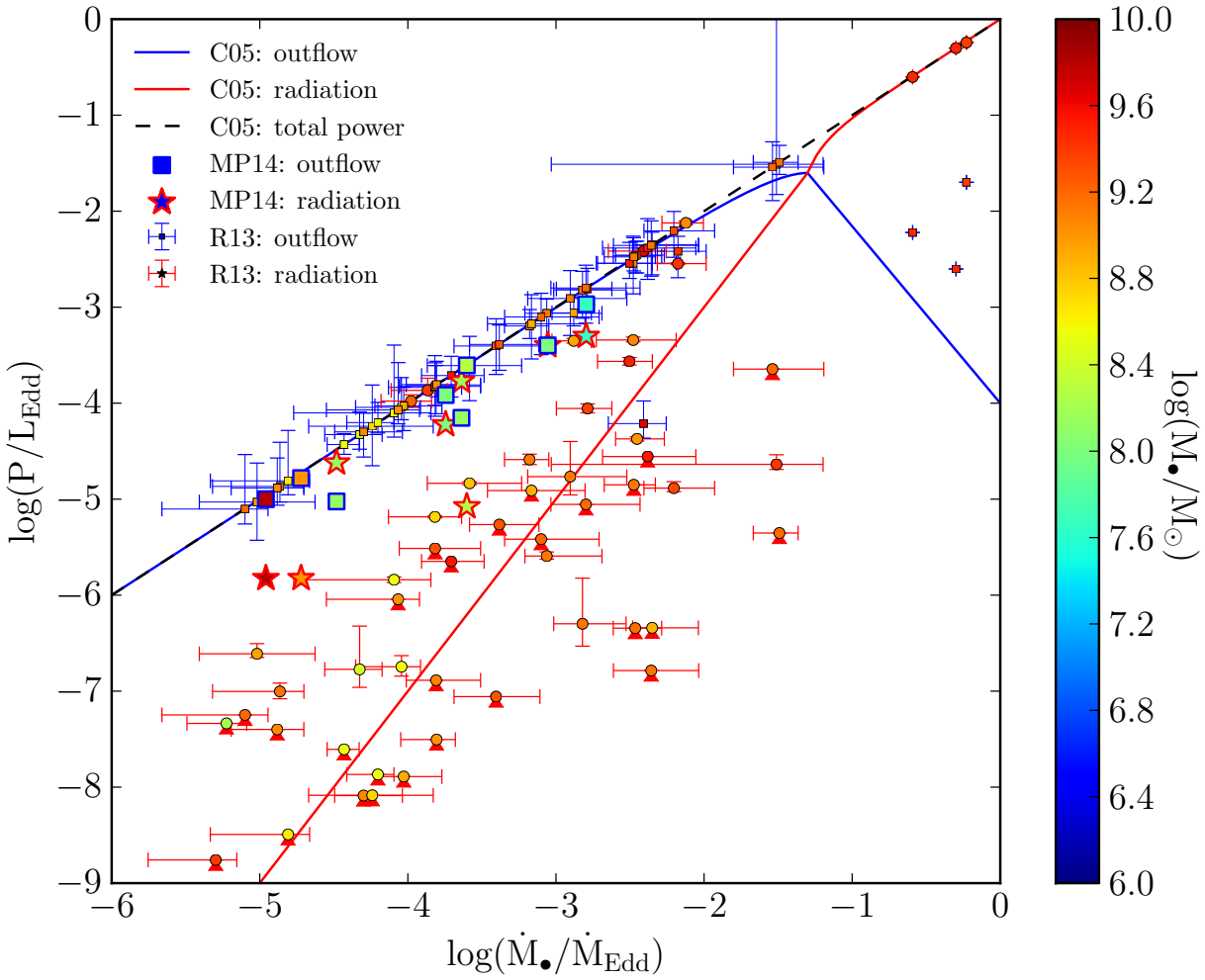

Figure 3.1: The lines show the predictions by Churazov et al. 2005 (C05) for the power of the radiation (red line), the mechanical outflow (blue line) and the sum of both (black dashed line). Observations of jet powers (blue errorbars and edges) and luminosities (red errorbars and edges) constrain the difference between both components. This figure includes two different observations: The big stars and squares show recent observations by Mezcua & Prieto 2014 (MP14) and the data with blue and black errorbars are observations by Russell et al. 2013 (R13). Black triangles mark upper limits. Furthermore, the black hole masses are indicated by the colors of the symbols. Since the masses used by R13 are based on K-band magnitudes, which are known to be inaccurate, we used the dynamical masses by McConnell & Ma (2013) for the sources included in both samples.

as a lower limit for the radiation, which is a consequence of advection-dominated accretion flows (Narayan & Yi, 1995). In the radiation-dominated regime the outflow decreases with the Eddington ratio:

$$\frac{P_\mathrm{o}}{L_\mathrm{Edd}} = 10^{-4} \cdot \left(\frac{\dot{M}_\bullet}{\dot{M}_\mathrm{Edd}} \right)^{-1.8431} . \tag{3.14}$$

This guarantees that the minimum value for the outflow efficiency is $\epsilon_\mathrm{o} = 10^{-5}$, which was calculated by Churazov et al. (2005) assuming that gas cooling and AGN feedback balance each other at the Eddington limit. We choose $\frac{\dot{M}_\bullet}{\dot{M}_\mathrm{Edd}} = 0.05$ as the threshold between radio and quasar mode. The value for the outflow at $\frac{\dot{M}_\bullet}{\dot{M}_\mathrm{Edd}} = 1$ follows the calculations of Churazov et al. (2005), who find $\epsilon_\mathrm{o} \approx 10^{-5}$ for black holes accreting with the Eddington accretion rate.

The feedback model of Churazov et al. (2005) was recently confirmed by observations (see also Russell et al. 2013) measuring luminosities and cavity powers of a large sample of unresolved nuclear X-ray sources. Most of the selected brightest cluster galaxies (BCGs) have large X-ray cavities. The data from Russell et al. (2013) show a large scattering of the luminosities in the radio regime illustrated by round filled circles with black errorbars in Fig. 3.1, implying that a secondary quantity influences the luminosity. A few data points are below the theoretical lower limit, albeit the uncertainties in the observations are relatively high. Uncertainties can occur, for example, when measuring the cavity volume due to projection effects. In Fig. 3.1, the black hole masses are color-coded as indicated by the colorbar. The masses from Russell et al. (2013) are based on K-band magnitudes, which is known to be problematic. Therefore, we use the dynamical masses from McConnell & Ma (2013) for the sources included in both samples. Nearly all black holes that lie below the prediction are very massive ($> 10^9 M_\odot$). For lower masses, the observations are in better agreement with the predictions. We will discuss the uncertainties in section 3.4.2 in more detail.

Recently, Mezcua & Prieto (2014) presented measurements of luminosities of a much smaller sample of AGN, but with sufficiently larger angular resolution and sensitivity. Their estimations for L_bol are more reliable than those presented in Russell et al. (2013), because they measure L_bol after integrating the radio to X-ray Spectral Energy Distribution (SED). Furthermore they explicitly provide values for X-ray cavity powers. For CenA, M87 and NGC1052, they used X-ray cavities of maser emission from the literature (Prieto et al. 2010, Russell et al. 2013, Fernández-Ontiveros et al. 2012). All other values were estimated using the correlation between core radio luminosity at 5 GHz and P_o of Merloni & Heinz (2007). The data from Mezcua & Prieto (2014) is also included in Fig. 3.1, where the filled stars represent the luminosities and the squares the cavity powers. Since equation (3.13) is a lower limit, their luminosities are in very good agreement with the predictions. The cavity powers do not always match the blue line, but as described by Mezcua & Prieto (2014), they are expected to be lower limits, because the estimations of P_o do not take into account the energy which is used to compress the gas when the jet advances the ISM/ICM.

In simulations, the theoretical and observational results shown in Fig. 3.1 can be used

to calculate the efficiencies $\epsilon_{\rm o}$ and $\epsilon_{\rm r}$. To estimate the radiative and outflow efficiencies, we first have to assume a value for the total efficiency η and then use the predictions from Churazov et al. (2005) to separate the AGN feedback into radiation and mechanical outflow. In theoretical studies, the total efficiency is often assumed to be 0.1 (e.g. Churazov et al. 2005), however, observations of Davis & Laor (2011) and Chelouche (2013) suggest a mass dependence of this parameter. In the model from Churazov et al. (2005), both $\epsilon_{\rm o}$ and $\epsilon_{\rm r}$ depend on the accretion rate and the total efficiency. For $\dot{M}_\bullet/\dot{M}_{\rm Edd} < 0.05$ the lower limit for $\epsilon_{\rm r}$ can be calculated with equation (3.8) and (3.13), i.e.

$$\epsilon_{\rm r,min} = 10\eta\frac{\dot{M}_\bullet}{\dot{M}_{\rm Edd}} \tag{3.15}$$

Since this is only a lower limit, all solutions between $\epsilon_{\rm r,min}$ and $\epsilon_{\rm r,max} = \eta$ are possible. Therefore, we introduce the slope β, which is in the range between 0 and 1, to get a general expression for $\epsilon_{\rm r}$:

$$\epsilon_{\rm r} = A \cdot \eta \left(\frac{\dot{M}_\bullet}{\dot{M}_{\rm Edd}}\right)^{\beta}, \tag{3.16}$$

where $A = 10^{-4} \cdot 0.05^{-2.8431-\beta}$. The outflow efficiency is calculated with equation (3.16) and (3.12).

For $\dot{M}/\dot{M}_{\rm Edd} > 0.05$ the radiation dominates. The origin of the blue line in Fig. 3.1 in this regime is the analytical calculation by Churazov et al. (2005), which is based on the equilibrium between gas cooling and heating of gas due to AGN feedback. Hence, it is not only a lower limit and it is not necessary to introduce a slope as in the radio regime. In that respect from equation (3.7) and (3.14) follows

$$\epsilon_{\rm o} = 10^{-4}\eta \left(\frac{\dot{M}_\bullet}{\dot{M}_{\rm Edd}}\right)^{-2.8431} \tag{3.17}$$

and thus $\epsilon_{\rm r} = \eta - \epsilon_{\rm o}$. This is shown in Fig. 3.2 for different black hole masses. The filled circles and diamonds in Fig. 3.2 are the observations from Davis & Laor (2011) and Chelouche (2013) illustrating that they are not consistent with the model for $\eta = 0.1$ (green lines). Therefore, we account for the observed spin of black holes by following the observations of Davis & Laor (2011) for quasars and of Chelouche (2013) for Seyfert 1 AGN, who both find a correlation between the radiative efficiency and the black hole mass. Hence, we use the relation found by Davis & Laor (2011) to estimate the total efficiency at the Eddington limit, which is approximately the same as the radiative efficiency at the Eddington limit:

$$\eta_{\rm Edd}(M_\bullet) \approx \epsilon_{\rm r,Edd}(M_\bullet) = 0.089 \left(\frac{M_\bullet}{10^8 M_\odot}\right)^{0.52}. \tag{3.18}$$

We limit $\eta_{\rm Edd}(M_\bullet)$ by the value 0.42, which is the theoretical maximum efficiency of a rotating black hole. To calculate the outflow efficiency, the constant value of $\eta = 0.1$ is used as it is currently difficult to estimate outflow efficiencies with observations (see section

3.4.2 for further discussion). Equation (3.12), (3.16) and (3.17) then lead to the following set of equations:

$$\epsilon_\mathrm{r} = \begin{cases} A\eta_\mathrm{Edd}(M_\bullet)\left(\frac{\dot{M}_\bullet}{\dot{M}_\mathrm{Edd}}\right)^\beta, \text{ if } \frac{\dot{M}_\bullet}{\dot{M}_\mathrm{Edd}} < 0.05, \\ \eta_\mathrm{Edd}(M_\bullet) - 10^{-4}\eta_\mathrm{Edd}(M_\bullet)\left(\frac{\dot{M}_\bullet}{\dot{M}_\mathrm{Edd}}\right)^{-2.8431}, \\ \text{otherwise} \end{cases} \tag{3.19}$$

and

$$\epsilon_\mathrm{o} = \begin{cases} 0.1 - A \cdot 0.1\left(\frac{\dot{M}_\bullet}{\dot{M}_\mathrm{Edd}}\right)^\beta, \text{ if } \frac{\dot{M}_\bullet}{\dot{M}_\mathrm{Edd}} < 0.05, \\ 10^{-5}\left(\frac{\dot{M}_\bullet}{\dot{M}_\mathrm{Edd}}\right)^{-2.8431}, \text{ otherwise.} \end{cases} \tag{3.20}$$

In our simulations both radiative and mechanical feedback are implemented as thermal feedback, since we do not resolve jets.

The three coloured lines in Fig. 3.2 show the model from Churazov et al. (2005) for $\beta = 0.5$ (thick dashed lines) and $\beta = 1$ (thin dashed lines) and different black hole masses. The red lines correspond to $M_\bullet = 10^{10} M_\odot$, the green ones to $M_\bullet = 10^8 M_\odot$ and the blue ones to $M_\bullet = 10^6 M_\odot$. This is in much better agreement with the observations than choosing a constant total efficiency. In the radio regime, we included observations by Russell et al. (2013) and Mezcua & Prieto (2014), who measured the power of the radiation and outflow as well as L_Edd. With equation (3.10) they calculated $\dot{M}/\dot{M}_\mathrm{Edd}$. Using the equations (3.7), (3.8) and (3.11) we can derive the efficiencies

$$\epsilon_\mathrm{o} = \eta \cdot \frac{P_0/L_\mathrm{Edd}}{\dot{M}_\bullet/\dot{M}_\mathrm{Edd}} \tag{3.21}$$

and

$$\epsilon_\mathrm{r} = \eta \cdot \frac{L/L_\mathrm{Edd}}{\dot{M}_\bullet/\dot{M}_\mathrm{Edd}}. \tag{3.22}$$

In the radio regime, it is justified to use $\eta = 0.1$. As can be seen in Fig. 3.2, the data points for the radiative efficiency do not show the simple trend as assumed in Churazov et al. (2005). In fact, they seem to be consistent with randomly scattering between 10^{-1} and 10^{-5}. There also seems to be no mass dependency in the radio regime[1].

For NGC 1097 and NGC 1386, the radiation dominates. The observations by Mezcua & Prieto (2014) show that these sources have small jets, whereas the other sources have larger jets. Interestingly both NGC 1097 and NGC 1386 have a bar at large scales, but they show no evidence of a bar on small scales. They both also have a ring of star-forming regions. This indicates that the morphology of the galaxies will play a key role for future studies. For simulations this implies that the resolution has to be high enough to resolve the morphology of galaxies. Note that this is not the case for the simulations performed in this work, but will be the aim for forthcoming studies.

[1]For the data from Russell et al. (2013) the dynamical masses from McConnell & Ma (2013) were taken if available. If not, the same masses were taken which Russell et al. (2013) used to calculate L_Edd.

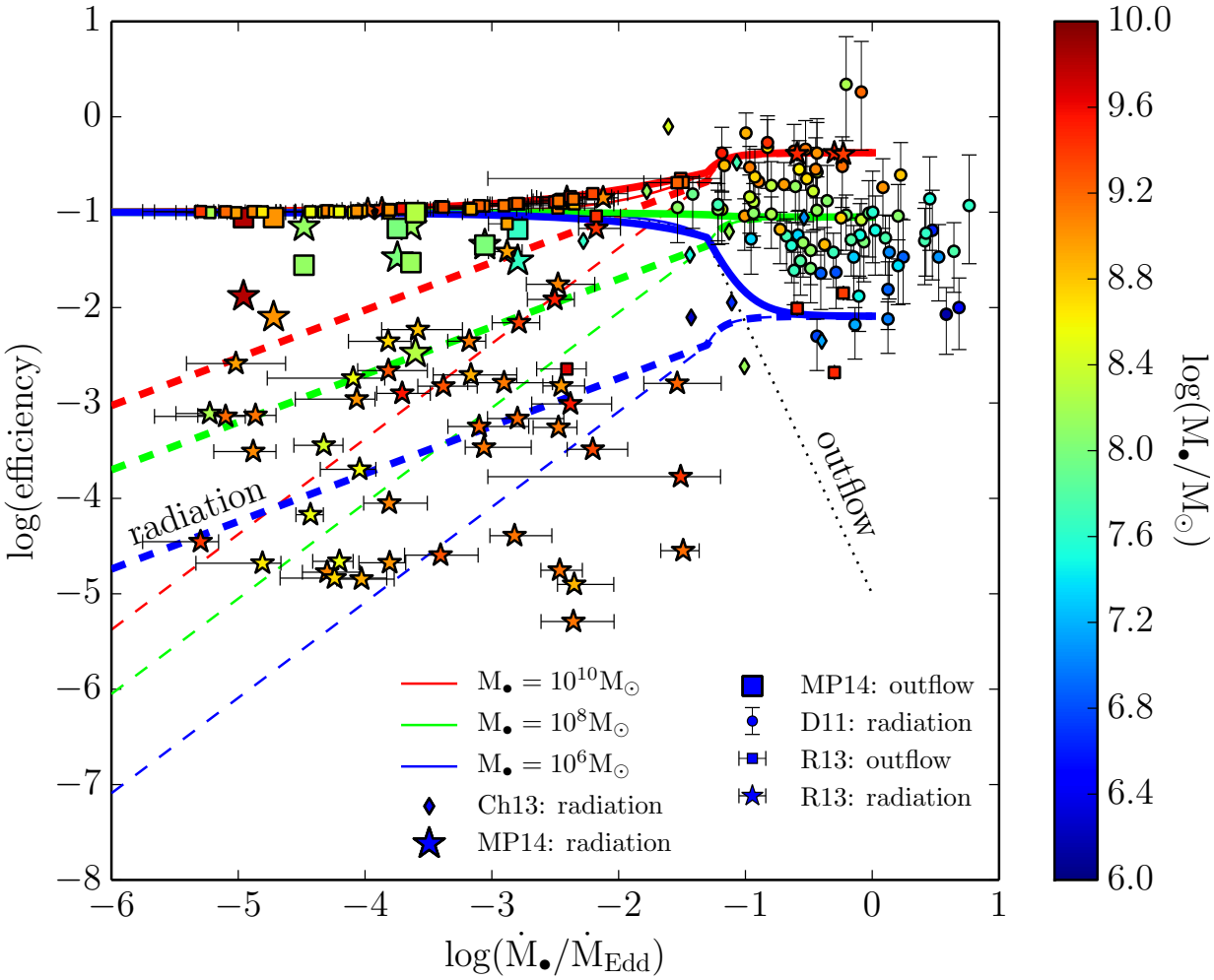

Figure 3.2: Our new feedback model includes both outflow (dotted line) and radiation (dashed lines) as described by Churazov et al. (2005) as well as a mass dependent radiative efficiency following Davis & Laor (2011). The solid lines show the sum of ϵ_o and ϵ_r. The small dots and diamonds are observations by Davis & Laor 2011 (D11) and Chelouche 2013 (Ch13), who both estimated radiative efficiencies. In the radio regime we assume $\eta = 0.1$. The large stars and squares correspond to recent observations by Mezcua & Prieto 2014 (MP14) of the outflow and radiation. From left to right the observed galaxies are M87, NGC 4594, NGC 1097, NGC 3169, NGC 1386, NGC 2911, NGC 1052 and Cen A. Small stars and squares correspond to observations by Russell et al. 2013 (R13). The black hole masses are color-coded as indicated by the colorbar.

	Box size $[(\mathrm{Mpc/h})^3]$	initial particle number	ϵ_f	ϵ_r	ϵ_o
68Mpc/hr fiducial model	48^3	$2 \cdot 216^3$	0.15	0.2	–
68Mpc/hr NFM	48^3	$2 \cdot 216^3$	0.2	variable	variable
68Mpc/hr NAM	48^3	$2 \cdot 216^3$	0.15	0.2	–
68Mpc/hr NFAM	48^3	$2 \cdot 216^3$	0.2	variable	variable
182Mpc/hr fiducial model	128^3	$2 \cdot 576^3$	0.15	0.2	–
182Mpc/hr NFAM	128^3	$2 \cdot 576^3$	0.2	variable	variable

Table 3.1: General settings of the simulations performed in this study. Variable values of ϵ_r and ϵ_o are calculated with equations (3.19) and (3.20).

3.2 The simulations

We performed six simulation runs with the hr resolution level. Four of our simulations are 'test' runs with a smaller box size of $(68\mathrm{Mpc})^3$, which were performed to be able to test the effect of the new black hole accretion and AGN feedback model separately. The first run adopts the 'original' black hole model as described in Hirschmann et al. (2014) to which we refer as the fiducial model. The second run adopts only the new accretion model (NAM), the third run only adopts the new feedback model (NFM), and finally, our fourth run combines both new implementations (NFAM).

The other two simulations have the same resolution but a larger box size of $(182\mathrm{Mpc})^3$ to achieve a larger statistical sample of galaxies and black holes. The first box uses the original implementation of black hole growth and the second box adopts the NFAM model, enabling us to statistically see the effects of the new model, in particular on the more massive galaxy and black hole population.

As described in section 3.1 in detail, the NAM, NFM and NAFM models contain improvements of the black hole model regarding the calculation of the accretion rate and/or the feedback energy of black holes:

1. NAM: For the estimation of the black hole accretion rate we use different boost factors for cold ($\alpha = 100$) and hot ($\alpha = 10$) gas. For this run we use the fiducial feedback model.

2. NFM: For the calculation of the energy of the AGN feedback we consider not only radiative, but also mechanical feedback. The two different feedback mechanisms have different efficiencies. The radiative efficiency ϵ_r depends on the black hole mass and the Eddington ratio, whereas the outflow efficiency ϵ_o depends only on the Eddington ratio. Like in the fiducial model only a fraction ϵ_f of the radiation couples to the surrounding medium. Both kinds of feedback are implemented as thermal feedback. Hence, the total feedback energy is computed with equation (3.9). We use the old accretion model for this simulation.

3. NFAM: Our final run contains both the new feedback and the new accretion model.

The new feedback model as shown in Fig. 3.2 was implemented into the code using equation (3.19) and (3.20). In reality the slope β can be between 0 and 1. However, the choice of β does not play a significant role for the simulations, as the mechanical outflow dominates over the radiation in the radio regime. Furthermore, the AGN luminosities are not calculated during the simulation but only for the analysis afterwards. Thus, we choose the fixed value of $\beta = 0.5$ for all simulations.

For the NAM run and the two fiducial runs we use the standard feedback model with $\epsilon_\mathrm{f} = 0.15$ and a constant radiative efficiency $\epsilon_\mathrm{r} = 0.2$ (Hirschmann et al., 2014). In the other runs we use $\epsilon_\mathrm{f} = 0.2$. The parameters of the simulations used in this work are summarized in Table 3.1.

Note that we identify the dark matter haloes and the corresponding galaxies in the simulation using the friends-of-friends and then the SUBFIND algorithm (Dolag et al. 2009, Springel et al. 2001).

3.3 Results

Black hole-galaxy mass scaling relations at $z = 0$

The upper panel in Fig. 3.3 shows the predictions for the present-day $M_\bullet$-M_* relation for the 68Mpc/hr NFAM simulation. In our simulations M_* is the total stellar mass of a galaxy and not only the stellar mass of the bulge, because our resolution is not high enough to resolve the internal structures of the individual galaxies. Hence, all galaxies consist mainly of a spheroidal component. The solid black lines in Fig. 3.3 indicate the observations of McConnell & Ma (2013) and the dashed line is the fit for all black holes in our simulations with $M_\bullet > 5 \cdot 10^7$. This threshold is necessary to exclude newly seeded black holes, as they are seeded far below the relation and need time to grow onto the relation. Black holes with masses above $M_\bullet > 5 \cdot 10^7$ are close enough to the $M_\bullet$-M_* relation to exclude seeding effects. The figure shows the excellent agreement of our NFAM model with observations, in particular in comparison to other simulations, i.e. the Illustris simulation (Sijacki et al., 2015) and the MassiveBlack-II simulation (Khandai et al., 2015). The dark grey shaded area marks the 1σ-scatter of the observations and the light grey shaded area the 1σ-scatter for our simulation. For a quantitative comparison with the observations, Table 3.2 shows the best-fitting parameters a and b corresponding to the fit function $\log(M_\bullet/M_\odot) = a + b \cdot \log(M_*/10^{11} M_\odot)$ for all six runs. It also contains the 1σ scatter of McConnell & Ma (2013) and our simulations. For the 182Mpc/hr runs, we consider only stellar masses below $10^{12} M_\odot$ to exclude the central galaxies of very massive clusters (see discussion in section 3.3.1). While the slope of the $M_\bullet$-M_* relation turns out to be relatively insensitive to the values of ϵ_r and ϵ_f, the normalization depends strongly on these parameters as already shown by Di Matteo et al. (2005), because the final black hole mass follows the proportionality $M_\bullet \propto (\epsilon_\mathrm{f} \epsilon_\mathrm{r})^{-1}$. Hence, many recent simulations which include black holes (e.g. Di Matteo et al. 2005, Robertson et al. 2006, Degraf et al. 2011, Hirschmann et al. 2014) tuned these parameters in order to reproduce the normalization

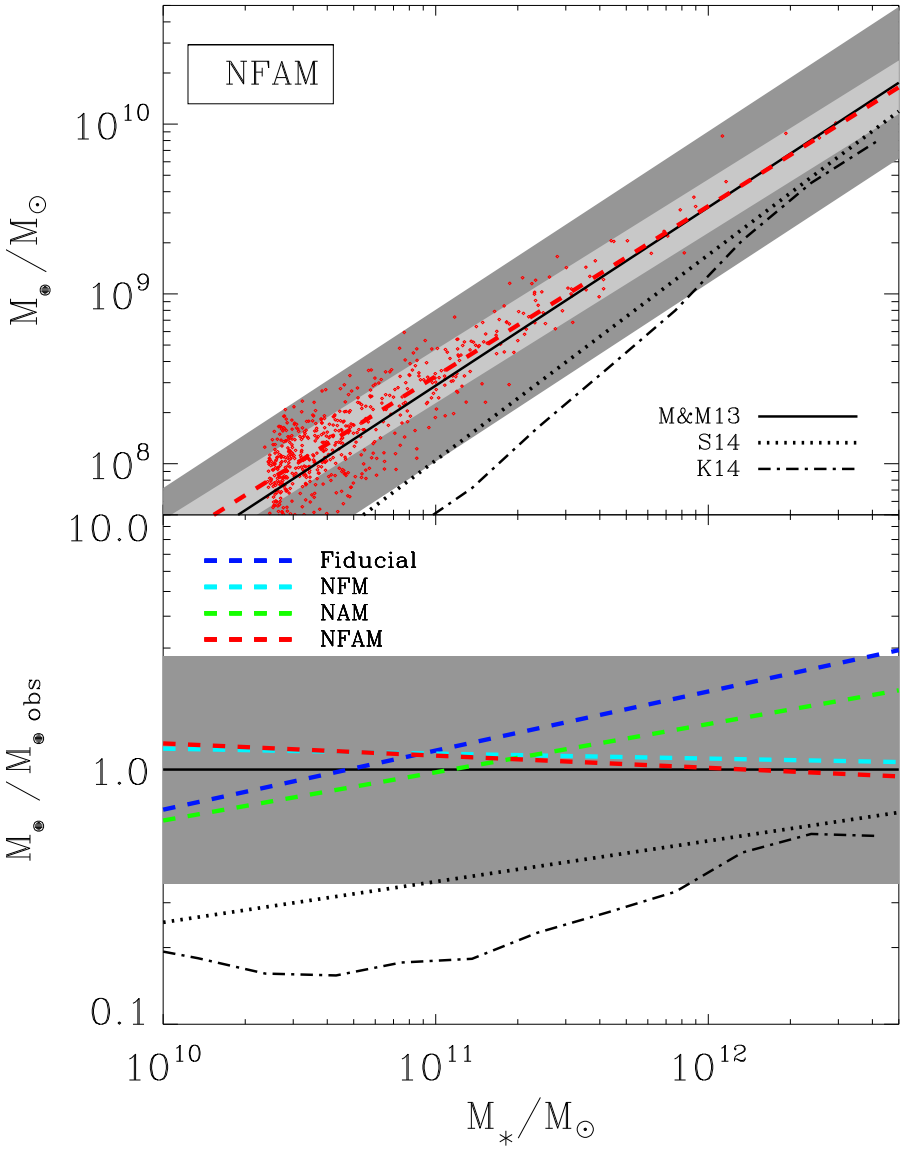

Figure 3.3: Upper panel: present-day relation between the black hole mass and the host galaxy stellar mass for 68Mpc/hr NFAM run. The dots represent the black holes in the simulations at $z = 0$. The solid black line shows the fit to the observations by McConnell & Ma 2013 (M&M13) and the dark shaded area the corresponding 1σ-error. The dashed lines illustrate the fit to our simulation for $M_\bullet > 5 \cdot 10^7 M_\odot$ (to exclude seeding effects) and the light shaded area the corresponding 1σ-error. For comparison with other simulations we also show the results from Sijacki et al. 2015 (S14) and Khandai et al. 2015 (K14) as dotted and dotted-dashed lines. Lower panel: Ratio of the simulated black hole mass in all different models (Fiducial: dark blue, NFM: light blue, NAM: green, NFAM: red) to the observed black hole mass $M_{\bullet\mathrm{obs}}$ (McConnell & Ma (2013), black solid line and grey shaded area) versus the galaxy stellar mass.

	a	b	σ
McConnell & Ma (2013)	8.46 ± 0.08	1.05 ± 0.11	0.45
68Mpc/hr fiducial model	8.53	1.28	0.17
68Mpc/hr NFM	8.52	1.03	0.16
68Mpc/hr NAM	8.44	1.24	0.19
68Mpc/hr NFAM	8.51	1.00	0.16
182Mpc/hr fiducial model	8.46	0.93	0.15
182Mpc/hr NFAM	8.40	1.09	0.14

Table 3.2: Best-fit parameters and standard deviation for our runs in comparison to the observations by McConnell & Ma (2013). All black holes with masses smaller than $5{\cdot}10^7 M_\odot$ have been excluded for the fit. For the 182Mpc/hr runs we took only stellar masses below $10^{12} M_\odot$ into account to exclude clusters.

of the observed $M_\bullet$-M_* relation. In addition, the normalization depends on the cooling function (Churazov et al., 2005), i.e. the values of ϵ_r and ϵ_f must be larger to get the same normalization if the cooling is more effective. Since ϵ_r is not a constant parameter in our new AGN feedback model, the slope of the $M_\bullet$-M_* relation changes. This is shown in the lower panel of Fig. 3.3. Here we show the ratio of the simulated to the observed black hole mass (from McConnell & Ma 2013) versus the galaxy stellar mass for all different models, i.e. the Fiducial, NFM, NAM and NFAM runs (colored dashed lines), as well as for the results from Sijacki et al. (2015) and Khandai et al. (2015) (black dotted and dotted-dashed lines, respectively). Since they use a constant radiative efficiency, their slopes are similar to our fiducial simulation. In our new feedback model, however, ϵ_r is not a free parameter anymore. Therefore, it is encouraging that *both the slope and the normalization of the $M_\bullet$-M_* relation are self-consistently predicted with less free parameters than in the standard model.*

However, even in our new model one free parameter remains, i.e. the fraction of radiation coupling to the surrounding medium ϵ_f, for which we choose a value of $\epsilon_\mathrm{f} = 0.2$ (to be consistent with the observed relation)[2]. For lower efficiencies the feedback would be higher and the black holes would grow too much. We would like to remark that the normalization of the $M_\bullet$-M_* relation in simulations always depends on the observations used for the calibration of ϵ_f. However, there are discrepancies in observational estimations of the $M_\bullet$-M_* relation. For example, Scott et al. (2013) find a slightly higher normalization, but a similar slope as McConnell & Ma (2013), which would change the calibration of ϵ_f.

In our simulations, the NFAM model reproduces the observed slope better than the Fiducial model, in which the black holes accrete slightly too much gas, resulting in too large masses, particularly at low redshifts and in the most massive galaxies. The new AGN feedback model is more efficient in preventing gas accretion onto massive black holes. Thus, the gas in the vicinity of the black hole has a higher thermal and kinetic energy, which

[2]Note that this value depends on the resolution, because at lower resolutions the feedback energy is spread further away from the black hole. Hence, for our simulations, this value is comparatively high.

results in lower accretion rates. Consequently, as can be seen in Fig. 3.3, the massive end of the $M_\bullet$-M_* relation is now in excellent agreement with the observations from McConnell & Ma (2013).

Our second implementation is the separation of hot and cold gas (NAM). For an increasing amount of hot gas in the vicinity of the black hole, this results in slightly lower accretion rates due to the smaller boost factor. Even if the new accretion model by itself cannot prevent the most massive black holes from growing too much, it can decrease the black hole masses slightly. Consequently, a combination of both modifications results in the best match with the observed $M_\bullet$-M_* relation.

The best-fitting parameters in Table 3.2 summarize the excellent agreement of the NFM-run and the NFAM-run with the observations. Particularly, the slope b is in better agreement with the observations than in the other runs and also in the analysis of the Illustris simulation shown by Sijacki et al. (2015). Note that in the simulations, the 1-σ scatter is significantly smaller than in the observations. As the typical measurement errors in the observations are still substantial, future observations are needed to distinguish, whether this relation indeed has such a small scatter as seen in the simulations, or if there are still additional processes missing in the simulations which influence the growth and evolution of the black holes.

Furthermore, the scatter in the black hole mass in the simulations decreases with increasing black hole mass. This is most likely a consequence of statistical merging (Peng 2007, Hirschmann et al. 2010, Jahnke & Macciò 2011) and is also visible in the Illustis simulation (Sijacki et al., 2015). Nevertheless, the relative role of AGN feedback and stasticial merging in establishing the $M_\bullet$-M_* relation and producing the observed slope still remains a matter of debate.

To explore black hole growth in our simulations in more detail, Fig. 3.4 shows the cosmic evolution of four black holes selected due to their different present-day mass (different colors) on the $M_\bullet$-M_* relation[3]. When black holes are merging, the most massive progenitor is followed back in time. As can be seen in this figure we can distinguish between two different phases of black hole growth: during the first phase, they grow rapidly until they reach the $M_\bullet$-M_* relation and thus the Eddington limit. In this phase black hole accretion is primarily triggered by smooth accretion of cold gas, because below the Eddington limit AGN feedback is not strong enough to suppress gas cooling. Hence, the cold gas reservoir is large enough to trigger black hole growth. In our simulations, this phase is a consequence of the small black hole seeding mass. However, recent observations seem to indicate that the slope of the $M_\bullet$-M_* relation is steeper for black holes with masses below $10^8 M_\odot$ (Graham & Scott 2013, Scott et al. 2013). Therefore, we can speculate that the phase of rapid black hole growth is actually present and that simulations in which black holes are seeded on or above the $M_\bullet$-M_* relation might miss the first phase of black hole growth.

In the second phase black holes grow along the $M_\bullet$-M_* relation. In this phase, gas cooling and AGN feedback are in equilibrium and hence both star formation and black

[3]The two outliers (black and red diamond with $M_\bullet \approx 2 \cdot 10^8 M_*$) are due to temporary attributions to different haloes.

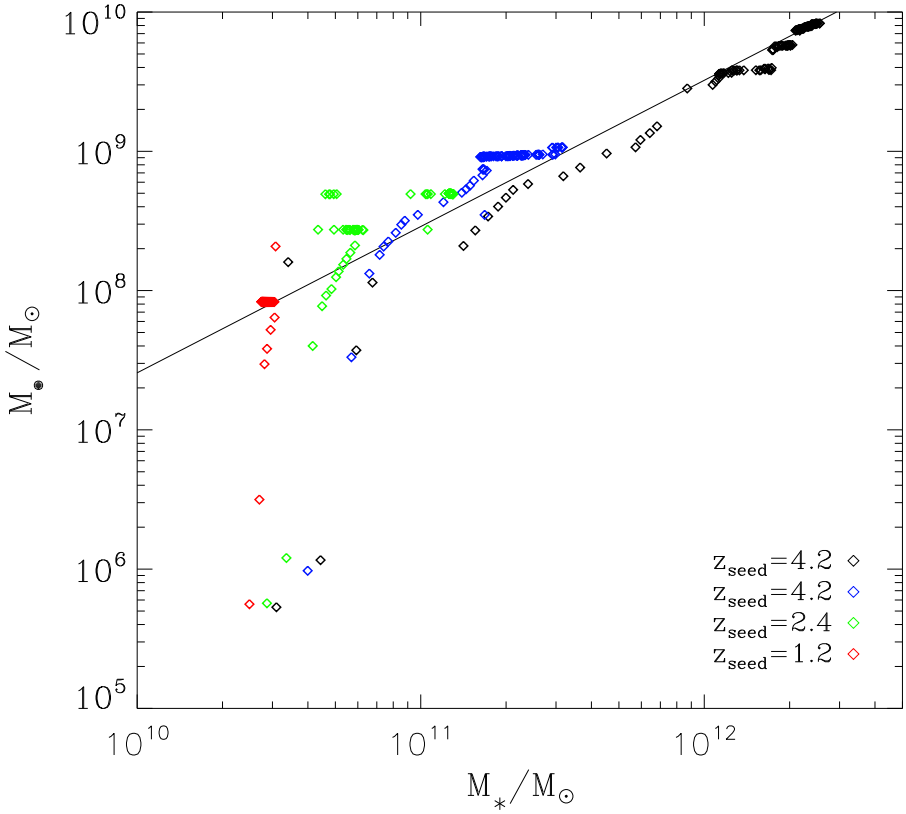

Figure 3.4: Evolution of the total black hole mass and the corresponding host galaxy stellar mass of four haloes (diamonds in different colors) in the 68Mpc/hr NFAM simulation. The black line shows the fit from McConnell & Ma (2013)

hole growth are suppressed. Only the in-fall of cold gas either in the form of streams or clumps as well as merger events can trigger star formation and black hole growth during this period.

To demonstrate that at low redshifts black holes grow faster compared to the growth of the stellar mass than at high redshifts, we show exemplarily the results for four typical objects, where we verified that they reflect the typical growth of BHs with the chosen final mass. For example, the stellar mass of the host galaxy corresponding to the red diamonds grows very little, whereas the black hole mass increases by more than two orders of magnitude. This galaxy reaches the $M_\bullet$-M_* relation already 1.08 Gyr after the seeding. In contrast, the stellar mass of the host galaxy corresponding to the black and blue diamonds grows much more during the first phase of black hole growth. Here, the object reaches[4] the $M_\bullet$-M_* relation after 2.29 Gyr. This trend is also visible in Fig. 3.6, which shows the $M_\bullet$-M_* relation at different redshifts, in particular when looking at the data points

[4]We excluded the outlier (black diamond on the left with $M_\bullet \approx 2 \cdot 10^8 M_*$).

corresponding to the lowest stellar masses. The figure will be discussed later in more detail. Hence, we suspect that the black hole mass at the threshold between the two phases – namely when the $M_\bullet$-M_* relation is reached – depends on the seeding redshift. We suggest, that these differences might be a consequence of the star formation rate, which decreases with time (see section 3.3.2).

Furthermore, since black holes are seeded upon a certain galaxy mass, they are seeded earlier in a dense environment and can thus become more massive. We plan to study the evolution of black holes and their host galaxies in a forthcoming study in more detail, performing a simulation with resolution high enough to resolve the internal structure of galaxies. In particular, we are interested in the effect of merger events on black hole growth and star formation, because the black hole and stellar masses in Fig. 3.4 seem to grow mainly in steps after reaching the $M_\bullet$-M_* relation. These steps also explain the scatter around the $M_\bullet$-M_* relation in our simulations. It furthermore indicates, that black hole growth and star formation are both triggered by merger events. However, for this study it is more important to increase the box size instead of the resolution, in particular to extend our simulation results towards more massive galaxies and black holes.

Evolution of the black hole mass function

Fig. 3.5 shows the black hole mass function of both the fiducial and the NFAM 182Mpc/hr run. We compare our simulations to observed black hole mass functions of the local universe by Marconi et al. (2004), Shankar et al. (2004), Shankar et al. (2009) and Shankar (2013). We would like to remark that the uncertainties in these relations are large, in particular because the black hole masses are estimated using different scaling relations as recently discussed by Shankar (2013) and therefore, we also show the black hole mass functions derived from the best fit velocity dispersion function and stellar mass function from Bernardi et al. (2010) using different scaling relations, i.e. from McConnell & Ma 2013 (dotted grey lines) and Kormendy & Ho 2013 (dashed grey lines). Since the high mass end of all of these curves is lower than in Shankar (2013), we take – following their discussion – the two data points at the high mass end of Shankar (2013) as upper limits. One should also keep in mind that as discussed in Tundo et al. (2007), the different black hole scaling relations are not necessarily consistent with each other or with the $M_\bullet$-M_* relation from McConnell & Ma (2013), which we use in this work to calibrate the value of the free parameter ϵ_f. The uncertainties in the scaling relations are also reviewed and discussed in Kormendy & Ho 2013.

The high mass end of the fiducial simulation is just in agreement with the upper limits of Shankar (2013), but the NFAM simulation matches previously published black hole mass functions much better, because the new accretion and feedback models suppress the growth of massive black holes more efficiently. As already shown in Fig. 3.3, the smaller masses of the most massive black holes are mainly caused by the new feedback scheme, where the mass dependency of the radiative efficiency for the model is taken from Davis & Laor (2011), which is quite similar to the results presented in Trakhtenbrot (2014). From a theoretical point of view, this relation is motivated by the fact that the spin of the black

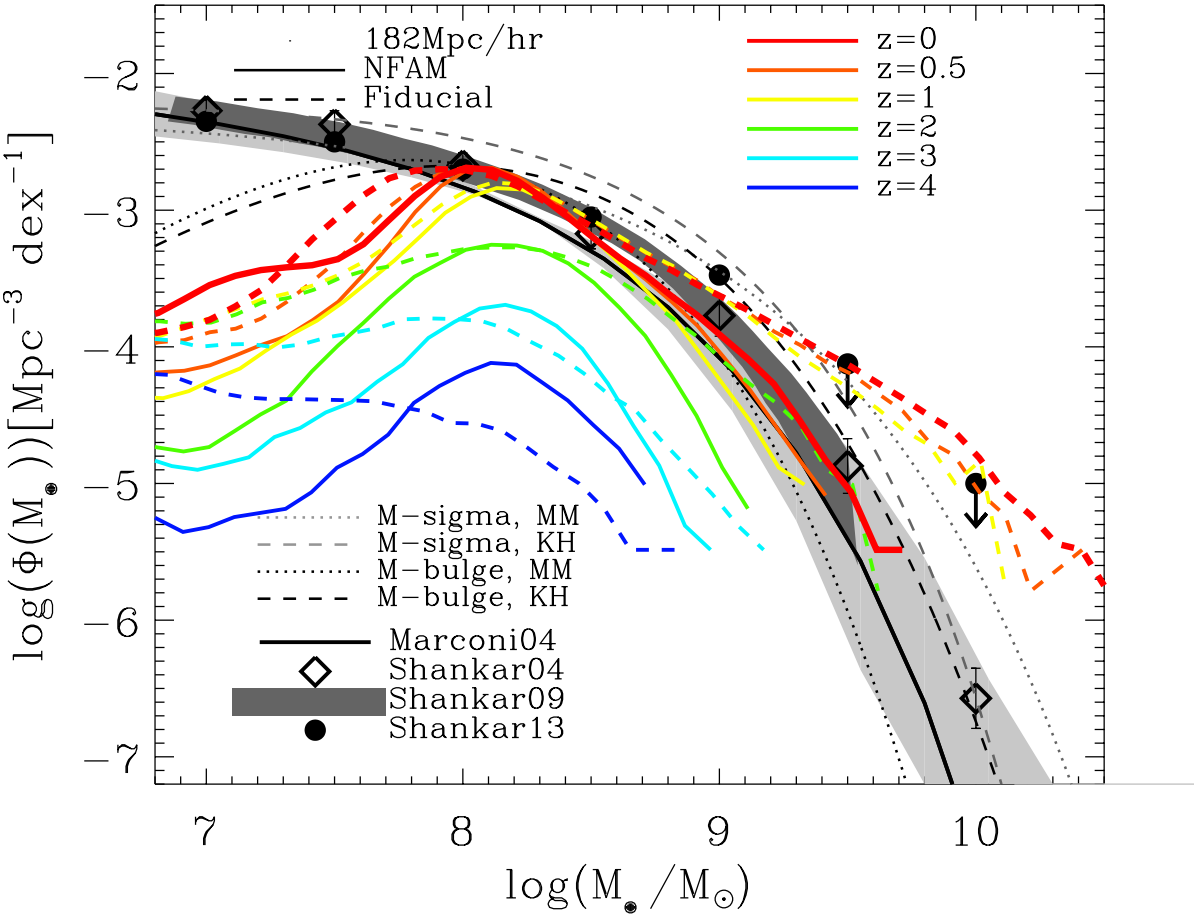

Figure 3.5: Black hole mass function of the fiducial (dashed coloured lines) and the NFAM (solid coloured lines) 182Mpc/hr simulation at different redshifts. For comparison we show observations from Marconi et al. 2004 (black solid line), Shankar et al. 2004 (black diamonds and lines with grey shaded areas), Shankar et al. 2009 (dark grey shaded area) and Shankar 2013 (black dots). To show the uncertainties in deriving black hole mass functions from observations, we show as dotted and dashed grey curves the black hole mass functions derived from the best fit velocity dispersion function and stellar mass function from Bernardi et al. (2010) using different scaling relations, i.e. from McConnell & Ma 2013 (MM) and Kormendy & Ho 2013 (KK).

hole should increase with mass. However, the slope of this relation might actually be flatter than in Davis & Laor (2011) due to selection effects (see discussion in Raimundo et al. 2012 and Laor & Davis 2011). Thus, the massive end of the black hole mass function of the NFAM simulation could be a lower limit. Furthermore, we already mentioned that it is uncertain whether in general the normalization of the $M_\bullet$-M_* relation could be larger than in McConnell & Ma (2013).

For less massive galaxies, the effects of the seeding become dominant which cause the deviation from the observed black hole mass function at small masses. However, especially at low masses, observations are uncertain and only give an upper limit (Shankar, 2013), in particular because pseudo-bulges do probably not follow the observed scaling relations like the $M_\bullet - \sigma$ relation or the $M_\bullet$-M_* relation as reviewed by Kormendy & Ho (2013).

Evolution of the black hole-galaxy mass scaling relations

Fig. 3.6 shows the relation between the black hole mass and the stellar mass of the host galaxy for our NFAM 182Mpc/hr run at different redshifts, again in comparison to the observations by McConnell & Ma (2013) and the simulations from Sijacki et al. (2015) and Khandai et al. (2015). Again, we only show black holes with masses above $5 \cdot 10^7 M_\odot$. Below this limit black holes generally grow fast, while M_* stays relatively constant until they reach the $M_\bullet$-M_* relation. The reason is the equilibrium between AGN feedback and gas cooling, when black holes accrete with $\dot{M}_{\rm Edd}$ as described by Churazov et al. (2005). Afterwards black holes can only grow along the $M_\bullet$-M_* relation together with their host galaxy through smooth accretion or merging.

In the NFAM run, the $M_\bullet$-M_* relation is much earlier in place than in the original run, namely already at $z = 3$. Furthermore, the panels at $z = 2$ and $z = 1$ show that in the fiducial simulation the slope of the $M_\bullet$-M_* relation is larger than at $z = 0$, where it is in agreement with the observed $M_\bullet$-M_* relation.

In our very massive galaxies ($M_* \approx 10^{13} M_\odot$), i.e. the central galaxies of galaxy clusters, most black holes are lying slightly below the $M_\bullet$-M_* relation. This is most likely caused by a still too large stellar mass in these very massive galaxies, also visible in the high mass excess of the stellar mass function and the still too large baryon conversion efficiency for large haloes as discussed later on. The reason for the overestimation of stellar masses of cluster galaxies might be the purely thermal feedback in our model, which fails to reproduce the mechanical feedback in such massive systems, visible as large X-ray cavities in observed clusters. Hence, an implementation of mechanical jets (e.g. Ostriker et al. 2010, Dubois et al. 2013, Choi et al. 2014) might play an important role for future simulations, in which both the resolution and the size of the cosmological boxes will get larger and larger. Furthermore, in our analysis we do not distinguish between the stars belonging to the central galaxy and the ones which would be related to the intra cluster light (ICL), which can be substantial for such massive systems. It is also possible that some merging systems are identified as one galaxy. Thus, the predicted stellar mass for cluster galaxies might actually be slightly larger than in observations.

For comparison, Fig. 3.6 also includes the fit to the data points of the fiducial model,

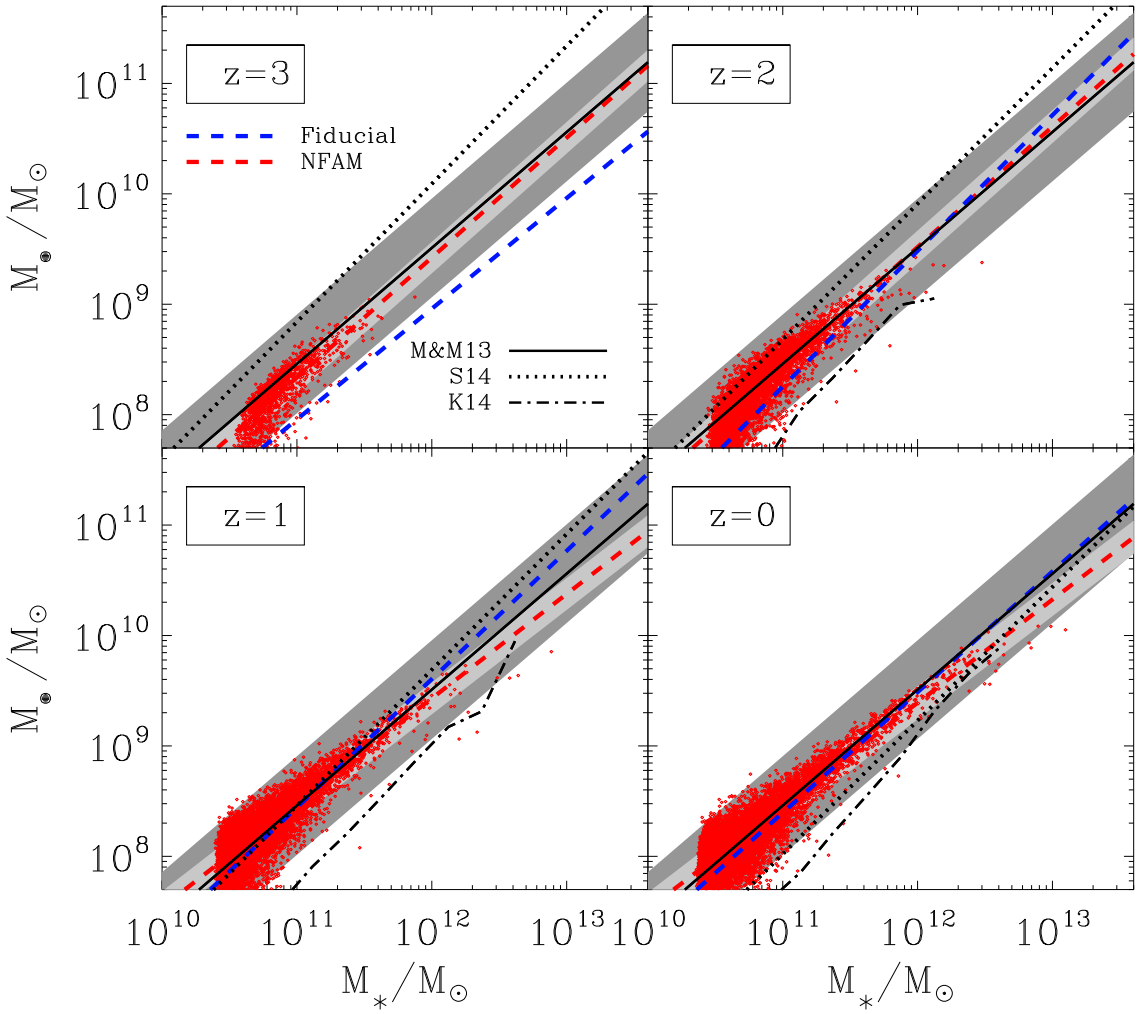

Figure 3.6: Evolution of the relation between the black hole mass and the host galaxy stellar mass for the NFAM 182Mpc/hr run (red dots). The dashed lines are fits for both 182Mpc/hr runs including all black holes with masses larger than $5 \cdot 10^7 M_\odot$ and stellar masses with masses smaller than $10^{12} M_\odot$ to exclude clusters. The light grey shaded area marks the corresponding 1σ-error of the NFAM run. The black line with the dark grey shaded area represents the fit through the observations from McConnell & Ma (2013) with the 1σ-error. The dotted and dotted-dashed lines show the results from other simulations, i.e. from Sijacki et al. (2015) and Khandai et al. (2015).

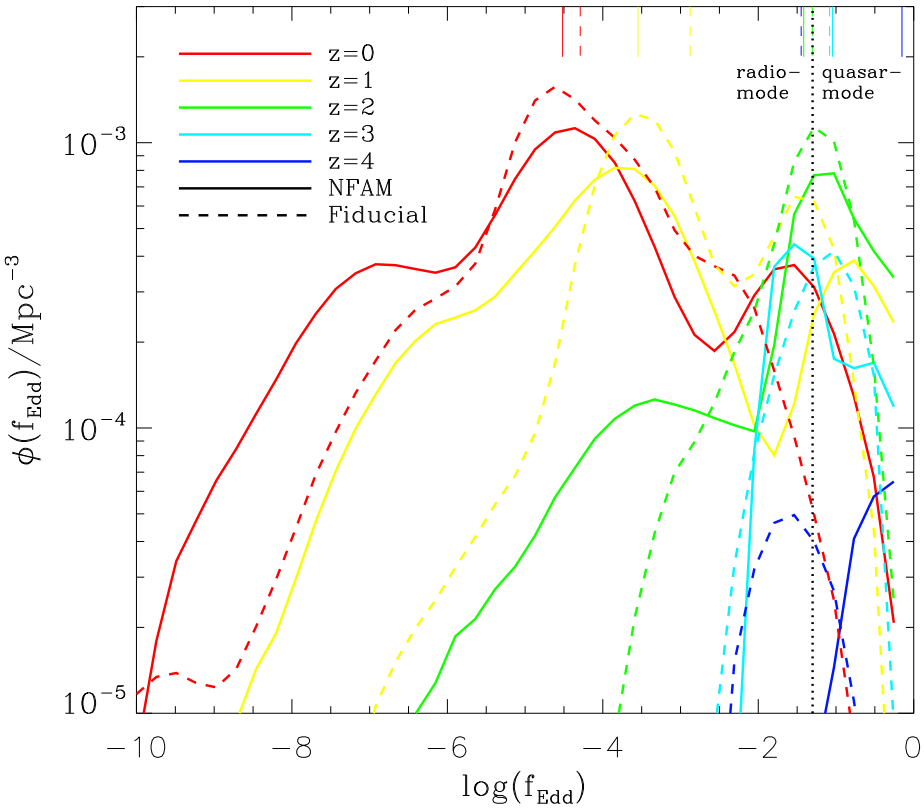

Figure 3.7: Eddington ratio distributions for the two 182Mpc/hr simulations at different redshifts. The black dotted vertical line marks the threshold between radio-mode and quasar-mode. The vertical lines in the top show the mean values.

where black holes in galaxy clusters are substantially more massive compared to the stellar mass, especially at redshifts around $z = 1$. Although the fit at $z = 0$ is in agreement with the fit from McConnell & Ma (2013), it is evident from the black hole mass function that the black hole masses are too large at the high-mass end implying that the galaxy stellar masses must be too large (compensating for the large black hole masses) which will be investigated in more detail in section 3.3.1.

Eddington ratio distribution

The modifications in our NFAM simulations are also expected to significantly affect the Eddington ratios of the black holes. Therefore, in Fig. 4.7 we present the Eddington ratio distributions of both 182Mpc/hr simulations at different redshifts. The black dotted vertical line shows the threshold between radio-mode and quasar-mode and the vertical lines in the top mark the mean values. For redshifts below $z = 3$ the Eddington ratios are clearly smaller in the NFAM run than in the fiducial simulation. For higher redshifts the

Eddington ratios in the NFAM run are larger than in the fiducial simulation. We suggest that the wide range of values for the feedback efficiency leads to broader distributions. Especially the range of very low accretion rates is represented much better in the NFAM simulation than in the fiducial run.

In contrast to the recent study from Sijacki et al. (2015) our simulations – in particular the NFAM run – show two peaks in the Eddington ratio distribution for $z < 4$, one in the radio-mode and a second peak either in the radio-mode or in the quasar-mode. This indicates that we have a clear separation between two accretion modes. In the fiducial model, where a step function was used to distinguish between radio-mode and quasar-mode (Hirschmann et al., 2014), the two peaks are only visible at $z = 1$. In the NFAM simulation, the second peak appears at $z = 3$ in the quasar-mode. For smaller redshifts it is much more distinct. Interestingly, at $z = 1$ and $z = 2$, which is the redshift range where most quasars are observed, a very clear second peak is visible in the quasar-mode. For $z = 4$ the Eddington ratios are even higher, because here the first phase of black hole growth is dominant. At $z = 0$ both peaks are in the radio-mode and even a third peak is visible at very low Eddington ratios.

3.3.1 Evolution of the stellar mass function

Fig. 3.8 shows the evolution of the stellar mass function in the simulations (blue: fiducial model, red: NFAM model) and observations (black symbols from Panter et al. 2004, Cole et al. 2001, Bell et al. 2003, Pérez-González et al. 2008, Borch et al. 2006, Bundy et al. 2005, Drory et al. 2004, Fontana et al. 2006 and Marchesini et al. 2007 and black lines from Muzzin et al. 2013 and Bernardi et al. 2013). The figure illustrates that the new feedback scheme can slightly suppress late star formation at the high-mass end, mainly because the radiative efficiency now depends on the black hole mass. Hence, compared to the fiducial model, the modifications in the NFAM model lower the amount of massive galaxies resulting in an overall better match with the massive end of the observed SMF, at least down to $z = 0.2$.

For the entire redshift range, a small peak in the SMFs is visible at stellar masses of about $2 \cdot 10^{10} M_{\odot}$. The origin of this peak is caused by a subtle effect of our black hole seeding. Since black holes are seeded below the $M_{\bullet}$-M_{*} relation, the AGN feedback is efficient during the first phase of black hole growth and hence suppresses star formation until the equilibrium between cooling and AGN feedback is reached. During that phase, the stellar mass stops growing and consequently, there are more galaxies with a certain stellar mass. The peak moves towards higher stellar masses at higher redshifts because of the effect seen in Fig. 3.4, namely that black holes which are seeded earlier have larger stellar masses when they reach the $M_{\bullet}$-M_{*} relation.

The overestimation of the low-mass end of the stellar mass function at high redshifts happens most likely due to the chosen wind model (constant winds as in Springel & Hernquist 2003) as described by Hirschmann et al. (2014) in more detail. Apart from that, our simulations - especially the NFAM run - are in good agreement with observations at high redshifts.

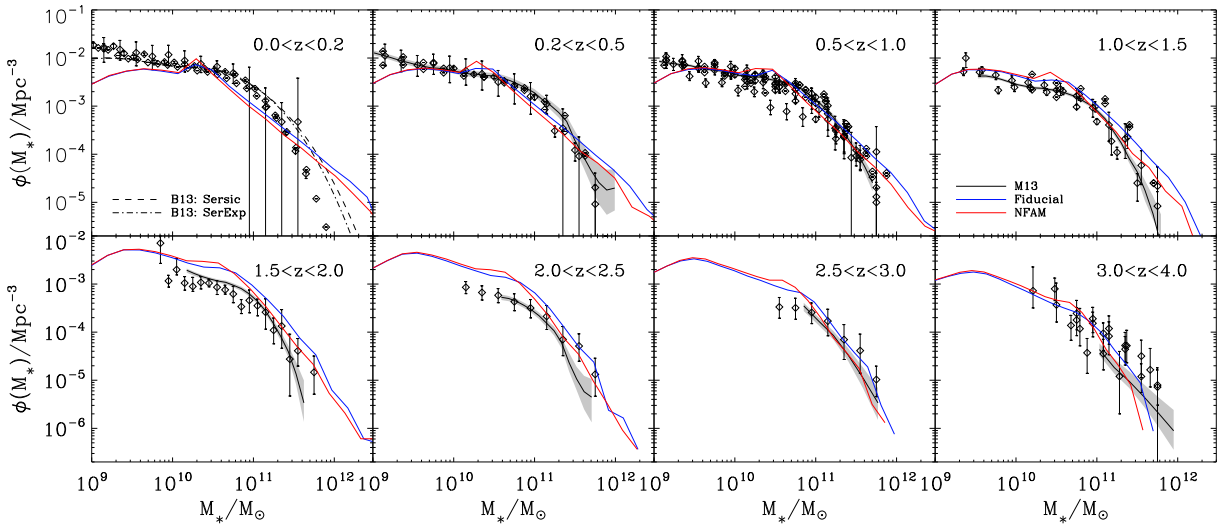

Figure 3.8: Stellar mass functions in different redshift ranges for the fiducial (blue lines) and the NFAM (red lines) 182Mpc/hr runs. The solid black lines with the shaded areas show the observed stellar mass functions presented by Muzzin et al. 2013 (M13) and their Poisson errors. The black diamonds are observations from Panter et al. (2004), Cole et al. (2001), Bell et al. (2003), Pérez-González et al. (2008), Borch et al. (2006), Bundy et al. (2005), Drory et al. (2004), Fontana et al. (2006) and Marchesini et al. (2007). The black dashed and dotted-dashed lines show the result from Bernardi et al. 2013 (B13) using a Sersic model and a Sersic-bulge + exponential-disc model.

For $z < 0.2$, the high-mass end is still overestimated. However, we have to keep in mind that observations in this mass range contain also relatively large uncertainties. Bernardi et al. (2013) showed that different measurements of stellar masses differ from each other significantly, especially at the high-mass end. They demonstrate that the stellar masses are higher using a Sersic model instead of standard models. Their fits using a single Sersic and a Sersic-bulge + exponential-disc model are shown as black dashed and dotted dashed line in the upper left panel of Fig. 3.8. In comparison to other observational estimates this is in better agreement with our simulations. Nevertheless, the high-mass end still appears to be slightly overestimated in our simulations as also indicated by the massive end of the $M_\bullet$-M_* relation (see lower right panel of Fig. 3.6).

To study the effect of our new accretion and feedback models on the stellar masses in more detail, Fig. 3.9 shows the stellar mass functions separately for quiescent and star-forming galaxies in our simulations – again in comparison to the observations from Muzzin et al. (2013). Following Franx et al. (2008) we use a specific star formation rate of $0.3/t_{\mathrm{Hubble}}$ as threshold to distinguish between quiescent and star-forming galaxies. We would like to mention that this is a different selection criterion than in the observations, where a threshold in the UVJ diagram is used (Muzzin et al., 2013). Hence, this criterion might lead to discrepancies with the observations, which may e.g. falsely identify metal-rich, star-forming galaxies to be red and thus quiescent.

Fig. 3.9 illustrates that our new implementations increase the amount of quiescent galaxies at $z > 1.5$. Consequently, for this redshift range, the discrepancies between simulated and observed SMFs are much smaller for the NFAM simulation than for the Fiducial run. Star formation is suppressed, when cooling and AGN feedback are in equilibrium (Churazov et al., 2005) and the gas in the vicinity of the AGN cannot cool enough to form stars. Hence, the increase of the amount of quiescent galaxies can be explained with the upper left panel in Fig. 3.6, which shows that the $M_\bullet$-M_* relation – and thus the phase of equilibrium – is earlier in place for the NFAM run. This is due to higher black hole accretion rates during the phase of rapid black hole growth as a consequence of both new implementations: firstly, the new accretion model leads to higher accretion rates when cold gas dominates. Secondly, the new feedback model results in less AGN feedback for low black hole masses and thus to lower gas temperatures.

In contrast to the equilibrium phase, which can be associated with the radio-mode, the phase of star formation and rapid black hole growth is not much affected by our new implementations. We conclude that the overestimation of the high-mass end is mainly due to star-forming galaxies. At $z < 1$ the amount of star-forming galaxies is too low for $2 \cdot 10^{10} M_\odot < M_* < 2 \cdot 10^{11} M_\odot$. Firstly, this is an effect of the low seeding mass of black holes, which also leads to the overproduction of quiescent galaxies. Secondly, it is a consequence of the overestimation of the high-mass end.

For both runs, Fig. 3.9 shows an artefact at low redshifts, namely that the amount of star-forming galaxies decreases rapidly after the seeding of black holes. We speculate that this decrease might be due to our very low black hole seeding mass, which leads to artificially high accretion rates. This also explains why the number of star-forming galaxies is reduced in the NFAM model compared to the fiducial one. Fig. 3.4 illustrates why this

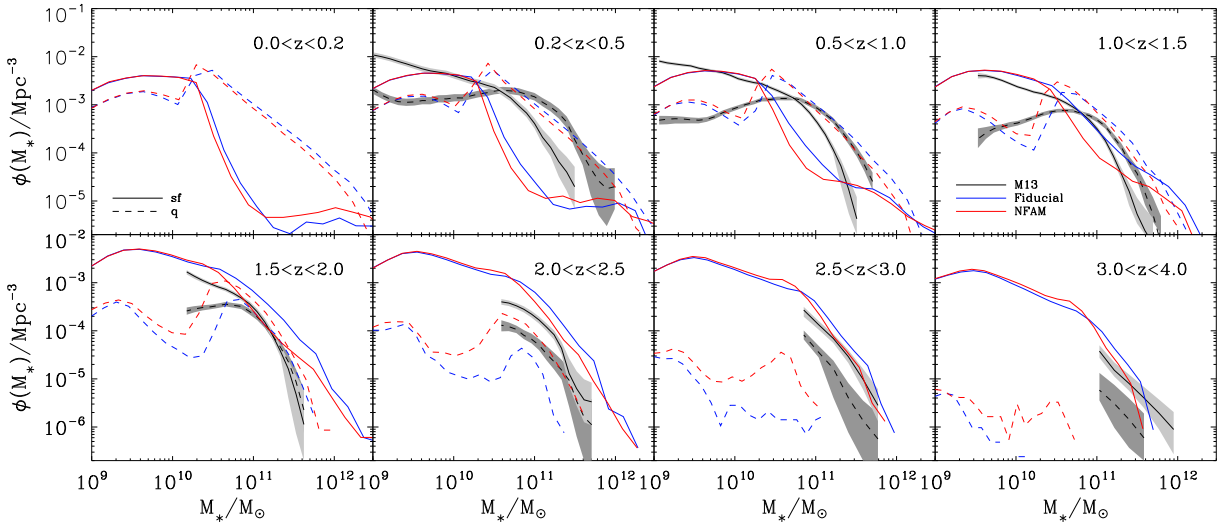

Figure 3.9: Stellar mass functions of quiescent (dashed lines) and star-forming (solid lines) galaxies in different redshift ranges for the fiducial (blue lines) and the NFAM (red lines) 182Mpc/hr runs. For the threshold between quiescent and star-forming galaxies we use the specific star formation rate of $0.3/t_{\mathrm{Hubble}}$ following Franx et al. (2008). The black lines with the shaded areas (light grey for star forming and dark grey for quiescent galaxies) show the observations from Muzzin et al. 2013 (M13) and their Poisson errors.

artefact becomes even larger with decreasing redshift: for black holes that are seeded later, the evolutionary track during the first phase of black hole growth is steeper then for early black hole seeds. All in all Fig. 3.9 shows that our new implementations cannot significantly improve the stellar mass functions at low redshifts, but at high redshifts they predict a larger amount of quiescent galaxies, which is in better agreement with observations.

To quantify how efficient baryons are converted into stars for a given halo mass, we calculate the mean baryon conversion efficiencies, which are defined as $M_*/(f_{\mathrm{bar}} M_{\mathrm{halo}})$, where $f_{\mathrm{bar}} = 0.17$ is the baryon fraction of the universe, for different redshifts. To be comparable to other studies we do not use M_{vir} for the halo mass, but $M_{200\mathrm{c}}$, which is the mass inside the radius where the density is 200 times larger than the critical density of the universe. Fig. 3.10 shows the conversion efficiencies versus halo mass for our two 182Mpc/hr runs (different panels illustrate $z = 0, 1, 2$). The black vertical line shows the resolution limit for the baryon content as estimated by Vazza et al. (2011), which is given by 500 dark matter particles. Furthermore, the dashed and solid red vertical lines mark the minimum and mean value of $M_{200\mathrm{c}}$, respectively, in the NFAM simulation corresponding to the minimum stellar mass for black hole seeds. Below the mean seeding limit our resolution does not allow reliable predictions (dashed lines). The figure clearly shows, that the new implementations lower the stellar content in a halo for a given mass above this limit, which is also reflected by the reduced high-mass end of the stellar mass functions (see Fig. 3.8). At $z = 2$ and $z = 1$, this effect is even stronger than at $z = 0$. The dotted and dotted-

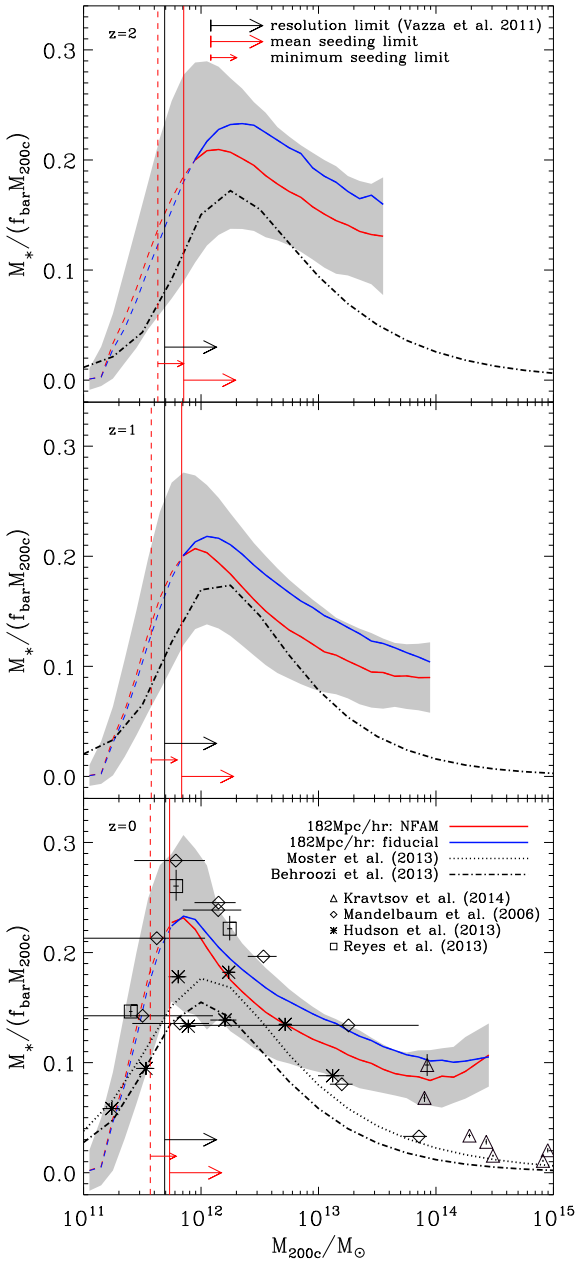

Figure 3.10: Mean baryon conversion efficiencies versus halo mass at different redshifts for the two 182Mpc/hr runs. The grey shaded area shows the 1σ-error of the NFAM run. The dashed and solid red vertical lines mark the minimum and mean value of M_{200c} in the NFAM simulation corresponding to the minimum stellar mass for black hole seeds. Below the mean seeding limit our resolution does not allow reliable predictions (dashed lines). The black vertical line shows the resolution limit for the baryon content as estimated by Vazza et al. (2011), which is given by 500 dark matter particles. We compare our simulation with abundance matching models (Moster et al. 2013, Behroozi et al. 2013) and with observations estimating the halo mass with weak lensing (Mandelbaum et al. 2006, Hudson et al. 2015, Reyes et al. 2012) or X-ray temperatures (Kravtsov et al., 2018).

dashed black lines show the predictions of the abundance matching models by Moster et al. (2013) and Behroozi et al. (2013). The peak at $M_{\rm halo} \approx 10^{12} M_\odot$ is in agreement with these models, which also find a maximum baryon conversion efficiency of around 20 per cent. At larger halo masses, the stellar content decreases due to AGN feedback and because the gas is consumed by star formation. Although the baryon conversion efficiencies in the NFAM simulation are smaller than in the fiducial run, they are still higher than in the abundance matching models of Moster et al. (2013) and Behroozi et al. (2013) for $M_{\rm 200c} > 10^{13} M_\odot$ galaxies.

For the NFAM simulation, at low redshifts a slight "upturn" of the baryon conversion efficiencies occurs for stellar masses above $10^{14} M_\odot$ corresponding to galaxy clusters due to too inefficient AGN feedback. This might indicate that other AGN feedback processes like mechanical jets should be included in future simulations. Since the most massive black holes accrete less in the NFAM model we suspect that there is more cold gas left to form stars than in the fiducial run. Therefore, the upturn is only visible in the NFAM simulation. However, except for the high-mass end, our simulations – in particular the NFAM run – are in agreement with observations using weak lensing (Mandelbaum et al. (2006), Reyes et al. (2012) and Hudson et al. (2015)) or X-ray temperatures Kravtsov et al. (2018) to estimate the total halo mass. [5]

3.3.2 Evolution of the star formation rate

Fig. 3.11 shows the SFR-stellar mass plane (number density is color-coded) for our two 182Mpc/hr runs at different redshifts. The panels illustrate all galaxies classified as subhaloes using the SUBFIND algorithm (Dolag et al. 2009, Springel et al. 2001). For comparison with observations, we also show the main sequence for star-forming galaxies estimated by Steinhardt et al. (2014) for $4 < z < 6$ (red line), by Daddi et al. (2007) for $z = 2$ (orange line) and by Elbaz et al. (2007) for $z = 1$ and $z = 0$ (yellow line). At $z = 2$ and $z = 1$, the simulated SFRs at a given stellar mass are slightly below the observations. This trend is also visible in the recently published analysis of the Illustris simulation by Sparre et al. (2015). At $z = 0$ and at redshifts above $z = 4$ our simulation results are in very good agreement with the observed main sequence, independent of the adopted black hole model. The redshift evolution of the SFR-stellar mass plane nicely demonstrates that the most massive galaxies become more and more quiescent with cosmic time. Furthermore, in the NFAM simulation star formation is suppressed earlier than in the fiducial one. This is consistent with Fig. 3.9, where we demonstrated that in the NFAM run the amount of quiescent galaxies is larger at earlier times. In the NFAM simulation, the SFRs of the most massive galaxies decrease already at redshifts above $z = 4.8$ such that they lie below the observed main sequence of star forming galaxies. In the fiducial simulation, this decrease starts at redshifts below $z = 4$. This may be unrealistic, because – as shown in Fig. 3.9 – Muzzin et al. (2013) observe much more quiescent galaxies at high redshifts ($z > 3$) than in our fiducial simulation. Looking at the star formation main sequence of the Illustris

[5] For the observations we computed $M_{\rm 200c}$ out of $M_{\rm 500c}$ using the NFW profile.

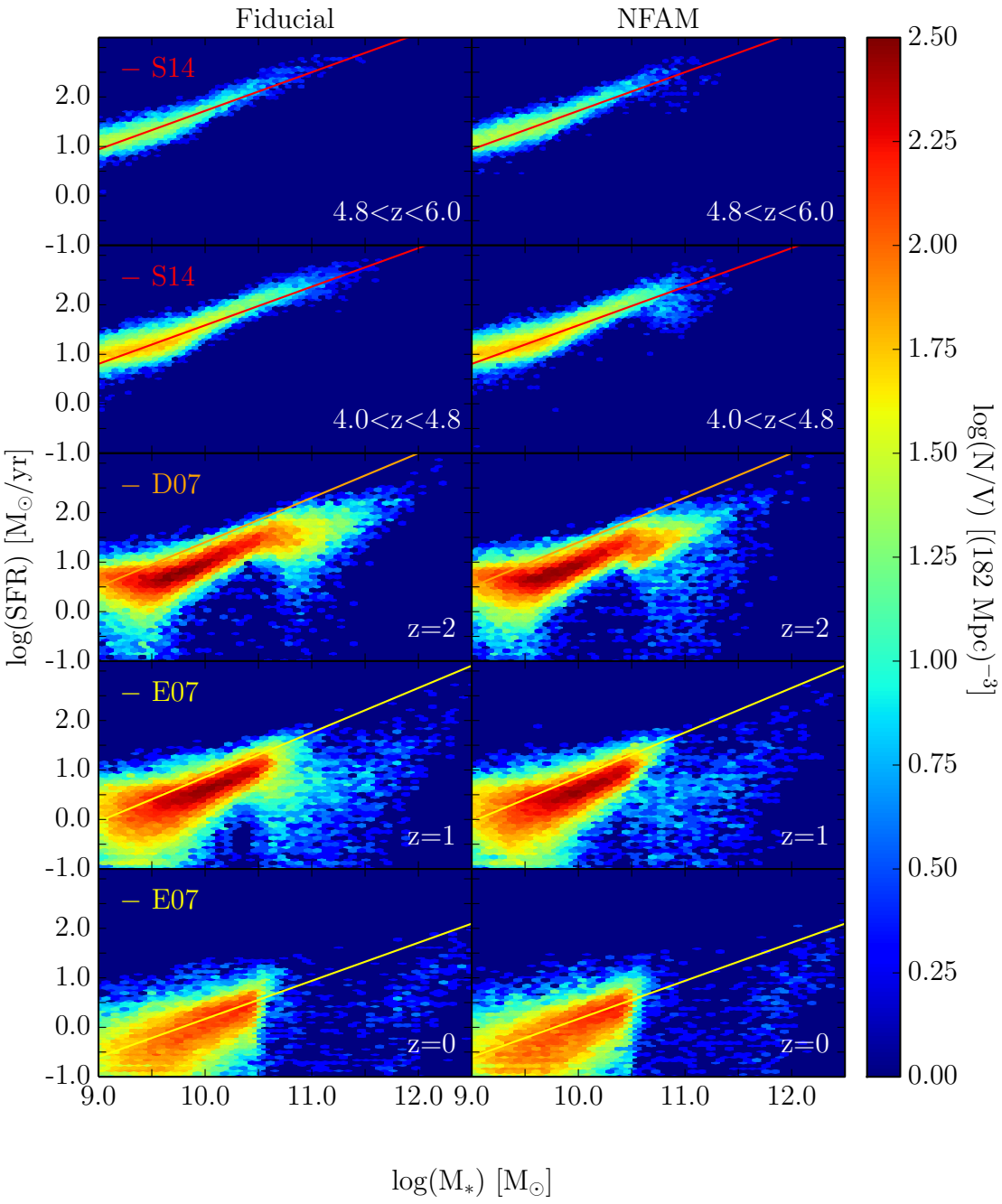

Figure 3.11: Comparison of the star formation rates of all galaxies in the two 182Mpc/hr runs at different redshifts. The solid lines represent the observed main sequence of galaxies derived by Steinhardt et al. 2014 (S14), Daddi et al. 2007 (D07) and Elbaz et al. 2007 (E07).

simulation (Sparre et al., 2015) shows that this is not only a problem in our fiducial run, but seems to be a general issue. Therefore, it is encouraging that in the NFAM run galaxies become quiescent much earlier due to both of our new implementations, even if there are still discrepancies between the observed and simulated SMFs for star-forming and quiescent galaxies. The new feedback model leads to a lower feedback energy for low black hole masses, whereas for large black hole masses the AGN feedback is stronger as long as the black holes are accreting in the quasar-mode and star formation is suppressed.

The new accretion model leads to lower accretion rates when the hot gas phase dominates. Hence, black holes grow less strongly and the SFR decreases already in less massive galaxies as can be seen in the panels corresponding to $z = 1$. From the earlier and more rapid decrease of the SFR follows that at $z = 1$ star-forming galaxies with stellar masses above $2 \cdot 10^{10} M_{\odot}$ are more concentrated along the observed main sequence in the NFAM simulation than in the fiducial one. At $z = 0$ there are only very few star-forming galaxies above $\log(M_*/M_{\odot}) = 10.5$, which is the mass at which AGN feedback becomes important. At that redshift both runs predict galaxies with similar SFRs at a given stellar mass. Hence, our modifications mainly affect the evolution of high redshift galaxies.

Fig. 3.12 depicts the redshift evolution of the mean specific SFR for our two 182Mpc/hr runs. As in Biffi & Maio (2013) – who studied early proto-galaxies at $z > 9$ – we compare our simulations with other theoretical models (i.e. Biffi & Maio 2013, Dayal et al. 2013, Davé et al. 2011) and observations (i.e. Noeske et al. 2007, Daddi et al. 2007, Dunne et al. 2009, Pannella et al. 2009, Stark et al. 2009, Yabe et al. 2009, Michałowski et al. 2010, Schiminovich et al. 2010, Reddy et al. 2012, Bouwens et al. 2014, González et al. 2012, Zheng et al. 2012, Stark et al. 2013 and Coe et al. 2013). Irrespectively of the assumed accretion and feedback models, our simulations are both in better agreement with observations than many other theoretical models, especially at low redshifts (where the observational constraints are tighter). Fig. 3.12 also demonstrates that our new implementations have no effect on the specific SFR. Hence, the changes in the SFR and in the stellar mass are the same.

However, star formation is certainly not only regulated by AGN feedback. Recent studies (e.g. Hopkins et al. 2014, Hirschmann et al. 2013, Aumer et al. 2013, Kannan et al. 2014) showed that stellar feedback also plays an important role, particularly for low mass galaxies. Fig. 3.13 provides further evidence that our model is still not sufficient for reproducing galaxies with realistic SFRs. It illustrates the history of the star formation and the black hole accretion rate densities as shown by Hirschmann et al. (2014) for our two 182Mpc/hr runs compared to observations of the SFR density (squares) by Hopkins & Beacom (2006). In comparison to the fiducial model, the star formation rate density in the NFAM model is slightly lower above $z \approx 1.5$, although it is still too high in comparison to the observations except for very high redshifts, which are, however, affected by resolution.

As expected due to the lower black hole masses in the NFAM model, the black hole accretion rate density is significantly lower at $z < 4.5$ than in the fiducial model. For higher redshifts, it is larger than in the fiducial model, which leads to a much shallower increase up to the maximum. Fig. 3.13 demonstrates that in the NFAM simulation the SFR and the black hole accretion rate evolve very similar with redshift. The reason is

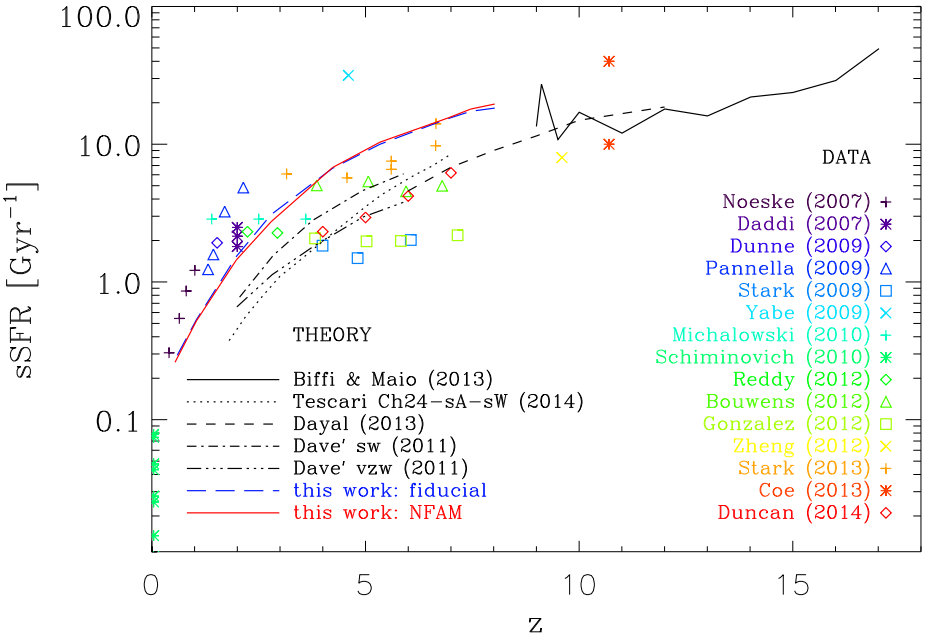

Figure 3.12: History of the specific star formation rate in our 182Mpc/hr runs in comparison to different observations and other theoretical predictions.

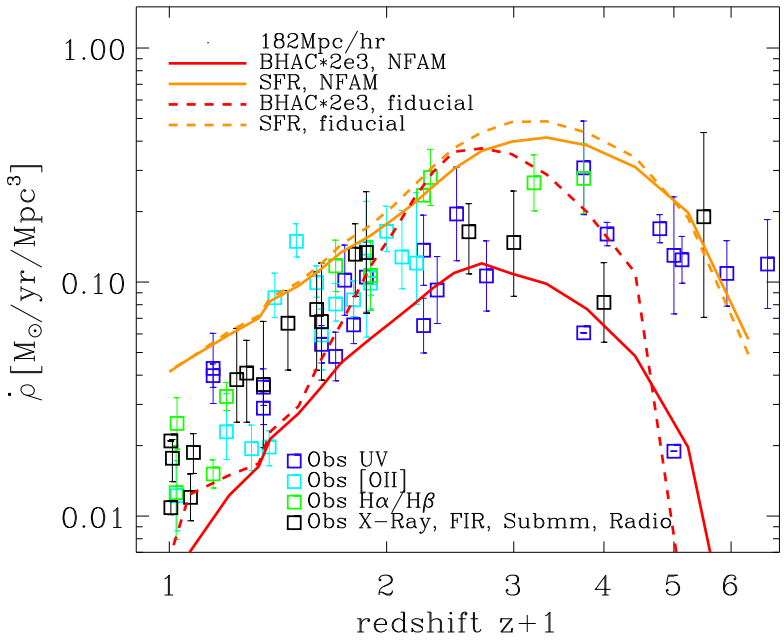

Figure 3.13: History of the star formation (orange lines) and black hole accretion rate (red lines) density in both 182Mpc/hr runs (fiducial model: dashed lines, NFAM: solid lines) in comparison to observations from Hopkins & Beacom 2006 (squares).

that both depend on the amount of cold gas. With our new accretion model the analogy between SFR and black hole accretion is even stronger, because the accretion factor for hot gas is smaller than for cold gas. Thus, in the NFAM simulation, hot gas results not only in less star formation, but also in smaller black hole accretion rates. This shows that the gas temperature plays a key role in both galaxy formation and black hole growth. A similar accordance between the history of the star formation and black hole accretion rate density was also found by Zheng et al. (2009), who adopted the luminosity functions from Hopkins et al. (2007) to estimate the black hole accretion rate densities.

3.4 Discussion

3.4.1 The effect of the feedback model onto the luminosity functions

As already mentioned before, the choice of the slope β of the feedback model should not have a significant influence on the resulting galaxy and black hole properties in the simulations since ϵ_r is much smaller than ϵ_o. However, it has an influence on the AGN luminosity functions, which are calculated during post-processing using the accretion rates calculated by the simulation and the radiative efficiencies, which can be varied.

In that way we can test the effect of the parameter β on the AGN luminosity function. We calculate the bolometric AGN luminosities of the NFAM simulation for different values of β using equation (3.8) and (3.19). Fig. 3.14 shows the resulting luminosity functions in comparison to the observational compilation of Hopkins et al. (2007). For a comparison of moderately luminous AGN, particularly at high redshifts, one has to keep in mind that simulations are affected by resolution (see discussion of Hirschmann et al. 2014). In addition, dust obscuration effects in observational data typically result in an underestimation of their number density (e.g. Hasinger 2008, Merloni et al. 2014) which complicates a comparison between simulations and observations. Even if luminosity-dependent obscuration effects on a torus level are already considered in Hopkins et al. (2007), an additional redshift-dependence (of X-ray luminosities, as suggested by e.g. Hasinger 2008 and Merloni et al. 2014) may change the low luminous end at high redshifts.

Fig. 3.14 shows that the effect of the choice of β on the AGN luminosity functions is not significant, especially at high redshifts, because β changes only the efficiencies in the radio-mode and not in the quasar-mode. For lower redshifts, when more black holes accrete with low Eddington ratios, it has an influence on the amount of AGN with luminosities smaller than 10^{45}erg/s in the sense that with decreasing β the radiative efficiency and thus the amount of moderately luminous AGN is increasing and thus the result is in better agreement with the observational constraints. However, due to the fact that observations constrain very low values of ϵ_r we suspect that the accretion rates in the quasar-mode are slightly underestimated in our simulations.

As shown in Fig. 3.2, the actual value of ϵ_r is entirely unconstrained in the radio regime. It might depend on many properties like the morphology of the host galaxy or the merger

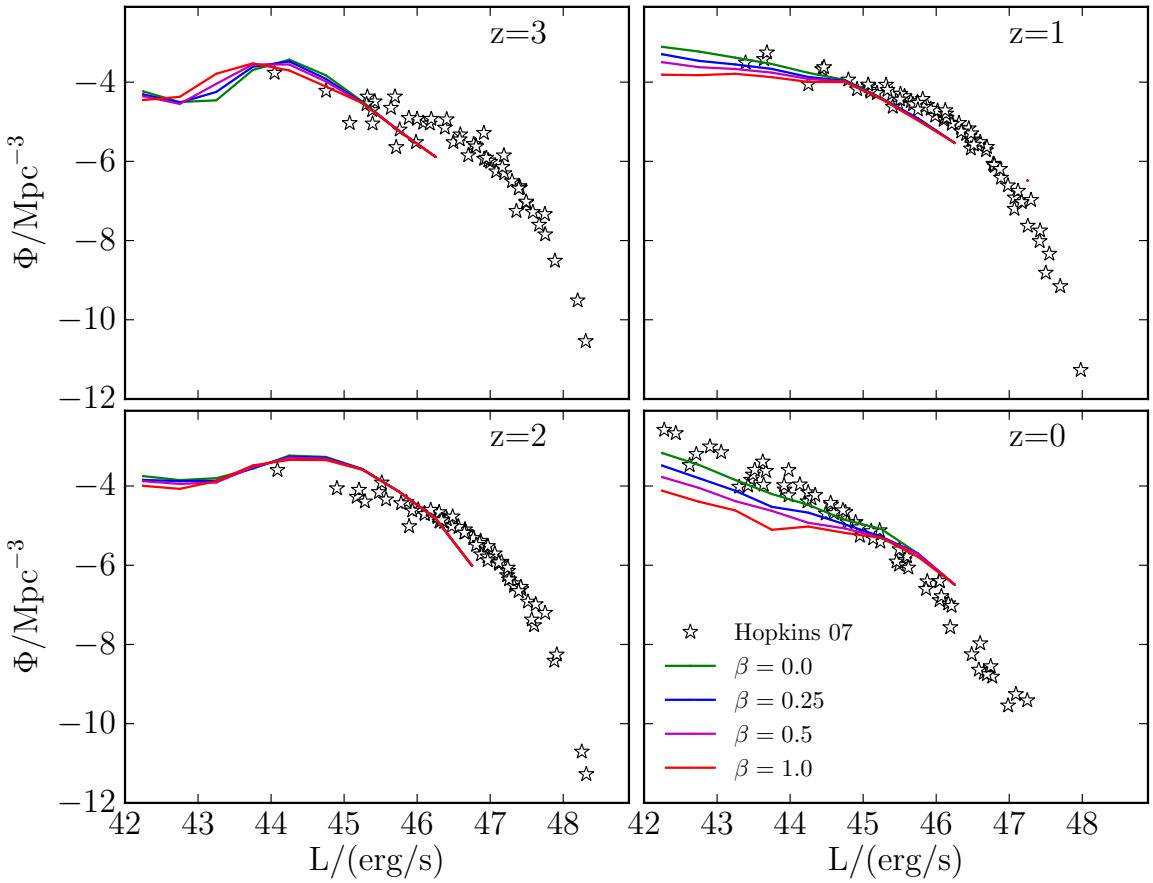

Figure 3.14: AGN luminosity function of our 182Mpc/hr NFAM run at different redshifts for different values for the slope β in comparison to the observational compilation by Hopkins et al. (2007).

history of an individual black hole. For that reason, calculating a more realistic value of ϵ_r is beyond the current feasibility.

Nevertheless, according to the observations by Russell et al. (2013), one should consider different models to estimate ϵ_r in the radio-mode. Fig. 3.15 shows the AGN luminosity functions in comparison to observational compilation by Hopkins et al. (2007) for four models adopting different values for ϵ_r in the radio regime:

1. The commonly used value $\epsilon_r = 0.1$ (green lines) seems to match the observations reasonably well, although such a value is unlikely according to the results from Russell et al. (2013) and Mezcua & Prieto (2014).

2. $\epsilon_r = 10^{-3}$ is the mean value of the data points from Russell et al. (2013). Because we change only values in the radio regime, the high luminosity end is not affected. At lower luminosities, the AGN number densities are significantly underestimated as

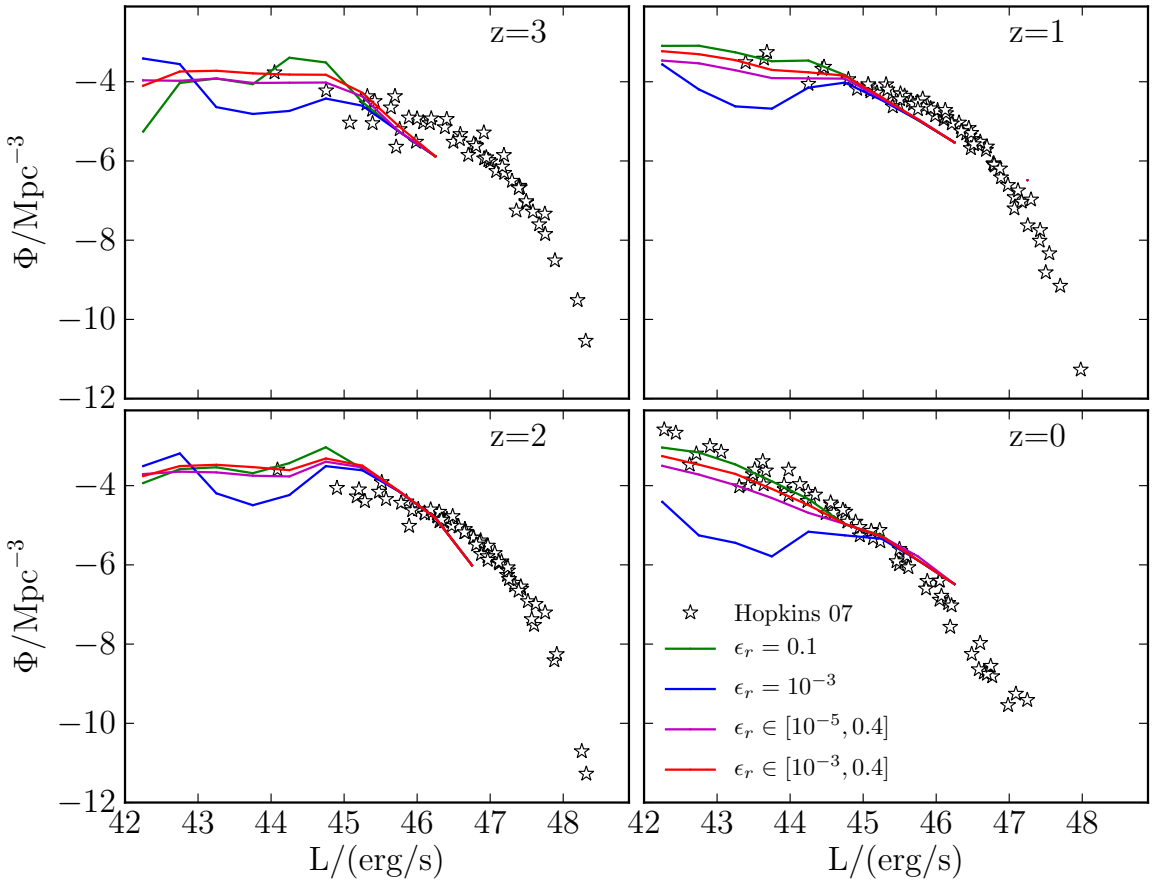

Figure 3.15: AGN luminosity function of our 182Mpc/hr NFAM run at different redshifts for different values of ϵ_r in the radio regime in comparison to the observational compilation by Hopkins et al. (2007). The green and blue curves show the result for two constant values of ϵ_r. For the purple and red curve we took random values in two different intervals.

AGN become way too faint[6] (blue lines).

3. We choose random values in log space in the range $10^{-5} < \epsilon_r < 0.4$. This is approximately the range of the data points from Russell et al. (2013) with a maximum value equal to the theoretical maximum efficiency of a rotating black hole (since we assumed $\eta = 0.1$). It leads to a reasonably good match (magenta line) with the observational constraints, even if the low luminous end is slightly lower than when adopting the commonly used value (green lines). Since we may speculate that the curve will probably be shifted upwards when choosing a higher resolution (Hirschmann et al., 2014), the concordance with the observations might be even better.

4. Now we exclude very low values for ϵ_r and hence choose random values in the range $10^{-3} < \epsilon_r < 0.4$. This leads to a slightly, but not significantly larger number density of moderately luminous AGN (red lines) and hence to a better agreement with observations.

In comparison to the AGN luminosity functions from the Illustris simulation (Sijacki et al., 2015), we have less luminous AGN for redshifts below $z = 1$, although our cosmological box is larger. Nevertheless, to investigate the high-mass end in more detail larger cosmological boxes are needed. Hirschmann et al. (2014) already presented luminosity functions of a larger box from the set of Magneticum Pathfinder Simulations, which are in good agreement with the observations from Hopkins et al. (2007). Furthermore, our simulation matches better with the observed amount of AGN with luminosities below $L \approx 10^{45}$erg/s than in Sijacki et al. (2015). This confirms the conclusion from Sijacki et al. (2015) that the radiative efficiency is not constant and might actually be very low in the radio regime.

This analysis shows that the efficiency of the radiative component in the radio regime is indeed not yet understood because the theoretical lower limit is not captured by observations. Interestingly, choosing random values for the radiative efficiency in the range of the observed values leads to a good agreement with observed AGN luminosity functions. This may indicate that in the radio regime the radiative efficiency depends neither on the mass of the black hole, nor on its accretion rate. It also implies that – as we are matching the observed luminosity function by randomly choosing the radiative efficiency within the observed values – the distribution of the accretion rates as predicted by the simulations are similar to the observed ones. We conclude, that it is theoretically not fully understood how efficient AGN radiate and we suspect that the morphology of the galaxy, but also turbulence or even magnetic fields might play an important role. Since jets dominate in the radio-mode, they can also prevent efficient accretion. The similar morphologies of the two radiation dominated sources from Mezcua & Prieto (2014), i.e. NGC 1097 and NGC 1386, give a first evidence for these speculations, because they both have a ring of

[6]The amount of black holes does not change, because we use the same simulations for all different feedback models. Consequently, lower number densities of AGN with $L > 10^{42}$erg/s are equivalent to higher number densities for fainter AGN.

star forming regions and a bar on large scales, but no bar on small scales. However, a better understanding of black hole accretion and AGN feedback processes is a great challenge for the future, because more accurate observations are needed to learn in which cases ADAF/Bondi models are a good estimate and in which cases we have to include additional physical processes.

3.4.2 The unconstrained total efficiency in the radio regime

Besides the radiative efficiency, the total efficiency η in the radio regime is also unconstrained. Throughout this study, we always assumed $\eta = 0.1$ to calculate ϵ_r and ϵ_o, making, thus, our conclusions for the radio regime rather uncertain. The reason for this assumption are missing or unconstrained estimations of $\dot{M}_\bullet$. According to equation (3.11), η is given by

$$\eta = \frac{L_\mathrm{Edd}}{\dot{M}_\mathrm{Edd} c^2} = \frac{L_\mathrm{bol} \frac{\dot{M}_\bullet}{\dot{M}_\mathrm{Edd}}}{\frac{L_\mathrm{bol}}{L_\mathrm{Edd}} \dot{M}_\bullet c^2}. \tag{3.23}$$

In observations, however, usually only the AGN luminosity, the jet power and the black hole mass are measured. Using the black hole mass, one can calculate L_Edd. Equation (3.10) is then used to calculate $\dot{M}_\bullet/\dot{M}_\mathrm{Edd}$. Hence $\dot{M}_\bullet$ is the parameter which is typically missing. Nevertheless, for some of the sources from Russell et al. (2013) and Mezcua & Prieto (2014), $\dot{M}_\bullet$ has been estimated. We use these estimations to calculate the corresponding total efficiencies with equation (3.23). With these values and equations (3.21) and (3.22) we then compute ϵ_o and ϵ_r.

Before we calculate the efficiencies for the selected sources, we want to focus on the nearest SMBH, namely Sagittarius A* (Sgr A*). For the luminosity we adopt $L_\mathrm{bol} = 2.1 \cdot 10^{36}$erg/s (Narayan et al., 1998) and for the power of the mechanical outflow we assume $P_\mathrm{o} = 1.2 \cdot 10^{41}$erg/s (Yusef-Zadeh et al., 2012). With these values and the mass $M_\mathrm{SgrA*} = 4 \cdot 10^6 M_\odot$ we calculate the Eddington ratio using equation (3.10). Although Sgr A* is the nearest SMBH, there are different estimates for the accretion rate. Quataert et al. (1999) estimated a Bondi accretion rate of $\sim 3 \cdot 10^{-5} M_\odot$/yr. However, there are other models suggesting the actual accretion rate might be much lower than the Bondi accretion rate (e.g. Quataert & Gruzinov 2000). Cuadra et al. (2006) derived $\dot{M} \approx 3 \cdot 10^{-6} M_\odot$/yr from stellar winds. We calculated the efficiencies corresponding to both values using equation (3.21) and (3.22). They are shown in Fig. 3.16. The upper data points belong to $\dot{M} \approx 3 \cdot 10^{-6} M_\odot$/yr and the lower ones to $\dot{M} \approx 3 \cdot 10^{-5} M_\odot$/yr. Assuming that the ADAF model really provides a lower limit, this illustrates that $\dot{M} \approx 3 \cdot 10^{-6} M_\odot$/yr is in good agreement with our model for the radiative efficiency. It also indicates that it is necessary to choose different lower limits for different black hole masses, because the dashed green line – which corresponds to $\eta \approx 0.1$ – is far above the data point. However, the corresponding value for ϵ_o is larger then the commonly used value 0.1. This indicates, that the outflow efficiencies might differ significantly from this value, which is not well constrained. For the second estimation of the accretion rate, i.e. $\dot{M} \approx 3 \cdot 10^{-5} M_\odot$/yr, the

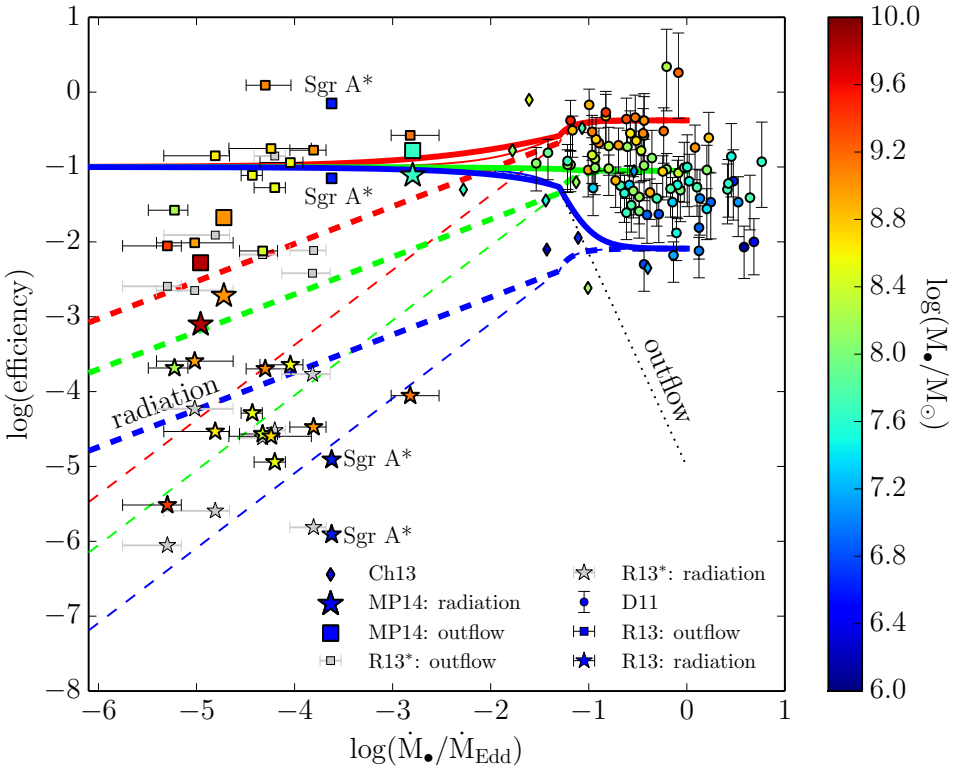

Figure 3.16: Same as in Fig. 3.2, but with efficiencies calculated using values for $\dot{M}_\bullet$ from Russell et al. 2013 (R13) and from other authors, i.e. Evans et al. 2004, Allen et al. 2006 and Li et al. 2011 (R13*, MP14). The three data points from Mezcua & Prieto (2014), for which we know estimations of $\dot{M}_\bullet$ are from left to right M87, NGC 4594 and CenA. We also included values for Sgr A*, which have been calculated using different estimations of $\dot{M}_\bullet$, i.e. $\dot{M} \approx 3 \cdot 10^{-6} M_\odot/\mathrm{yr}$ from Cuadra et al. 2006 (upper symbols) and $\dot{M} \approx 3 \cdot 10^{-5} M_\odot/\mathrm{yr}$ from Quataert & Gruzinov 2000 (lower symbols).

radiative efficiency is clearly below the prediction, although ϵ_o is near 0.1. This implies that Bondi estimations of the accretion rate indeed tend to be too high.

Now, we consider the sources from Russell et al. (2013) and Mezcua & Prieto (2014), for which $\dot{M}_\bullet$ has been estimated using the Bondi model. Russell et al. (2013) investigated a subsample of 13 objects for which they estimated $\dot{M}_\bullet$. The efficiencies corresponding to these sources are plotted in Fig. 3.16 (R13). Other authors also estimated $\dot{M}_\bullet$: for Centaurus A and NGC 4216 we use the result from Evans et al. (2004) and for the Sombrero galaxy (NGC 4594) we take $\dot{M}_\bullet$ from Li et al. (2011). For M87, M84, M89, NGC 4636, NGC 4472, NGC407 and NGC5846 we take values from Allen et al. (2006). The efficiencies calculated with these values and the data from Russell et al. (2013) are marked with grey symbols (R13*). Most of these sources are also in the selected sample from Russell et al. (2013). We can, thus, directly compare the results of two independent measurements. This shows a clear discrepancy between different estimations of $\dot{M}_\bullet$. Overall, the efficiencies are

larger using the $\dot{M}_\bullet$ from Russell et al. (2013). In contrast to Fig. 3.2, the lowest values of the radiative efficiency now tend to increase with increasing Eddington ratio as predicted by theory. Nevertheless, the observations are in better agreement with theory using only the 13 objects of the selected subsample. Furthermore, Fig. 3.16 indicates that the value $\epsilon_\mathrm{o} = 0.1$ is indeed a reasonable assumption for the mean value of the observed values, although the observations can be nearly two dex lower.

However, all these estimations are highly uncertain and very speculative. On the one hand, all data points are upper limits due to the approximation of using the Bondi model. On the other hand, there are studies showing that accretion rates can also be much smaller than $\dot{M}_\mathrm{B}$ (i.e. Li et al. 2013, Baganoff et al. 2003, Quataert & Gruzinov 2000). Moreover, values for L_bol might be underestimated when the jet is emitting in the plane of the sky. In that case, the measured flux is smaller than if the jet were located close to the line of sight. This would lead to higher radiative efficiencies and to an even better agreement with our model. Furthermore, uncertainties in the determination of black hole masses make it almost impossible to investigate whether the lower limit for the radiative efficiency splits up for different black hole masses as seen in the quasar regime (Davis & Laor 2011,Chelouche 2013).

Nevertheless, the data shown in Fig. 3.16 is one of the best constrained samples. The comparison between Fig. 3.16 and Fig. 3.2 shows that we need more accurate measurements to learn more about the feedback of radio jets and the corresponding efficiencies. Due to the fact that knowing the efficiencies is (at least with the currently available computational power) essential for performing large-scale cosmological simulations, it is worth and necessary spending more effort on observational estimates of black hole accretion rates.

3.4.3 Comparison with other simulations

During the last couple of years, several other groups have also been working on large cosmological simulations including baryons and black holes. As our simulations, some of these simulations, for example the MassiveBlack-II simulation (Khandai et al. 2015), earlier simulations from Di Matteo et al. (2008) and the new EAGLE simulation (e.g. Schaye et al. 2015), are based on the SPH code GADGET-3, but differ in their physical sub-resolution models, including the model for black hole growth. In contrast, the recent Illustris simulation (e.g. Vogelsberger et al. 2014, Genel et al. 2014) has been performed with a different hydrodynamic scheme, the moving mesh code AREPO (Springel, 2010), and also slightly different sub-resolution models. A comparison between these models can help to understand which effects the different sub-resolution models for black hole growth and AGN feedback may have on basic galaxy and black hole properties.

Fig. 3.17 shows the stellar mass function in the NFAM model below $z = 0.2$ in comparison to other simulations. As for the black hole mass function, the number density of massive galaxies in the Illustris simulation (Genel et al. 2014, green lines) is by half an order of magnitude larger than the one in the Magneticum simulation. For stellar masses below $4 \cdot 10^{11} M_\odot$ the galaxy number densities in the Illustris simulation are in reasonably good agreement with the observations, while our simulations produce slightly too few low

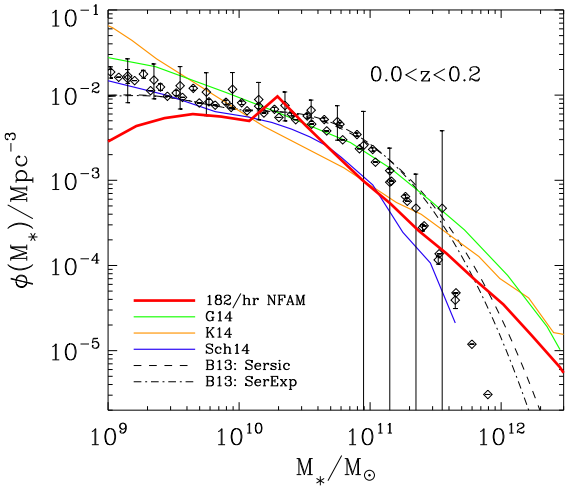

Figure 3.17: Comparison of the SMF in the NFAM model (red line) at $z = 0$ with the Illustris simulation (Genel et al. 2014/G14, green line), the MassiveBlack-II simulation (Khandai et al. 2015/K14, orange line) and the EAGLE simulation (Schaye et al. 2015/Sch14, blue line). The observations shown are the same as in Fig. 3.8.

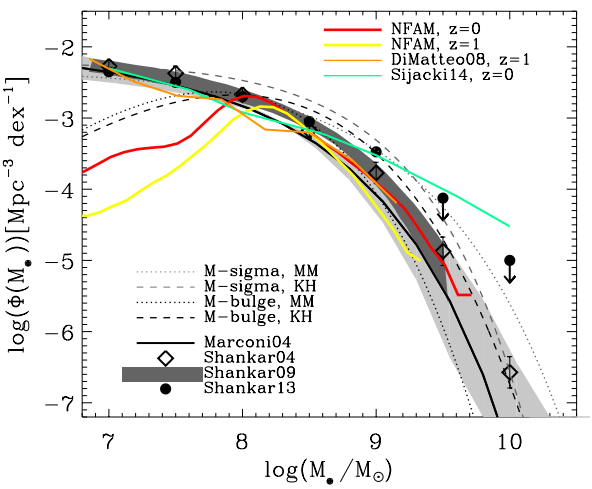

Figure 3.18: Comparison of the black hole mass function in the 182Mpc/hr NFAM run with that in the Illustris simulation (Sijacki et al., 2015) at $z = 0$ and with that in the MassiveBlack-II simulation (Di Matteo et al., 2008) at $z = 1$. The observations shown are the same as in Fig. 3.5.

mass galaxies. Since the difference between the SMFs of the fiducial model and the NFAM model are very small at $z = 0$ we suggest that other physical processes (e.g. stellar feedback or cooling) or the lower resolution might be the reason for the lower stellar masses. The prediction from the MassiveBlack-II simulation (Khandai et al. 2015, orange line) has no pronounced exponential cut-off with the consequence that they over-estimate the low and the high mass end, but slightly under-estimate the number density of galaxies around the exponential cut-off. In contrast, the stellar mass function obtained by the EAGLE simulation (Schaye et al. (2015), blue line), where the feedback is especially calibrated to match the stellar mass functions, is in good agreement with observations for the entire stellar mass range.

Compared to our results – the black holes in the Illustris simulation are much more massive than in the Magneticum simulation (as shown in Fig. 3.18). This discrepancy might have several reasons, for example the different implementations of radiative AGN feedback. Furthermore, given that there may still be resolution dependent details of the black hole feedback model (e.g. the estimation of the Bondi accretion rate or the distribution of the feedback) the higher resolution of the Illustris simulation could contribute to these differences. In addition, there could be differences due to the different numerical techniques, namely SPH and moving mesh, especially in the way the feedback gets transported away from the centre of the galaxies. In addition, a more efficient gas cooling in

AREPO (Nelson et al., 2013) might lead to higher black hole accretion rates. Furthermore, the underlying physics referring to the energy transport might influence how much gas is driven outward and which fraction of this gas is recycled as for instance discussed by Nelson et al. (2015).

Due to the large uncertainties in different observational estimates it is not clear which simulation matches the observations of the local Universe best. At $z = 1$ we also compare the black hole mass function of our NFAM model to the predictions of Di Matteo et al. (2008). This simulation produces slightly more massive black holes than the Magneticum simulation, which might be due to a more inefficient AGN feedback of massive black holes in Di Matteo et al. (2008).

Obviously, the other simulations shown here capture black holes down to smaller black hole masses. Firstly, this is due to the higher resolutions. Secondly, they use the so-called 'pinning' to keep the black holes at the potential minimum and therefore in the centre of the galaxies. Hence, they can seed the black holes in less massive galaxies. In our simulations this is not possible, because the black holes in less well defined galaxies would not be able to stay in the centre of their host galaxy due to numerical effects. However, not using the so-called 'pinning' avoids other drawbacks of this method as discussed in Hirschmann et al. (2014). As discussed by Shankar (2013), also the low mass end of the black hole mass function is relatively uncertain and depends on the black hole scaling relations. For example, the low mass end could be significantly smaller when excluding galaxies with pseudo-bulges. Therefore, it will be quite challenging to compare observed black hole mass functions to any simulation at the low mass end.

Fig. 3.19 shows a comparison of the AGN luminosity function in our NFAM run (purple line) with the predictions from the Illustris simulation (Sijacki et al. 2015, green solid line) and from the MassiveBlack-II simulation (Khandai et al. 2015, orange solid line). The luminosity function of the Illustris simulation matches both the observations and our simulation, whereas the MassiveBlack-II simulation widely fails to reproduce the observed shape of the observed luminosity functions of Hopkins et al. (2007). Since the latter simulation contains the original model from Springel et al. (2005) with only one mode of AGN feedback, we can speculate that this might be one possible reason for the discrepancies. The Illustris simulation uses a so-called 'radiative' efficiency, which is implemented as a change in the net cooling rate and is most efficient in the quasar-mode (Sijacki et al., 2015). This seems to have a similar effect as our variable radiative efficiency, which increases for large black hole masses in the quasar mode.

Nevertheless, we want to emphasize that despite of the general importance for understanding the (physical or numerical) origin of different simulation predictions, such a comparison must remain speculative: besides different models for black hole growth and AGN feedback, many other physical details (e.g. models for star formation, stellar feedback) or different hydrodynamic schemes may cause more fundamental changes in basic galaxy properties. Such an investigation is, however, clearly beyond the scope of this work.

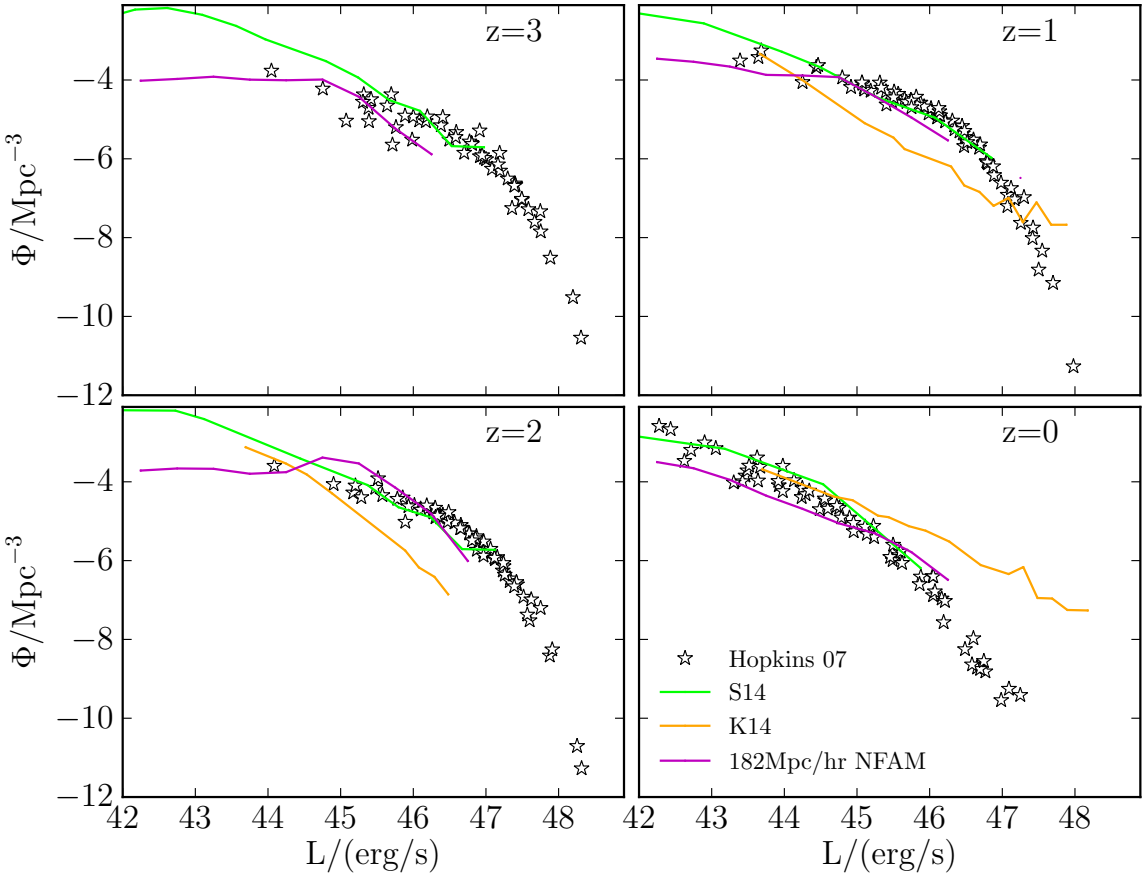

Figure 3.19: Comparison of the AGN luminosity function in the NFAM model (using random radiative efficiencies in the radio regime in the range $10^{-5} < \epsilon_r < 0.4$) with the predictions of the Illustris simulation (Sijacki et al. 2015/S14, green solid lines) and of the MassiveBlack-II simulation (Khandai et al. 2015/K14, orange solid lines).

3.5 Summary and conclusions

In this paper, we presented an improved implementation of the black hole model originally introduced by Springel et al. (2005). We combined theoretical predictions of Churazov et al. 2005, Narayan & Yi 1995 and Gaspari et al. (2013) with observations from Russell et al. 2013, Mezcua & Prieto 2014, Davis & Laor 2011 and Chelouche 2013 in order to model the underlying sub-grid processes more realistically.

The new model includes a combination of mechanical outflow and radiation, which we both implemented as thermal feedback due to the inability of resolving sub-kpc scales, where jets provide the mechanical feedback. Both feedback processes are modelled as a function of the actual accretion rate with respect to the Eddington rate, which leads to a smooth transition between the outflow-dominated radio-mode and the radiation-dominated quasar-mode. In addition, our model includes a mass dependent radiative efficiency to account for the observed spin of the black holes.

Furthermore, we distinguish between the hot and the cold gas component within the environment of the black holes and calculate the accretion rate for these two components separately. This allows us to model the Bondi accretion differently for the two phases, where we use two different boost factors ($\alpha = 10$ for the hot and $\alpha = 100$ for the cold gas) according to the results of small-scale simulations of Gaspari et al. (2013).

Besides that, free parameters of the model (like the various efficiencies) are now more strictly linked to values inferred from observations. Compared to the fiducial model, our new implementations predict a more realistic population of black holes and their host galaxies, when compared to fundamental observational constraints, in several aspects:

1. The slope and normalization of the produced $M_\bullet$-M_* relation are in much better agreement with observations over a larger range of galaxy masses and redshifts than in the fiducial model. In particular, these improvements are due to the faster black hole growth at large redshifts and the lower black hole masses at the massive end for redshifts below $z \approx 2$.

2. Our new feedback scheme is also able to efficiently suppress the late growth of massive black holes. Hence, the resulting present-day black hole mass function provides an excellent match to the observed one.

3. In the NFAM simulations, the equilibrium between gas cooling and AGN feedback within the galaxies is reached earlier. Consequently, star formation starts to be suppressed at earlier times. This leads to a better agreement with observed stellar mass functions than before. In particular, in the NFAM simulation there are much more quiescent galaxies at high redshifts than in the fiducial simulation, in which galaxies become quiescent far too late. However, some inconsistencies between observed and simulated SMFs for quiescent and star-forming galaxies remain.

4. The baryon conversion efficiencies are more consistent with observations and abundance matching predictions than before, although they are still too high by a factor of 2-3 at very high stellar masses.

A comparison with other large cosmological simulations (e.g. Illustris, MassiveBlack-II) illustrates that the original black hole model from Springel et al. (2005) needs to be extended to be able to reproduce observations. In particular, we find that

1. our NFAM simulation successfully matches the observed $M_\bullet$-M_* relation. As our fiducial model, the simulations from Sijacki et al. (2015) and Khandai et al. (2015) do not manage to entirely reproduce the observed slope. This may be due to the constant values adopted for their radiative efficiencies.

2. In contrast to the MassiveBlack-II simulation, both our NFAM simulation and the Illustris simulation are able to reproduce the observed luminosity functions. We suggest that this might be due to the distinction between quasar-mode and radio-mode.

3. our model predicts a lower high mass end of the black hole mass functions than other simulations (i.e. Di Matteo et al. 2008, Sijacki et al. 2015), because the new AGN feedback model is more efficient in limiting black hole growth at higher masses. Although all simulations are compatible with the upper limits of the black hole mass function estimated from observations by Shankar (2013), our model is in excellent agreement with the observational data from Marconi et al. (2004), Shankar et al. (2004) and Shankar et al. (2009).

4. We predict lower stellar masses than Genel et al. (2014) and Khandai et al. (2015). Since our new implementations do not change the SMFs at $z = 0$ significantly, we suggest that other physical processes like stellar feedback or cooling might be the reason for the differences. In addition, we find that improvements in the model for star formation and stellar feedback like in Schaye et al. (2015) might be necessary to better reproduce the observed shape of the SMFs.

Despite of the overall success of the NFAM model, open questions regarding the actual values of the feedback efficiencies remain. In contrast to the quasar-mode, the radiative efficiency in the radio-mode does not show clear trends in observations, which generally have large uncertainties, especially due to the difficulties in accurately determining the accretion rate. At high redshifts, the quasar luminosity function predicted by the simulations is quite insensitive to the choice of the radiative efficiency in the radio-mode. However, the best match between simulated and observed quasar luminosity functions – especially at low redshifts – is obtained when applying a random radiative efficiency to the simulated AGN in the radio-mode with no dependency on black hole mass or actual accretion rate.

Studying the growth of black holes in more detail (i.e. for individual objects) provides evidence for a two phase process controlling the evolution of the accretion onto the black hole and the associated feedback:

1. As long as black holes have masses below the $M_\bullet$-M_* relation, they grow mainly due to continuous gas accretion. This phase is primarily driven by cold gas accretion with an accretion rate that increases up to the Eddington limit. In this phase, AGN

are observed as luminous X-ray sources. This means that the most luminous AGN are not necessarily driven by merger events as long as they are below the $M_\bullet$-M_* relation.

2. When the $M_\bullet$-M_* relation is reached, gas cooling and AGN feedback are in equilibrium. Consequently, hot gas accretion begins to dominate. This means that the accretion rate, compared to the original implementation, is lowered since we correctly reduce the boost factor for the hot phase. In this phase, AGN feedback is mostly visible as radio jets. This low accretion phase can be disturbed by mergers or other processes driving cold gas into the centre of the galaxy. In a forthcoming study of the most luminous AGN in a simulation with higher resolution we will investigate in more detail whether those objects are mainly triggered by major mergers.

Regarding the latter point, more detailed studies are needed to better differentiate the AGN triggering mechanisms (as galaxy major and minor mergers) and their correlation with the black hole accretion processes within a cosmological context. The next generation of simulations will also allow to distinguish between morphological types of galaxies in more detail and thus, to investigate the connection between AGN luminosities and the host galaxy morphologies, hopefully shedding more light on the main trigger mechanisms for AGN activity in different redshift and luminosity regimes. Such future simulations will also help to understand the dependency of the AGN driving mechanisms on the large-scale environment.

In addition, we plan to further improve the current implementations by taking the angular momentum of the accreted material into account, which in turn would allow to better model the direction of the feedback. This would especially have an important effect on the spatial distribution of the feedback energy in the surroundings of the AGN. Indeed, current black hole accretion and feedback models are purely empirically motivated and have the major drawback that they do not capture the underlying small-scale physical processes, which is, within the framework of large-scale cosmological simulation, currently not feasible due to limited computational power. Nevertheless, despite of the rather crude approximations, the black hole model, in particular with our new modifications, seems to capture the essence of how black holes grow and how feedback affects the host galaxies in reality.

Future observations will improve our understanding of the different accretion modes and their relation to the multi phase nature of the ICM/IGM. In particular, studies of Seyfert galaxies (Mezcua et al. in prep.) will allow an investigation of the role of warm H2 gas (with temperatures of $\sim 10^3$K). In combination with X-ray observations, this will shed more light on the complicated interplay between the various accretion modes of AGN.

Chapter 4

Origin and properties of dual and offset AGN in a cosmological simulation at $z = 2$

The content of this chapter has been published in Steinborn et al. (2016):

> **Lisa K. Steinborn**, Klaus Dolag, Julia M. Comerford, Michaela Hirschmann, Rhea-Silvia Remus, Adelheid F. Teklu: *Origin and properties of dual and offset AGN in a cosmological simulation at z=2*, 2016, MNRAS, 458, 1013

Abstract

In the last few years, it became possible to observationally resolve galaxies with two distinct nuclei in their centre. For separations smaller than 10kpc, dual and offset active galactic nuclei (AGN) are distinguished: in dual AGN, both nuclei are active, whereas in offset AGN only one nucleus is active. To study the origin of such AGN pairs, we employ a cosmological, hydrodynamic simulation with a large volume of $(182\mathrm{Mpc})^3$ from the set of Magneticum Pathfinder Simulations. The simulation self-consistently produces 35 resolved black hole (BH) pairs at redshift $z = 2$, with a comoving distance smaller than 10kpc. 14 of them are offset AGN and nine are dual AGN, resulting in a fraction of $(1.2 \pm 0.3)\%$ AGN pairs with respect to the total number of AGN. In this paper, we discuss fundamental differences between the BH and galaxy properties of dual AGN, offset AGN and inactive BH pairs and investigate their different triggering mechanisms. We find that in dual AGN the BHs have similar masses and the corresponding BH from the less massive progenitor galaxy always accretes with a higher Eddington ratio. In contrast, in offset AGN the active BH is typically more massive than its non-active counterpart. Furthermore, dual AGN in general accrete more gas from the intergalactic medium than offset AGN and non-active BH pairs. This highlights that merger events, particularly minor mergers, do not necessarily lead to strong gas inflows and thus, do not always drive strong nuclear activity.

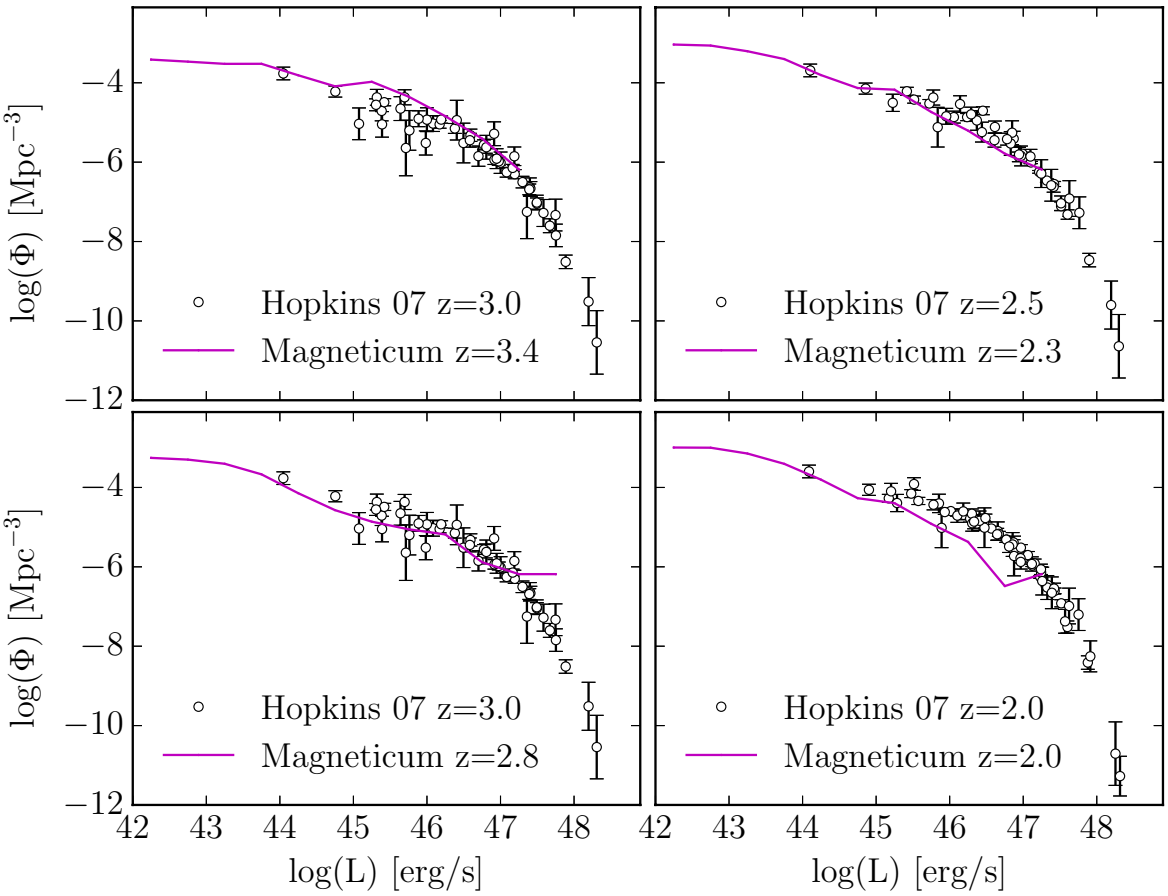

Figure 4.1: Bolometric AGN luminosity function of our simulation (solid magenta lines) at different redshifts in comparison to the observations (black circles with error bars) from Hopkins et al. (2007).

4.1 AGN luminosities

The bolometric AGN luminosities of our simulated BHs are calculated according to

$$L = \epsilon_{\rm r} \dot{M}_\bullet c^2. \tag{4.1}$$

Fig. 1 shows the bolometric AGN luminosity function at different redshifts. Our simulation (solid magenta lines) is successful in reproducing the observations from Hopkins et al. (2007) at roughly the same redshifts (black circles with error bars), particularly between $z = 3.4$ and $z = 2.3$. At $z = 2$ the simulation slightly underestimates the number density of AGN, in particular at the very bright end of the luminosity function. However, this is most likely due to the inefficient size of the simulation volume. Our simulation at $z = 2$ contains only 19 AGN with $L_{\rm bol} > 10^{46}$erg/s, so a much larger volume would be needed to properly capture the bright end of the AGN luminosity function (see also Hirschmann et al. 2014). Nevertheless, the simulation volume is large enough to produce a

statistically realistic population of AGN and therefore provides a good base to study dual and offset AGN for the first time in cosmological simulations.

4.2 Sample of BH pairs

Our simulation contains a total number of 14,903 BHs at $z = 2$ which are more massive than $10^7 M_\odot$. Seeding galaxies with BHs marks an abrupt change of the galaxy formation physics. As described in Section 2.4.1, the seed mass of our BHs is chosen to be significantly smaller than expected for the stellar mass of the galaxy. The BH will then grow and evolve into a self-regulated state and thereby release the associated feedback energy, compensating partially this missing feedback in the early evolution of these galaxies. BHs which did not yet evolve into this self-regulated state are referred to as 'unresolved BHs'. The chosen mass threshold of $10^7 M_\odot$ corresponds roughly to the cut-off in the BH mass function for the high-resolution simulation shown in Hirschmann et al. (2014). [1] For lower BH masses, it is possible that the system did not yet have time to evolve into a self-regulated state and therefore, the luminosity of the BH is difficult to interpret.

We identify a sample of 34 BH pairs with a comoving distance smaller than 10kpc at $z = 2$, where at least one BH is resolved in mass. Throughout this paper, we define a BH as an AGN if it has a bolometric luminosity larger than 10^{43} erg/s. We distinguish between four different classes of BH pairs:

- dual AGN,
- offset AGN (both BHs are more massive than $10^7 M_\odot$),
- unresolved offset AGN (while the AGN is more massive than $10^7 M_\odot$, the second BH is below this resolution limit), and
- dual BHs without AGN.

We distinguish between resolved and unresolved offset AGN, because it is not clear to which class unresolved offset AGN would belong if both BH masses were resolved. Since the unresolved, non-active BH should actually be more massive, and since the luminosity depends on the BH mass, BH pairs in this class would be either classified as dual AGN or offset AGN, if the masses of both BHs were resolved. The reason for the too low BH mass is not only the progenitor galaxy itself, but also the more massive counterpart, which suppresses BH accretion, as we will describe in Section 4.3.2 in more detail. Thus, although the BHs and their environment might not be totally realistic, it is still an interesting question why the smaller BH could not grow as much as the larger one. For that reason and to have a sample as complete as possible, we also consider unresolved offset AGN in this analysis. We remark that there are also two dual AGN pairs and several BH pairs

[1] We choose a relatively low BH mass threshold, since this cut-off and thus the transition from resolved to unresolved BHs, is very smooth for the high-resolution simulation.

without AGN where one BH is below the mass resolution limit. We do not treat them as a separate class for the following reasons: (i) if a BH below the mass resolution limit is active and thus grows properly, we do not treat it as unresolved, because the AGN feedback is a self-regulated process, which depends mainly on the gas properties and not on the BH mass; (ii) if a BH in a pair without AGN is not resolved, but its counterpart is massive enough to be resolved and is also not active, we expect that, since the environment of the two BHs is roughly the same, the unresolved BH would also be inactive if it was more massive.

Our chosen luminosity threshold is clearly arbitrary and leads to some overlap between the properties of the different classes of BH pairs. We refer to Section 4.4, in particular Fig. 4.14, where we show the contribution of the four different classes for different luminosity thresholds. However, we want to emphasize that a different definition does not change our results qualitatively.

That luminosity threshold gives us 1864 AGN[2] and our sample of 34 BH pairs then splits up into:

- 9 dual AGN pairs (∼0.5% of all AGN),
- 6 offset AGN (∼0.3% of all AGN),
- 8 unresolved offset AGN (∼0.4% of all AGN) and
- 11 dual BHs without AGN.

The fraction of dual and offset AGN with respect to the total amount of AGN then sums up to $\sim 1.2\%$. The fraction of dual AGN varies between $\sim 0.48\%$ and $\sim 0.91\%$, accounting for the fact that the unresolved offset AGN might actually be dual AGN.

Fig. 4.2 shows the fraction of dual and offset AGN with respect to the total amount of AGN for a given luminosity bin. The simulation predictions for $z = 2$ are shown as red diamonds, where the red error bars illustrate the corresponding $\sqrt{N}/N_{\rm tot}$ error. Despite the rather large scatter due to our low number of AGN pairs we see a trend of an increasing fraction of AGN pairs with luminosity. Since our simulation ran only down to $z = 2.0$, we cannot directly compare it with observations, which are only available for very low redshifts. Nevertheless, observations at low redshifts ($z < 0.21$, Comerford & Greene 2014) find the same trend as we see in our simulation at $z = 2$, in the sense that the amount of candidate offset AGN increases with AGN luminosity (see black dotted line in Fig. 4.2). This could indicate that this trend with luminosity is already in place at $z = 2$. Furthermore, these findings might be directly connected to other observational results showing that the fraction of AGN triggered by galaxy mergers seems to increase with AGN luminosity (e.g. Treister et al. 2012).

In Tables 4.1 and 4.2 we summarize the most important properties of the simulated dual and offset AGN pairs, where d is the comoving distance of the BHs to each other and the indices 1 and 2 correspond to the more and less luminous AGN. We see no dependence

[2]Dual AGN pairs are counted as one AGN to be consistent with observations.

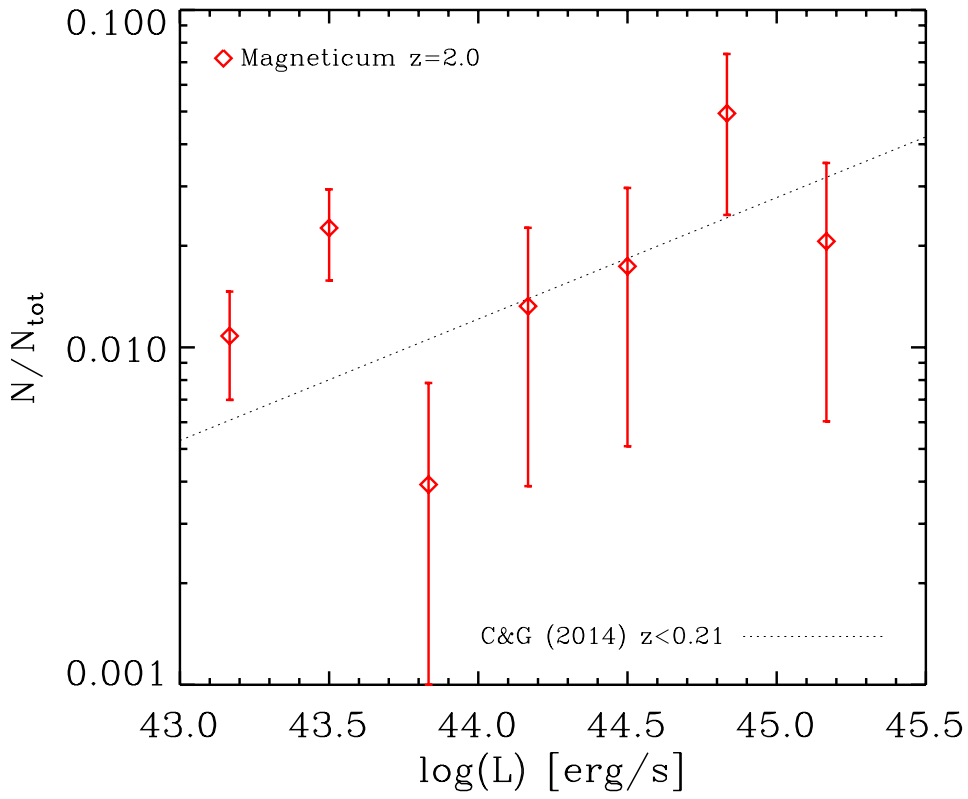

Figure 4.2: The red diamonds show the fraction of AGN in pairs with respect to the total number of AGN in bins of the bolometric luminosity, where N is the number of offset and dual AGN in bins of the bolometric luminosity and $N_{\rm tot}$ is the total number of AGN in the same luminosity range. The error bars show the corresponding $\sqrt{N}/N_{\rm tot}$ error. We see a trend of an increasing fraction of AGN pairs with luminosity. Since Comerford & Greene (C&G, 2014) found a similar trend in their observations at low redshifts, we also show for orientation their best fit for observed offset AGN candidates at $z < 0.21$ as black dotted line, although a direct comparison at the different redshifts is not possible.

ID	d [kpc]	$\log(L_1)$ [erg/s]	$\log(L_2)$ [erg/s]	$M_{\bullet 1}$ $[M_\odot]$	$M_{\bullet 2}$ $[M_\odot]$	f_{Edd1}	f_{Edd2}
1	9.68	43.58	43.57	$5.94 \cdot 10^7$	$4.42 \cdot 10^7$	$5.14 \cdot 10^{-3}$	$6.73 \cdot 10^{-3}$
2	8.78	43.20	43.06	$2.90 \cdot 10^7$	$4.16 \cdot 10^7$	$4.38 \cdot 10^{-3}$	$2.20 \cdot 10^{-3}$
3	2.40	43.20	43.17	$2.88 \cdot 10^7$	$1.84 \cdot 10^7$	$4.40 \cdot 10^{-3}$	$6.41 \cdot 10^{-2}$
4	2.67	44.77	44.76	$4.49 \cdot 10^7$	$3.62 \cdot 10^7$	$1.04 \cdot 10^{-1}$	$1.27 \cdot 10^{-1}$
5	8.91	45.32	43.49	$1.39 \cdot 10^8$	$2.04 \cdot 10^7$	$1.21 \cdot 10^{-1}$	$1.20 \cdot 10^{-2}$
6	3.50	43.42	43.33	$1.52 \cdot 10^8$	$1.19 \cdot 10^8$	$1.37 \cdot 10^{-3}$	$1.43 \cdot 10^{-3}$
7	8.25	44.53	43.35	$3.97 \cdot 10^8$	$1.59 \cdot 10^8$	$6.83 \cdot 10^{-3}$	$1.12 \cdot 10^{-3}$
8	7.11	44.46	44.06	$3.79 \cdot 10^7$	$5.10 \cdot 10^6$	$6.11 \cdot 10^{-2}$	$1.81 \cdot 10^{-1}$
9	7.17	44.72	43.20	$2.35 \cdot 10^7$	$8.98 \cdot 10^6$	$1.79 \cdot 10^{-1}$	$1.40 \cdot 10^{-2}$

Table 4.1: Properties of the dual AGN pairs in our simulation at $z = 2.0$. The indices 1 and 2 always correspond to the more and less luminous BH, respectively. The two dual AGN below the horizontal line contain one BH with $M_\bullet < 10^7 M_\odot$.

ID	d [kpc]	$\log(L_1)$ [erg/s]	$\log(L_2)$ [erg/s]	$M_{\bullet 1}$ $[M_\odot]$	$M_{\bullet 2}$ $[M_\odot]$	f_{Edd1}	f_{Edd2}
10	5.05	43.59	41.82	$1.57 \cdot 10^8$	$1.62 \cdot 10^7$	$1.97 \cdot 10^{-3}$	$3.26 \cdot 10^{-4}$
11	9.23	43.26	42.65	$6.94 \cdot 10^7$	$4.29 \cdot 10^7$	$2.09 \cdot 10^{-3}$	$8.37 \cdot 10^{-4}$
12	5.91	43.01	41.80	$2.72 \cdot 10^7$	$2.52 \cdot 10^7$	$3.00 \cdot 10^{-3}$	$1.99 \cdot 10^{-4}$
13	6.85	44.20	42.88	$5.14 \cdot 10^7$	$4.38 \cdot 10^7$	$2.44 \cdot 10^{-2}$	$1.37 \cdot 10^{-3}$
14	4.83	43.49	40.16	$5.71 \cdot 10^8$	$1.08 \cdot 10^8$	$4.30 \cdot 10^{-4}$	$1.73 \cdot 10^{-6}$
15	7.91	43.59	42.37	$1.49 \cdot 10^8$	$3.13 \cdot 10^7$	$2.08 \cdot 10^{-3}$	$5.88 \cdot 10^{-4}$
16	8.88	44.68	37.23	$3.52 \cdot 10^8$	$1.24 \cdot 10^6$	$1.07 \cdot 10^{-2}$	$1.10 \cdot 10^{-7}$
17	1.40	43.44	41.79	$1.04 \cdot 10^7$	$6.19 \cdot 10^6$	$2.10 \cdot 10^{-2}$	$7.89 \cdot 10^{-4}$
18	7.76	43.77	41.51	$4.57 \cdot 10^7$	$2.51 \cdot 10^6$	$1.02 \cdot 10^{-2}$	$1.03 \cdot 10^{-3}$
19	7.41	43.40	40.98	$1.35 \cdot 10^7$	$2.41 \cdot 10^6$	$1.48 \cdot 10^{-2}$	$3.12 \cdot 10^{-4}$
20	9.16	43.39	41.82	$4.59 \cdot 10^7$	$3.21 \cdot 10^6$	$4.23 \cdot 10^{-3}$	$1.65 \cdot 10^{-3}$
21	5.94	44.03	39.79	$1.04 \cdot 10^8$	$2.50 \cdot 10^6$	$8.20 \cdot 10^{-3}$	$1.97 \cdot 10^{-5}$
22	5.59	43.14	39.34	$2.92 \cdot 10^7$	$1.22 \cdot 10^6$	$3.74 \cdot 10^{-3}$	$1.42 \cdot 10^{-5}$
23	6.20	45.21	39.66	$1.36 \cdot 10^7$	$1.23 \cdot 10^6$	$9.45 \cdot 10^{-1}$	$2.98 \cdot 10^{-5}$

Table 4.2: Same as table 4.1 but for resolved (upper 6 lines) and unresolved (lower 8 lines) offset AGN.

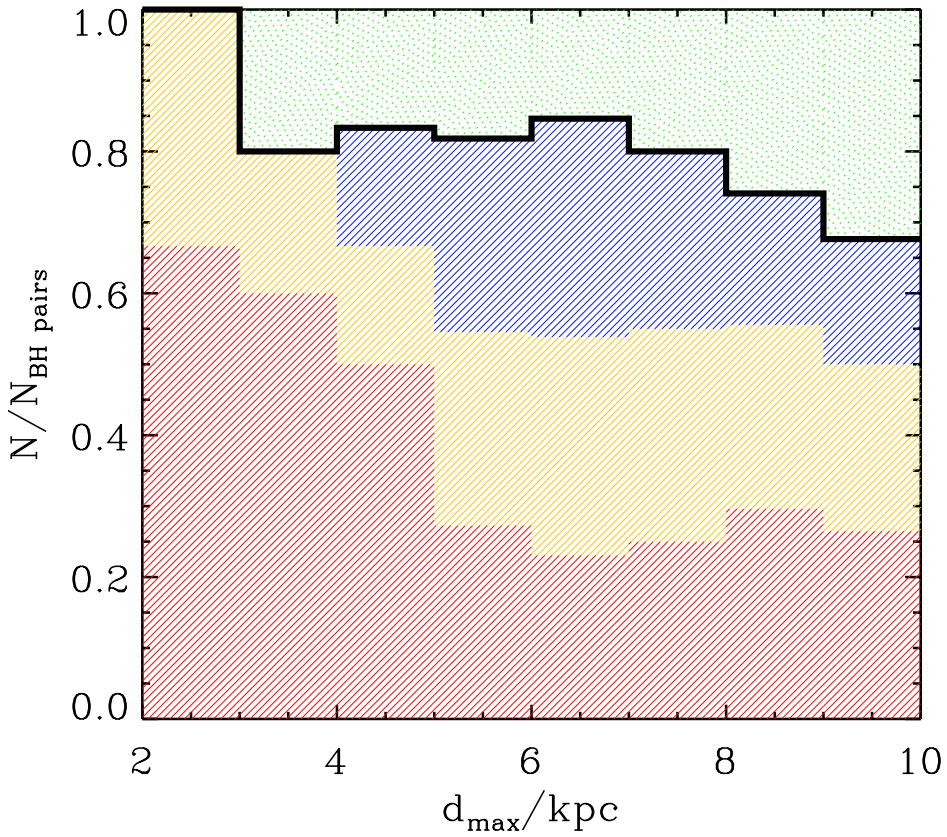

Figure 4.3: The black line shows the cumulative fraction of dual and offset AGN in bins of the maximum separation $d_{\rm max}$ between the two BHs. The coloured areas indicate the contribution from dual AGN (red), offset AGN (blue), unresolved offset AGN (yellow) and BH pairs without AGN (green).

of the luminosities on the distance between the BHs. We calculated the luminosities L_1 and L_2 of the two BHs as described in Steinborn et al. (2015). The Eddington ratios $f_{\rm Edd1}$ and $f_{\rm Edd2}$ are defined as $f_{\rm Edd} := L/L_{\rm Edd}$. [3]

Fig. 4.3 shows the cumulative fraction of dual and offset AGN for a given maximum separation $d_{\rm max}$ between the two BHs. The coloured areas indicate the contribution from the four different classes of BH pairs: dual AGN (red), offset AGN (blue), unresolved offset AGN (yellow) and BH pairs without AGN (green). Although our sample size is rather small, it is clearly visible that dual AGN dominate at small separations, whereas the fraction of BH pairs without AGN is the largest when allowing separations up to 10kpc. Furthermore, all resolved offset AGN have separations larger than 4kpc. This is also the case for the unresolved offset AGN, except for one example with an extremely low sep-

[3]Note that in our model $L/L_{\rm Edd}$ is not the same as $\dot{M}_\bullet/M_{\rm Edd}$ (Steinborn et al., 2015), since the total accretion rate splits up into luminosity and mechanical outflows: $\dot{M}_\bullet/M_{\rm Edd} = L/L_{\rm Edd} + P_o/L_{\rm Edd}$, where $L = \epsilon_r \dot{M}_\bullet c^2$ is the luminosity and $P_o = \epsilon_o \dot{M}_\bullet c^2$ is the power of mechanical outflows.

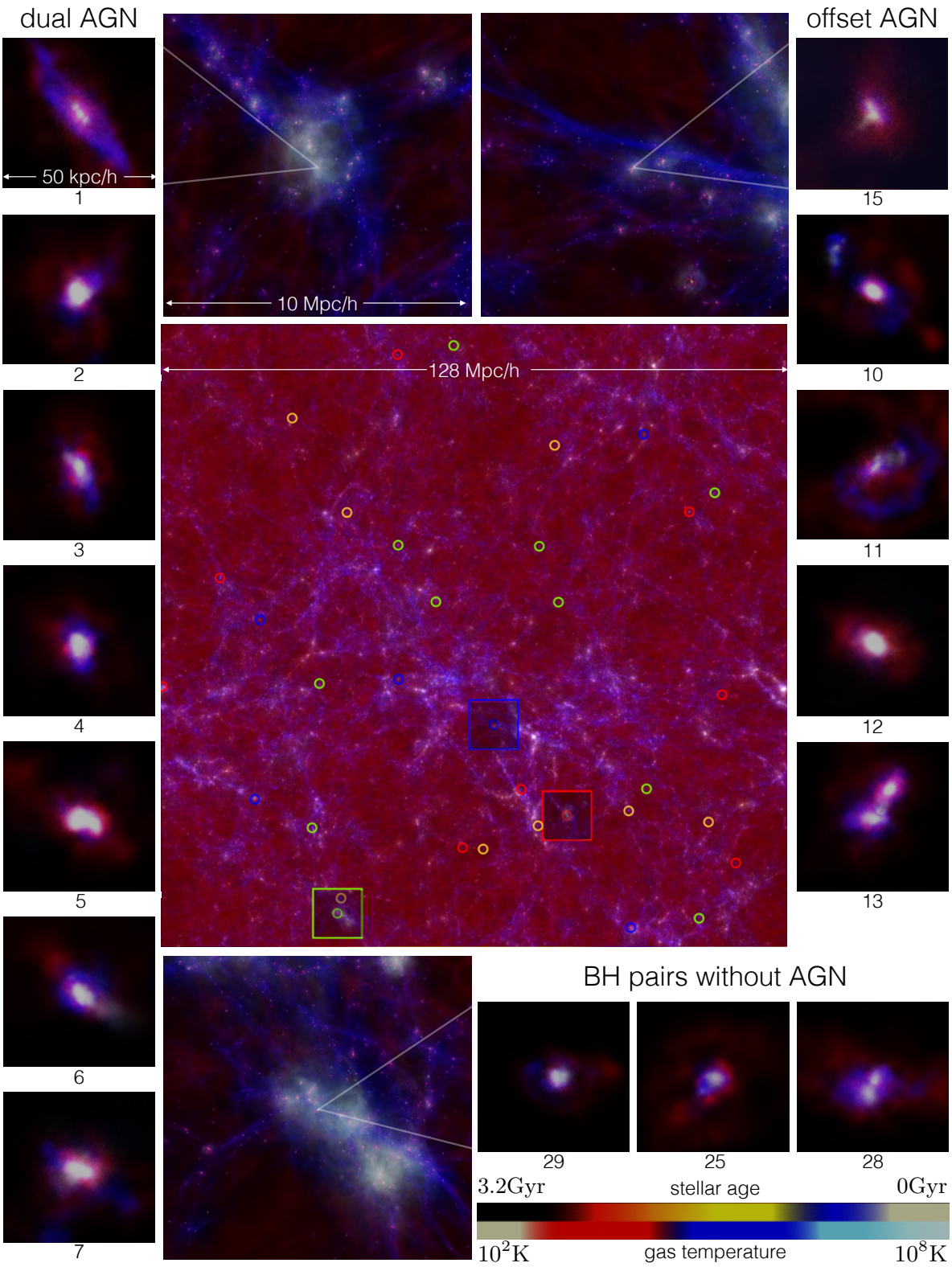
dual AGN
offset AGN
50 kpc/h
10 Mpc/h
128 Mpc/h
1
2
3
4
5
6
7
15
10
11
12
13
BH pairs without AGN
29
25
28
3.2Gyr
stellar age
0Gyr
10^2K
gas temperature
10^8K

Figure 4.4

Figure 4.4: The large panel in the middle shows a visualization of our cosmological simulation. The red, blue and green circles mark the positions of all dual AGN pairs, offset AGN and BH pairs without AGN, respectively. Exemplarily, we show the large-scale environment, i.e. a box of 10 Mpc/h length around the host galaxy of one dual AGN pair, one offset AGN and one BH pair without AGN. The positions of these boxes are also marked in the large picture. We remark that the box is so large that structures are often not visible because they are overlaid by something else. Furthermore, we show a few examples of the host galaxies of the dual AGN (left images), offset AGN (right images) and BH pairs without AGN (images in the middle bottom), where we always show a box with a length of 50 kpc/h. The IDs of the BH pairs are the same as in Table 4.1 and 4.2 and the numbering continues to BH pairs without AGN (IDs 24-34). The colour bars are the same for all pictures, where the upper colour bar represents the age of the stars (from old to young in logarithmic scale of the cosmic age a, converted to the stellar age) and the lower one the gas temperature (from cold to hot in logarithmic scale).

aration. Overall, our simulation predicts the same trend at $z = 2$ like the observations from Comerford et al. (2015) at lower redshifts, which indicate that the fraction of AGN increases with decreasing BH distances. Such a trend was also observed much more accurately for larger separations between 10kpc and 100kpc (Ellison et al. 2011, Koss et al. 2012).

In Fig. 5.1, we show visualizations[4] of a few examples of the three different classes of AGN/BH pairs. The images illustrate the baryonic component only. Gas and stars are colour-coded by the gas temperature and the stellar age, respectively (as indicated by the colour bars). In the middle we show the total box. To check whether the different BH pairs are located in different large scale environments, we highlight the positions of all BH pairs as coloured circles, where the colours red, blue, yellow and green represent dual AGN pairs, offset AGN, unresolved offset AGN and BH pairs without AGN, respectively. At first sight, there seems to be no obvious difference between the environment of the different types. However, this could be a consequence of overlaid structures due to the large volume. Hence, for three examples, we additionally show a smaller box of 10Mpc/h around the BH pair. We show larger illustrations of these regions in the three medium sized images at the middle top and middle bottom. The panel at the bottom demonstrates, for example, that non-active BHs are not necessarily located in a gas poor environment. Overall, we can suspect that, in contrast to offset AGN and inactive BH pairs, dual AGN (left large image at the top) have a higher probability to be located in the centre of large-scale filaments, which can provide the gas supply for the galaxy. In Section 4.3.4 we will address this issue in more detail.

[4]performed with the free software Splotch, http://www.mpa-garching.mpg.de/∼kdolag/Splotch from Dolag et al. (2008)

4.3 Results

In this section, we investigate different properties of the BH pairs to understand the underlying mechanisms leading to the differences in their AGN activity.

4.3.1 BH and stellar masses

In the following figures, we illustrate dual AGN as red stars, offset AGN and their less luminous counterparts are represented by blue diamonds, unresolved offset AGN and their counterparts are illustrated by yellow diamonds and dual BHs without AGN are shown as green squares. The more luminous BH in a pair is always represented by a large symbol and the less luminous one by a smaller one. Fig. 4.5 shows the masses of the BHs in our sample versus the stellar mass of their host galaxies. We estimate the stellar mass as the total mass of all stars corresponding to the subhalo identified with SUBFIND (Dolag et al. 2009, Springel et al. 2001) which contains the BH. In some cases SUBFIND still identifies two different subhaloes for the two BHs in a pair although the smaller subhalo is clearly within the larger one. In these cases we sum up the stellar mass of both subhaloes.

The black solid line illustrates the best fit for the observations of McConnell & Ma (2013) at $z = 0$. Since we found in Hirschmann et al. (2014) and Steinborn et al. (2015) that the Magneticum Pathfinder Simulations agree very well with these observations and that this relation does not change significantly between $z = 0$ and $z = 2$, we can use the black line also at $z = 2$ for orientation. As expected, almost all BHs lie below the observed relation from McConnell & Ma (2013), since the merger triggered star formation activity starts earlier than the fuelling of the BHs and the actual BH merger. This is in excellent agreement with the findings from Kormendy & Ho (2013).

Fig. 4.5 also shows that offset AGN are mostly more massive than their inactive counterparts. Furthermore, above $M_\bullet \sim 7 \cdot 10^7 M_\odot$, all BHs are either dual or offset AGN. For lower masses, active and non-active BHs cover the same mass range. By definition, the inactive counterparts of unresolved offset AGN are below the resolution limit of $M_\bullet = 10^7 M_\odot$ (black dotted line). These BHs would not necessarily be inactive, if they were properly resolved. The stellar mass of their host galaxies is very large compared to the BH mass, probably due to the merger. The BH growth is suppressed, which is very untypical, since the BHs usually grow very fast right after the seeding because they are seeded with an artificially low BH mass. This could explain why the unresolved counterparts of offset AGN (small yellow diamonds) have even lower BH masses than most BHs in pairs without AGN (green squares). We suspect that without this seeding and resolution effect, our simulation might contain more dual AGN.

4.3.2 Triggering versus suppressing accretion

Comerford et al. (2015) found that all dual AGN and dual AGN candidates in their sample have one interesting similarity: The BH in the less luminous galaxy always has the higher Eddington ratio. Since their sample is very small, additional data is needed to constrain

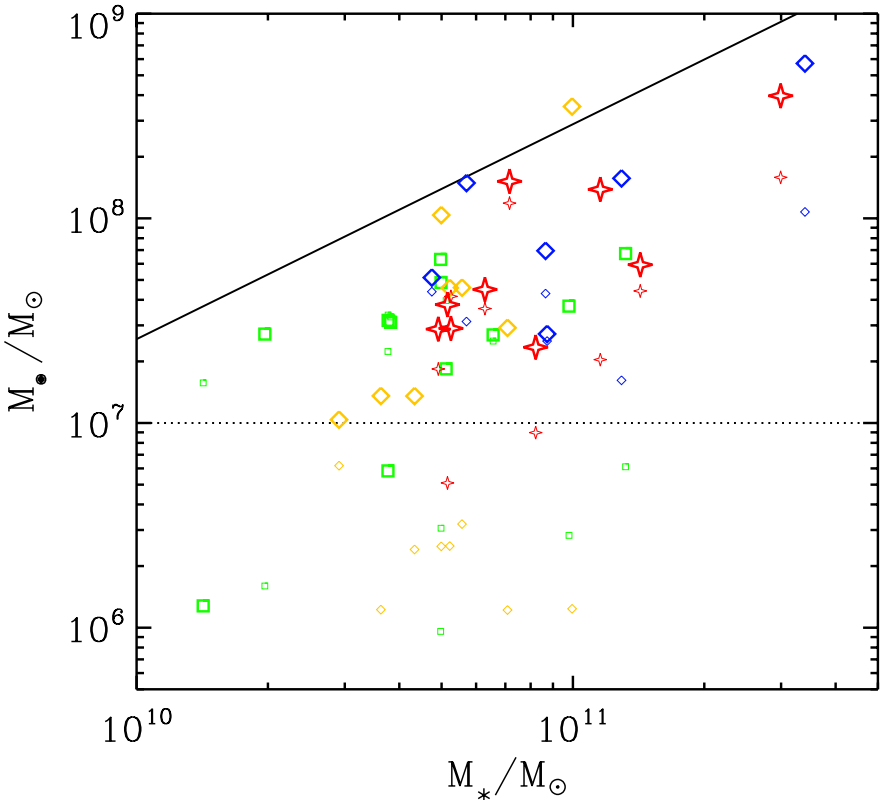

Figure 4.5: Relation between the BH mass and the stellar mass of the host galaxy for our sample of BH pairs. The different symbols illustrate the different classes of BH pairs, where large symbols correspond to the more luminous BHs in a pair and the small symbols to the less luminous ones. The black solid line shows the fit from McConnell & Ma (2013) and the black dotted line marks our resolution limit.

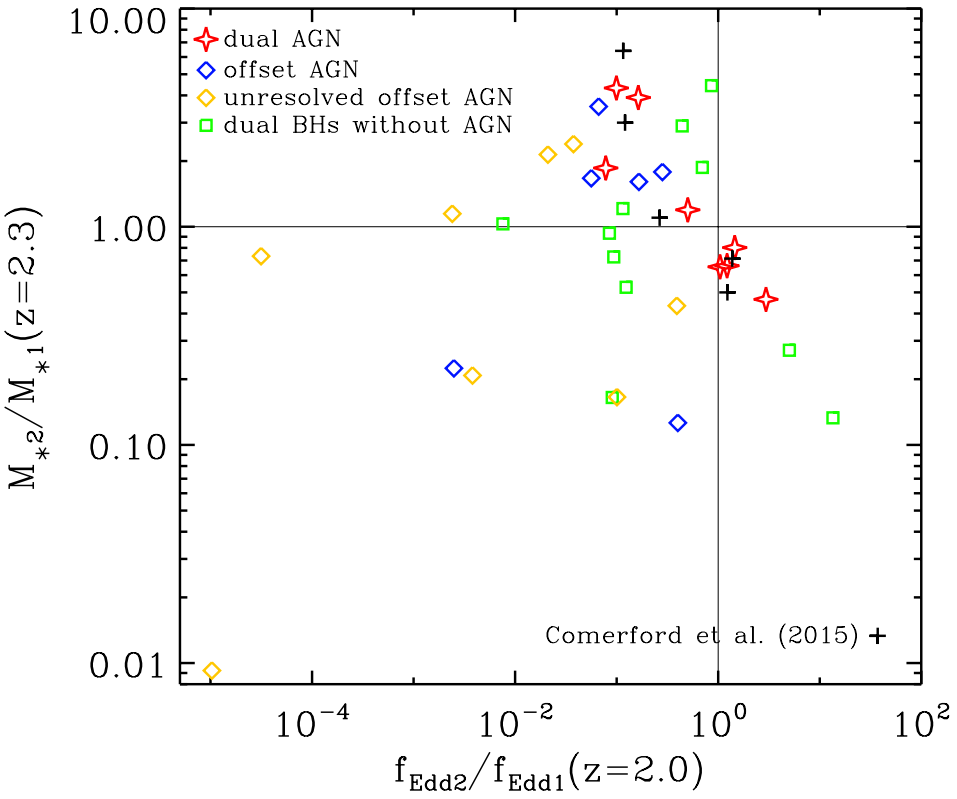

Figure 4.6: The ratio of the Eddington ratios compared to the stellar mass ratio. The indices 1 and 2 correspond to the more and less luminous BH, respectively. For all dual AGN the more luminous AGN originates from the less massive progenitor galaxy, whereas offset AGN always have a higher Eddington ratio than their less luminous counterpart. Our dual and offset AGN lie in the same range as observed ones (black crosses) from Comerford et al. (2015). Note that we show only 8 dual AGN in this plot because we cannot give a secure estimate for the merger mass ratio of dual AGN number 1 due to a merger of three galaxies.

this result. At that point our simulation can be helpful: In contrast to observations, it has the advantage that we know the exact stellar mass before the merger and thus we are not biased by effects like stellar stripping. Although we study much higher redshifts, we interestingly find the same behaviour in our simulation for dual AGN. To characterize the processes which drive our results we traced our merging systems 0.5 Gyr back in time (to $z = 2.3$) to infer the stellar masses of the progenitor galaxies. This is demonstrated in Fig. 4.6, showing the stellar mass ratio of the two progenitor galaxies at $z = 2.3$ versus the ratio of the corresponding Eddington ratios at $z = 2$. The indices 1 and 2 correspond to the more and less luminous BH, respectively. For dual AGN, the galaxy with the higher Eddington ratio has the lower stellar mass ratio and vice versa. Offset AGN, on the contrary, behave differently: as expected intuitively, the BH appearing as an AGN always has the higher Eddington ratio, irrespectively of the host galaxy mass. BH pairs without AGN activity can behave like either dual or offset AGN. Fig. 4.6 also shows that the simulation predictions cover the same range as the observed ones (black crosses). Together with the findings in Section 4.2, where we also found similar trends like in observations at low redshifts, this indicates that the underlying physical processes which drive the formation of dual and offset AGN are the same at $z = 2$ as at low redshifts.

Fig. 4.7 shows a comparison of the Eddington ratios of the progenitor systems at $z = 2.3$ and for the BH pairs at $z = 2.0$, where the symbols are the same as in Fig. 4.5. Non-active BHs scatter over the whole range, but mostly correspond to the jet-mode (or radio-mode), which is typically defined as $f_{Edd} < 5 \cdot 10^{-2}$. As shown in Steinborn et al. (2015), in this mode the gas reservoir in the vicinity of the inactive BHs is either heated or consumed, leading to rather low BH accretion rates and thus, low AGN luminosities.

For dual and offset AGN, the simulations predict one clear difference: for the majority of dual AGN, the Eddington ratio significantly increases for both BHs between the progenitors at $z = 2.3$ and the pairs at $z = 2.0$. For the offset AGN (both resolved and unresolved) on the contrary, the Eddington ratio also increases for the active AGN, but for the non-active counterparts (small blue and yellow diamonds) it either hardly changes or it even decreases with time (except in one case). This indicates that, in contrast to dual AGN, offset AGN might prevent their counterparts from accreting more gas.

One explanation may be related to the effect of AGN feedback. Single BHs usually grow rapidly until AGN feedback and gas cooling are in equilibrium, where feedback leads to lower accretion rates and gas cooling to higher accretion rates. When the equilibrium is reached, they grow along the M-σ relation (Churazov et al., 2005). In BH pairs, feedback from two BHs heats the same gas reservoir, and hence the heating may dominate compared to gas cooling, leading to low Eddington ratios. This could prevent the less massive BH from growing further, as it 'starves' because of the feedback of the more massive BH, whereas the other BH is massive enough to appear as AGN also at low Eddington ratios.

To understand whether gravity or feedback dominates, we show in Fig. 4.8 the distribution of the mean gas temperature inside the accretion radius[5] of the less luminous BH. We are only interested in the less luminous BH, because whether AGN activity is suppressed

[5]The accretion radius is set by the most distant gas particle used to calculate the Bondi accretion rate.

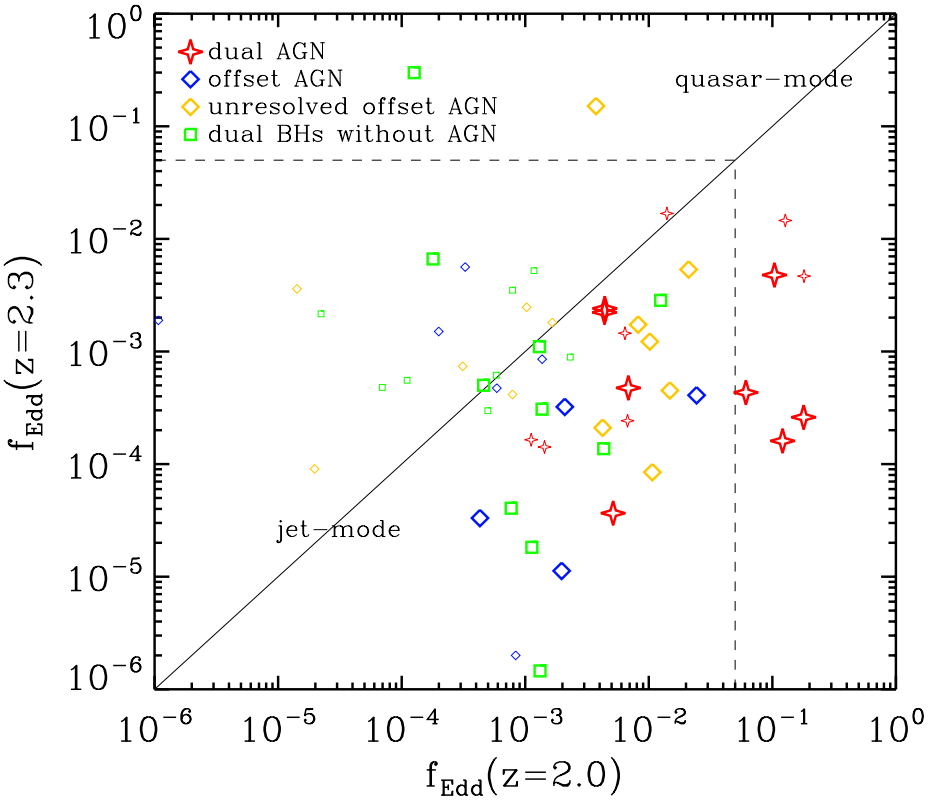

Figure 4.7: Comparison of the Eddington ratio at $z = 2.0$ and $z = 2.3$. For almost all dual AGN the Eddington ratio increases in this time interval. In pairs with only one AGN the Eddington ratio of the AGN increases, whereas it decreases for the less luminous BH. Dual BHs without AGN scatter in the range up to $f_{Edd} \approx 10^{-2}$. Note that some BH do not yet exist at $z = 2.3$ and hence, there are less than 60 data points.

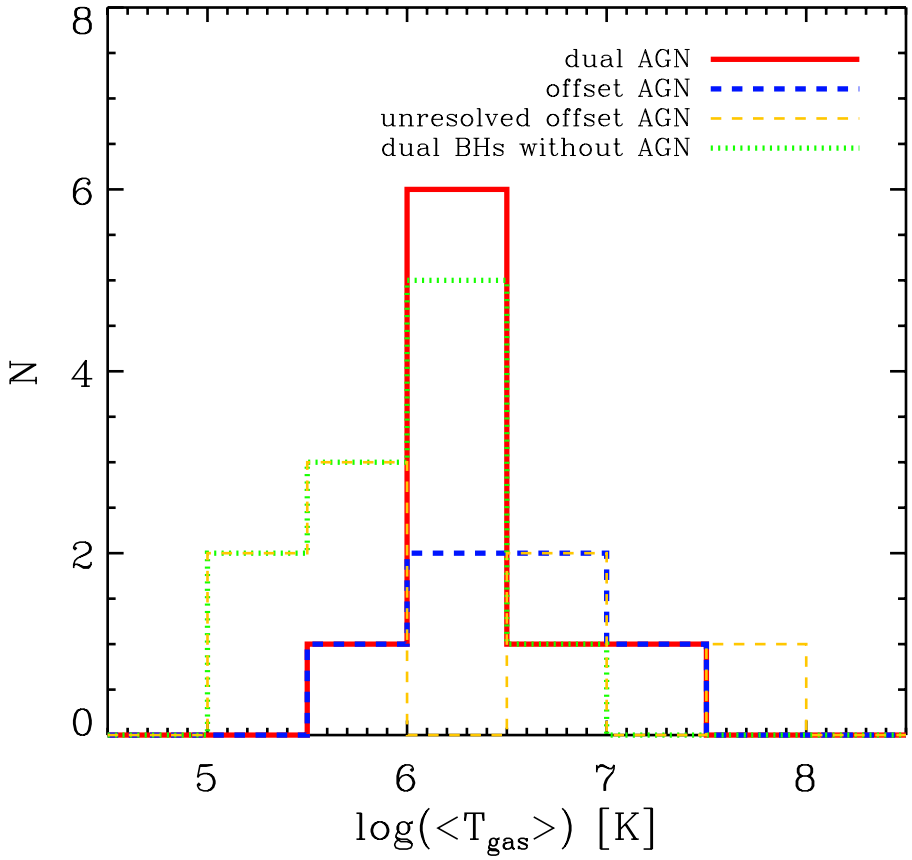

Figure 4.8: Distribution of the mean gas temperature inside the accretion radius. The figure shows only the gas temperatures around the less luminous BH, because we are interested in the mechanisms which suppress AGN activity in the less luminous counterparts of offset AGN (blue dashed histogram) and BH pairs without AGN (green dotted histogram) in contrast to dual AGN (red solid histogram).

in these BHs or not makes the difference between dual (red solid histogram) and offset AGN (blue dashed histogram), as we saw in Fig. 4.6 and Fig. 4.7. We find that most dual AGN have a surrounding gas temperature between 10^6K and $10^{6.5}$K. This indicates that AGN feedback already heats up the surrounding gas, but is still not strong enough to fully suppress the AGN activity. There are also two dual AGN surrounded by extremely hot gas ($> 10^{6.5}$K). For one of them the stellar masses of the progenitor galaxies are similar such that none of the BHs can dominate over the other one. In the other dual AGN pair the more luminous AGN has the less massive progenitor galaxy.[6] There are three resolved and three unresolved offset AGN which are also surrounded by such extremely hot gas, which indicates that in these cases, AGN feedback is more important in suppressing the accretion. In general however, offset AGN (also the unresolved ones) are typically characterized by a wider distribution of the surrounding temperatures. Five of the unresolved counterparts of offset AGN are surrounded by gas with a lower temperature and hence, the AGN feedback of the second, more massive and resolved BH, is not relevant. We assume that gravity might play the most important role in these cases.

The green dotted histogram in Fig. 4.8 shows the temperature distribution around BH pairs without AGN. Five of these BHs are hosted by less massive young galaxies which contain a lot of cold gas but the BHs are simply too small to show AGN activity, although the distribution peaks in the same range as that of the dual AGN.

Finally, we would like to caution the reader that the gas temperature is not only affected by AGN feedback. However, in our cosmological simulation it is not possible to directly distinguish between different heating mechanisms, but since we consider only gas inside the accretion radius, the contribution of AGN feedback is probably large, especially for very high gas temperatures.

In addition, we expect that not only the mass difference of the BHs and their associated feedback might play a role, but also the total mass difference of the two progenitor galaxies, which we will address in more detail in the next Section.

4.3.3 Merger mass ratio

To explicitly demonstrate the importance of the mass difference between the two merging BHs for the activity of BH pairs, we compare their masses in the snapshot before the merger, at $z = 2.3$ (see Fig. 4.9). It is evident that for dual AGN the BH masses are similar, whereas for pairs with one or no AGN, they can differ by more than one order of magnitude. This indicates that a large difference between the BH masses, and thus also between the galaxy stellar masses, leads to a gas transfer from the smaller to the larger galaxy (e.g. review by Barnes & Hernquist 1992).

That offset AGN are a consequence of mergers with large mass differences, not only in the BH but also in the stellar mass, is supported by Fig. 4.17 and Fig. 4.18 in Appendix B, showing environmental dependencies of AGN pairs. Both dual and offset AGN pairs

[6] At that point we would like to refer the reader to Appendix A, in which we show that the differences between dual and offset AGN described in this section are not driven by an overlap of the accretion radii.

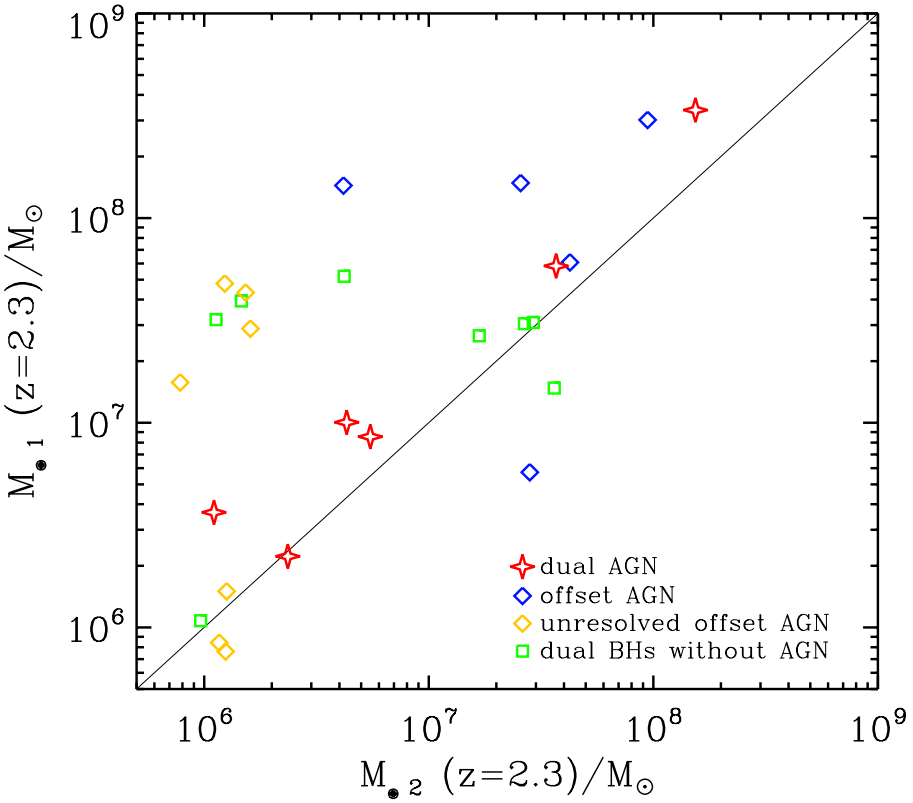

Figure 4.9: Comparison of the masses of the more ($M_{\bullet 1}$) and the less ($M_{\bullet 2}$) luminous BH around 0.5 Myr before (at $z = 2.3$) they were detected as dual BHs. For dual AGN the masses are similar, whereas for pairs with one or no AGN they can differ by more than one order of magnitude. BHs with masses lower than $5 \cdot 10^6 M_\odot$ are found in all three types of BH pairs. Again, there are less than 60 data points, because some BHs are not yet seeded at $z = 2.3$.

live in similar, rather high-density regions so that the large-scale environment is apparently not causing the different behaviour of BH pairs.

Fig. 4.10 illustrates the merger mass ratios of the progenitor galaxies at $z = 2.3$ as a function of the gas masses of the galaxies hosting the BH pairs at $z = 2.3$ (coloured crosses) and at $z = 2.0$ (other coloured symbols), where the lines connect the values at the two different epochs. If the two BHs are related to different subhaloes, we sum up the gas masses associated with their galaxies. Like in Fig. 4.6, M_{*1} and M_{*2} are the stellar mass of the galaxy with the more and less luminous BH at $z = 2.0$. For values below one, M_{*2}/M_{*1} equals the merger mass ratio, whereas for values larger than one it corresponds to the inverted merger mass ratio and the more luminous AGN originates from the less massive progenitor galaxy.

We find that dual AGN preferably live in galaxies with a large gas content and a high stellar mass ratio. There are two exceptions with gas masses lower than $9 \cdot 10^{10} M_{\odot}$ at $z = 2.0$. In one of these galaxies, the AGN have luminosities of $L_1 = L_2 = 10^{43.2}$ erg s^{-1}, just above the threshold for our definition of AGN ($L > 10^{43}$ erg s^{-1}). For the other one, which is represented by the second red cross and the first red star (from left to right) at $M_{*2}/M_{*1} \approx 0.7$, the gas mass decreases by more than a factor of two between $z = 2.3$ and $z = 2.0$, which is in contrast to the other dual AGN pairs, where the gas mass mostly increases. Interestingly, this is the only BH pair in our sample which is located in the most massive cluster of the simulation. It has a total halo mass of $M_{\rm halo} = 1.3 \cdot 10^{14} M_{\odot}$ and is the only cluster with $M_{\rm halo} > 10^{14} M_{\odot}$ at $z = 2.0$. This might be a hint that AGN are triggered differently in a cluster environment. We suspect that the gas exchange between galaxies in a cluster might continuously feed the BHs, such that they are not switched off, although the Eddington ratios are relatively low due to the hot environment and the AGN feedback energy is relatively large due to the high luminosity. In the case of our dual AGN pair, the total gas mass of the cluster is $1.4 \cdot 10^{13} M_{\odot}$, which is by far larger than the gas mass of the host galaxy only. Indeed, Krumpe et al. (2015) find that the mass of the dark matter halo is related to the BH mass. However, to take a closer look at BH pairs in clusters, we would need a larger sample of clusters, which is beyond the scope of this paper.

Fig. 4.10 also illustrates that we can roughly distinguish between two different regimes for offset AGN: A large gas mass would, in principal, allow to feed both BHs, but if one progenitor galaxy is much more massive than the other one, its gravitational potential dominates and hence the BH residing in the more massive galaxy may use up the gas from the smaller one. Thus, offset AGN can have rather low stellar merger mass ratios, in contrast to dual AGN (see also Fig. 4.9). For lower gas masses, the merger mass ratio of dual AGN is still relatively large, i.e., all of them are major mergers, but as $M_{*2}/M_{*1} < 1$, this means that the more massive galaxy contains the more luminous BH. In contrast, offset AGN are hosted by the less massive galaxy. For one offset AGN, the gas mass increases by more than one order of magnitude from z=2.3 to z=2. This is not only a consequence of the major merger, but also several minor mergers drive new, cold gas into the center of the host galaxy.

However, there might also be other mechanisms than those described above which

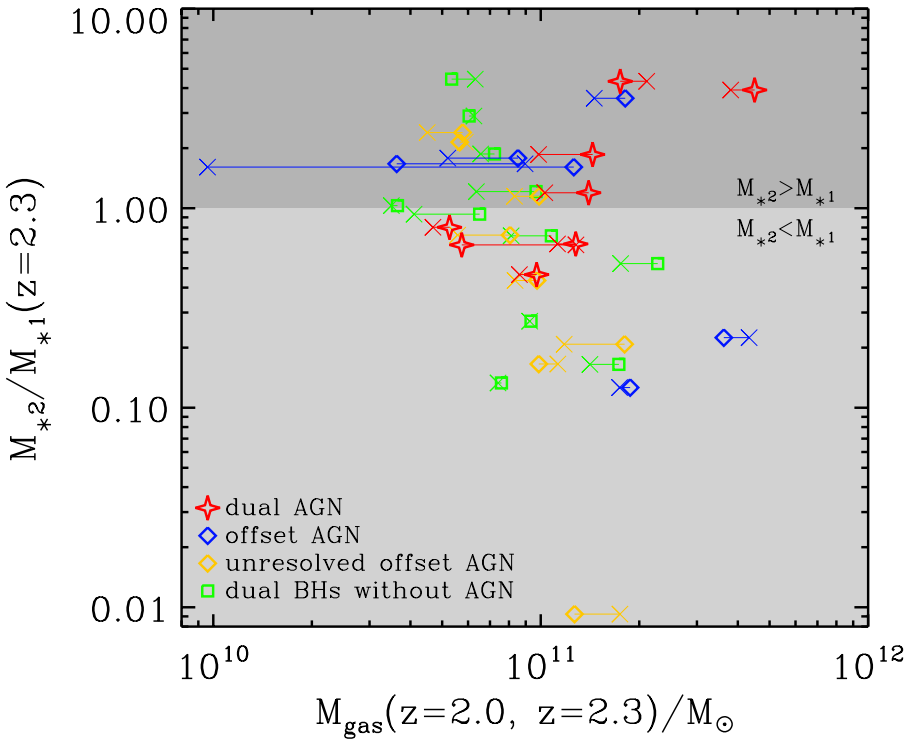

Figure 4.10: The stellar mass ratio of the progenitor galaxies at $z = 2.3$ in comparison with the gas mass of the galaxy hosting the BH pair at $z = 2.0$. In cases where the two BHs are associated with different subhaloes we sum up their gas masses. The coloured crosses show the gas mass at $z = 2.3$, where the lines connect the values at the two different epochs. Like in Fig. 4.6, we do not plot the dual AGN for which we cannot give a reliable estimate of the merger mass ratio.

could cause offset AGN, since some offset AGN reside in systems with intermediate gas masses and similar BH and stellar masses. In these cases, external forces, e.g., related to the environment, might play a role, which could distribute the gas such that one BH is surrounded by more gas than the other one.

Interestingly, one offset AGN has also a relatively high gas mass, but a high mass ratio – the typical regime of most dual AGN. If we take a closer look at this BH pair, we find that the two BHs have a distance of 5.9 kpc with no overlap of the radii used for the calculation of the BH accretion rates. Furthermore, the more luminous BH (the AGN) was seeded during the last 0.5 Gyr and hence the luminosity peak might be an effect of our seeding model. Nevertheless, we find an interesting result when considering the progenitor galaxy of the AGN when looking at the galaxy morphology. As shown by Teklu et al. (2015), a good indicator for the galaxy morphology is the so-called b-value, which describes the position in the $M_* - j_*$-plane, where j_* is the specific angular momentum of the stars. The connection between morphology and the position on the $M_* - j_*$-plane was first noticed by Fall (1983) and was revisited by Romanowsky & Fall (2012), who proposed scaling relations for disks and elliptical galaxies, which would correspond to large and small b-values, respectively. Interestingly, the progenitor galaxy of the AGN has a very low b-value of -5.75, which is the lowest one in our sample and hence, the galaxy is very likely a compact spheroidal galaxy. This comes along with a very low gas mass of $M_{\rm gas} = 2.1 \cdot 10^{10} M_\odot$. The stellar mass of this galaxy is also low with $M_* = 7.2 \cdot 10^9 M_\odot$ and the BH is not yet seeded at $z = 2.3$. The second progenitor galaxy has a larger stellar mass of $M_* = 2.6 \cdot 10^{10} M_\odot$, a larger gas mass of $M_{\rm gas} = 1.2 \cdot 10^{11} M_\odot$ and also a higher b-value of -4.57. We suspect that the gas from this galaxy feeds the BH from the smaller spheroidal galaxy during the merger, whereas its own BH already accreted much gas in the past so that the surrounding gas has already been heated up by AGN feedback.

To summarize, the different outliers described in this subsection indicate that there exist no specific conditions for a BH pair to become a dual AGN pair or an offset AGN. Nonetheless, as expected, both the gas mass and the merger mass ratio are indeed crucial quantities for shaping different types of BH pairs.

4.3.4 Gas accretion history

We investigate the evolution of the gas content feeding the central BHs. Therefore, we trace the gas particles inside the accretion radius of the more luminous BH at $z = 2.0$ back in time to check the origin of these gas particles within the progenitors at $z = 2.3$ and exemplarily visualize their spatial distribution for two dual AGN pairs, two offset AGN and two BH pairs without AGN (see Fig. 4.11). Each panel shows a comoving volume of $(700\mathrm{kpc/h})^3$ at $z = 2.3$. The red cross and the red plus sign show the positions of the more and less luminous BHs (luminosities at $z = 2.0$), respectively. The density of the gas particles is illustrated by the grey shades, while the traced gas particles are indicated by the coloured circles. In other words, all of the gas shown as coloured circles will contribute to the accretion rate of the BH represented as a red plus sign one snapshot later, i.e. at $z = 2.0$. Blue and yellow circles mark gas which is, at $z = 2.3$, associated to the host

galaxy of the more and less luminous BHs (luminosities at $z = 2.0$), respectively[7], whereas green circles are gas particles which are associated to none of the two progenitor galaxies.

The top left panel shows an example of a dual AGN residing in a gas filament along which the two galaxies merge. In this case, gas from both progenitor galaxies, but also gas from the filament, feeds the central BHs and thus triggers nuclear activity, although the larger galaxy contributes more gas than the smaller one. The second example of a dual AGN, on the top right shows a different case, where gas from only one progenitor galaxy triggers both AGN.

For offset AGN we also show two fundamentally different cases. In the first case, almost all of the gas that triggers AGN activity originates from the smaller galaxy (see middle left panel). Alternatively, if the more massive galaxy has a large gas reservoir, the smaller BH may be simply not massive enough to "compete" with the massive one.

The bottom panels show two examples for BH pairs without AGN. In both cases, gas from both the larger galaxy and the in-falling substructure as well as gas from outside the galaxies can contribute to the BH accretion rate. However, no matter how large or small the overall gas reservoir around the BH is, the gas in these inactive BH pairs is typically spread over a larger area, i.e., the gas density is lower. This, together with the typically low BH masses, can explain the rather low BH accretion rates, since – according to the Bondi formalism – BH accretion rates scale with the gas density and the BH mass.

To quantify how strongly dual AGN might be triggered by gas filaments, we divide the traced gas particles into the following three groups: gas which was in progenitor galaxy 1, progenitor galaxy 2 or in none of them at $z = 2.3$. In the latter case, the gas was probably accreted by the galaxies between $z = 2.3$ and $z = 2.0$ either through gas filaments, the infall of gas clumps or additional minor mergers. Fig. 4.12 shows the distribution of the gas masses belonging to one of these three groups with respect to the total mass of all gas particles which contribute to the BH accretion. We show these distributions for dual AGN (red solid histogram), offset AGN (blue dashed histogram), unresolved offset AGN (yellow dashed histogram) and BH pairs without AGN (green dotted histogram), where we consider only the more luminous BH in a pair. The small vertical lines in the top indicate the mean values of each distribution. For dual AGN the contribution of gas, which was never residing in any of the two progenitor galaxies, is clearly enhanced compared to offset AGN and inactive BH pairs (see lowest panel of Fig. 4.12). This indicates that dual AGN indeed accrete more gas from filaments than the other, less active BH pairs. Between the other three classes we see no clear differences. Nonetheless, the contribution of gas from none of the two progenitor galaxies is for almost all BH pairs at least 50%.

In Fig. 4.13, we compare the contribution of the two galaxies to the calculation of the BH accretion with each other. Like in Fig. 4.12, it shows that for dual AGN in general less internal gas from the galaxies contributes to the BH accretion than for offset AGN. In most cases, this internal gas originates from both progenitor galaxies. In contrast, for the offset AGN mostly one of the two progenitor galaxies contributes much more gas to

[7]Note that if the blue or yellow gas particles correspond to the main subhalo, it can occur that they surround substructures.

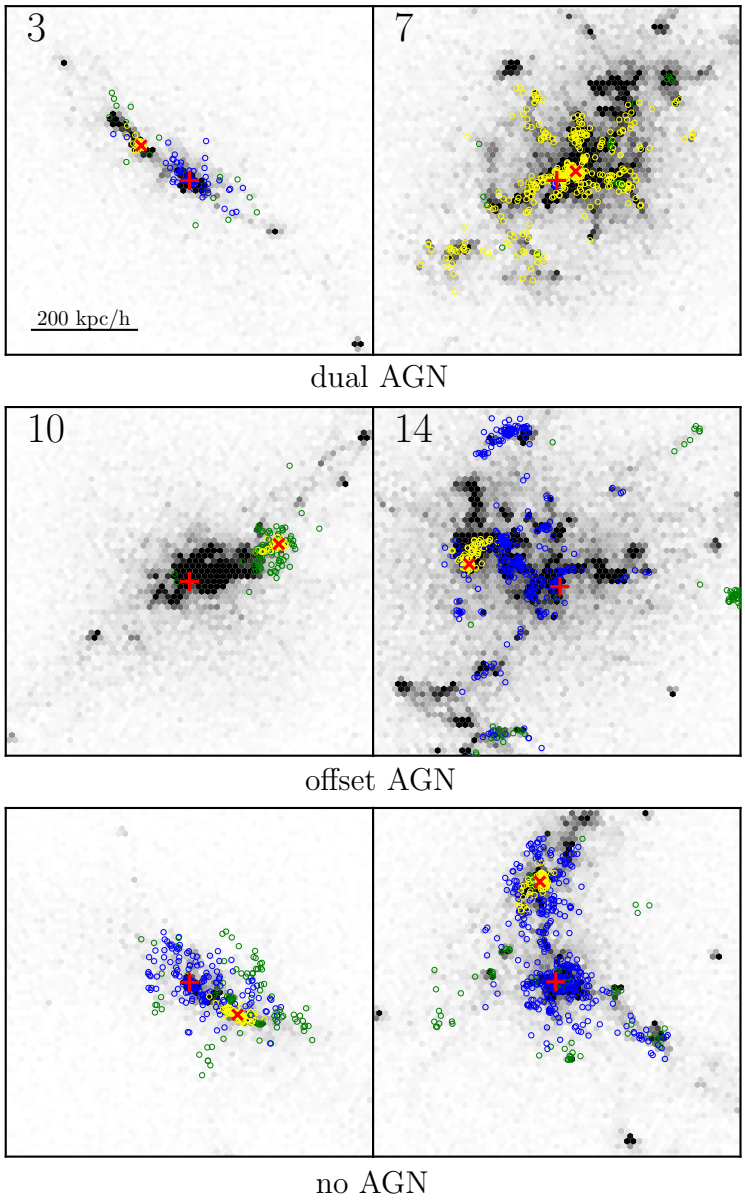

Figure 4.11: The figure shows the progenitor galaxies of two dual AGN pairs, two offset AGN and two BH pairs without AGN at $z = 2.3$, where the IDs are the same as in Table 4.1, Table 4.2 and Fig. 5.1. The grey shades visualize the overall gas distribution and the coloured circles show where the gas which is accounted for the estimation of the BH accretion rate of the more luminous BH at $z = 2$ was located one snapshot earlier, i.e. at $z = 2.3$. In that way, we can see where the gas which feeds the more luminous BH comes from. Blue and yellow circles indicate gas from the progenitor galaxy of the more and less luminous BH, respectively, whereas green circles represent gas which was associated to none of the two galaxies. In every panel, the red plus sign marks the more luminous BH of the pair and the red 'x' sign the less luminous one.

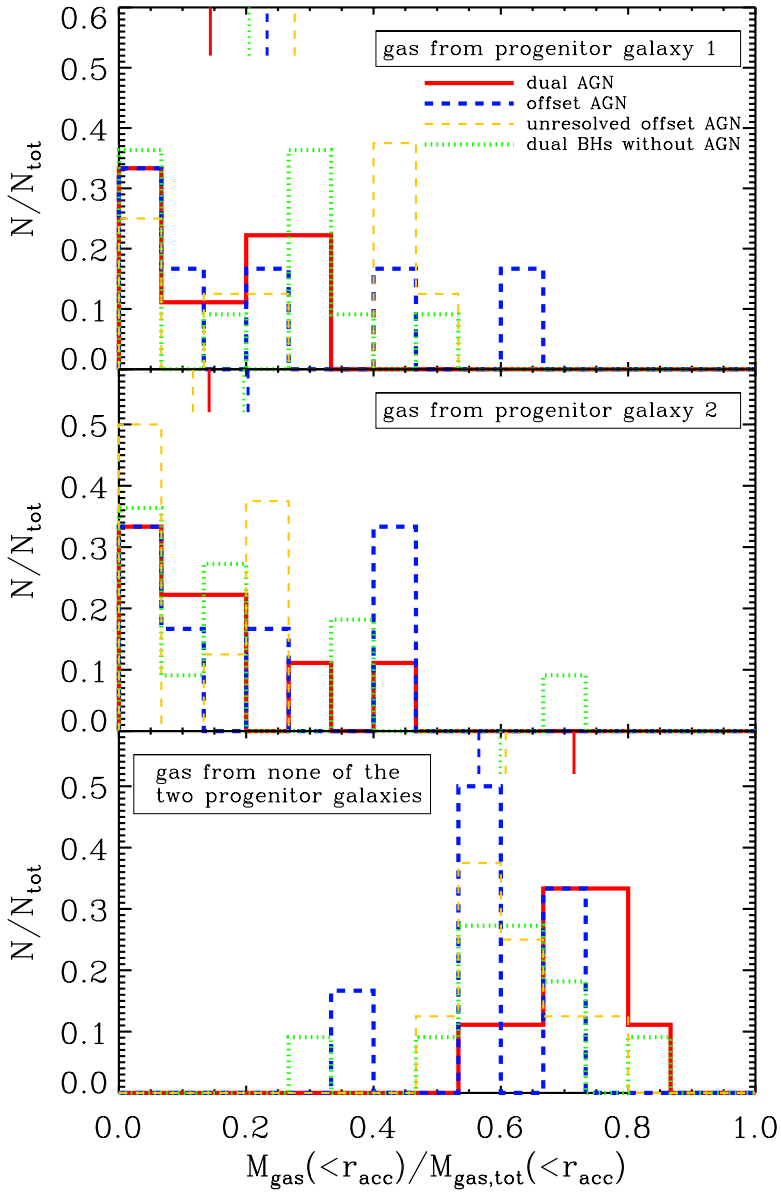

Figure 4.12: For this figure we traced back all gas particles inside the accretion radius at $z = 2.0$ and checked whether they have been in galaxy 1 (progenitor galaxy of the more luminous BH), galaxy 2 (progenitor galaxy of the less luminous BH) or in none of them at $z = 2.3$. The upper panel shows the gas mass from galaxy 1, the middle panel the gas mass from galaxy 2 and the bottom panel shows the gas mass which was hosted by neither of the two progenitor galaxies with respect to the total mass of the traced gas, respectively. The small vertical lines at the top indicate the mean values of each distribution.

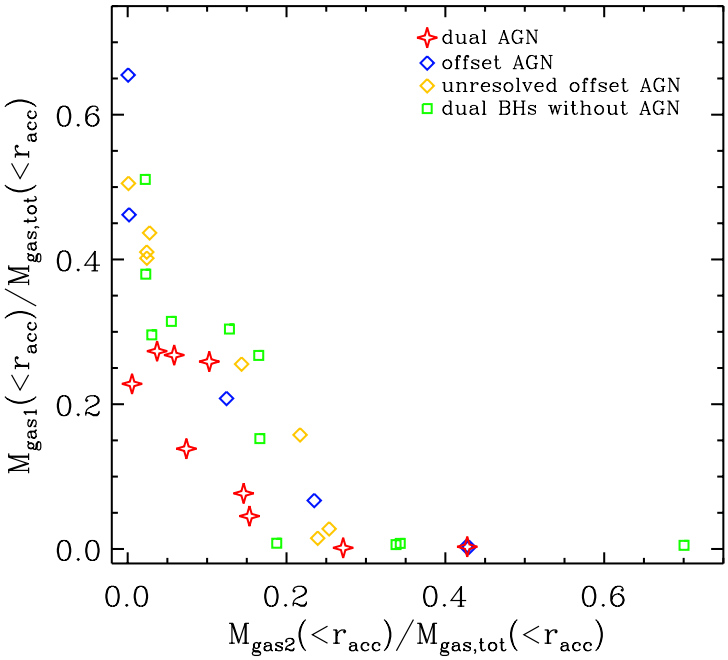

Figure 4.13: Comparison of the fraction of gas mass with respect to the total gas mass inside the accretion radius at $z = 2.0$ which comes from galaxy 1 and galaxy 2.

the BH accretion than the other one. This can be the progenitor galaxy of either the less luminous BH or the more luminous one. In the specific case of unresolved offset AGN, the progenitor galaxy of the more luminous BH is in most cases the main contributor.

4.4 Comparison with other theoretical studies

Finally, we would like to put our work in a larger context and compare our results with other theoretical studies, i.e. Yu et al. (2011), Van Wassenhove et al. (2012) and Blecha et al. (2013), which use either phenomenological models or isolated merger simulations. However, these methods are different from our ansatz of using cosmological simulations. Yu et al. (2011), for example, construct a phenomenological model for AGN pairs up to $z = 1.2$, i.e. they do not make a prediction for $z = 2$. They find that the fraction of dual AGN with respect to the total amount of AGN decreases significantly with increasing redshift up to $z = 0.5$. Above that redshift, the dual AGN fraction seems to saturate, i.e. it does not change significantly in the range $0.5 < z < 1.2$. With our simulation we can check whether this saturation holds for higher redshifts up to $z = 2$. The luminosity threshold from Yu et al. (2011), above which a BH is defined as an AGN, is $L_{[OIII]} > 10^{7.5} L_{\odot}$, which roughly corresponds to $L_{bol} > 10^{44.6}$erg/s assuming $L_{bol}/L_{[OIII]} \approx 3500$ (Heckman et al., 2004). Above this threshold they predict a dual AGN fraction of about 0.02%-0.06% for $0.5 < z < 1.2$. Our sample contains only one dual AGN above that luminosity threshold

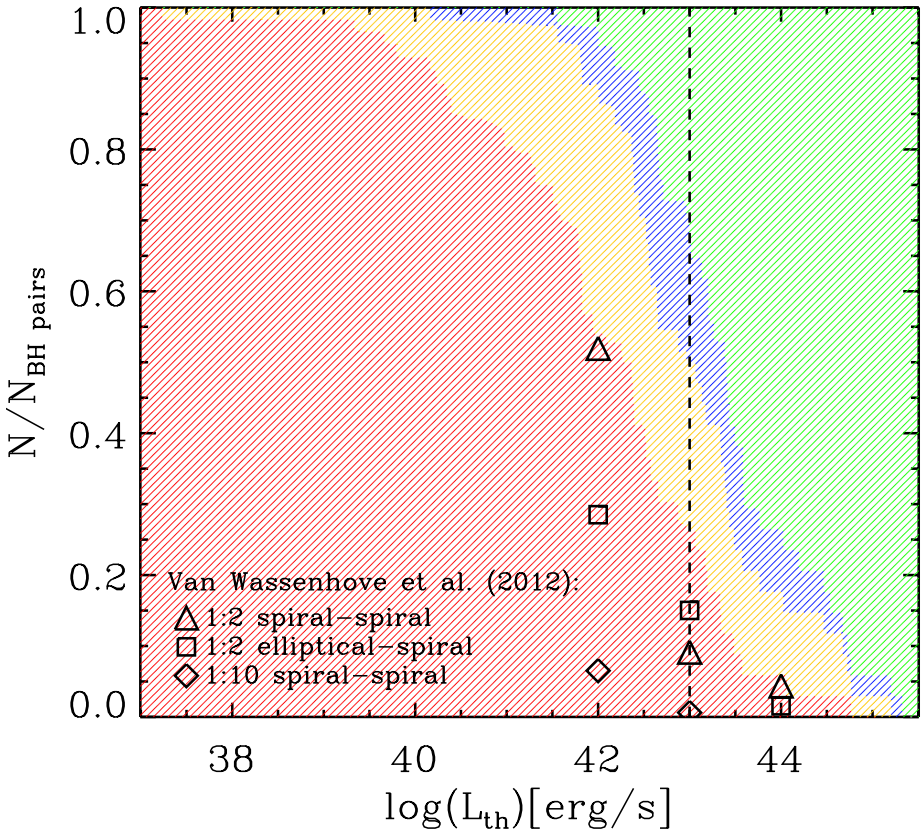

Figure 4.14: The coloured areas indicate the fraction of simulated dual AGN (red), offset AGN (blue), unresolved offset AGN (yellow) and BH pairs without AGN (green) with respect to the total number of BH pairs, if we choose different luminosity thresholds $L_{\rm th}$ for our definition of AGN. The black dashed line marks the threshold we choose for the analysis in this paper, i.e 10^{43}erg/s. The black symbols show the results from Van Wassenhove et al. (2012) for separations $d >$ 1kpc with respect to the total amount of dual AGN and offset AGN only.

corresponding to $\sim 0.05\%$, being in agreement with Yu et al. (2011). Hence we indeed find that the saturation holds for larger redshifts. But we caution the reader since this value is based on only one dual AGN pair.

Van Wassenhove et al. (2012) performed three high resolution simulations of isolated galaxy mergers: (i) a 1:2 merger between two spiral galaxies, (ii) a 1:2 merger between an elliptical galaxy and a spiral galaxy and (iii) a 1:10 merger between two spiral galaxies. The two major mergers are supposed to occur roughly around $z = 2$, while the minor merger occurs around 1 Gyr later. However, while we can make predictions of the actual number of dual AGN at a given time, Van Wassenhove et al. (2012) can make predictions about the dual AGN fraction only in a temporal manner, i.e. they predict how long a BH pair is a dual AGN. Thus, their predictions always refer only to one specific galaxy merger.

In agreement with our results, Van Wassenhove et al. (2012) find that the gas content

and the merger mass ratio play an important role in triggering dual AGN activity. In their simulations, the fraction of dual AGN activity also increases with decreasing separation between the two BHs, which is consistent with our analysis (see Fig. 4.3).

In addition, Van Wassenhove et al. (2012) provide estimates for the dual AGN fraction with respect to the total time a BH pair spends as either dual or offset AGN for different luminosity thresholds. In Fig. 4.14, we show the contribution of the different types of our simulated BH pairs with respect to the total number of BH pairs, depending on the luminosity threshold $L_{\rm th}$, where the shaded areas illustrate the contribution of dual AGN (red), offset AGN (blue), unresolved offset AGN (yellow), and BH pairs without AGN (green). Our choice for the analysis in this work, i.e., $L_{\rm th} = 10^{43}$erg/s, is marked by the black dashed line. At that threshold, the contribution of the different types of BH pairs is similar. The different black symbols show the results of the three simulations from Van Wassenhove et al. (2012) for separations larger than 1kpc (1kpc higher resolution than ours). Since this is slightly below our resolution limit, we expect that their dual AGN fraction might be even lower if they also chose a limit of 2kpc. Furthermore, they do not have an upper limit for the BH separations, which should mainly affect the values at $L_{\rm th} = 10^{42}$erg/s, since they find that most AGN activity occurs at small separations, in particular above $L_{\rm th} = 10^{43}$erg/s. Nevertheless, we see a similar increase of the dual AGN fraction with decreasing luminosity threshold like for the 1:2 spiral-spiral merger from Van Wassenhove et al. (2012). In contrast to the major mergers, the number of BH pairs in minor mergers is smaller than our prediction and regarding the elliptical-spiral merger, the number of BH pairs is also smaller – except for $L_{\rm th} = 10^{43}$erg/s – than our estimate. We suspect that their estimates are in general lower than our predictions, because their spiral galaxies have a much lower gas fraction of $f_{\rm g} = 0.3$ than spiral galaxies in the Magneticum Simulations at $z = 2$, where $f_{\rm g} \sim 0.6-0.8$ (Teklu et al., 2015). In addition, the environment in simulations of isolated galaxy mergers is different to that in cosmological simulations, because there is a finite gas supply, whereas galaxies in cosmological simulations can continuously accrete new gas as long as the hot halo does not shut off the gas supply. We conclude that dual AGN activity is indeed mainly triggered by gas-rich major mergers. Furthermore, we want to emphasize that we are in very good agreement with the results from Van Wassenhove et al. (2012) at $L_{\rm th} = 10^{45}$erg/s, where the effect of the maximum separation should not affect our results.

Finally, our results agree with those of Blecha et al. (2013), who present hydrodynamic simulations of major mergers with different merger mass ratios and gas fractions. They also find that the dual AGN activity increases with both the merger mass ratio and the gas fraction, although the effect of the mass ratio is not entirely clear, probably due to the fact that they only consider major mergers. Furthermore, like Van Wassenhove et al. (2012), they find that the AGN activity is larger in the late phase of a merger, i.e. when the separations between the two BHs are small, which is also in agreement with our results.

4.5 Conclusion

In this study we explore the properties and the origin of dual and offset AGN, as well as BH pairs without AGN, taking advantage of a cosmological simulation covering $(182\text{Mpc})^3$, taken from the set of Magneticum Pathfinder Simulations. The simulation includes an improved treatment of super-massive BHs and ran down to redshift $z = 2$. It predicts an evolution of the AGN luminosity function which is consistent with observations. The novel treatment of the black holes in the simulation offers a unique testbed to study the properties and evolution of BH pairs. At $z = 2$, the simulation contains 34 BH pairs with a comoving separation smaller than 10kpc. Nine of them are pairs of dual AGN, 6 are offset AGN and 8 are unresolved offset AGN, where the mass of the smaller counterpart is not resolved. However, the remaining 11 BH pairs show no actual AGN activity. In the simulation, all BH pairs originate from galaxy mergers independent of whether there is an AGN or not, which implies that merger activity by itself is not always sufficient to trigger AGN activity. To investigate the mechanisms which trigger the AGN activity in detail, we traced the BHs, their progenitor galaxies and the gas which contributes to the calculation of the accretion rate back in time. Our main results are the following:

- Almost all BHs in pairs lie below the observed $M_\bullet$-M_* relation. Whilst the most massive BHs appear typically as AGN, less massive ones can be both, either active or non-active.

- We find that the merger mass ratio, the gas mass and the gas accretion history are important factors in triggering dual AGN activity.

- Dual AGN activity dominates for small spatial separations between the two BHs, whereas inactive BH pairs tend to have larger separations.

- In dual AGN pairs, the less massive progenitor galaxy always hosts the BH which later on has the higher Eddington ratio.

- Dual AGN have similar BH masses and grow together, i.e., the Eddington ratio of both BHs in a pair increases during the merger.

- At $z = 2.0$, the gas which triggers dual and offset AGN consists mainly of freshly accreted gas, which encounters the progenitor galaxies during or right before the merger, probably through gas filaments or through accretion of smaller substructures. The contribution of this accretion to the BH accretion is on average clearly larger for dual AGN than for BH pairs with only one or no AGN.

- In most cases, one of the two progenitor galaxies contributes much more gas to the BH accretion than the other galaxy, especially for offset AGN. This can be either the progenitor galaxy of the more luminous or the less luminous BH.

- Offset AGN can exist in galaxies with relatively low gas masses, if the BH masses are so small that the gas reservoir is still large enough that at least one BH can accrete with a high Eddington ratio, i.e., in the radiatively efficient regime.

- Offset AGN can also be the consequence of a merger of a larger with a smaller galaxy, where the large BH accretes and heats up so much gas that it either uses up or evaporates the cold gas reservoir of the smaller BH. The same effect can be seen in BH pairs without AGN, with the difference that there is even too little gas to accrete for the more massive BH for being classified as an AGN.

This study is based on a state-of-the-art large-scale cosmological simulation for which for the first time not only the resolution is high enough to resolve galaxies, but also the volume is large enough to capture the generally rare events of dual AGN. With our sample of BH pairs we can explain fundamental differences between dual AGN, offset AGN and inactive BH pairs. However, due to the limited computational power we can only study the triggering mechanisms down to $z = 2.0$, where galaxy properties like the gas fraction are significantly different from observed dual and offset AGN at low redshifts. We expect that this does not qualitatively influence our results regarding the differences between dual and offset AGN, but with decreasing redshift quantitative results are very likely to change. We expect, for example, that the contribution of smooth gas accretion might be less important for driving nuclear activity at lower redshifts. Since we find such a process to be essential for producing dual AGN, we may speculate that in the local Universe a smaller amount of dual AGN may exist with respect to that of offset AGN.

In future work we plan to extend this study by investigating AGN trigger mechanisms and the relative role of internal and external processes in global BH populations, and not only for BH pairs. This may shed further light on the still heavily debated question to what extent merger events are responsible (and needed) for driving nuclear activity.

Appendix A: Intersection between accretion radii

Fig. 4.15 and 4.16 demonstrate that our analysis is not driven by numerical effects due to our BH model. $V_{\rm intersect}$ is the volume inside the accretion radius which intersects between the two BHs, and $V_{\rm tot} = V_1 + V_2 - V_{\rm intersect}$ is the total volume. Since both dual and offset AGN spread over the whole range of $V_{\rm intersect}/V_{\rm tot}$ we can rule out that the two different classes are a numerical effect due to our choice of the accretion radius. There is one trend visible, namely that most dual AGN do not intersect at all. Many pairs without AGN have a very low gas temperature, because the BH has just been seeded and the galaxy is not very evolved yet. Of course this can be an effect of the seeding model. The few offset AGN with high gas temperatures seem indeed to be triggered by AGN feedback, whereas for the others feedback does not play an important role. The BH masses of the one dual AGN with an extremely high gas temperature are very similar such that none of the two BHs dominates over the other one.

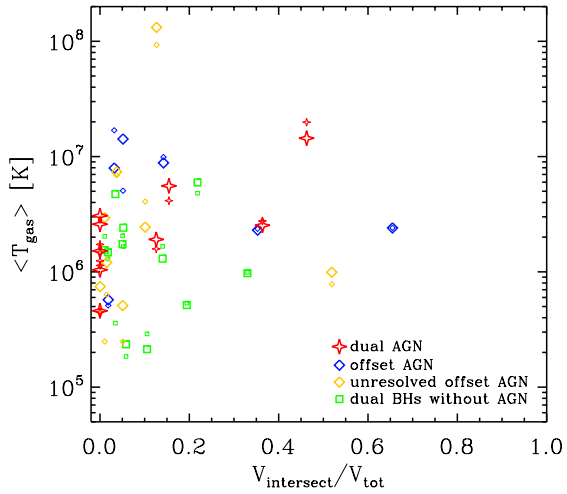

Figure 4.15: Fraction of the intersection of the volumes used to calculate the accretion rate at $z = 2$ with respect to the total volume compared with the mean gas temperature inside the accretion radius of each BH, also at $z = 2$.

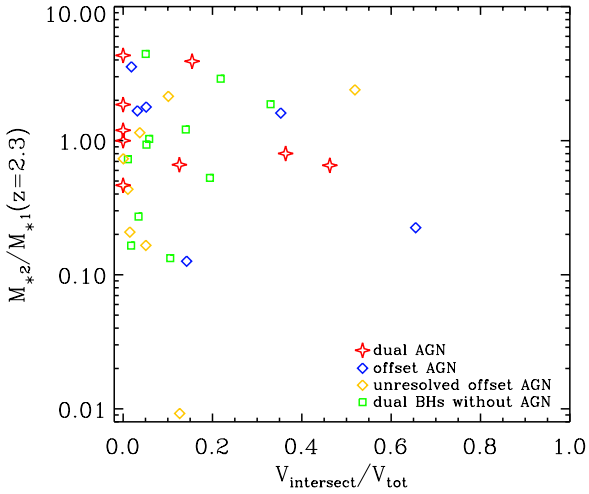

Figure 4.16: Fraction of the intersection of the volumes used to calculate the accretion rate at $z = 2$ with respect to the total volume compared with the stellar mass ratio, where M_{*1} and M_{*2} are the stellar masses at $z = 2.3$ and correspond to the more and less luminous BH at $z = 2.0$, respectively.

Appendix B: Environment

In Fig. 4.17 and Fig. 4.18 we show two different measures of the environment against the total the dark matter halo: i) the distance to the 4th nearest galaxy and ii) the number of galaxies within a radius[8] of 8Mpc/h (e.g. Haas et al. 2012, Muldrew et al. 2012 and references therein). For both approaches we choose a mass threshold of $M_* > 10^{10} M_\odot$ for the neighbouring galaxies (Baldry et al., 2006). Especially in Fig. 4.18 it is visible that both dual and offset AGN prefer a dense environment, although BH pairs without AGN can as well have many neighbouring galaxies. The two figures also show that all simulated BH pairs in haloes with $M_{\rm halo} > 4 \cdot 10^{12} M_\odot$ contain at least one AGN. Hence, looking for a dense environment might help to find dual and offset AGN, although we also produce them in less denser environments.

Furthermore, the two figures show clearly that our simulation produces offset AGN only in haloes above $M_{\rm halo} \approx 2 \cdot 10^{12} M_\odot$. Below that threshold there are only unresolved offset AGN. In contrast, dual AGN scatter over the whole range of halo masses. This might be a consequence of our findings that dual AGN often reside in major mergers, whereas differences in the BH and stellar mass can cause offset AGN. Thus, in low mass haloes offset AGN need, in contrast to dual AGN, an even less massive counterpart and hence

[8] We tested several radii and it turned out that using 8 Mpc/h it is best visible that both dual AGN prefer a denser environment.

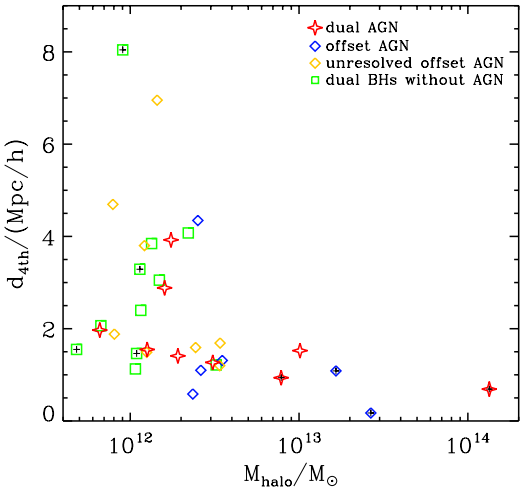

Figure 4.17: Distance to the forth nearest neighbour galaxy with $M_* > 10^{10} M_\odot$. The black crosses mark mergers between two substructures, i.e., they do not occur in the central galaxy.

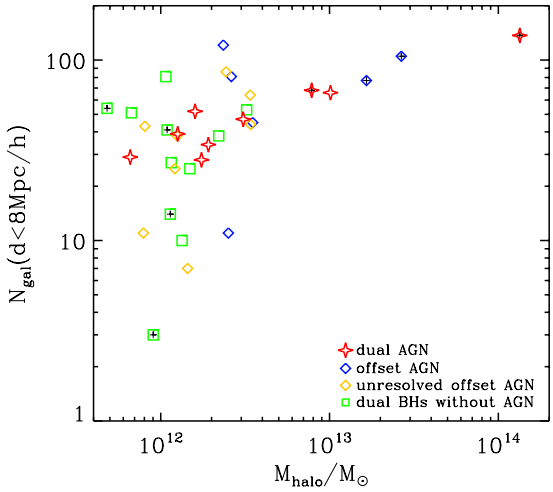

Figure 4.18: Number of neighbour galaxies within a radius of 8Mpc/h which are larger than $10^{10} M_\odot$. The black crosses mark mergers between two substructures, i.e. they do not occur in the central galaxy.

the smaller BH mass is not resolved. Considering this resolution effect, we do not see a different environment for dual and offset AGN. However, the approaches used to measure the environment are both spherically symmetric and thus large-scale filaments are not captured by this method. Hence, it turned out that measuring the gas accretion history like in Fig. 4.12 is more useful to investigate AGN triggering mechanisms.

In Fig. 4.17 and Fig. 4.18 we also mark mergers between two substructures with black crosses, in contrast to mergers involving the central galaxy. Although our sample contain only a few groups and only one cluster at $z = 2.0$, it is a remarkable result that most of the mergers in these massive haloes occur between two substructures. This might indicate that, at least at such a high redshift, the central galaxy does not yet play such a dominant role as known from the local Universe.

Chapter 5

How (in)significant are merger events for fuelling nuclear activity?

The content of this chapter has been published in Steinborn et al. (2018) and submitted to a peer reviewed journal:

> **Lisa K. Steinborn**, Michaela Hirschmann, Klaus Dolag, Francesco Shankar, Stéphanie Juneau, Mirko Krumpe, Rhea-Silvia Remus, Adelheid F. Teklu: *Cosmological simulations of black hole growth II: how (in)significant are merger events for fuelling nuclear activity?*, 2018, ArXiv: 1805.06902

Abstract

Which mechanism(s) are mainly driving nuclear activity in the centres of galaxies is a major unsettled question. In this study, we investigate the statistical relevance of galaxy mergers for fuelling gas onto the central few kpc of a galaxy, potentially resulting in an active galactic nucleus (AGN). To robustly address that, we employ large-scale cosmological hydrodynamic simulations from the Magneticum Pathfinder set, adopting state-of-the-art models for BH accretion and AGN feedback. Our simulations predict that for luminous AGN ($L_{\rm AGN} > 10^{45}$ erg/s) at $z = 2$, more than 50 per cent of their host galaxies have experienced a merger in the last 0.5 Gyr. These high merger fractions, however, merely reflect the intrinsically high merger rates of massive galaxies at $z = 2$, in which luminous AGN preferentially occur. Apart from that, our simulation predictions disprove that merger events are the statistically dominant fuelling mechanism for nuclear activity over a redshift range $z = 0 - 2$: irrespective of AGN luminosity, less than 20 per cent of AGN hosts have undergone a recent merger, in agreement with a number of observational studies. The central ISM conditions required for inducing AGN activity can be, but are not necessarily caused by a merger. Despite the statistically minor relevance of mergers, at a given AGN luminosity and stellar mass, the merger rates of AGN hosts can be by up to three times higher than that of inactive galaxies. Such elevated merger rates still point towards an

intrinsic connection between AGN activity and mergers, consistent with our traditional expectation.

5.1 Simulations

5.1.1 Simulation set

In the course of this section, we analyse the following two cosmological simulations from the Magneticum simulation set:

- **68Mpc/uhr:** This simulation has a volume of $(68\text{Mpc})^3$ combined with a comparably high resolution, with dark matter and gas particles masses of $M_{\text{dm}} = 3.7{\cdot}10^7 M_\odot/h$ and $M_{\text{gas}} = 7.3 \cdot 10^6 M_\odot/h$, respectively. This resolution is high enough to largely capture the internal structure and morphology of galaxies (Teklu et al., 2015, 2017). Note that BH accretion rates in the intrinsic, code-based time resolution are stored only at $z \geq 1.5$, allowing us to study detailed BH light curves down to that redshift (Fig. 5.2).

- **500Mpc/hr:** The second simulation considered in this work comprises a large volume of $(500\text{Mpc})^3$ with a resolution of $M_{\text{dm}} = 6.9{\cdot}10^8 M_\odot/h$ and $M_{\text{gas}} = 1.4{\cdot}10^8 M_\odot/h$, enabling us to study the evolution of a large AGN population, including very massive and very luminous AGN (Hirschmann et al., 2014). This simulation run is publicly available via our web interface (see Ragagnin et al., 2017).

The two simulations are performed with the same settings in terms of physical processes and cosmology, but cover different mass ranges due to different box sizes and resolutions. The 68Mpc/uhr simulation is solely used to study individual AGN light curves of five test cases (Section 5.2.1). In the remainder of the paper, we show the results for the 500Mpc/hr simulation due to its better statistics. For this simulation run we consider only galaxies above a certain resolution threshold of $M_* > 10^{11} M_\odot$ (corresponding to a particle number of roughly 2800 particles)[1]. We have explicitly verified that the results qualitatively[2] converge towards higher resolution.

5.1.2 Halo identification and merger tree construction

The simulation predictions are output in 145 snapshots with equal time intervals between the snapshots[3]. For each snapshot, haloes and subhaloes are identified using the friends-of-friends algorithm (FOF, Davis et al., 1985) assuming a linking length of 0.16 in combination with SUBFIND (Dolag et al. 2009, Springel et al. 2001).

[1] Since we trace the galaxies back in time, the progenitor galaxies can have much smaller masses, especially the less massive galaxies in minor mergers. Therefore, the resolution limit is chosen to be fairly conservative.

[2] Note that a direct comparison between the two simulations is not possible due to the different mass ranges.

[3] For redshifts $z > 1$ the simulation output has larger time intervals than for $z < 1$.

We continue to connect haloes and subhaloes over time, i.e. we construct merger trees using the L-HaloTree algorithm, which is described in the supplementary information of Springel et al. (2005). In short, to determine the appropriate descendant, the unique IDs that label each particle are tracked between outputs. For a given halo, the algorithm finds all haloes in the subsequent output that contain some of its particles. These are then counted in a weighted fashion, giving higher weight to particles that are more tightly bound in the halo under consideration. The weight of each particle is given by $(1+j)^{-\alpha}$, where j is the rank, based on its binding energy, as returned by SUBFIND, and α is typically set to 2/3. This way, preference is given to tracking the fate of the inner parts of a structure, which may survive for a long time upon in-fall into a bigger halo, even though much of the mass in the outer parts can be quickly stripped. Once these weighted counts are determined for each potential descendant, the one with the highest count is selected as the descendant. Additionally, the number of progenitors is calculated for each possible descendant. L-HaloTree is constructing descendants (and its associated progenitors) for $A \rightarrow B$ as well as $A \rightarrow C$. Therefore, as an additional refinement, some haloes are allowed to skip one snapshot B in finding a descendant, if either there is a descendant found in C but none found in B, or, if the descendant in B has several progenitors and the descendant in C has only one. This deals with cases where the algorithm would otherwise lose track of a structure that temporarily fluctuates below the detection threshold.

In this approach, two galaxies are defined to have merged, as soon as they are identified as only one galaxy by SUBFIND, i.e. as soon as they are gravitationally bound to each other. For the following analysis, we connect an AGN with a merger signature of its host galaxy, if a merger happened up to 0.5 Gyr before the time step the AGN luminosity is computed. The time interval of maximum 0.5 Gyr is motivated by our case studies in Section 5.2.1 showing that mergers have hardly any effect onto the AGN activity after 0.5 Gyr. This is supported by previous simulations of isolated galaxy mergers (e.g. Hopkins et al., 2008; Johansson et al., 2009), also finding no significant effect on the AGN activity more than 0.5 Gyr after the merger event. It is also unlikely that merger signatures would be visible/detectable in observations after such a time period. But note that we explicitly tested larger time intervals up to 1.5 Gyr, without finding any qualitative difference in our results.

Throughout this analysis, once merger events have been identified, we divide our galaxies and AGN hosts into three different "merger" classes, depending on the stellar merger mass-ratio M_{*2}/M_{*1} (M_{*1} and M_{*2} are the stellar masses of the more and less massive progenitor galaxy, respectively):

- **no mergers**, including very minor mergers with $M_{*2}/M_{*1} < 1:10$,
- **at least one minor merger:** $1:10 < M_{*2}/M_{*1} < 1:4$ (but no major mergers)
- **at least one major merger:** $M_{*2}/M_{*1} > 1:4$ (eventually additional minor mergers).

Note that, if a galaxy/AGN host has experienced both major and minor mergers during

the last 0.5 Gyr, it is added to the major merger class (due to the common believe that major mergers are more significant for nuclear activity than minor mergers).

Such a division into different merger classes is further complicated by defining/deriving mass-ratios for merger events, potentially affected by artificial false estimations of the stellar merger mass-ratios, as a consequence of the SUBFIND algorithm. In fact, the physically most meaningful estimation of the merger mass-ratio is not necessarily made at the time when the merger is identified by SUBFIND, since at that time in-falling galaxies can have already suffered from tidal stripping and other environmental effects (distracting the intrinsic mass-ratio). In order to circumvent such problems, we consider the *maximum* stellar mass-ratio between two merging galaxies during the past 1.5 Gyr. In the appendix, we describe our merger identification algorithm and the estimation of the stellar merger mass-ratio in more detail.

5.2 Relation between merger events and nuclear activity

In this section, we investigate to what degree nuclear activity of a galaxy is related to its recent merger history. We remind the reader that due to limited resolution in state-of-the-art large-scale cosmological simulations (including the Magneticum simulations considered here), BH accretion is governed by ISM properties (density, temperature and relative velocity) in the central few kiloparsec of a galaxy, following the Bondi-Hoyle approach (equation 3.1). Thus, by construction, we are only able to examine *the impact of merger events on fuelling the gas onto the central few kpc, and on the correspondingly estimated nuclear activity.*

We first consider five representative test cases of AGN galaxies above $z = 2$ from the 68Mpc/uhr simulation, individually discussing their AGN light curves with respect to the underlying merger history (subsection 5.2.1). Turning to the full AGN population, as predicted by the 500Mpc/hr simulation run (subsection 5.2.2), we analyse the statistical incidence for nuclear activity in galaxies as a function of their merger history and the AGN luminosity. We further quantify the maximum probability for AGN to be potentially fuelled by mergers by computing the merger fractions of AGN host galaxies, confronting them with observational estimates. Note that throughout this study, bolometric AGN luminosities are calculated from the BH accretion rates following Hirschmann et al. (2014).

5.2.1 Five case studies

The evolutionary sequence of AGN hosts at $z = 2$

We start with investigating the AGN-merger connection by selecting five different example AGN hosts at $z = 2$, having experienced a major or minor merger event in the past 1 Gyr, i.e. between $z = 2.0$ and $z = 2.8$. Fig. 5.1 visualises the gaseous and stellar distributions

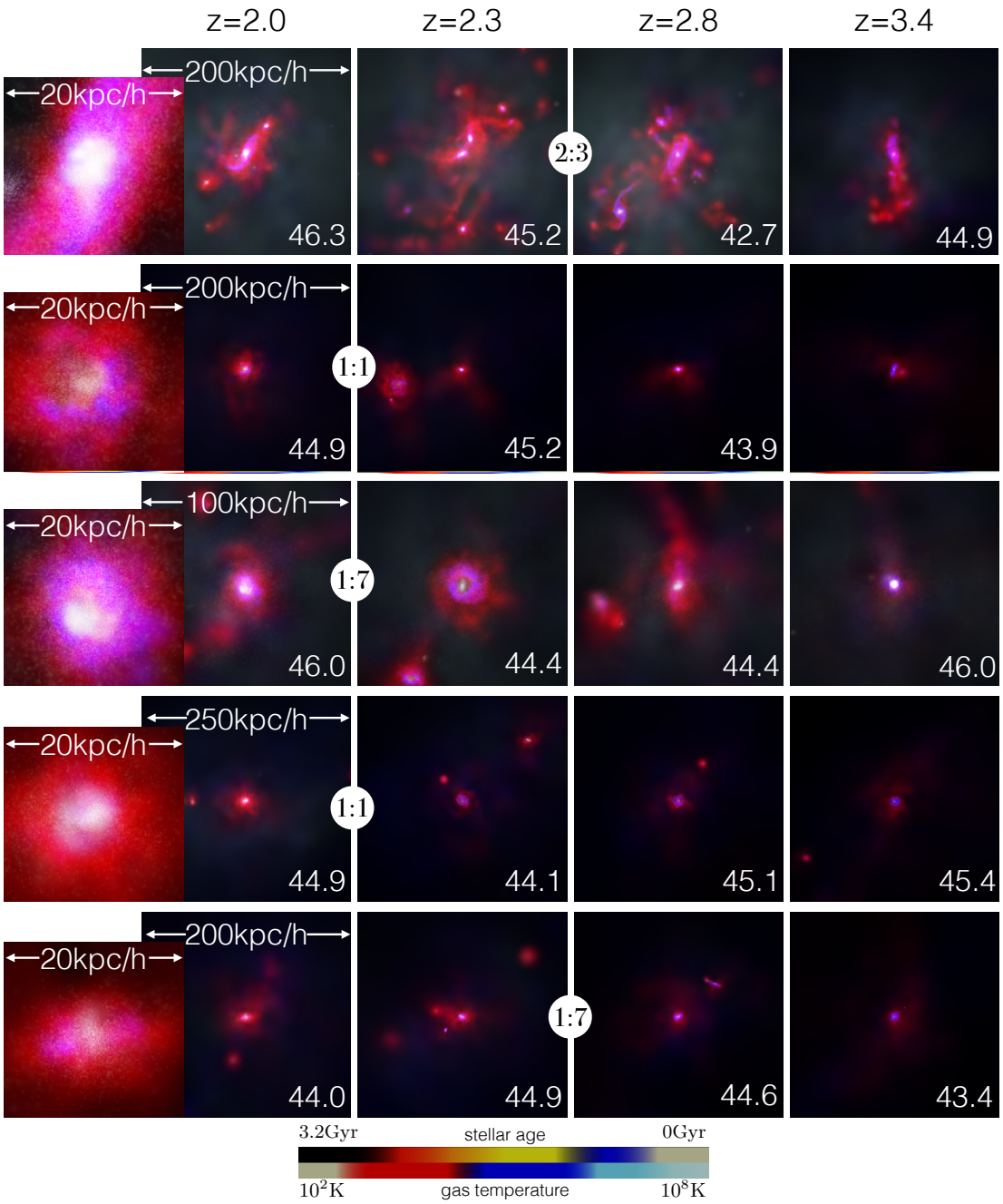

Figure 5.1: The different columns visualize the gaseous and stellar component (colour-coded by the gas temperature and the stellar age, respectively, as indicated by the colour-bar) of five different merging galaxies (different rows) in the 68Mpc/uhr simulation at $z = 2.0$ (left-hand panels), and their progenitors 0.5 Gyr, 1.0 Gyr, and 1.5 Gyr before $z = 2$ (columns towards the right-hand side). When the galaxies host a SMBH, its luminosity ($\log(L)$ in [erg/s]) is specified in the bottom right of each panel. The white circles and their numbers indicate the stellar merger mass ratio and their positions correspond to the time at which the merger mass ratio has been determined.

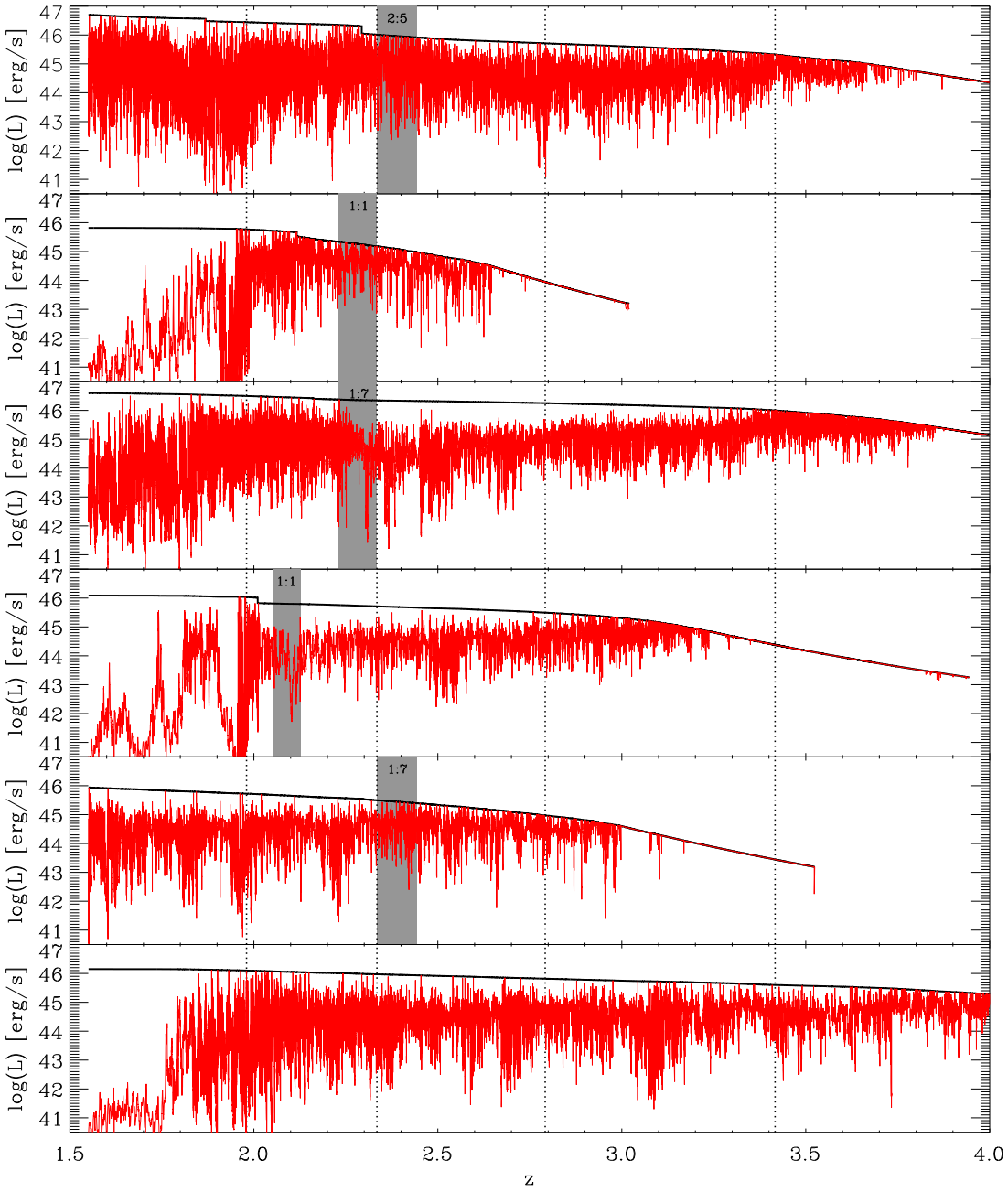

Figure 5.2: Red lines show the light curves for the examples shown in Fig. 5.1 (row 1-5, same order) as well as for one additional example without a recent merger (bottom row). The black solid lines show the Eddington luminosity, i.e. the maximum luminosity allowed in the simulation. Black dotted lines indicate the snapshots taken from the simulation. The grey shaded areas show the redshift range within which the merger has been identified. The corresponding merger mass ratio is given in the top of these areas.

(colour-coded as indicated by the colour bar)[4] of the five example galaxies at $z = 2$ (first and second columns) and that of their progenitors at $z = 2.3$, $z = 2.8$, and $z = 3.4$ (third, fourth and fifth column, respectively). The stellar merger mass-ratios (M_{*2}/M_{*1}) are shown by the white circles, whose positions indicate at which time the merger mass-ratio has been computed. In all cases, merger signatures such as tidal tails are still visible at $z = 2$. The AGN luminosities ($\log(L_{\rm bol})$ in [erg/s]) are specified in the bottom right of each panel[5]. In four out of five examples the luminosity increases during the merger, for some AGN, however, only marginally.

The first row in Fig. 5.1 shows two gas-rich spiral-like galaxies, which merge between $z = 2.8$ and $z = 2.3$. Between these redshifts, the AGN luminosity increases by 2.5 dex. In the second row, a 1:1 merger is identified between $z = 2.3$ and $z = 2.0$, but the AGN luminosity slightly decreases. The third row illustrates a minor merger of two gas-rich galaxies. Although the merger mass-ratio is much smaller than in the first example, the AGN luminosity increases significantly, from $\log(L_{bol}) = 44$ erg/s to 46 erg/s. The last two examples show the evolutionary sequence of two moderately luminous AGN whose host galaxies have experienced a major (fourth row) and a minor (fifth row) merger. In both cases, the luminosity is hardly changing during the merger. Thus, the five examples shown in Fig. 5.1 suggest that merger events *may*, but do not *necessarily* boost the accretion onto BHs.

AGN light curves

For a deeper understanding of the inconclusive AGN-merger connection seen so far, Fig. 5.2 explicitly illustrates the AGN light curves of our five example galaxies from $z = 4$ down to $z = 1.5$ as well as, for reference, of one example AGN without a recent merger (bottom row). Note that, while the simulation code stores BH accretion rates also between two snapshots, i.e. for very small time steps of ~ 0.1Myr, the host galaxy properties are only accessible at the time of the snapshots (i.e. with larger time steps). The simulation snapshots (as depicted in Fig. 5.1) are indicated by the black dotted lines in Fig. 5.2. The times during which the mergers have been identified in the simulation are marked as grey shaded areas, with the merger mass-ratio indicated in the top of these areas.

The first five light curves in Fig. 5.2 illustrate that right after the seeding of the BH in a galaxy, the BH accretes gas at rates close to or at the Eddington limit, which are by default the maximum luminosity allowed in the simulation (black solid line in Fig. 5.2). During that phase, the accretion rates are likely artificially high due to our low BH seeding mass relative to the galaxy stellar mass[6]. After this first accretion phase at or close to the Eddington-limit, AGN luminosities become highly variable over smallest time steps of ~ 0.1Myr.

[4]performed with the free software Splotch, http://www.mpa-garching.mpg.de/~kdolag/Splotch from Dolag et al. (2008)

[5]In the right panel in the second row, no BH luminosity has been specified since the BH has not yet been seeded.

[6]See Fig. 4 and the corresponding discussion in Steinborn et al. (2015) for further details.

In the top, second and fifth panel of Fig. 5.2, both minor and major mergers increase or decrease the AGN luminosity *only marginally*. In these cases, already before the merger, the BH can accrete at/close to the Eddington limit, due to large amounts of gas available at these early times, so that a merger does not have any significant, additional effect. As the amount of gas in galaxies varies with redshift, this may imply that the relevance of mergers for nuclear activity is also dependent on redshift. Despite the higher BH mass after the BH merger, resulting in a higher Eddington limit, and thus, higher maximum AGN luminosity (solid black line), the high AGN variability leads to an AGN luminosity at $z = 2$ not being necessarily larger at the time of "observation" (i.e. when the snapshot is written) than before the merger and can, in fact, also be lower (see, e.g., the second panel in Fig. 5.2).

The light curve for a merger-free AGN in the bottom panel of Fig. 5.2 additionally shows that similarly high AGN luminosities as seen in the top, second and fifth panel can also be induced by processes other than mergers. Interestingly, similar to our two test cases of 1:1 mergers (second and fourth panel), the AGN activity declines rapidly from $z = 2$ to $z = 1.5$, possibly either due to starvation or due to disturbances of the morphology and/or the dynamics of the gas within the central kpc.[7]

In the light curves shown in the third and the fourth panels of 5.2, the average AGN luminosity significantly rises during and right after the merger event. In both cases, the BH accretes at fairly low Eddington-ratios before the merger, while after the merger, the BH accretion can reach the Eddington limit. This seems to suggest that a merger is more likely to boost AGN luminosity, if the BH was rather inactive before the merger (due to low amount of gas, missing gas inflows etc.).

To summarize, our five case studies demonstrate that analysing the effect of merger events on nuclear activity is significantly complicated by strong variations in the evolution of BH accretion rates. The net increase or decrease in AGN luminosity between the times of two snapshots, (see Fig. 5.1), is distorted by the significant flickering in AGN luminosity: considering the AGN luminosity only at a specific time of one of our snapshots (dashed black lines) does not necessarily reflect the *average* AGN luminosity in a representative way (but note, this is the same for observations).

To still find a meaningful connection between the nuclear activity and the merger history of the host in our simulations, we can either average over the BH accretion rates of a galaxy within a given time interval (centred at the time of the snapshot), or we can investigate the AGN luminosities of a *statistically large sample* at a given time-step. In this study, we follow the latter approach. Nevertheless, we verified that an additional averaging over the AGN luminosities within a given time interval does not affect our results, even when restricting to the most luminous AGN.

[7] We verified that there is also no merger between $z = 1.5$ and $z = 2$.

5.2.2 AGN population study

The results presented for the five AGN test cases raise the questions, (i) how frequently mergers increase AGN activity on a statistical basis and (ii) to what extent such a boost is dependent on AGN luminosity or the merger mass-ratio. To ensure sufficiently high statistics, in this section we consider large populations of AGN and their host galaxies in the 500Mpc/hr run of the Magneticum set. First, we examine the statistical incidence of nuclear activity in galaxies as a function of their recent merger history, giving us the maximum probability that a merger event can fuel nuclear activity in galaxy populations. Then, we quantify the maximum likelihood that nuclear activity in AGN populations can be merger-induced and their dependence on AGN luminosity, also compared to observations. Further comparing merger fractions of AGN hosts to that of inactive galaxies allows us to assess to what extent merger events are actual drivers for nuclear activity.

Incidence for nuclear activity in galaxies as a function of their merger history

Fig. 5.3 shows the number density of all galaxies (light blue hatched area), of moderately luminous and luminous active galaxies with 10^{43}erg/s$< L_{\rm bol} < 10^{45}$erg/s and $L_{\rm bol} > 10^{45}$erg/s (solid and dashed lines), respectively, having experienced either no mergers (left bar), minor (middle bar) or major mergers (right bar) in the last 0.5 Gyr at $z = 2, 1, 0.5, 0$ (panels from top to bottom). As expected from a hierarchical structure formation scenario, the number density of all galaxies with major or minor mergers is decreasing from z=2 to z=0. Over the same redshift range, the number density of all galaxies *without* recent mergers is marginally increasing.

Instead, the number density of AGN *always* decreases from $z = 2$ to $z = 0$, also for host galaxies *without* a recent merger. The more luminous AGN are, the stronger AGN number densities are declining towards lower redshift. While at $z = 2$ nearly all galaxies with a recent merger event host a luminous AGN, at $z = 0.1$, it is only a small fraction of less than 10 per cent for moderately luminous and of less than 1 per cent for luminous AGN.

Fig. 5.4 further quantifies such AGN fractions: shown is the redshift evolution of the *ratio* of the number (density) of moderately luminous and luminous AGN hosts (dark blue circles/lines and light blue squares/lines, respectively) to that of all galaxies (i.e., the AGN duty cycle), having experienced in the past 0.5 Gyr either no mergers (solid lines), $N_{\rm AGN}/N_{\rm galaxies\ with\ no\ merger}$, or minor/major mergers, $N_{\rm AGN}/N_{\rm galaxies\ with\ minor/major\ merger}$, (dotted/dashed lines). The error-bars indicate the binomial confidence intervals.

At $z = 2$ almost 100 per cent of all galaxies host an AGN, and more than 90 per cent even a luminous AGN ($> 10^{45}$ erg/s), irrespective of the recent merger history. This result implies that mergers do not necessarily play any role for nuclear activity at these early times: large amounts of turbulent gas available in and around such young galaxies can lead to radial gas inflows onto the central few kpc, and thus, to high accretion rates onto BHs, also without any recent merger event.

Towards lower redshifts ($z < 2$), the situation changes: independent of the recent

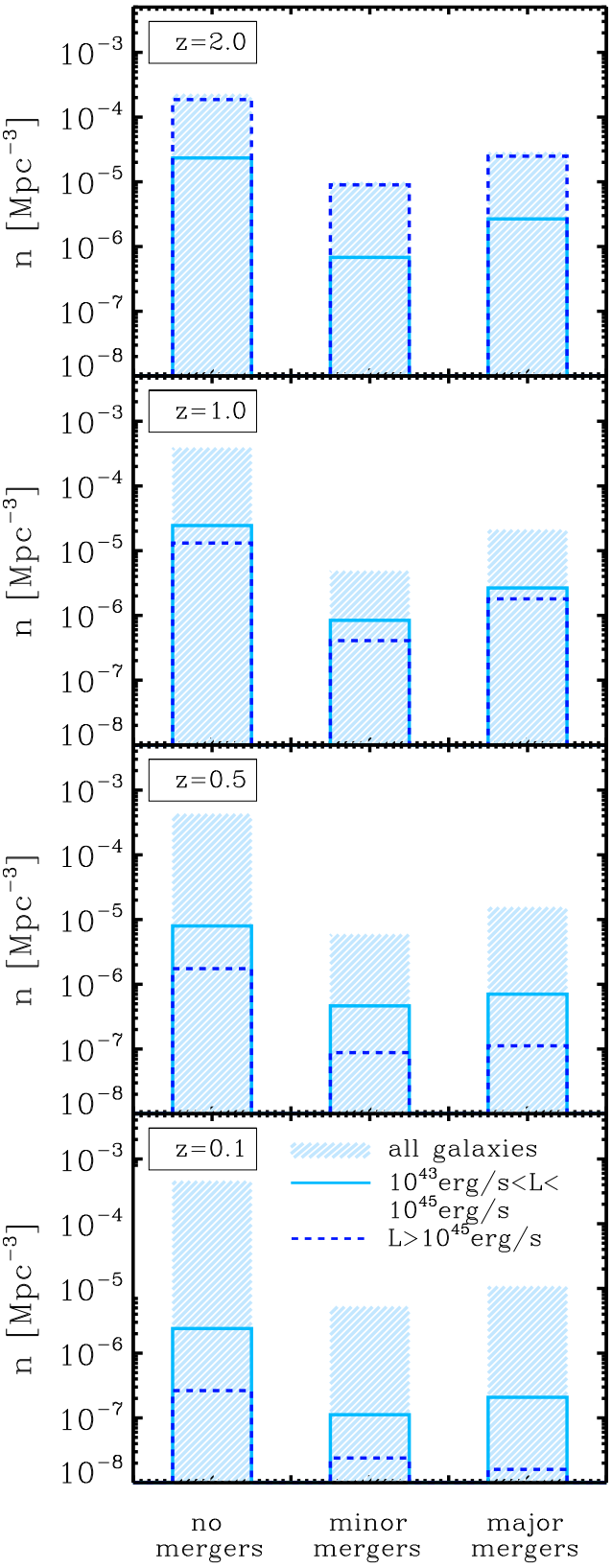

Figure 5.3: Number density of all galaxies (hatched areas), moderately luminous AGN (10^{43}erg/s< $L < 10^{45}$erg/s; solid light blue lines), and luminous AGN ($L_{\rm bol}10^{45}$ erg/s; dashed dark blue lines). We include only galaxies with stellar masses above our resolution limit ($M_* > 10^{11} M_\odot$) and distinguish between galaxies which have experienced no mergers (including very minor mergers with $M_{*2}/M_{*1} < 1:10$), minor mergers ($1:10 < M_{*2}/M_{*1} < 1:4$), and major mergers ($M_{*2}/M_{*1} > 1:4$) in the past 0.5 Gyr at $z = 2.0, 1.0, 0.5, 0.1$ (panels from top to bottom).

merger history, the fractions of luminous AGN are strongly declining to less than 1 per cent at z=0.1, as a consequence of the generally reduced gas content and density in the inner region of a galaxy (see Section 5.4 for further discussion). Particularly at late times mergers of more massive galaxies are often "dry" with little amounts of cold gas involved, thus, hardly inducing high levels of nuclear activity.

Turning to moderately luminous AGN, the trends are somewhat different: from $z = 2$ to $z = 1$, the probability of hosting a moderately luminous AGN ($\sim$10 per cent) marginally decreases for galaxies without a recent merger event, but slightly increases for those with both major and minor mergers, suggesting that mergers may get more relevant for driving AGN activity in this redshift interval. Below $z = 1$, the fractions of moderately luminous AGN are dropping down to 2 per cent at z=0.1 with mergers, and down to 0.5 per cent without mergers. The stronger decline of AGN fractions in galaxies without recent mergers points towards a slightly increased relevance of mergers for fuelling nuclear activity on a kpc-level in galaxies at and after $z = 1$, although the probability that a galaxy with a recent merger event shows nuclear activity is still fairly low ($\lesssim$10 per cent).

Finally, we compare our simulation results with observed fractions of local moderately luminous and luminous AGN (grey and black bar[8], respectively) obtained from an SDSS galaxy sample at low-redshift ($z \sim 0.1$) using optically-selected AGN from emission lines as described by Juneau et al. (2014). The predicted AGN fractions of local galaxies are systematically lower by approximately half an order of magnitude. This rather minor difference might be caused by our limited resolution, also limiting the BH mass and thus the AGN luminosity. More likely, however, it is caused by selection effects, particularly since our AGN luminosity functions agree very well with observations (Hirschmann et al., 2014; Biffi et al., 2018).

The redshift evolution of merger fractions of AGN hosts

After having demonstrated that at and below $z \sim 1$, mergers may induce nuclear activity in less than 10 per cent of galaxies (with recent mergers), in this subsection, we explore the probability that AGN host galaxies have experienced a merger event in the past 0.5 Gyr, i.e. the total, minor, and major merger fraction of AGN hosts, $N_{\mathrm{AGN,\ major+minor}}/N_{\mathrm{AGN}}$, $N_{\mathrm{AGN,\ major}}/N_{\mathrm{AGN}}$ and, $N_{\mathrm{AGN,\ minor}}/N_{\mathrm{AGN}}$,[9]. This quantity represents the *maximum* possible likelihood that the nuclear activity of an AGN population was fuelled (on a kpc level) by mergers.

Fig. 5.5 shows the redshift evolution of the total, major, and minor merger fractions (blue solid lines, red dashed lines, and green dotted lines, respectively) of AGN with $L > 10^{43}$erg/s ($N_{\mathrm{AGN,major+minor/major/minor}}/N_{\mathrm{AGN}}$, bottom panel), compared to the merger fractions of inactive galaxies ($N_{\mathrm{inactive,\ major+minor/major/minor}}/N_{\mathrm{inactive}}$, middle panel) and to that

[8]The bars originate from measurements in different mass ranges and include all values for $M_* > 10^{11} M_\odot$.

[9]Note that the absolute value of the merger fraction strongly depends on the definition of mergers, i.e. during which time interval they are identified. We tested different time intervals of up to 1.5 Gyr, where the merger fraction is about twice as high as for our fiducial choice of 0.5 Gyr. Qualitative trends, however, remain unaffected.

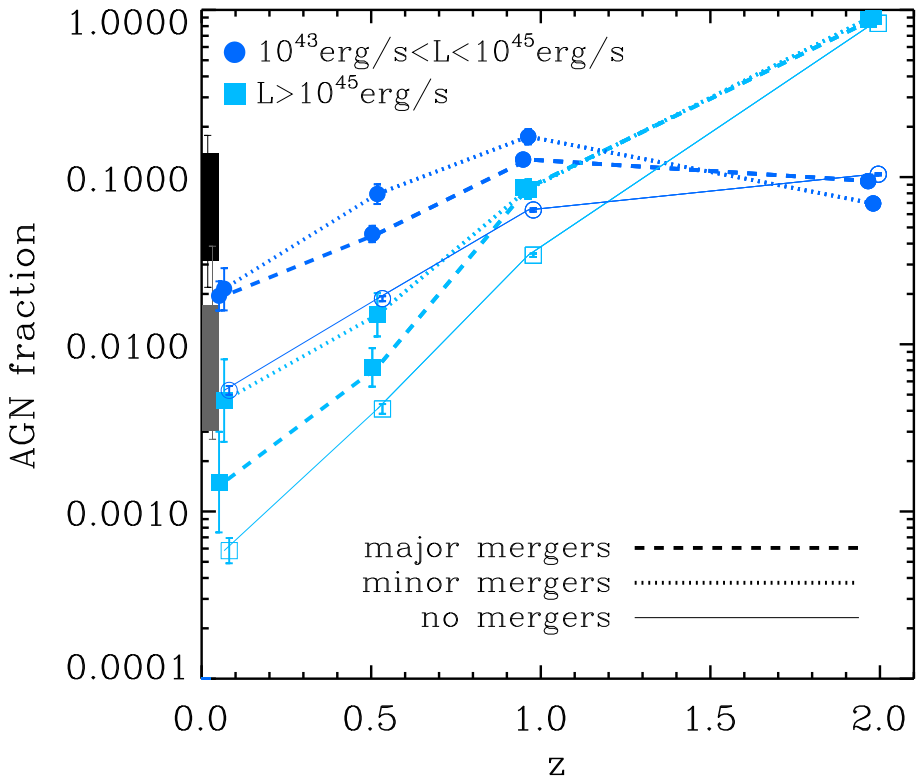

Figure 5.4: Redshift evolution of fractions of AGN host galaxies with 10^{43}erg/s$< L < 10^{45}$erg/s (dark blue circles) and $L_{\rm bol} > 10^{45}$erg/s (light blue squares) having experienced a major (dashed lines), minor (dotted lines) or no merger (solid lines) in the past 0.5 Gyr assuming a stellar mass cut of $M_* > 10^{11} M_\odot$. Error bars in the AGN fractions indicate the binomial confidence intervals. The grey and black bars show observed fractions of local AGN with $L > 10^{45}$erg/s and 10^{43}erg/s$< L < 10^{45}$erg/s, respectively (Juneau et al., 2014).

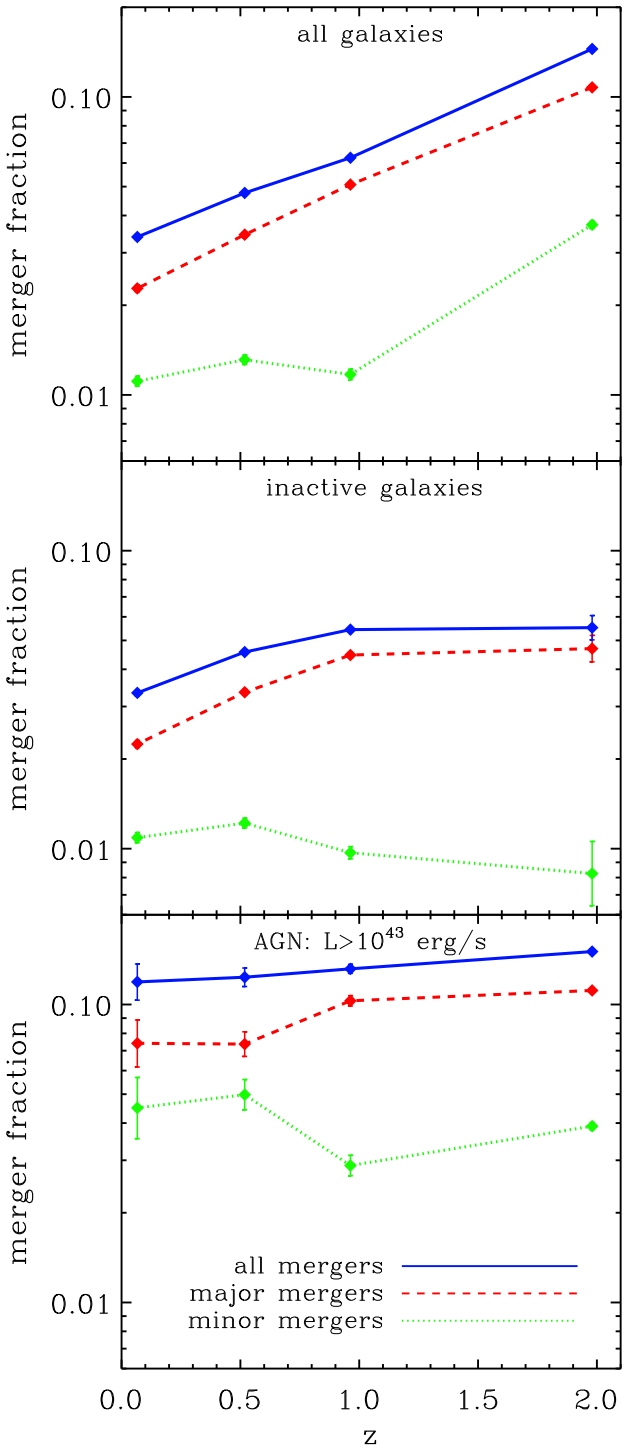

Figure 5.5: Redshift evolution of the total, major, and minor merger fractions (blue solid, red dashed, and green dotted lines, respectively) of all (top panel), inactive (middle panel), and active galaxies with $L_{\rm bol} > 10^{43}$ erg/s (bottom panel), assuming a stellar mass cut of $M_* > 10^{11} M_\odot$. Error bars indicate binomial confidence intervals.

of all galaxies, i.e. active *and* inactive ones ($N_{\rm AGN+inactive,\ major+minor/major/minor}/N_{\rm AGN+inactive}$, top panel).

For all galaxies, the total (major) merger rates are strongly declining from 15 (10) per cent at $z = 2$ to less then 4 (3) per cent at $z = 0.1$. The predicted decrease of the total merger rates from high to low redshifts is a direct consequence of an expanding, hierarchically growing Universe, and also qualitatively consistent with observations of Kartaltepe et al. (2007) and Xu et al. (2012) as well as with other simulation studies (e.g., Millennium simulation, Genel et al., 2009). Instead, the minor merger fractions hardly evolve with redshift, and stay always below 4 per cent at $z = 0 - 2$. Such rather low minor merger fractions and their weak evolutionary trend may be caused by our definition of merger classes (galaxies in the major merger group can also have experienced minor mergers in the past 0.5 Gyr), not reflecting the *actual number* of major and minor mergers galaxies experienced during the past 0.5 Gyr.

When separating between active and inactive galaxies, total and major merger fractions of both active and inactive galaxies only exhibit a weak evolutionary trend, in contrast to all galaxies. In addition, active galaxies have on average a three times higher probability for a minor and/or major merger event in the recent past compared to inactive galaxies, whose total merger fractions stay always below 6 per cent. But also the merger rates of active galaxies reach a maximum value of only 15 per cent, suggesting that the majority of nuclear activity of an AGN population at $z = 0 - 2$ is unlikely to be caused by merger events.

AGN merger fractions as a function of the AGN luminosity

To understand whether the maximum probability that an AGN was fuelled by a merger is related to the respective AGN luminosity, in Fig. 5.6, we explore the total, major, and minor merger fractions as a function of AGN luminosity (blue solid, green dotted and red dashed lines, respectively) at different redshift steps ($z = 2.0, 1.0, 0.5, 0.1$, panels from top to bottom). To avoid low number statistics, we consider only bins of AGN luminosity containing at least 20 active galaxies. Fig. 5.6 shows that the global trends seen in Fig. 5.5, namely that total, major, and minor merger fractions of active galaxies are larger than that of inactive ones (illustrated by the arrows on the left-hand side in each panel of Fig. 5.6), remain the same for each AGN luminosity, irrespective of the redshift step.

Turning to the dependence of the merger rates on AGN luminosity, at $z = 2$ the total, major, and minor merger fractions strongly increase from less than 10, 8 and 2 per cent for faint AGN to up to more than 50, 30 and 30 per cent for most luminous AGN with $L_{\rm bol} \geq 10^{47}$ erg/s, respectively. Towards lower redshifts, at $z \leq 1$, the increase of the merger rates with AGN luminosity is significantly weaker or even negligible, at maximum raising from 10 per cent for faint AGN up to 20 per cent for more luminous AGN. This trend may be due to the fact that at and below $z = 1$, even our large 500Mpc/hr simulation run does not contain sufficient statistics for AGN more luminous than $L_{\rm bol} \sim 5 \times 10^{46}$ erg/s at $z = 1$, $L_{\rm bol} \sim 5 \times 10^{45}$ erg/s at $z = 0.5$, and $L_{\rm bol} \sim 10^{45}$ erg/s at $z = 0.1$, impeding us by construction to find any potential increase of the merger fractions for these most luminous

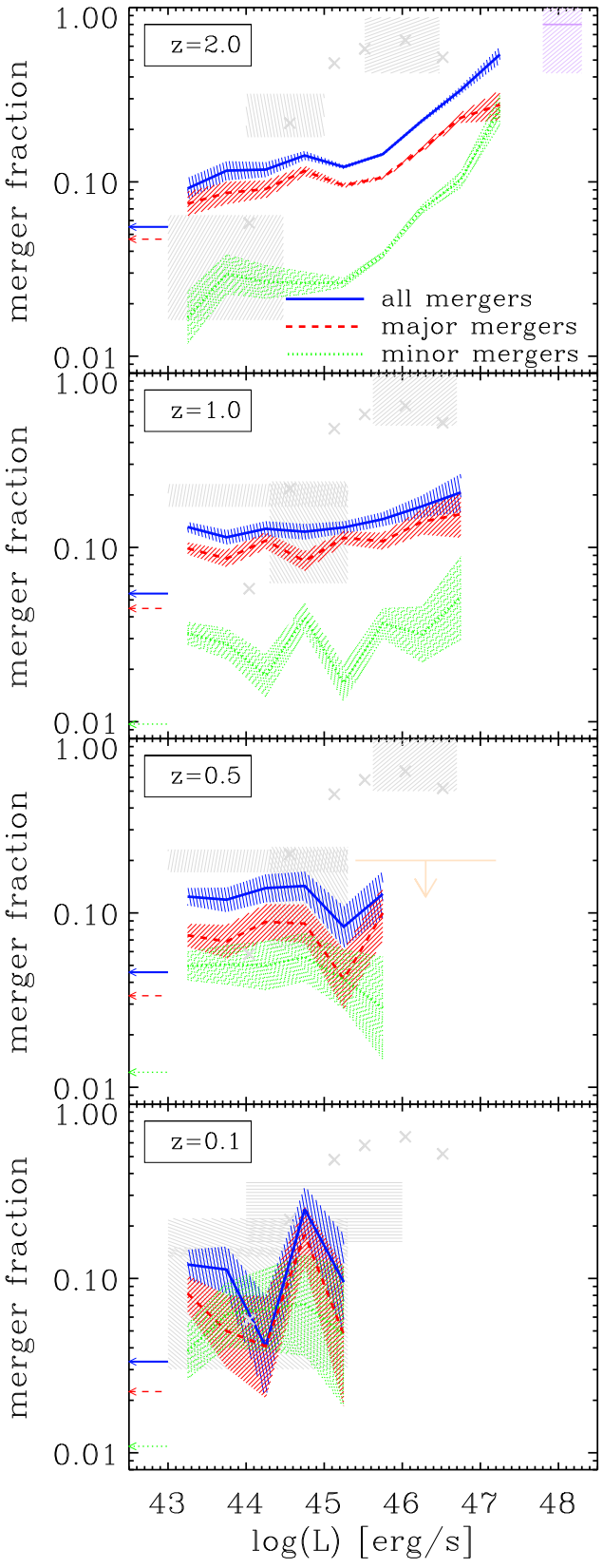

Figure 5.6: Total, major, and minor merger fractions (blue solid, red dashed, and green dotted lines and shaded areas, respectively) of AGN host galaxies versus their bolometric AGN luminosity at different redshift steps ($z = 2.0, 1.0, 0.5, 0.1$, panels from top to bottom) compared to that of inactive galaxies (depicted by the horizontal arrows at the left-hand side of each panel). Simulation predictions are compared to observed major merger rates of AGN hosts (compilation of Treister et al. 2012: grey crosses and grey shaded area, the latter illustrates the entire observed luminosity range and the error on the y-axis; Glikman et al. 2015: purple horizontal line and shaded area; Villforth et al. 2017: orange line with the arrow indicating the upper limit and the observed luminosity range).

AGN.

Compared to observed major merger fractions of the compilation of Treister et al. (2012, grey crosses and grey shaded areas, illustrating the observed luminosity range and the uncertainty in the merger fraction) and to observations from Glikman et al. (2015, purple horizontal line and shaded area), we find at $z = 2$ a qualitative (even if not quantitative) agreement between the observed steep raise of the merger fraction towards higher AGN luminosities and our simulated AGN merger fractions. In contrast, at lower redshifts ($z \leq 1$), the predicted dependence of the merger fraction on AGN luminosity is significantly weaker than that of Treister et al. (2012), despite their rather large scatter at low redshifts (due to low number statistics). However, most of the observed data-points cover a very large redshift range, in particular the grey crosses, making a comparison at specific redshifts difficult. Compared to Villforth et al. (2017, orange line with the arrow indicating the upper limit of the merger fraction and the observed luminosity range), our simulated major merger rates of the most luminous AGN at $z = 0.5$ are in good agreement with their maximum merger fraction of less than 20 per cent, being significantly lower than that of Treister et al. (2012) in the same luminosity range. We however emphasize that such a comparison between observed and simulated AGN merger rates is complicated by a lot of caveats, not only due to the already mentioned various selection criteria, but also because of different merger identifications in observations and simulations (see section 5.5.3 for further discussion).

To summarize, except for very luminous AGN at $z = 2$, our simulation predictions do not favour any prevalence (>50 per cent) of mergers for fuelling nuclear activity in AGN populations at $z = 0-2$, irrespective of the AGN luminosity. Nevertheless, the probability for AGN hosts of any AGN luminosity having experienced a major and/or minor event in the last 0.5 Gyr, can be up to three times higher than that for inactive galaxies. Such elevated merger rates of active galaxies still point towards a connection between nuclear activity and merger events, even if mergers do not appear to be the statistically dominant fuelling mechanism for nuclear activity in our simulations.

5.3 The dependence of AGN merger rates on host galaxy properties

In this section, we aim to understand the origin of (i) the slightly enhanced merger fractions of active galaxies, compared to that of inactive galaxies and (ii) the steep up-turn of AGN merger fractions towards high AGN luminosities at $z = 2$, as shown in the last two subsections. We explore to what extent these features of active galaxies can be explained by a combination of an intrinsic dependence of merger rates on different galaxy properties, such as stellar mass and specific SFRs, and of a bias of AGN preferentially residing in galaxies with specific properties. To reveal that, we compare, *at fixed galaxy stellar mass or specific SFR*, the merger fractions of active to that of inactive galaxies, and we relate the former, the merger fraction of AGN, with the respective probability that such AGN

are hosted by galaxies of a given stellar mass or specific SFR.

5.3.1 Galaxy stellar mass

Starting with the dependence of AGN merger fractions on galaxy stellar mass, the bottom row in Fig. 5.7 visualises the total AGN merger fractions (major and minor mergers) versus AGN luminosity at different redshift steps (differently coloured lines) separately for massive ($M_\star > 5\times10^{11} M_\odot$, left panel) and less massive host galaxies ($10^{11} M_\odot < M_\star < 5\times10^{11} M_\odot$, right panel). As seen for *all* galaxies/AGN in Fig. 5.6, also for a given stellar mass bin, the merger fractions of AGN are elevated (by up to half a dex) at any redshift and AGN luminosity, compared to that of inactive galaxies (illustrated by arrows at the left-hand side of each panel). This implies that at fixed galaxy mass (and thus, also at fixed BH mass), AGN hosts are also more likely to have experienced a recent merger than inactive galaxies, and thus, that nuclear activity of an AGN population can be fuelled by merger events – to a low degree, though, hardly exceeding 20 per cent.

In addition, the bottom row in Fig. 5.7 shows that AGN merger fractions of massive hosts are larger, by a factor of three at $z = 2$, than that of less massive ones, at a given AGN luminosity and redshift. This difference is largely caused by the intrinsically up to half an order of magnitude higher merger fractions of massive inactive galaxies compared to less massive ones (left-hand arrows). This dependence of merger rates on the galaxy stellar mass is a natural consequence of a hierarchically growing Universe, in which massive galaxies experience a much more complex merger history than low mass galaxies (e.g. Fakhouri & Ma, 2008; Genel et al., 2009).

Interestingly, at a given host stellar mass the AGN merger fraction is at any redshift largely independent of the AGN luminosity. At $z = 2$, this is in stark contrast to the strongly raising merger fractions of *all* AGN hosts towards higher AGN luminosity, as shown in the top panel of Fig. 5.6. To understand this difference, we have to consider the probability that an AGN resides in a massive or less massive host as a function of the AGN luminosity (see top row of Fig. 5.7). While most luminous AGN (with $L_{\rm bol} > 3\times10^{46}$ erg/s) are preferentially hosted by massive galaxies at $z = 2$, less luminous AGN are mostly living in less massive galaxies (see lila curves in top panels of Fig. 5.7). Thus, this bias in AGN host stellar mass, together with the intrinsic dependence of merger fractions on the galaxy stellar mass, can, to some extent, explain the steep up-turn of AGN merger fractions towards higher AGN luminosities at $z = 2$. In other words, the high merger rates of luminous AGN at $z = 2$ partly reflect the intrinsically higher merger rates of massive galaxies, in which luminous AGN predominantly reside. Note that this result is consistent with recent findings from phenomenological models of Weigel et al. (2018). Nevertheless, as pointed out before, the more than twice as large merger fractions of luminous AGN at $z = 2$ (ca 50 per cent) compared to that of massive inactive galaxies (ca 20 per cent), still indicate the relevance of mergers for fuelling nuclear activity in most luminous AGN.

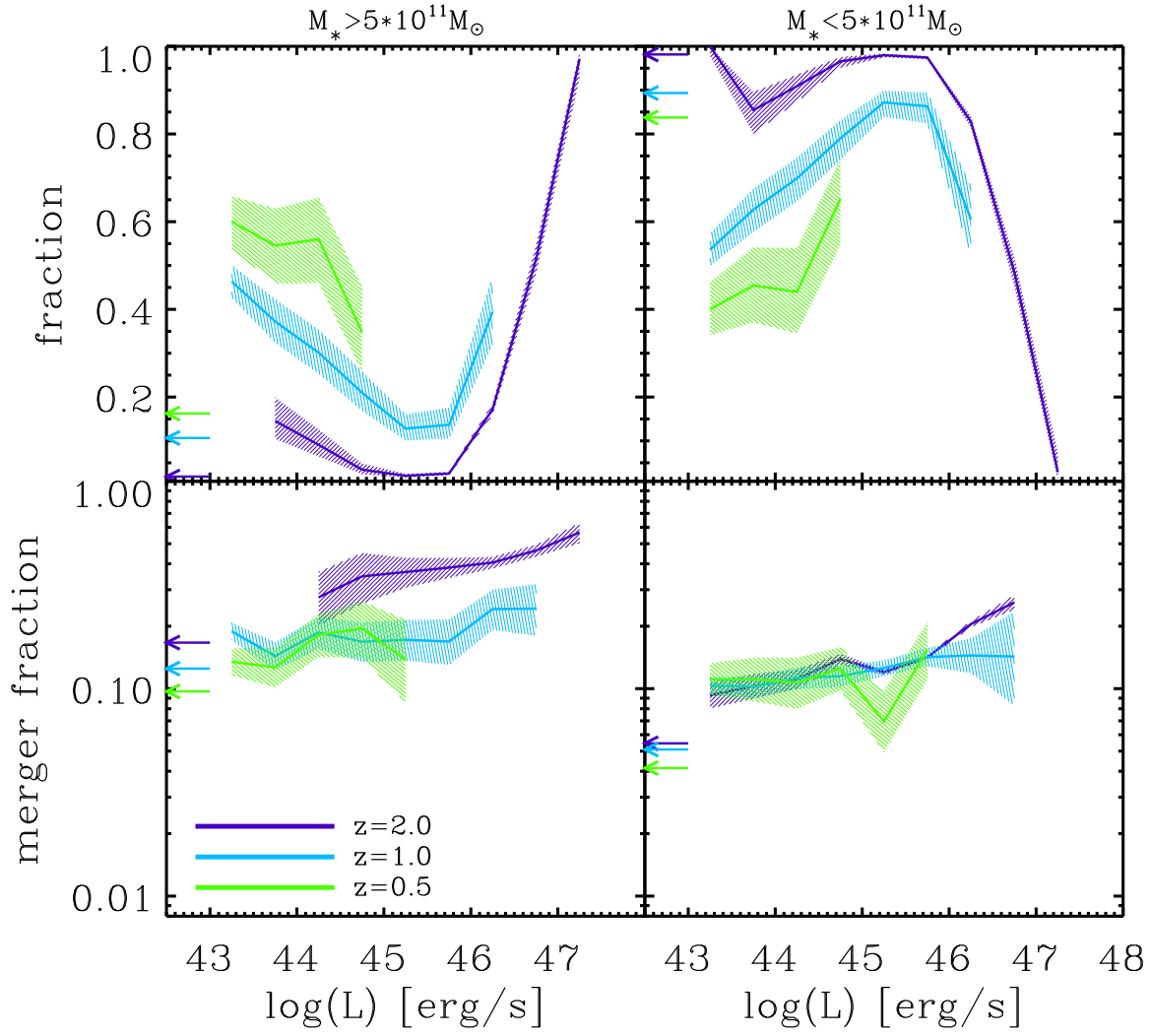

Figure 5.7: Fraction of active galaxies (top row) and total AGN merger fractions (major *and* minor mergers, bottom row) versus AGN luminosity separating between massive (left column) and less massive host galaxies (right column) with galaxy stellar masses of $M_\star > 5 \times 10^{11} M_\odot$ and $10^{11} M_\odot < M_\star < 5 \times 10^{11} M_\odot$, respectively, at $z = 0.5, 1, 2$ (differently coloured lines) compared to inactive galaxies (arrows at the left-hand side of each panel).

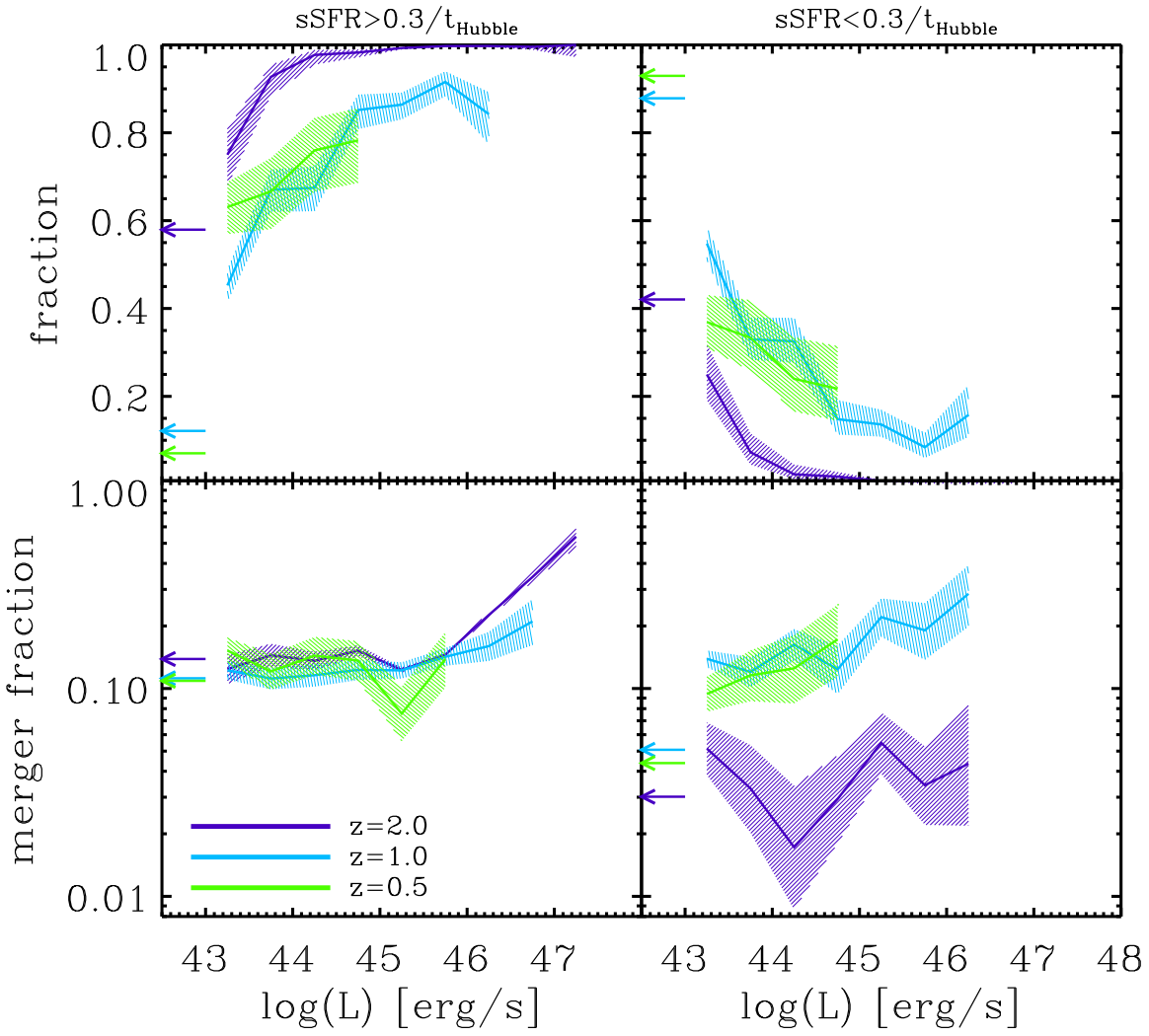

Figure 5.8: Same as Fig. 5.7, but when distinguishing between star-forming (left column) and quiescent galaxies (right column) with specific SFR $> 0.3/t_{\rm Hubble}$ and specific SFR $< 0.3/t_{\rm Hubble}$, respectively.

5.3.2 Specific star formation rate

Next, we turn to the dependence of AGN merger fractions on the specific SFRs of their hosts, i.e. to what extent AGN merger fractions are different for star-forming (SF) and passive galaxies, i.e. galaxies with specific SFRs above and below $0.3/t_{\rm Hubble}$, respectively.

The bottom left panel of Fig. 5.8 shows that the AGN merger fractions of SF hosts at $z = 0.5, 1, 2$ (differently coloured lines) are widely independent of AGN luminosity, except for the up-turn of the merger rates for the most luminous AGN at $z = 2$,[10] and have very similar values ($10 - 20$ per cent) as the merger fractions of inactive SF galaxies (arrows on the left). Moreover, as the top left panel of Fig. 5.8 illustrates, AGN predominantly reside in SF galaxies, in particular at $z = 2$ (>80 per cent) and to lesser extent also at $z = 1$ (>70 per cent) and $z = 0.5$ (>60 per cent). These results suggest that star formation and nuclear activity are related on a statistical level, and both SF/starbursts, and BH fuelling may be induced by merger events (on average up to 10-20 per cent of AGN/SF galaxies). The generally higher merger rates of *all* active compared to *all* inactive galaxies, i.e. not distinguishing between SF and passive galaxies (see e.g., Fig. 5.5), thus reflect the intrinsically higher merger rates of SF galaxies, in which AGN predominantly occur. This is largely consistent with observations finding a close link between AGN activity and star formation activity (e.g. Juneau et al., 2013).

AGN merger rates of passive hosts are half as high as that of SF hosts at $z = 2$, while at $z \leq 1$ they are similar to that of SF hosts. In addition, for passive galaxies, AGN merger rates are always higher (by ca 0.5dex) than the merger fraction of inactive galaxies, suggesting that a merger may raise the gas supply and density within the central few kpc, but the gas does not get cold or dense enough to induce significant levels of SF. Note that per se nuclear activity in passive galaxies can be explained by (i) warm/hot gas being accreted on the central BH, not fullfilling SF criteria, and (ii) the computed Bondi accretion rate's strong dependence on BH mass so that for massive BHs, already small amounts of gas and lower gas densities are sufficient to ignite moderately luminous AGN. However, only a small fraction (< 30 per cent) of passive galaxies host moderately luminous AGN, and less than 10 per cent of passive galaxies host luminous AGN, showing that it is not very likely to have nuclear activity in galaxies without on-going SF.

To summarize section 5.3, the high merger fractions of luminous AGN at $z = 2$ in the top panel of Fig. 5.6, reflect, on the one hand, the intrinsically high merger rates of massive galaxies, and on the other hand, an enhanced role of mergers for providing the gas fuel in the central few kpc for BH accretion. The generally elevated merger fractions of active with respect to inactive galaxies (Figs. 5.6 and 5.5) are to large degree connected to the intrinsically high merger rates of SF galaxies, in which AGN primarily appear. Also at any given galaxy stellar mass or specific SFR, higher merger rates of active galaxies (but on average not exceeding 20 per cent, except for luminous AGN at $z = 2$), compared to inactive passive galaxies, indicate only a weak, albeit still non-negligible role of mergers for nuclear activity (and star formation).

[10] This up-turn is a consequence of luminous galaxies being mostly hosted by *massive* SF galaxies (see Fig. 5.7).

5.4 Central gas properties and BH masses in (in)active galaxies with different merger histories

Up to now, we have shown that the fraction of active galaxies having recently experienced a merger event is generally larger than that of inactive galaxies, indicating that mergers may fuel nuclear activity on a kpc-level. In this section, our goal is to obtain a deeper physical understanding for this result, by investigating the quantities governing the accretion rates onto BHs in our simulations, i.e. used to compute the Bondi accretion rate by virtue of eq. 3.1: the BH mass, the gas density, the gas temperature, and the gas velocity relative to the BH *within the resolved accretion region*, $r_{\rm acc}$[11]. Specifically we address the following two questions:

1. Which central ISM conditions around the BHs and which BH masses in our modelling approach are necessary for causing nuclear activity in galaxies, i.e. how do ISM conditions and BH masses differ between active and inactive galaxies?

2. To what extent is a merger needed for generating conditions necessary for nuclear activity in galaxies, i.e. how do central ISM conditions and BH masses of merging active galaxies differ from non-merging active galaxies?

Note that we consider the central gas properties and BH masses shortly (at the snapshot) *before* the merger happened or, for galaxies without a recent merger, shortly before the considered redshift. Naively, we would expect that these ISM properties would scale *by construction* with the accretion rate onto the BH and thus with AGN activity. However, as we shall see, the complex interplay between various physical processes in cosmological simulations, such as AGN and stellar feedback, gas cooling and the related in-flowing cold gas streams, disproves such an expectation.

Fig. 5.9 shows the redshift evolution of the mean BH mass, gas density, gas temperature, relative gas velocity and angular momentum of the gas within $r_{\rm acc}$ (rows from top to bottom), separating between inactive galaxies, moderately luminous, and luminous AGN (left, middle, and right columns, respectively), to address question (i). To also investigate point (ii), we additionally split the samples into galaxies/AGN hosts with major (red filled circles), minor (green filled squares), and no merger events (black open diamonds).

The first row of Fig. 5.9 shows that at $z = 2$, the average BH masses are not significantly different for active and inactive galaxies. Towards lower redshift, at $z = 1$ and $z = 0.5$, the situation changes: more luminous AGN host on average *less* massive BHs than moderately luminous AGN and inactive galaxies, *irrespective of the merger history*. Thus, a higher AGN luminosity is improbably caused by a larger BH mass. Moderately luminous AGN without any merger at low redshifts, in particular at $z = 0.1$, have by a factor of three higher BH masses than inactive galaxies without any merger, indicating that large BH masses in galaxies without any mergers promote nuclear activity at moderate levels.

[11]The accretion radius (not to confuse with the Bondi radius) is defined as the radius, inside which the gas particles are used to compute the Bondi accretion rate. Since the number of gas particles used for that calculation is fixed, the accretion radius varies for different BHs.

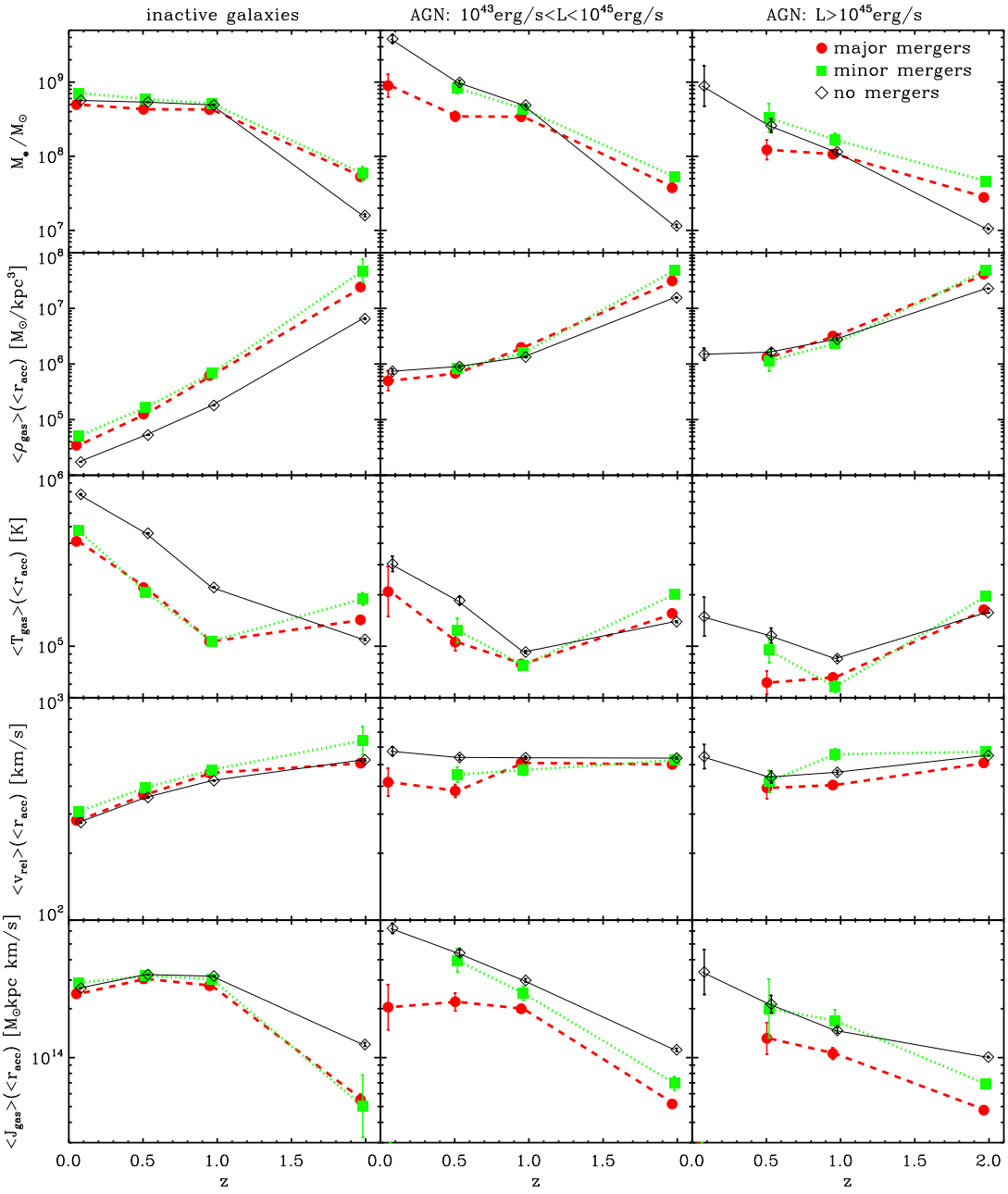

Figure 5.9: Redshift evolution of the mean of the BH mass, density, temperature, relative velocity and angular momentum of the gas within the resolved accretion regions around the BH (rows from top to bottom) for inactive galaxies (left panels), moderately luminous AGN (middle panels), and high-luminosity AGN (right panels), having experienced either a recent major merger (filled red circles), minor merger (filled green squares), or no merger (black open diamonds). All parameters are computed at the time of the snapshot, when the merger has been identified, or in case of "no mergers", 0.5 Gyr before the respective redshift. Error bars indicate the bootstrapping errors. For better readability, symbols and error-bars are slightly shifted around the redshift-values $z = 0.1$, $z = 0.5$, $z = 1.0$, and $z = 2.0$.

Turning to the gas density within $r_{\rm acc}$, the second row in Fig. 5.9 illustrates that this quantity generally decreases from high to low redshifts, for both merging and non-merging galaxies/AGN. Contrasting the gas densities of inactive with that of active galaxies, at $z = 2$, we find hardly any difference, in particular for galaxies under-going a merger, where the mean inner gas density is always larger than $10^7 M_\odot/{\rm kpc}^3$. The generally high central gas densities in galaxies at $z = 2$ favour AGN activity independently of merger events, leading to the high AGN fraction shown in Fig. 5.4. A small fraction of galaxies, though, do not reach the threshold for being an AGN ($L > 10^{43}$erg/s) despite the high inner gas densities shortly before the merger. Towards lower redshifts $z \leq 1$, the central gas densities of active galaxies stay on average always at or above $10^6 M_\odot/{\rm kpc}^3$ and are by more than one order of magnitude higher than that of inactive galaxies, which, instead, drop below $10^5 M_\odot/{\rm kpc}^3$ towards $z = 0$. This demonstrates that an enhanced gas density is a necessary (but not sufficient) condition for nuclear activity.

Comparing gas densities of merging and non-merging galaxies, we find that merging, inactive galaxies have by a factor of 5 increased central gas densities compared to non-merging inactive galaxies. Interestingly, active galaxies instead, in the process of having a major or minor merger, have similarly high gas densities as those without any merger event, suggesting that *central gas densities can be enlarged not only by merger events, but also by other processes* (see discussion 5.5).

Exploring the mean gas temperatures within $r_{\rm acc}$ (third row of Fig. 5.9) largely reveals opposite trends compared to the gas densities: the gas temperatures *increase* towards $z = 0$, as gas gets heated by various heating processes (e.g. gravitational heating, AGN feedback), simultaneously becoming less and less dense. On average and irrespective of the presence of a merger, active galaxies have lower ($< 3 \times 10^5$ K) inner gas temperatures than inactive galaxies, at least at $z \leq 1$, resulting in higher BH accretion rates (see eq. 3.1). During that redshift range, the average gas temperature right before a merger is reduced in both active (at maximum 2×10^5 K) and inactive galaxies (at maximum 5×10^5 K) compared to *non-merging* active/inactive galaxies, possibly as a consequence of (pre-)merger-induced cooling flows.

Considering the relative gas velocities $v_{\rm rel}$ within $r_{\rm acc}$ (fourth row of Fig. 5.9), at $z \leq 1$, this quantity is by a factor of up to 3 higher for active galaxies, at least when they have no merger or only a minor merger, than for inactive galaxies. This is surprising as, by construction, a higher relative gas velocity *decreases* the Bondi accretion rate (eq. 3.1). A high relative gas velocity may, however, indicate increased gas inflows towards the centre. Such inflowing gas does not only seem to counteract the intrinsically reduced Bondi accretion rate, but also appears to be crucial to provide sufficient fuel to induce nuclear activity (in galaxies with mergers as well as without mergers).

Tightly connected to the relative gas velocity is the angular momentum of the gas (bottom row in Fig. 5.9), even if not explicitly considered, when estimating the Bondi accretion rate. While at $z = 2$ the mean angular momentum is not significantly different in active and inactive galaxies, at $z \leq 1$ the mean angular momentum of gas in luminous AGN hosts is lower than that in moderately luminous AGN hosts and inactive galaxies, showing that a lower angular momentum of the gas promotes strong nuclear activity. Over

the entire redshift range, active galaxies right before a major merger (and to lesser extent, also before a minor merger) have a by up to a factor of three lower angular momentum of the central gas than active galaxies *without* a merger, possibly due to the (on average) different environments of merging and non-merging galaxies.

To summarise this section, to induce significant levels of AGN activity in galaxies, comparably high central gas densities, and low gas temperatures are prerequisites. Since at $z \leq 1$, these ISM properties already differ on average significantly right before the merger between active and inactive galaxies, nuclear activity in merging galaxies is not necessarily related to the merger event. Compared to non-merging AGN hosts, active galaxies undergoing a (major) merger are largely characterised by having lower gas temperatures and lower relative velocities, possibly due to (pre-)merger-induced cooling flows, promoting nuclear activity. Instead, the higher gas temperatures and higher relative velocities of non-merging AGN hosts, in particular for moderately luminous AGN, are likely compensated by higher BH masses, resulting in similar levels of nuclear activity as for merging AGN hosts.

5.5 Discussion

In this section, we discuss our results with respect to (i) the importance of mechanisms other than mergers for driving nuclear activity (section 5.5.1), (ii) limitations and caveats of our analysis (section 5.5.2), and (iii) to what extent our results (dis)agree with observations (5.5.3) and with previous model predictions (semi-analytic and semi-empirical models, section 5.5.4).

5.5.1 AGN fuelling processes: the role of the large-scale environment

Since our simulation predictions indicate that the majority of AGN, i.e. more than ∼80 per cent, cannot be fuelled by mergers (except for the most luminous AGN at $z = 2$), the question arises which mechanisms instead predominantly cause nuclear activity. In cosmological simulations, AGN activity can be principally driven by smooth accretion of gas originating from cooling from a hot halo, from mass loss via stellar winds, or gas inflows from and, thus, depending on the large-scale filamentary structure[12]. While a detailed analysis of the relative importance of such different mechanisms clearly goes beyond the scope of this paper, we briefly discuss the possible importance of the environment/filamentary structure of galaxies on their nuclear activity.

When employing an often used density criterion to characterise the environment (number counts of neighbouring galaxies within 1 or 2 Mpc), we do not find any relation between the central gas density (governing BH accretion) and the density of the environment. Instead, Steinborn et al. (2016) showed that to specifically study the role of the filamentary

[12]Note that gas flows via violently unstable disks and/or secular evolution disk instabilities cannot be resolved in our simulations.

structure, the environment is well characterised by "tracing back" gas inflows: Steinborn et al. (2016) analyse 34 dual AGN, offset AGN and inactive BH pairs at $z = 2$ extracted from the Magneticum Pathfinder Simulations. They find that dual AGN on average accrete more gas originating from the surrounding medium (e.g. from filaments) than offset AGN or inactive BH pairs, suggesting the AGN activity is indeed correlated to "external" gas accretion (opposed to stellar mass loss and halo gas cooling) from large-scale filaments. To robustly address this issue, we plan to relate the gas density at large radii to that in the inner region in future work.

5.5.2 Caveats of large-scale cosmological simulations

All state-of-the-art cosmological simulations, also the Magneticum simulations considered in this work, generally suffer from limited resolution (> 0.7 kpc) and adopt phenomenologically motivated sub-grid schemes to model small-scale physical processes, such as BH accretion and AGN feedback. Here we discuss potential caveats originating from these short-comings for our analysis.

Inner gas flows and BH accretion

Due to limited resolution in cosmological simulations, innermost gas inflows ($<$ kpc) onto the central BHs cannot be resolved, likely affecting the resulting AGN luminosities, and potentially causing some further delay between the merger event and the peak in BH accretion. We additionally cannot resolve inner gas flows due to violently unstable discs, or secular evolution disk instabilities, impeding us to draw any conclusion on their potential role for causing AGN activity.

BH accretion is estimated by the idealized Bondi model by virtue of equation (3.1), which is known to be a good approximation just for spherical accretion (i.e., for hydrostatic hot gas). However, not only that cosmological simulations hardly resolve the Bondi radius, the Bondi scheme seems to be also a poor model for describing the accretion of cold, turbulent gas (e.g., Hopkins & Quataert, 2011; Gaspari et al., 2013; Steinborn et al., 2015; Anglés-Alcázar et al., 2017). Thus, particularly at higher redshifts and/or lower mass galaxies, when a lot of cold gas is likely to be accreted onto the BH (Hopkins & Quataert, 2011), AGN luminosities could strongly be affected. Also increasing the resolution, which decreases the accretion radius, can influence BH accretion rates and AGN luminosities due to changing gas properties in the vicinity of the BH. Even if adopting different BH accretion models or increasing the resolution would not affect merger histories of AGN hosts, AGN merger fractions could change, because of the dependence of the AGN luminosities on the accretion model/resolution. Nonetheless, we do not expect that such modifications would dramatically increase AGN merger fractions so that merger events would still play only a minor role for fuelling nuclear activity.

AGN feedback

To model AGN feedback, a fraction of the released accretion energy is injected into the ambient medium as a purely thermal energy input. Steinborn et al. (2015) and Hirschmann et al. (2014) have shown that such an AGN feedback scheme is a bit too inefficient, resulting in too many too massive and too star-forming galaxies. Moreover, even if the evolution of AGN luminosity functions is well reproduced (Hirschmann et al., 2014), we over-estimate the number density of massive, radiatively efficient BHs at low z (Schulze et al., 2015). A different AGN feedback model, which regulates more efficiently the gas content around massive BHs in massive galaxies (see, e.g., Weinberger et al., 2017; Choi et al., 2017) would lead to an earlier shut-down of AGN. As a result, at low redshifts, the amount of AGN originating from smooth gas accretion onto a massive BH might be reduced, which may slightly increase AGN merger fractions. To test this hypothesis, for the future, we plan to run a new simulation set with an improved AGN feedback model, where the effect of the feedback model on the AGN merger rates can be investigated in detail.

5.5.3 Comparison to observations

We have demonstrated that the predictions from our simulations are consistent with recent observations, in the sense that the majority of nuclear activity is unlikely caused by merger events. Simulations can also reproduce the observed increase of AGN merger fractions with increasing luminosity (Treister et al., 2012, Fan et al., 2016) at $z = 2$, but not at $z \leq 1$. These observations are, however, collected from different data sets of various studies in different redshift and luminosity ranges, applying different selection criteria (Bahcall et al., 1997; Urrutia et al., 2008; Georgakakis et al., 2009; Koss et al., 2010; Kartaltepe et al., 2010; Cisternas et al., 2011; Schawinski et al., 2011; Kocevski et al., 2012; Schawinski et al., 2012; Lanzuisi et al., 2015; Kocevski et al., 2015; Hong et al., 2015; Glikman et al., 2015; Del Moro et al., 2016; Wylezalek et al., 2016). Thus, a quantitative comparison of merger rates in simulations and these observations is complicated by two main reasons: (i) the huge variety of different selection criteria adopted in various observational studies and (ii) the intrinsically different merger identifications in observations and simulations.

Regarding the latter, we adopt a specific definition for tagging a galaxy major or minor merger in simulations: the SUBFIND algorithm defines the exact snapshot/time, at which two galaxies are bound to each other for the first time, such that the exact merger history of AGN hosts can be quantified. How long galaxies/AGN hosts are traced back in time to identify mergers, i.e. 0.5 Gyr, is a choice we made to capture typical timescales of galaxy mergers.

In profound contrast, in observations the identification of merger events is usually done on a visual basis at the same time the AGN luminosity is measured, thus neglecting any potential delay between the merger and significant levels of nuclear activity. A further consequence of a visual merger classification is that mostly/only major mergers can be identified, since minor mergers are not resolved properly and/or do not leave any clear visual signature in the morphological structure of a galaxy. These limitations of observa-

tions imply that observed merger detections might be underestimated, compared to our theoretical definition in simulations. For an accurate comparison between simulations and observations, a construction of mock images would be necessary, applying the same visual merger classification criteria and combining them with other observational selection criteria – clearly beyond the scope of this study.

5.5.4 Comparison to previous theoretical predictions

In previous studies, both semi-empirical as well as semi-analytic models have been used to investigate the relevance of different fuelling mechanisms, including merger events, for nuclear activity in galaxies. We now briefly discuss, how previous results compare to our findings in this work.

Semi-empirical models

The very first tools to study BH evolution in a statistical context have been phenomenological and semi-empirical models. These are characterized by a bottom-up approach. The least possible assumptions and associated parameters initially define the models. Gradually, additional degrees of complexities can be included, wherever needed. In semi-empirical models (e.g. Hopkins et al., 2009; Zavala et al., 2012; Shankar et al., 2014) galaxies (and eventually their central BHs) are not grown from first principles but they are assigned to host dark matter haloes via abundance matching techniques (e.g. Vale & Ostriker, 2004; Shankar et al., 2006) and allowed to merge following their dark matter merger trees.

Among the results obtained from these type of models more relevant to the present work, we recall: (i) the declining AGN duty cycle and characteristic Eddington ratio of active BHs with time, possibly following an overall cosmic starvation (e.g. Shankar et al., 2013); (ii) the relatively minor role of mergers in building galaxies (and their BHs) with stellar mass $\log M_{\rm stellar} \leq 11 M_{\odot}$ (e.g., Lapi et al. 2018 and references therein); (iii) the key role of AGN feedback in shaping in particular the most massive galaxies (e.g. Fiore et al., 2017).

Semi-empirical models have shown that galaxy-galaxy mergers can easily account for the vast majority of AGN at least at $z > 1$ (e.g. Wyithe & Loeb, 2003; Shen et al., 2009). However, at high redshifts and high masses, haloes are rarely destroyed once formed (e.g. Sasaki, 1994). Thus halo merger rates can be also viewed more straightforwardly as halo formation rates, usually conducive to gas-rich and rapid galaxy/BH formation episodes (e.g. Granato et al., 2004; Lapi et al., 2006; Di Matteo et al., 2012). Only at $z < 1 - 1.5$ the merger/halo formation model starts breaking down and becoming distinct from more general gas-rich galaxy/BH triggering events (e.g. Menci et al., 2003; Vittorini et al., 2005; Draper & Ballantyne, 2012). Thus, all semi-empirical studies tend to align with the conclusion that intermediate-to-major mergers may fall short in accounting for the full statistics of low-luminosity AGN at $z < 1$ (e.g. Scannapieco & Oh, 2004; Shen et al., 2009; Draper & Ballantyne, 2012).

Semi-analytic models

In contrast to phenomenological and semi-empirical models, in SAMs, dark matter halo merger trees are populated with galaxies and BHs via modelling baryonic processes *from first principles*. Historically motivated by binary merger simulations, "last-generation", but also most "state-of-the-art" SAMs (Somerville et al., 2008; Croton et al., 2006; De Lucia & Blaizot, 2007; Bonoli et al., 2009; Henriques et al., 2015; Hirschmann et al., 2016) assume that AGN activity is purely triggered by merger events (see, however, Bower et al., 2006), even though different implementations regarding minor/major mergers and BH growth curves have been developed. Such merger-driven BH models disagree with the results from cosmological simulations, presented in this work.

It has been, however, repeatedly shown that adopting a purely merger-driven BH growth scenario in SAMs largely fails to reproduce the evolution of the observed AGN luminosity function and the corresponding antihierarchical trend in BH growth, due to severely underestimating the number density of faint/moderately luminous AGN at low redshifts (see, however, Bonoli et al., 2009). To overcome this deficiency, different solutions have been proposed: nuclear activity has been adopted to be additionally driven by (i) secular evolution disk instabilities (Hirschmann et al., 2012), (ii) galaxy fly-bys (Menci et al., 2012), and/or (iii) hot gas accretion onto the BH (ADAF model, Fanidakis et al. 2012), or a combination of these processes. In most of these enhanced SAMs, merger events are, however, still necessary to predict a large enough amount of most luminous AGN (Hirschmann et al., 2012; Menci et al., 2014) – a trend, qualitatively consistent with cosmological simulations (at least at $z = 2$). Overall, in SAMs (as in cosmological simulations), it remains unclear, which is the main driving mechanism for the majority of (moderately luminous) AGN.

5.6 Conclusion

In this work, we theoretically investigated the statistical significance of merger events for fuelling nuclear activity (on scales of a few kpc) in galaxies at $z = 0 - 2$. To conduct this analysis, we employed two cosmological hydrodynamic simulations from the Magneticum Pathfinder Simulation set: first, a simulation with a comparably small volume of $(68\mathrm{Mpc})^3$, but a resolution high enough to resolve galaxies' morphological structures, was used to explore light curves of central BHs of six individual example galaxies. Secondly, another simulation run, featuring large populations of even most luminous AGN, thanks to a fairly large cosmological volume of $(500\mathrm{Mpc})^3$, allowed us to study the relevance of mergers for fuelling nuclear activity over a wide AGN luminosity range in a global statistical context.

Analyzing our five test cases showed that merger events may significantly increase the probability for nuclear activity of a galaxy, but they do not necessarily boost the accretion onto BHs. In fact, analyzing the effect of a merger on nuclear activity is complicated by the high time-variability of BH accretion/AGN luminosity. To still perform a meaningful analysis, we investigated the effect of the recent merger history on AGN luminosity *for a statistically large sample of AGN* at a given time-step. Specifically, we can summarise the

following main results:

- In galaxy populations, recent major/minor events can increase the probability for nuclear activity in galaxies by up to half an order of magnitude at ≤ 1, never exceeding 20 per cent though, compared to that of galaxies with a quiet accretion history. At $z \sim 2$, instead, irrespective of the merger history, almost all galaxies contain an AGN, thanks to large amounts of dense gas present in galaxies at these early epochs.

- In AGN populations, *mergers cannot be the statistically prevalent fuelling mechanism for nuclear activity at* $z = 0 - 2$ *(hardly ever exceeding 20 per cent)*, except for very luminous AGN at $z \sim 2$. The high merger fractions (> 50 per cent) of such very luminous AGN at $z = 2$ reflect, however, to some extent intrinsically high merger rates of massive galaxies, in which luminous AGN preferentially reside.

- Despite the statistically minor relevance of mergers for nuclear activity, the probability for AGN hosts to have experienced a recent major and/or minor merger event can be *by up to three times higher* than that for inactive galaxies. Such elevated merger rates of active galaxies still point towards a connection between nuclear activity and merger events – consistent with the expectations from binary merger simulations.

- Investigating the ISM properties (gas density, gas temperature, relative velocity between BH and gas) in the vicinity of BHs shows that comparably high central gas densities and low gas temperatures are required (partly by construction via equation 3.1) to induce nuclear activity in galaxies. Such prerequisites can be already present right before a merger and thus, they are not necessarily caused by a merger event.

- Active, merging galaxies are characterised by lower gas temperatures and relative velocities compared to active non-merging galaxies, promoting nuclear activity. The higher gas temperatures and relative velocities of non-merging AGN hosts, instead, are compensated by higher BH masses, still enabling nuclear activity at moderate luminosities.

We conclude that, even if mergers may increase the probability for nuclear activity by a factor of three, they still play only a minor role for causing nuclear activity in the overall AGN population (< 20 per cent). This result is in profound disagreement with the traditional theoretical view, favouring a predominantly merger-driven BH growth/AGN activity, but it is consistent with a number of recent observational studies.

Despite this progress, our simulations/analysis do not allow us to draw any robust conclusion on the dominant fuelling mechanisms for AGN activity (disk instabilities, smooth accretion from hot halo, cold inflows, stellar mass loss etc.) and on the processes, which are actually driving the gas onto the central BHs at sub-kpc and sub-parsec scales, because of limited resolution and phenomenologically motivated models for BH accretion and feedback. Future theoretical studies performing "precision" cosmological simulations, by unifying a cosmological framework with the accuracy of detailed, small-scale simulations for modelling BH accretion and AGN feedback, will be certainly necessary to obtain

a full understanding of the relative, statistical importance of different fuelling/triggering mechanisms for nuclear activity.

Appendix: estimation of the merger mass ratio

In our simulations, the SUBFIND-output is given in smaller time-steps than the snapshots of the simulation, which are mostly about 0.5 Gyr apart. These snapshots are for example used to compute the gas parameters within the accretion radius. Since the information about galaxy mergers is given by the SUBFIND-output only, we can identify mergers also on smaller time-steps $t < 0.5$Gyr.

In Fig. 5.10 we illustrate our definition of galaxy mergers and how we estimate the stellar merger mass ratio, showing three different possible scenarios. The most massive galaxy is shown as red filled circle and the less massive progenitor galaxy is shown as blue filled circle. We know about the merger as soon as SUBFIND identifies the two progenitor galaxies as separate subhaloes (snapshot 3 in our example). These subhaloes can already be associated to the same dark matter halo, shown as black dashed circle. Let us at first concentrate on the example shown in the bottom row to understand why choosing the stellar masses in the snapshot right before the merger of the subhaloes would lead to artificially small merger mass ratios:

- SUBFIND associates the intra-cluster light (ICL, illustrated as stars) always to the most massive galaxy within a dark matter halo. Consequently, stars which originally belonged to the smaller progenitor galaxy (blue stars in the sketch) are associated to the larger galaxy as soon as the two progenitors are within the same dark matter halo (snapshots 2 and 3 in our example). Thus, the mass of the less massive galaxy would be underestimated and the mass of the more massive galaxy would be overestimated.

- In addition, it is possible that the two galaxies already interact. In that case effects like stellar stripping can also lead to an association of the stripped stars to the larger galaxy. Furthermore, some of the stars from the less massive galaxy might already have been accreted by the more massive one.

To avoid these artificial problems, the merger mass ratio is generally computed before the two dark matter haloes merge (upper row in Fig. 5.10). However, this is often long before the actual merger of the galaxies. Thus, between the merger of the dark matter haloes and the merger of the subhaloes, the galaxies might for example accrete or form a significant amount of stars. Therefore, to further improve the method, we use the masses before the merger of the dark matter haloes only in cases, where the mass of the satellite galaxy is larger than afterwards. Therefore, we always trace the progenitor galaxies back to the last snapshot where they had separate dark matter haloes (snapshot 1 in our examples). All in all we get the best estimate for the merger mass ratio when we choose the maximum stellar mass of the smaller progenitor galaxy within all snapshot from the identification of the merger to the last snapshot with separate dark matter haloes. This might be, as

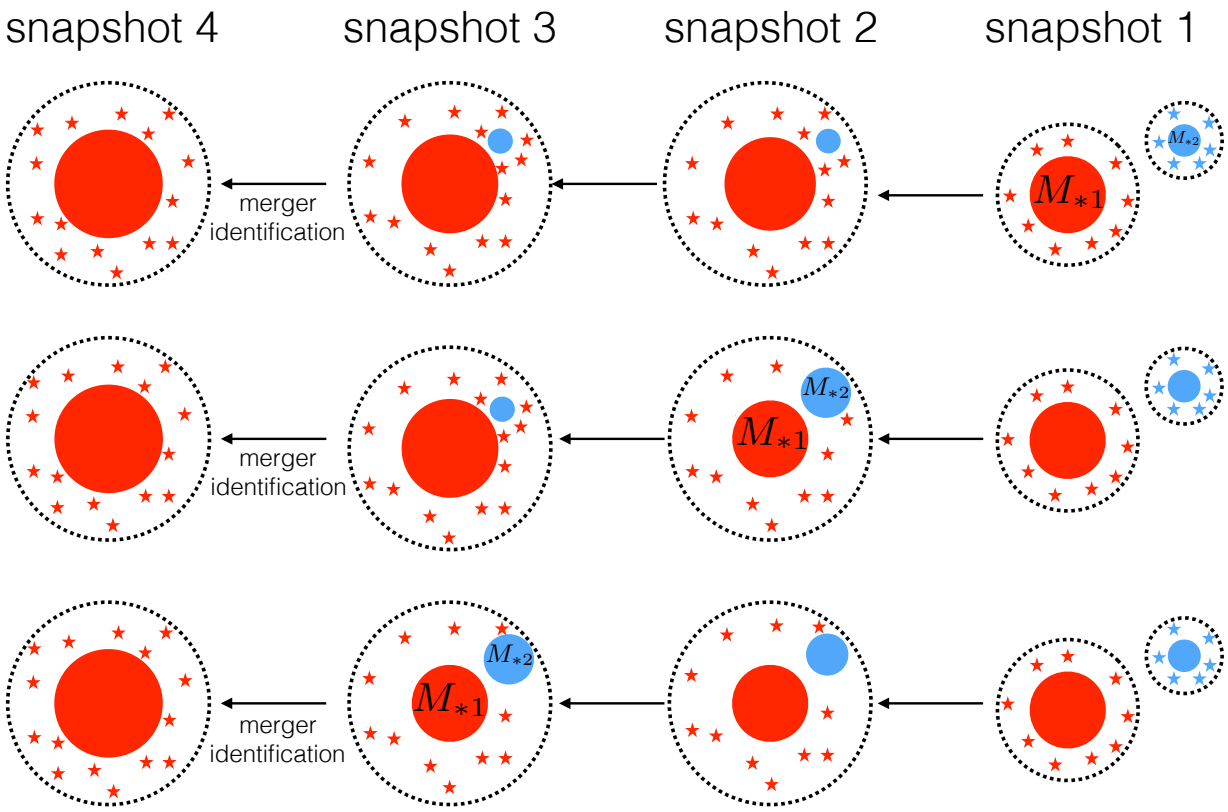

Figure 5.10: This sketch shows three different scenarios to illustrate of our definition of mergers and of the stellar merger mass ratio. The arrows show the direction of the time-line. The most massive galaxy is shown in red and the smaller progenitor is shown in blue. The filled circles show the galaxies and the dark matter halo is shown as dashed black line. The stars illustrate the intra-cluster light (ICL), which is always associated to the most massive galaxy within a dark matter halo. The size of the circles is associated to the stellar mass, which consists of the galaxy plus the ICL. Due to that definition of the stellar mass including the ICL and also to exclude effects like stellar stripping, the stellar masses in the last snapshot where SUBFIND identifies two galaxies are no good proxy to estimate the stellar merger mass ratio. Thus, we trace the progenitor galaxies from the snapshot in which the merger was identified back until they were associated to different haloes. To estimate the stellar merger mass ratio we use the maximum mass of the second progenitor galaxy within all snapshots from the identification of the merger to the last snapshot in which they belonged to different haloes. In the three examples from top to bottom, the mass of the second progenitor galaxy is the largest in snapshot 1, 2, and 3, respectively.

generally assumed, before the merger of the dark matter haloes (upper row in Fig. 5.10), right before the identification of the galaxy merger with SUBFIND (bottom row in Fig. 5.10), or in between (middle row in Fig. 5.10).

Chapter 6

AGN clustering predictions by a large-scale hydrodynamic simulation: the halo occupation distribution

The content of this chapter is part of an upcoming paper (Steinborn & Krumpe et al., in prep.), which will soon be submitted:

> **Steinborn** & Krumpe et al. (in prep.): *AGN clustering predictions by a large-scale hydrodynamic simulation I: the halo occupation distribution*

Abstract

Using a large-scale, cosmological hydrodynamic simulation from the Magneticum Pathfinder Simulation set, we present predictions for the halo occupation distribution (HOD) of AGN. The large simulation volume of $(909\mathrm{Mpc})^3$ allows us to study clustering properties even for very luminous AGN, while the resolution is sufficiently high to model the accretion onto black holes (BHs) and their related AGN feedback self-consistently. Without any additional tuning, the simulation reproduces the observed HOD of galaxies sufficiently well. In combination with our advanced dynamical treatment of BHs, this provides an ideal testbed to study how the HOD of AGN differs from that of the overall BH sample and how it depends on different selection criteria. We find that the HOD of AGN is much more complex than the HOD of galaxies and can be described as a superposition of the HOD of three distinct AGN populations: satellite AGN and two different populations of central AGN, which are characterized by different environments, BH masses, and accretion modes. These results strongly indicate that AGN are not random events. Instead, different AGN types represent different evolutionary stages of their host galaxies.

6.1 The HOD of galaxies

Before we have a look onto the HOD of AGN, we want to verify that our simulated galaxies are distributed realistically. To obtain the HOD observationally, correlation functions are measured and, later-on, an HOD model is used to obtain the mean number of objects in haloes with mass M_h. In contrast to the HOD of AGN (e.g. Miyaji et al., 2011; Richardson et al., 2012; Kayo & Oguri, 2012), the parameters describing the HOD of galaxies are well known (e.g. Tinker et al., 2005; Zheng et al., 2009; Zehavi et al., 2011). The mean number of galaxies within dark matter haloes of mass M_h can generally be obtained using a five parameter fit (Zehavi et al., 2011):

$$\langle N(M_\mathrm{h})\rangle = \frac{1}{2}\left[1+\mathrm{erf}\left(\frac{\log M_\mathrm{h}-\log M_\mathrm{min}}{\sigma_{\log M}}\right)\right]\cdot\left[1+\left(\frac{M_\mathrm{h}-M_0}{M_1'}\right)^\alpha\right] \tag{6.1}$$

where α is the HOD slope, M_min gives the halo mass where the power law breaks down, $\sigma_{\log M}$ describes how smooth this break-down is, and M_0 and M_1' are normalization parameters. Thereby, the two parts of equation (6.1) correspond to central and satellite galaxies, respectively. In Fig. 6.1, we compare the HOD of our simulated galaxies with the best fit of the observations from Zehavi et al. (2011) for different r-band magnitude thresholds $M_\mathrm{r} < -20.5, -21.0, -21.5, -22.0$, shown as dotted lines. The upper panel shows the HOD of all galaxies, in the middle and bottom panel we split up between satellites and central galaxies.

In contrast to observations, simulations have the advantage that we know the exact three dimensional position of each galaxy at different times. Furthermore, we know which galaxies are gravitationally bound to each other and form groups or clusters of galaxies, where several galaxies live within the same dark matter halo. Within a galaxy cluster or a group, SUBFIND always identifies one central galaxy, which is surrounded by satellite galaxies (also called substructures). Hence, simulations allow us to *directly* estimate the number of galaxies within a dark matter halo. Our simulation results and the corresponding bootstrapping errors are show as blue solid lines and shaded areas. Since M_r is difficult to obtain from simulations, we instead use stellar mass thresholds: $M_* > 10^{11}M_\odot, 10^{11.5}M_\odot, 10^{12}M_\odot$. Due to these different selections of simulated and observed galaxies, the break-down of the power law is much less smooth for the simulated galaxy samples than for the observed ones. However, this break-down is anyway artificial due to the selection and does not have any physical implications. Also, the exact values of M_* or M_r are not important for this study, because we are only interested in the distribution of the galaxies. A better orientation for comparing simulations and observations is given by the number density, which is given in $10^{-2}h^3\mathrm{Mpc}^{-3}$ above the lines in the legend of Fig. 6.1, for each galaxy sample. Thus, we can for example compare the HOD of our simulated galaxies with stellar masses $M_* > 10^{11.5}M_\odot$ (middle blue line) with that of observed galaxies with $M_\mathrm{r} < -21.5$ (orange dotted line). Besides the difference in the curvature of the break-down, there is a little shift between the observed and the simulated HOD curves, which probably originates from the difference in the dark matter halo mass function of our simulation and the one used in Zehavi et al. (2011). Nonetheless, the HOD slope of the simulated galaxies is always

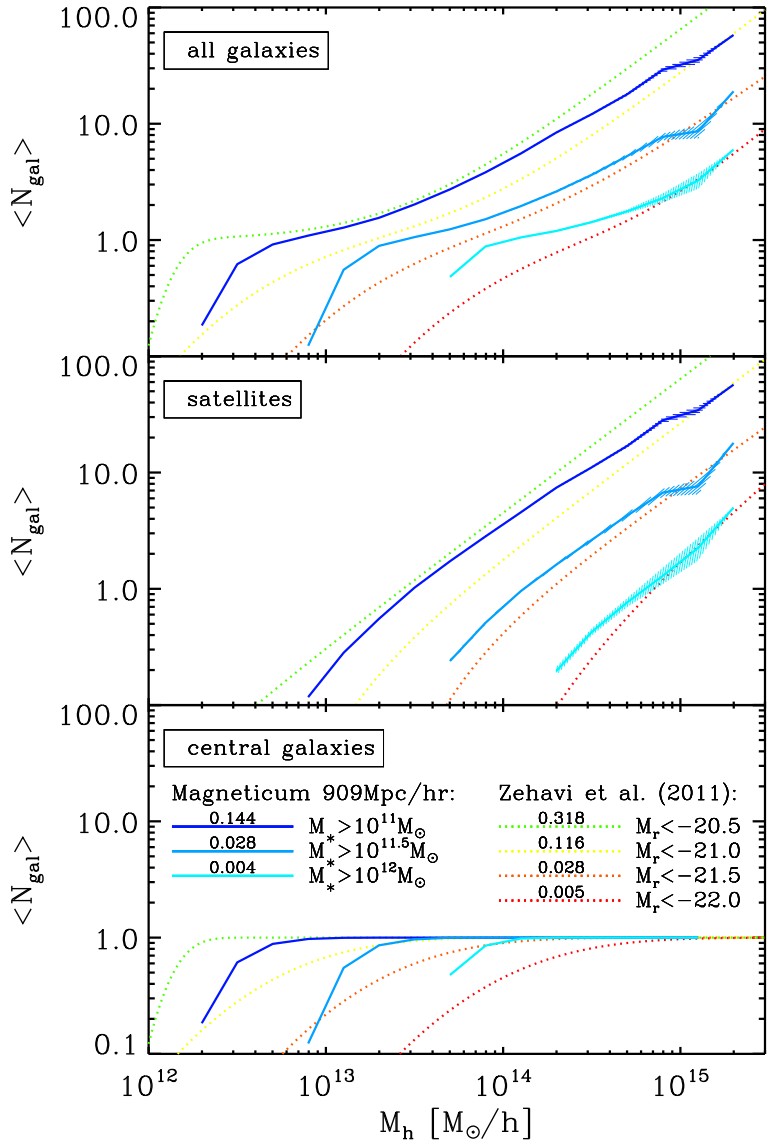

Figure 6.1: Mean number of all galaxies (upper panel), satellite galaxies (middle panel), and central galaxies (bottom panel) within a dark matter halo of mass M_h at $z = 0.25$. The blue solid lines show the simulation results above different stellar mass thresholds ($10^{11} M_\odot$, $10^{11.5} M_\odot$, and $10^{12} M_\odot$). The shaded area shows the corresponding bootstrapping errors. We compare the simulated HOD with that of observations from Zehavi et al. (2011, dotted lines). The observed galaxies are selected by their r-band magnitudes M_r, which, however, cannot be estimated exactly from the simulation. To still compare the simulation with the observations, the number density of each galaxy sample is given in $10^{-2} h^3 \mathrm{Mpc}^{-3}$ above the lines in the legend. Since the simulated galaxies are selected by their mass, the curvature of the cut-off is larger for the simulated galaxies than for the observed ones. However, the HOD slopes are very similar for simulated and observed galaxies (always ~ 1).

around $\alpha \sim 1$, which is in very good agreement with the observations. Thus, switching to simulated AGN, we verify that all trends we will show in Section 6.3 are due to the underlying (simulated) physics which drive AGN activity.

6.2 Comparison of simulated AGN samples with observations

6.2.1 Adopting selection effects from observations

Obscuration

X-ray observations of AGN have the caveat that only Type1 AGN are detected. Therefore, we select unobscured AGN randomly. Following Hasinger (2008), the fraction of obscured AGN for $z \leq 2$ is given by

$$f_{\rm obsc}(z, L_{\rm SXR}) = -0.281(\log(L_{\rm SXR}) - 43.5) + 0.279(1+z)^{\beta}, \tag{6.2}$$

where $\beta = 0.62$. For $z > 2$, $f_{\rm obsc}$ is approximately the same for $z = 2$. However, selecting Type1 AGN has only a minor effect on our AGN sample (Fig. 6.2). Throughout this analysis, we show the HOD only for unobscured AGN, to be comparable to observations as good as possible. Thereby, we explicitly verified that our results show no qualitative difference between the total and the unobscured AGN sample.

X-ray luminosity

We convert $L_{\rm bol}$ into a soft X-ray (SXR) luminosity in the 0.5-2keV band following Marconi et al. (2004):

$$\log(L_{\rm SXR}/L_{\rm bol}) = -1.65 - 0.22\mathcal{L} - 0.012\mathcal{L}^2 + 0.0015\mathcal{L}^3 \tag{6.3}$$

with $\mathcal{L} = \log(L_{\rm bol}/L_{\odot}) - 12$. Throughout this analysis, we will always use the SXR-luminosity, except for Section 6.2.2, where we compare with the observed RASS AGN from Krumpe et al. (2010) and convert $L_{\rm SXR} = L_{0.5-2keV}$ into $L_{0.1-2.4keV}$ following Lusso et al. (2012):

$$L_{0.1-2.4keV} = 3.56 \cdot L_{0.5-2keV}. \tag{6.4}$$

We note that this conversion is only appropriate for high luminosity AGN, which is the case for our selected AGN sample.

Flux limit

Finally, we convert $L_{0.1-2.4\rm keV}$ into a ROSAT X-ray flux $f_{0.1-2.4\rm keV}$ following Krumpe et al. (2007):

$$L_{\rm X} = \frac{4\pi d_{\rm L}^2}{(z+1)^{0.5}} f_{\rm X}, \tag{6.5}$$

where $d_{\rm L}$ is the luminosity distance. To obtain the observed flux cut, we use the completeness function from the observations.

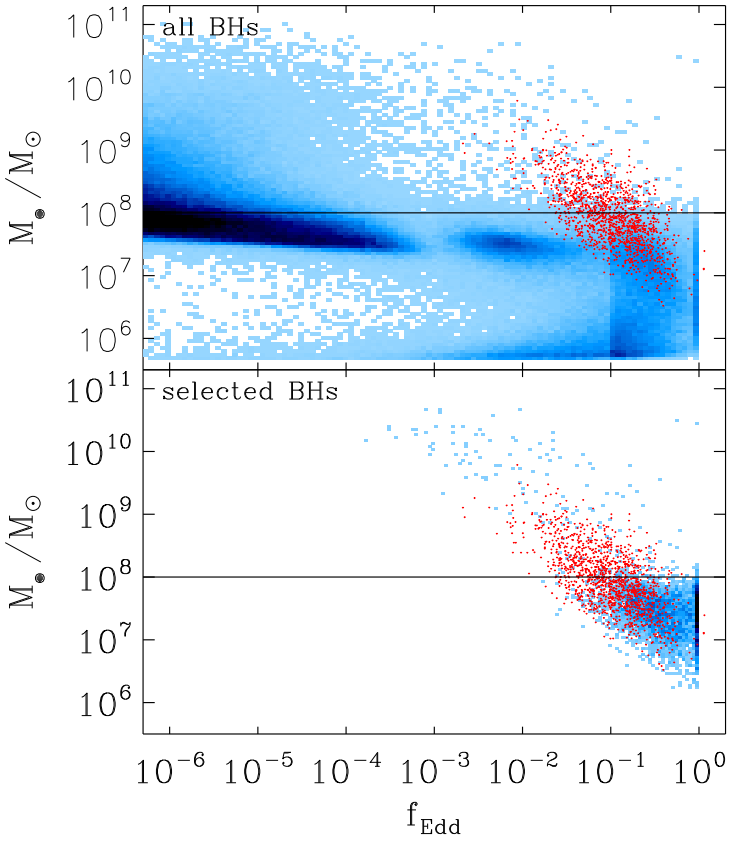

Figure 6.2: Simulated BH mass versus $f_{\rm Edd} = L_{\rm Xray}/L_{\rm Edd}$ (blue contours) for the 500Mpc/hr simulation run, compared with observations (red dots) from Krumpe et al. (2010). *Upper panel:* all simulated BHs. *Lower panel:* unobscured BHs above the same flux cut as in the observations.

6.2.2 The $M_\bullet$-$f_{\rm Edd}$ plane and simulation limits

In Fig. 6.2 we show the distribution of BHs in the $M_\bullet$-$f_{\rm Edd}$ plane for the 500Mpc/hr simulation run. Throughout this analysis, $f_{\rm Edd}$ is defined as $f_{\rm Edd} = L_{\rm Xray}/L_{\rm Edd}$. Simulated BHs are depicted as blue contours and red dots are observed BHs from Krumpe et al. (2010). The upper panel shows all simulated BHs, while the lower panel shows only Type1 AGN after obtaining the flux limit from the observations. The black horizontal line marks our resolution limit of $10^8 M_\odot$, which corresponds to the break-down in our simulated BH mass function (Fig. 5 in Hirschmann et al., 2014). Although the majority of simulated AGN is located below the black line, a direct comparison with observations is only possible excluding observed BHs below this mass threshold for both the simulated and the observated data.

The distribution of simulated BHs in the $M_\bullet$-$f_{\rm Edd}$ plane clearly shows the limits of

current state-of-the-art cosmological simulations, as well as of observations. In particular, many under-massive BHs accrete at the Eddington limit. In the model described in Steinborn et al. (2015) this issue is solved by smoothing out the accretion process using a mass dependent feedback efficiency. However, the simulated volume from Steinborn et al. (2015) is too small to make predictions for AGN clustering measurements. Since the affected BHs are below the resolution limit, we decided to use the much larger simulation run without the model from Steinborn et al. (2015) for this analysis. The apparent disagreement between observations and the simulation at large BH masses and low $f_{\rm Edd}$ values is expected, since AGN with $f_{\rm Edd} \lesssim 0.01$ are not visible in the X-ray observations from Krumpe et al. (2010). However, observations of AGN in the central galaxies of very massive galaxy clusters do reveal that such relatively inefficiently accreting luminous AGN do indeed exist (Russell et al. 2013, see Fig. 2 in Steinborn et al. 2015). Despite that, efficiently accreting BHs grow too massive, leading to a slight overestimation of the high luminosity end. However, although the BH masses are overestimated, we expect that these BHs would still be visible in observations, but with a smaller luminosity. Since we are not interested in the exact AGN properties, but in the overall distribution of AGN, we conclude that our AGN sample is still sufficient to make predictions for the HOD of AGN, at least within our resolution limits.

6.3 The HOD of AGN

While galaxy HOD parameters are very well known from observations (e.g. Zehavi et al. 2011), the HOD of AGN is not yet fully understood. Since the observed number density of AGN is much smaller than the number density of galaxies, in particular at low redshifts, statistics are not good enough to perform a five parameter fit like in equation 6.1. Instead, a very simplified model, reduced to only two parameters, i.e. the cut-off mass $M_{\rm min}$ and the HOD slope α, is fitted (e.g. Miyaji et al., 2011). While $M_{\rm min}$ is due to the observational limits, in particular the flux cut, α is a measurement of the distribution of AGN. Since this model is very simple, simulations are very useful to better understand the HOD of AGN and to construct more sophisticated, physically motivated HOD models. In this section we show the HOD for different simulated AGN samples, depending on the minimum BH mass, redshift, X-ray luminosity, as well as for AGN with low/high f_{Edd} values.

6.3.1 The BH mass threshold

In Fig. 6.3 we show the HOD of AGN above different BH mass thresholds at $z = 0.25$, considering all AGN with $L_{\rm SXR} > 10^{42}$erg/s. The grey dashed line marks our conservatively chosen resolution limit of $M_{\rm h} > 10^{12} M_{\odot}/h$. For orientation the grey dashed line shows an arbitrary line with a slope of $\alpha = 1$, which is expected for satellite galaxies. The differently coloured lines show the HOD for different BH mass thresholds. However, before we will have a look at these different mass thresholds, we will concentrate on the total simulated AGN sample above our resolution limit $M_{\bullet} > 10^{8} M_{\odot}$, which is represented by the blue

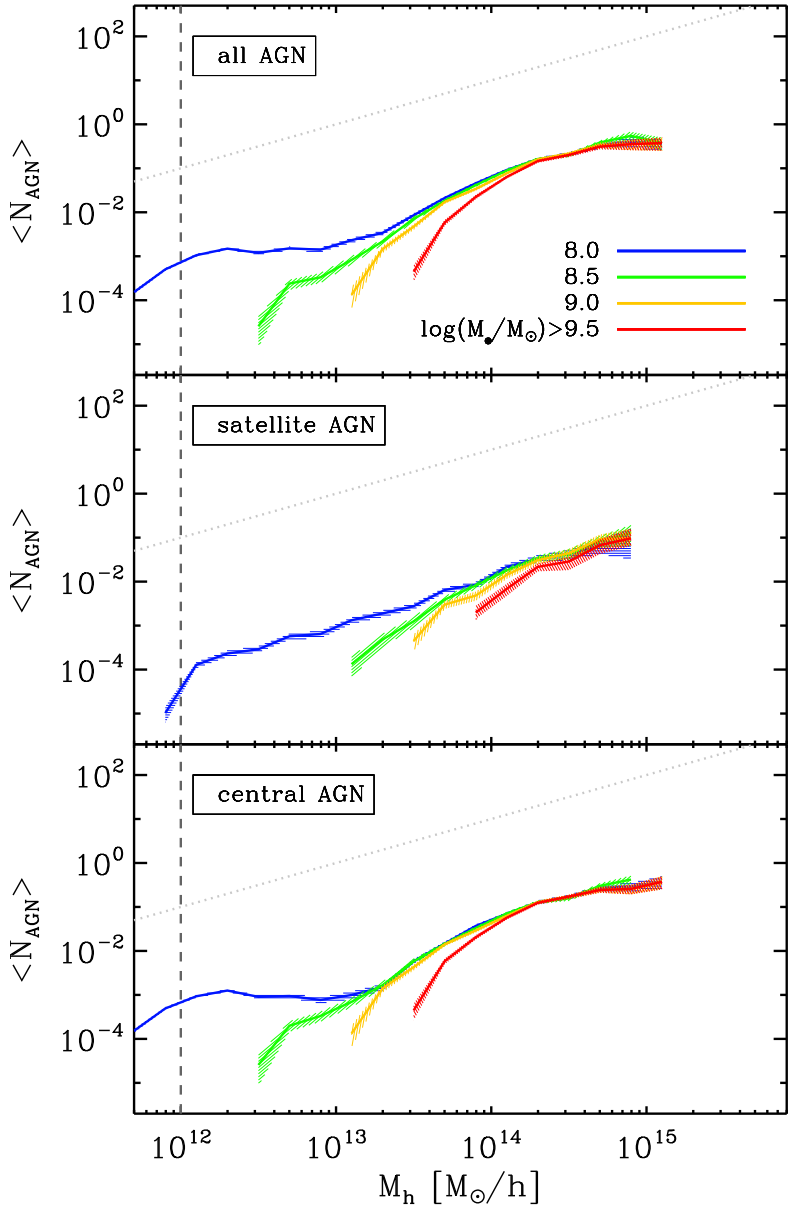

Figure 6.3: Mean number of AGN in a halo with mass $M_{\rm h}$ for different thresholds in the BH mass (differently coloured lines), at $z = 0.25$. The shaded areas are the corresponding bootstrapping errors. For this figure, we consider all unobscured AGN with $L_{\rm SXR} > 10^{42}$erg/s. The three panels show the total AGN sample (upper panel), only AGN in satellite galaxies (middle panel), and central AGN (bottom panel). The grey dashed line marks our resolution limit and the grey dotted line is, for orientation, an arbitrary line with slope $\alpha = 1$.

curves. Similar to the HOD of satellite galaxies (Fig. 6.1), the HOD of satellite AGN (middle panel of Fig. 6.3) converges towards a line with slope α. The break-down of this line at low halo masses is below our resolution limit. Turning towards central AGN (bottom panel), we find a much more complex shape of the HOD curve, which can roughly be divided into AGN within less massive haloes (mostly isolated galaxies) and AGN in more massive haloes (galaxy groups and clusters). Thus, the HOD of AGN cannot be described with equation (6.1). As a natural consequence of the $M_\bullet$-M_* relation and the relation between M_* and M_h, massive BHs reside in more massive dark matter haloes. Thus, setting higher BH mass thresholds (green, yellow, and red curve), only the AGN population in more massive haloes is visible. Comparing the differently coloured curves shows that the break-down at low halo masses clearly depends on the minimum BH mass: the larger the BH mass threshold the larger is the cut-off halo mass. For halo masses above this cut-off mass the curves saturate towards a line with slope α. For central AGN, this slope appears to be zero. Thus, the fraction of central AGN is a constant value for very massive haloes, probably since AGN activity follows a well defined duty cycle as soon as a halo is relaxed. For satellite AGN, there might also be a break-down, which shifts towards larger halo masses with increasing BH mass threshold. However, this is not clearly visible in Fig. 6.3.

6.3.2 Redshift evolution

Fig. 6.4 shows the redshift evolution of the mean number of AGN with $L_\mathrm{SXR} > 10^{42}\mathrm{erg/s}$ and $M_\bullet > 10^8 M_\odot$ in a halo within a certain mass range. The redshift evolution of the corresponding HOD slope is summarized in the first panel of Fig. 6.7. At high redshift, we expect that AGN activity occurs randomly, since all galaxies should contain enough gas to feed an AGN. Therefore, the number of central AGN converges to a constant value, which decreases with time. For the same reason, the mean number of AGN increases with redshift for $z \leq 2.0$. For $z = 4.2$ the haloes are in general too less massive such that we do not yet reach the halo mass limit, above which the saturation occurs. Thus, the HOD slope has to be taken with great caution at that redshift, but also at $z = 3.6$. Especially, large values of α would imply that on average more than one AGN is hosted by each central galaxy, which is, despite the small fraction of dual AGN, unphysical. Therefore, the upturn in the second panel of Fig. 6.7 at high redshifts reflects our resolution limit rather than the distribution of AGN.

At lower redshifts ($z \leq 2$), the HOD slope decreases with redshift. This is probably a consequence of the evolution of dark matter haloes and the related driving mechanisms of AGN activity: at high redshifts, enough gas is present to drive strong AGN activity, also of less massive BHs, which reside in less massive haloes. With time, the gas reservoir is used up due to AGN activity and star formation and thus, AGN activity is mostly very inefficient. To still reach high AGN luminosities, large BH masses are required (equation 3.1), thus increasing the fraction of AGN in massive haloes with respect to that in less massive haloes.

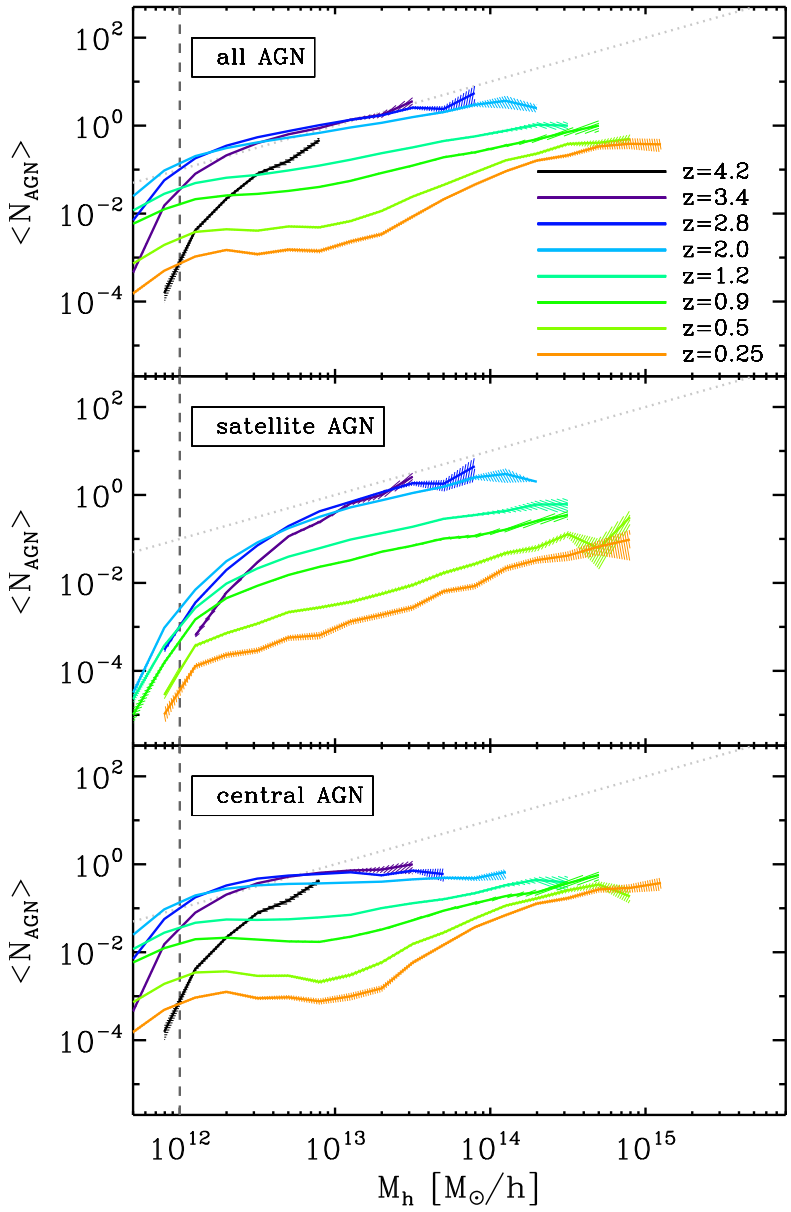

Figure 6.4: Same as Fig. 6.3, but for different redshifts. We consider all unobscured AGN with $L_{\rm SXR} > 10^{42}$ and $M_\bullet > 10^8 M_\odot$.

6.3.3 Dependence on the AGN luminosity

Fig. 6.5 shows the HOD of AGN in different luminosity ranges: 10^{42}erg/s $< L_{\rm SXR} < 10^{43}$erg/s (light blue lines), 10^{43}erg/s $< L_{\rm SXR} < 10^{44}$erg/s (green lines), and $L_{\rm SXR} > 10^{44}$erg/s (red lines). For comparison, the black solid line shows the HOD for all resolved BHs above our resolution threshold. For satellites the slope of this line is with $\alpha = 0.9$ below the value of $\alpha = 1.0$ (dashed line) for galaxies. However, since we do show only BHs with masses above $M_\bullet = 10^8 M_\odot$, we do not expect an agreement with the overall HOD slope of galaxies.

Comparing the slope of different AGN populations with that of the overall BH population reveals insights into their clustering and their typical environment. Compared to all resolved BHs, AGN have a slightly steeper HOD slope. This implies that AGN are not distributed randomly. Instead, they cluster slightly towards more massive haloes. Surprisingly, we find no dependence of the HOD slope on the luminosity threshold. For satellite AGN the HOD curve just shifts towards lower values the higher we choose the luminosity range. One reason might be that the luminosity itself does not contain information about the accretion mode or the BH mass, since it combines both quantities. Thus, the effect of the accretion mode and the BH mass on the shape of the HOD curve cancel out. We will have a closer look on the accretion modes in the next section.

Turning towards central AGN, we find similar HOD curves for the two luminosity ranges below 10^{44}erg/s. More luminous AGN, however, are much rarer in haloes with $M_{\rm h} \lesssim 10^{13} M_\odot/h$. In more massive haloes the HOD curve does not saturate towards a constant value, but has a relatively constant slope. This increase already begins at lower halo masses than for less luminous AGN. However, the constant slope might just be due to our limited simulation volume, limiting the number of very luminous AGN. Whether the curve would saturate at larger halo masses ($M_{\rm h} \gtrsim 10^{15} M_\odot/h$) remains unknown from our simulation.

6.3.4 Dependence on the Eddington ratio

In Fig. 6.6, we split up our sample into radiatively efficient AGN ($f_{\rm Edd} > 0.01$, green lines) and radiatively inefficient AGN ($f_{\rm Edd} < 0.01$, yellow lines). For a clearer separation between the two modes, we show the HOD for AGN with $f_{\rm Edd} > 0.001$ (light blue lines) and $f_{\rm Edd} < 0.001$ (red lines). For comparison, we also show the HOD of all resolved AGN (dark blue lines) and all resolved BHs (black lines). As expected, since the most massive BHs have low Eddington ratios, the central galaxies of galaxy groups and especially galaxy clusters ($M_{\rm h} > 10^{13} M_\odot/h$) mainly host very inefficiently accreting AGN with $f_{\rm Edd} < 0.001$. In contrast, AGN in less massive haloes (both satellite and central AGN) have larger $f_{\rm Edd}$ values, mostly above $f_{\rm Edd} = 0.01$. Hence, the HOD slope of AGN with lower $f_{\rm Edd}$ values is slightly flatter than for AGN with higher $f_{\rm Edd}$ values, although it is difficult to determine due to the low number of inefficiently accreting AGN in satellite galaxies (red line in the middle panel). Nevertheless, this is particularly interesting since it implies that efficiently accreting AGN are distributed differently than inefficiently accreting AGN. This

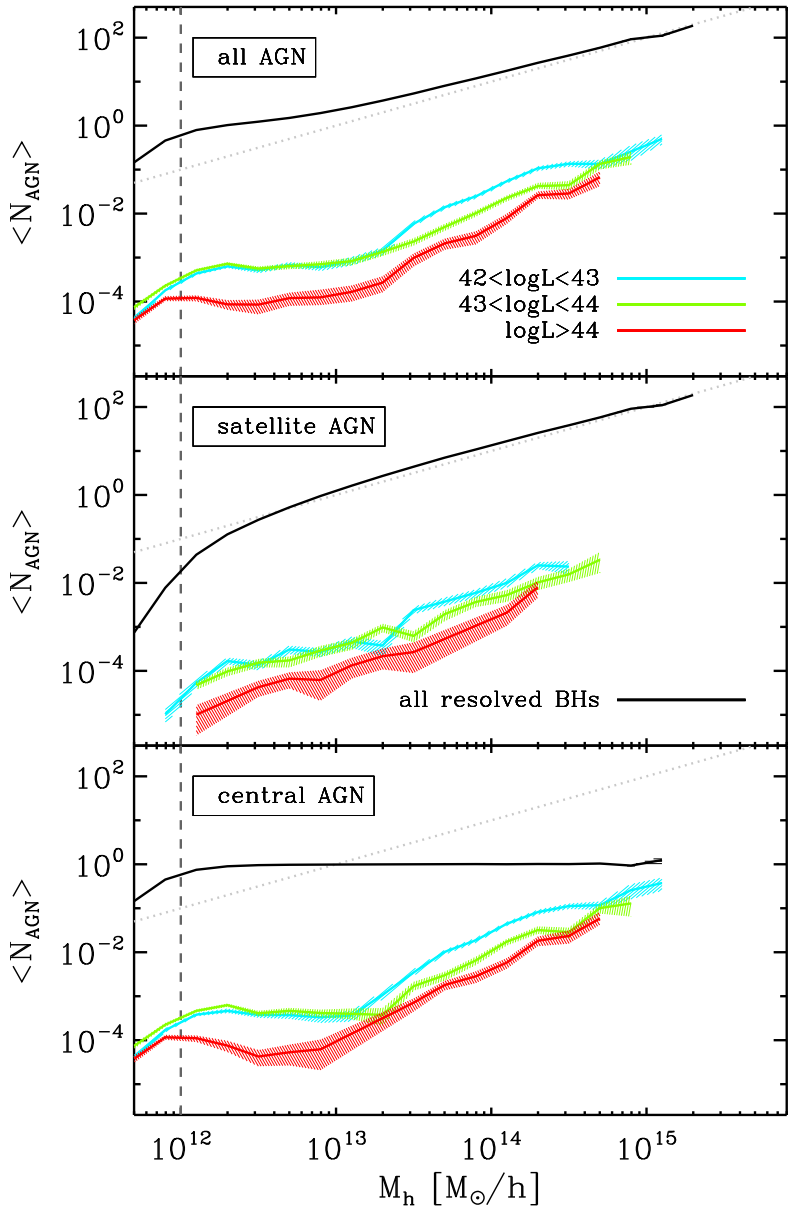

Figure 6.5: Same as Fig. 6.3, but for different luminosity ranges at $z = 0.25$. We consider all unobscured AGN with $M_\bullet > 10^8 M_\odot$.

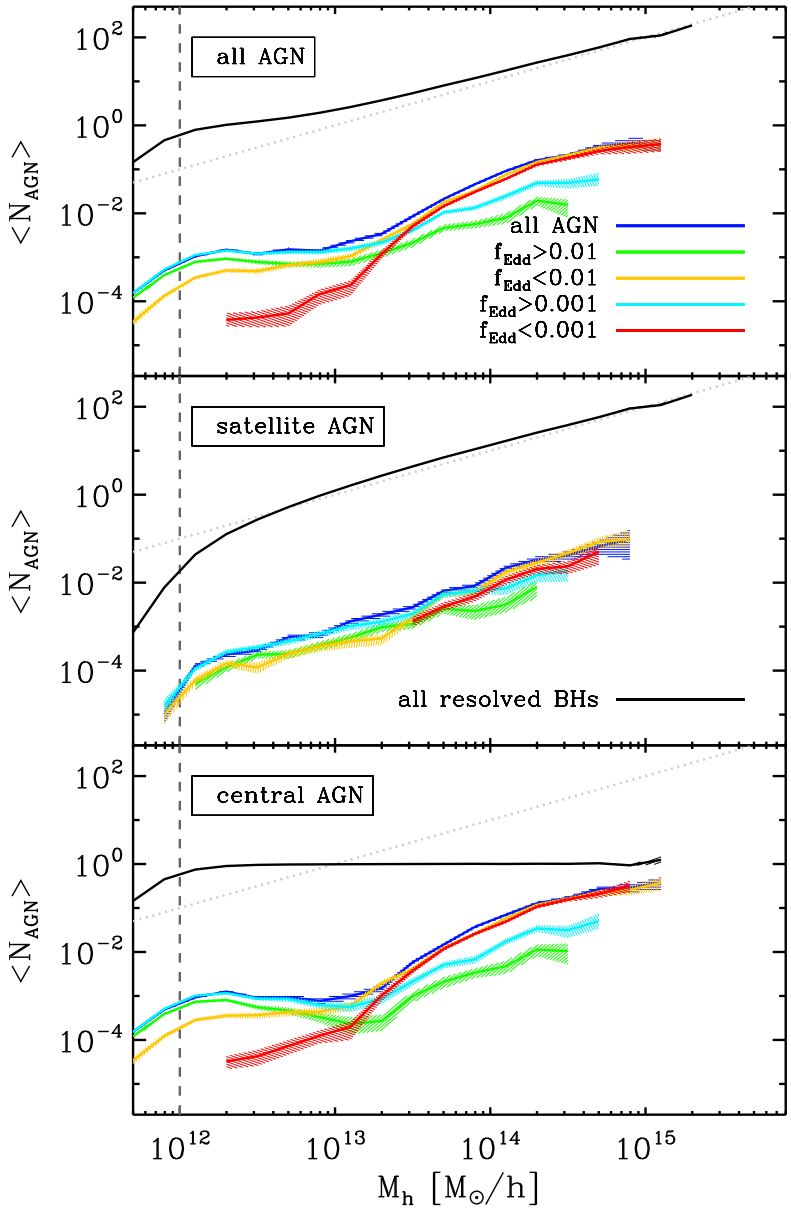

Figure 6.6: Same as Fig. 6.3, for AGN with low Eddington ratios ($f_{\rm Edd} < 0.01$, $f_{\rm Edd} < 0.001$) and with high Eddington ratios ($f_{\rm Edd} > 0.01$, $f_{\rm Edd} > 0.001$) at $z = 0.25$. We consider all AGN with $L_{\rm SXR} > 10^{42}$ and $M_\bullet > 10^8 M_\odot$.

can be understood with the evolutionary sequence of AGN, due to which quasars are an evolutionary stage driven by the available amount of cold gas in the host galaxy, which in general decreases with time. Thus, the distinction between radiatively efficient and radiatively inefficient AGN is largely a consequence of the different environments.

6.3.5 How to fit the HOD of AGN?

In literature the HOD of AGN is generally fit using only two parameters: the HOD slope α and the cut-off mass $M_{\rm min}$. However, we have seen in the previous sections that our simulation strongly points towards a more complex shape of the HOD curve. Specifically, Fig. 6.3 - 6.6 suggest that the total AGN population cannot be fitted by only splitting up into satellite AGN and central AGN, as it is done for galaxies. Instead, central AGN again split up into a low-mass population and a high-mass population (we refer to these populations as c1 and c2, respectively). All three populations can separately be fitted using a similar parameter fit than usually obtained for galaxies (equation 6.1), however, reducing it to only four parameters by adjusting the normalization parameters:

$$\langle N_{\rm x}(M_{\rm h})\rangle = f_{\rm x}\cdot\frac{1}{2}\left[1+{\rm erf}\left(\frac{{\rm log}M_{\rm h}-{\rm log}M_{\rm min,x}}{\sigma_{{\rm log}M,{\rm x}}}\right)\right]M_{\rm h}^{\alpha_{\rm x}}, \tag{6.6}$$

where x denotes the according AGN population, $C_{\rm x}$ is the normalization factor, ${\rm log}M_{\rm min,x}$ is the cut-off halo mass, $\sigma_{{\rm log}M,{\rm x}}$ describes the curvature of the cut-off, and $\alpha_{\rm x}$ is the HOD slope. The total HOD is then given by

$$\langle N_{\rm AGN}(M_{\rm h})\rangle = \langle N_{\rm s}(M_{\rm h})\rangle + \langle N_{\rm c1}(M_{\rm h})\rangle + \langle N_{\rm c2}(M_{\rm h})\rangle, \tag{6.7}$$

where s, c1, and c2 denote satellite AGN and the two distinct central AGN populations, respectively. Equation (6.7) has twelve free parameters – a far too complex model. In our simulations, however, we can easily distinguish between satellite and central AGN, reducing the problem to a four parameter problem for satellite AGN and an eight parameter problem for central AGN. The eight parameters for central AGN can be reduced to seven parameters by assuming that the fraction of AGN saturates towards a constant value for large $M_{\rm h}$ as soon as haloes are in equilibrium. Except for special merger events (which are not relevant for the overall AGN population), AGN activity then follows a constant duty cycle and thus, we can fix the slope of the high mass central AGN population to $\alpha_{\rm c2} = 0$. This assumption is valid for all of our subsamples except for the most luminous AGN with $L_{\rm SXR} > 10^{44}$erg/s (red line in the bottom panel of Fig. 6.5), where no saturation is visible. To get a first guess for the remaining seven free parameters, we assume a rough mass cut of $M_{\rm h} < 10^{13}M_{\odot}/h$ for population c1 and $M_{\rm h} > 2\cdot10^{13}M_{\odot}/h$ for population c2. Then, we fit $\langle N_{\rm c1}(M_{\rm h})\rangle$ and $\langle N_{\rm c2}(M_{\rm h})\rangle$ separately below/above these mass thresholds. Finally, we fit $\langle N_{\rm c1}(M_{\rm h})\rangle + \langle N_{\rm c2}(M_{\rm h})\rangle$, using the parameters obtained from the two separate fits as initial values in the fitting routine. The resulting fitting parameters for the HOD of satellite and central AGN are listed in Table 6.1 and Table 6.2, respectively. The total HOD of AGN is then given by the sum of the HOD of satellite and central AGN (equation 6.7). When we

z	$\log L_{\rm SXR}$ [erg/s]	$\log(M_\bullet)$ $[M_\odot]$	$f_{\rm Edd}$	$C_{\rm s}$	$\log M_{\rm min,s}$ $[M_\odot/h]$	$\sigma_{\log M,s}$	$\alpha_{\rm s}$
0.25	all	> 8.0	all	-11.45	12.58	0.77	0.90
0.25	> 42.0	> 8.0	all	-16.86	–	–	1.07
3.4	> 42.0	> 8.0	all	-20.79	12.51	0.34	1.57
2.8	> 42.0	> 8.0	all	-11.48	12.65	0.42	0.87
2.0	> 42.0	> 8.0	all	-4.96	12.90	0.57	0.35
1.2	> 42.0	> 8.0	all	-9.93	12.45	0.46	0.68
0.9	> 42.0	> 8.0	all	-10.95	12.33	0.45	0.72
0.5	> 42.0	> 8.0	all	-14.99	11.93	0.037	0.96
0.25	$42.0 - 43.0$	> 8.0	all	-17.88	–	–	1.13
0.25	$43.0 - 44.0$	> 8.0	all	-16.79	–	–	1.03
0.25	> 44.0	> 8.0	all	-19.66	–	–	1.21
0.25	> 42.0	> 8.0	> 0.01	-14.20	12.07	0.21	0.83
0.25	> 42.0	> 8.0	< 0.01	-19.12	–	–	1.22
0.25	> 42.0	> 8.0	> 0.001	-14.55	12.05	0.10	0.89
0.25	> 42.0	> 8.0	< 0.001	-20.13	12.00	0.50	1.28

Table 6.1: HOD fitting parameters of simulated satellite AGN for different selection criteria.

include all BHs (not only AGN), the HOD is in principle that of galaxies, assuming that all galaxies host a SMBH. It can thus be described distinguishing only between satellite and central BHs. At redshifts $z \gtrsim 2$ the HOD of AGN can also be fitted using only one central AGN population, namely c1, since at such high redshifts almost all AGN accrete very efficiently and thus, almost every halo hosts a central AGN. Vice versa, the HOD of the subsample for $f_{\rm Edd} < 0.001$ is fitted using only population c2, because such inefficiently accreting AGN are very rare in haloes with $M_{\rm h} \lesssim 10^{13} M_\odot/h$. Note that we did not perform fits for satellite AGN with BH mass thresholds $M_\bullet > 8.5, 9.0, 9.5$ (green, yellow, and red line in the middle panel of Fig. 6.3), since it is not clear from our data whether α is similar to that of our total AGN sample and just the cut-off changes, or whether α increases with increasing mass threshold.

6.4 Summary

We made use of the 909Mpc/hr simulation run from the Magneticum Pathfinder simulation set to make predictions for clustering measurements of AGN with focus on their HOD. The large sample of simulated AGN allows to robustly investigate the shape of the HOD of AGN, which is a superposition of three sub-populations, which can all be described separately with equation (6.7):

- AGN in satellite galaxies,
- AGN in central galaxies of haloes with relatively low masses ($M_{\rm h} \lesssim 10^{13} M_\odot/h$),

z	$\log L_{\rm SXR}$ [erg/s]	$\log(M_\bullet)$ $[M_\odot]$	$f_{\rm Edd}$	$\log C_{\rm c1}$	$\log M_{\rm min,c1}$ $[M_\odot/h]$	$\sigma_{\log M,c1}$	$\alpha_{\rm c1}$	$\log C_{\rm c2}$	$\log M_{\rm min,c2}$ $[M_\odot/h]$	$\sigma_{\log M,c2}$
0.25	all	> 8.0	all	-0.13	11.88	0.41	0.0098	–	–	–
0.25	> 42.0	> 8.0	all	1.86	12.08	0.064	-0.38	-0.45	14.46	0.62
0.25	> 42.0	> 8.5	all	–	–	–	–	-0.17	14.81	0.78
0.25	> 42.0	> 9.0	all	–	–	–	–	-0.43	14.52	0.64
0.25	> 42.0	> 9.5	all	–	–	–	–	-0.57	14.33	0.42
4.2	> 42.0	> 8.0	all	-25.5	12.15	0.20	1.95	–	–	–
3.4	> 42.0	> 8.0	all	-3.44	12.34	0.39	0.25	–	–	–
2.8	> 42.0	> 8.0	all	-1.56	12.16	0.31	0.10	–	–	–
2.0	> 42.0	> 8.0	all	-2.27	12.00	0.31	0.14	–	–	–
1.2	> 42.0	> 8.0	all	0.00583	12.05	0.078	-0.10	-0.12	14.36	1.00
0.9	> 42.0	> 8.0	all	14.3	12.37	0.50	-1.3	0.32	15.37	1.35
0.5	> 42.0	> 8.0	all	2.61	11.04	0.10	-0.41	-0.43	14.35	0.66
0.25	$42.0 - 43.0$	> 8.0	all	8.95	12.34	0.51	-0.97	-0.48	14.66	0.71
0.25	$43.0 - 44.0$	> 8.0	all	1.74	12.09	0.04	-0.40	-0.52	15.07	0.83
0.25	> 44.0	> 8.0	all	1.22	7.86	0.85	-0.43	1.37	17.45	1.38
0.25	> 42.0	> 8.0	> 0.01	8.26	12.12	0.39	-0.91	-1.88	14.11	0.55
0.25	> 42.0	> 8.0	< 0.01	-1.81	11.99	0.52	-0.13	-0.40	14.60	0.68
0.25	> 42.0	> 8.0	> 0.001	4.78	12.05	0.38	-0.62	-1.17	14.41	0.66
0.25	> 42.0	> 8.0	< 0.001	–	–	–	–	-0.35	14.69	0.71

Table 6.2: HOD fitting parameters of simulated central AGN for different selection criteria.

- AGN in central galaxies of haloes with relatively high masses ($M_\mathrm{h} \gtrsim 10^{13} M_\odot/h$).

While we can directly distinguish between satellite and central galaxies in our simulation, the separation between the two central AGN populations c1 and c2 is not directly feasible and depends on various properties:

- environment: c1 AGN are mostly located in isolated galaxies, whereas c2 AGN are hosted by galaxy groups and clusters.
- BH mass: c1 AGN do generally have smaller BH masses than c2 AGN.
- Redshift: a distinction between c1 and c2 AGN is only suitable at redshifts below $z \sim 2$, since at larger redshifts, almost every halo contains a central AGN.
- Accretion mode: in our simulation c1 AGN are dominated by AGN with high f_Edd values (quasar-mode AGN), whereas c2 AGN mostly have relatively low f_Edd values (radio-mode AGN).

We conclude that different environments make AGN appear differently, namely as quasar-mode or radio-mode AGN. This strongly supports an evolutionary scenario, in which different AGN types represent different evolutionary stages of galaxies.

Making use of the three AGN populations, we obtained fits for the total HOD of AGN, depending on different selection criteria (BH mass, redshift, AGN luminosity, and f_Edd). Thereby, the HOD slope is the most important parameter. Comparing the HOD slope of different AGN subsamples with each other and with the HOD slope of the overall BH population reveals insights into the connection between AGN activity in different AGN types and their environment. Fig. 6.7 summarizes our fitting results for the HOD slopes α_s (green lines) and α_c1 (magenta lines), depending on the redshift (left panel), AGN luminosity (middle panel), and f_Edd (right panel), always including only unobscured AGN. Our results for the HOD slope can be summarized as follows:

- Panel 1: the HOD slope of satellite AGN, α_s, generally decreases with redshift up to $z = 2$. For higher redshifts, it increases, which, however, might be due to our limited simulation volume. The slope of population c1, i.e. the one at low halo masses, has negative values for $z \lesssim 1$, since population c2 strongly dominates in the central galaxies of very massive haloes. At higher redshifts the HOD of satellite AGN can be described with a single central AGN population with a slope, which is slightly above zero. The large slope at $z = 4.2$ must be taken with caution, since it might be due to our limited volume, not capturing halo masses where the HOD curve might possibly saturate.
- Panel 2: in all three luminosity ranges ($10^{42}\mathrm{erg/s} < L_\mathrm{SXR} < 10^{43}\mathrm{erg/s}$, $10^{43}\mathrm{erg/s} < L_\mathrm{SXR} < 10^{44}\mathrm{erg/s}$, and $L_\mathrm{SXR} > 10^{44}\mathrm{erg/s}$, where the bars indicate the luminosity ranges), α_s is slightly larger than the HOD slope of all resolved BHs (solid horizontal lines), indicating that AGN are not distributed randomly. However, we do not find

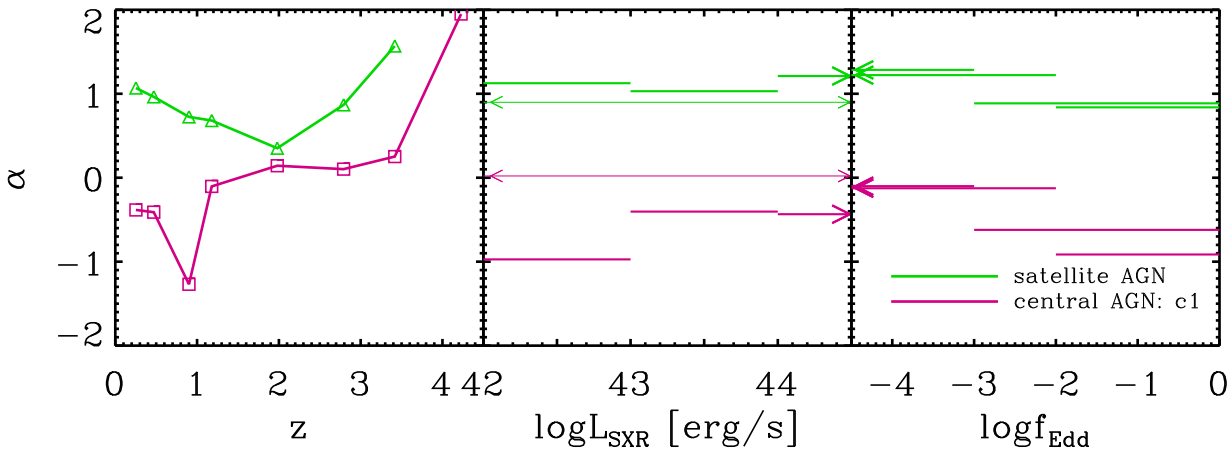

Figure 6.7: Dependence of the HOD slope α on redshift (left panel), X-ray luminosity (middle panel), and $f_{\rm Edd}$ (right panel). Green and magenta lines show the HOD slope for satellite AGN ($\alpha_{\rm s}$) and for the central AGN population at low halo masses ($\alpha_{\rm c1}$), respectively (note that $\alpha_{\rm c2} = 0$). Again, we consider only unobscured AGN. The bars in the middle and right panel indicate the luminosity/$f_{\rm Edd}$ ranges, where arrows mark that the corresponding bars continue towards the minimum/maximum value.

a dependence of $\alpha_{\rm s}$ on the luminosity range. For c1 AGN the HOD slope is below zero in all three luminosity ranges and thus clearly below the value for the overall BH population. Hence, at least at $z = 0.25$, c1 AGN are events which become more unlikely the more massive haloes are.

- Panel 3: We find that quasar-mode AGN ($f_{\rm Edd} > 0.01$) have a smaller HOD slope than radio-mode AGN ($f_{\rm Edd} < 0.01$), for both satellite and c1 AGN. This trend becomes even clearer when also distinguishing between $f_{\rm Edd} > 0.001$ and $f_{\rm Edd} < 0.001$. Thus, in our simulation, these different AGN types are distributed differently. This indicates that quasar-mode and radio-mode AGN are different evolutionary stages of the same kind of objects. Thereby, the distinction between c1 and c2 AGN is by a large amount driven by the different accretion modes.

The results presented throughout this chapter are of particular importance since the large simulation volume and the improved dynamical description of SMBHs in the Magneticum simulations allows to directly estimate the clustering properties of a simulated AGN sample, capturing also very massive and very luminous AGN. Our results have important implications for the HOD modelling of observed AGN samples, since they strongly contradict a simple two parameter model. In future work, we plan to use our results to obtain an improved HOD modelling of observed AGN samples and, thus, to compare observations and simulations as directly as possible. Subsequently, the HOD parameters of simulated AGN samples can be used as an additional constraint for the underlying sub-grid model for AGN. Thereby, we plan to run new large simulations with refined AGN models (see, for example, Section 3) to obtain how the HOD parameters depend on the AGN

model and, thus, to further explore what makes AGN so special with respect to inactive galaxies.

Summary

In this thesis we made use of the Magneticum Pathfinder simulation set, one of the most sophisticated sets of hydrodynamic cosmological simulations to date. The different simulation runs with different resolutions and volumes provide an ideal testbed to investigate (i) the role of the AGN feedback model onto simulated BHs and their host galaxies, and (ii) the driving mechanisms of nuclear activity on different scales, ranging from kpc scales up to the large scale distribution of AGN.

In the scope of this thesis we developed a refined model for accretion onto BHs and AGN feedback, in which the efficiency of the AGN feedback depends on the mass and the accretion rate of the BH, considering both radiation and mechanical outflows. This model is based on observations and theoretical models and describes a smooth transition between quasar-mode and radio-mode. The simulations which include this new model reproduce observed properties of BHs and their host galaxies better than simulations with the standard BH model, for example the BH mass function, the scaling $M_\bullet$-M_* relation, the star formation rate of galaxies, and their stellar mass functions, also when distinguishing between quiescent and star forming galaxies.

Furthermore, the simulations used in this thesis are the largest simulations to date which follow the dynamical evolution of BHs during galaxy mergers self-consistently down to the resolution limit. In combination with the large simulated volumes, this enabled us to study dual and offset AGN directly within a cosmological simulation for the first time and to get insights into their driving mechanisms, which are difficult to obtain from observations. Since the probability for dual AGN activity increases with decreasing separations between two BHs, one might expect that galaxy mergers do in general drive AGN activity. Indeed, some of the most luminous simulated AGN can calearly be associated to recent galaxy mergers. However, turning towards the overall AGN population, we surprisingly find that most simulated AGN are not triggered by galaxy mergers and that the apparent relation between mergers and AGN activity is by a large amount driven by the different intrinsic properties of galaxies with and without a recent merger.

Another approach to reveal the driving mechanisms of AGN is to investigate their clustering properties. In the scope of this thesis we analysed in detail the halo occupation distribution (HOD) of AGN, which is given by the mean number of AGN depending on the dark matter halo mass. Comparing the HOD of AGN with that of the overall BH population reveals that AGN are not distributed randomly and that different AGN types reside in different environments. This strongly supports an evolutionary sequence, in which

different AGN types are associated to different evolutionary stages of galaxies and, thus, challeges the classical unified model of AGN.

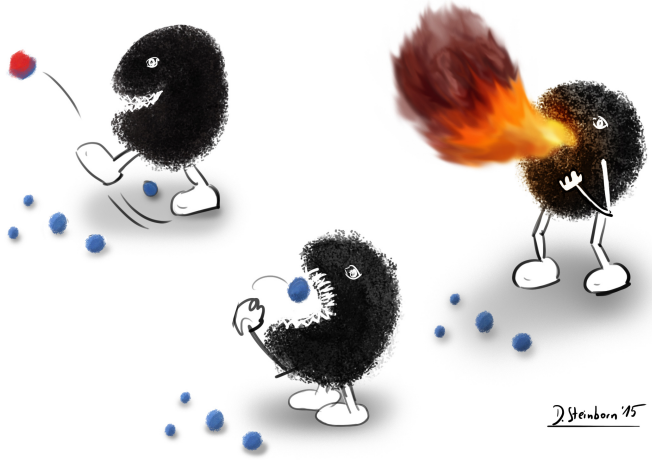

Figure 6.8: Cartoon of three active BHs, provided by my husband Daniel Steinborn.

Bibliography

Aarseth S. J., 1963, MNRAS , 126, 223

Allen S. W., Dunn R. J. H., Fabian A. C., Taylor G. B., Reynolds C. S., 2006, MNRAS , 372, 21

Allevato V., Finoguenov A., Civano F., Cappelluti N., Shankar F., Miyaji T., Hasinger G., Gilli R., Zamorani G., Lanzuisi G., Salvato M., Elvis M., Comastri A., Silverman J., 2014, ApJ , 796, 4

Altamirano-Dévora L., Miyaji T., Aceves H., Castro A., Cañas R., Tamayo F., 2016, Rev. Mexicana Astron. Astrofis. , 52, 11

Anglés-Alcázar D., Davé R., Faucher-Giguère C.-A., Özel F., Hopkins P. F., 2017, MNRAS , 464, 2840

Anglés-Alcázar D., Özel F., Davé R., 2013, ApJ , 770, 5

Antonucci R., 1993, ARA&A , 31, 473

Arth A., Dolag K., Beck A. M., Petkova M., Lesch H., 2014, ArXiv e-prints: 1412.6533

Aumer M., White S. D. M., Naab T., Scannapieco C., 2013, MNRAS , 434, 3142

Baade W., Minkowski R., 1954, ApJ , 119, 206

Baganoff F. K., Maeda Y., Morris M., Bautz M. W., Brandt W. N., Cui W., Doty J. P., Feigelson E. D., Garmire G. P., Pravdo S. H., Ricker G. R., Townsley L. K., 2003, ApJ , 591, 891

Bahcall J. N., Kirhakos S., Saxe D. H., Schneider D. P., 1997, ApJ , 479, 642

Baldry I. K., Balogh M. L., Bower R. G., Glazebrook K., Nichol R. C., Bamford S. P., Budavari T., 2006, MNRAS , 373, 469

Barai P., Murante G., Borgani S., Gaspari M., Granato G. L., Monaco P., Ragone-Figueroa C., 2016, MNRAS , 461, 1548

Barnes J., Hut P., 1986, Nature , 324, 446

Barnes J. E., 1992, ApJ , 393, 484

Barnes J. E., Hernquist L., 1992, ARA&A , 30, 705

Barrows R. S., Sandberg Lacy C. H., Kennefick J., Comerford J. M., Kennefick D., Berrier J. C., 2013, ApJ , 769, 95

Bartlett M. S., 1963, Sankhyā: The Indian Journal of Statistics, Series A (1961-2002), 25, 245

Battaglia N., Bond J. R., Pfrommer C., Sievers J. L., Sijacki D., 2010, ApJ , 725, 91

Beck A. M., Murante G., Arth A., Remus R.-S., Teklu A. F., Donnert J. M. F., Planelles S., Beck M. C., Förster P., Imgrund M., Dolag K., Borgani S., 2016, MNRAS , 455, 2110

Begelman M. C., Blandford R. D., Rees M. J., 1984, Reviews of Modern Physics, 56, 255

Behroozi P. S., Wechsler R. H., Conroy C., 2013, ApJ , 770, 57

Bell E. F., McIntosh D. H., Katz N., Weinberg M. D., 2003, ApJS , 149, 289

Bellovary J. M., Governato F., Quinn T. R., Wadsley J., Shen S., Volonteri M., 2010, ApJ , 721, L148

Berger M. J., Oliger J., 1984, Journal of Computational Physics, 53, 484

Bernardi M., Meert A., Sheth R. K., Vikram V., Huertas-Company M., Mei S., Shankar F., 2013, MNRAS , 436, 697

Bernardi M., Shankar F., Hyde J. B., Mei S., Marulli F., Sheth R. K., 2010, MNRAS , 404, 2087

Bianchi S., Chiaberge M., Piconcelli E., Guainazzi M., Matt G., 2008, MNRAS , 386, 105

Biffi V., Dolag K., Merloni A., 2018, ArXiv e-prints: 1804.01096

Biffi V., Maio U., 2013, MNRAS , 436, 1621

Binney J., Tremaine S., 2008, Galactic Dynamics: Second Edition. Princeton University Press

Blandford R. D., Rees M. J., 1974, MNRAS , 169, 395

Blecha L., Loeb A., Narayan R., 2013, MNRAS , 429, 2594

Blecha L., Sijacki D., Kelley L. Z., Torrey P., Vogelsberger M., Nelson D., Springel V., Snyder G., Hernquist L., 2016, MNRAS , 456, 961

Bocquet S., Saro A., Dolag K., Mohr J. J., 2016, MNRAS , 456, 2361

Bondi H., 1952, MNRAS , 112, 195

Bondi H., Hoyle F., 1944, MNRAS , 104, 273

Bonoli S., Marulli F., Springel V., White S. D. M., Branchini E., Moscardini L., 2009, MNRAS , 396, 423

Booth C. M., Schaye J., 2009, MNRAS , 398, 53

Borch A., Meisenheimer K., Bell E. F., Rix H.-W., Wolf C., Dye S., Kleinheinrich M., Kovacs Z., Wisotzki L., 2006, A&A , 453, 869

Bournaud F., Dekel A., Teyssier R., Cacciato M., Daddi E., Juneau S., Shankar F., 2011, ApJ , 741, L33

Bourne M. A., Nayakshin S., Hobbs A., 2014, MNRAS , 441, 3055

Bouwens R. J., Bradley L., Zitrin A., Coe D., Franx M., Zheng W., Smit R., Host O., Postman M., Moustakas L., Labbé I., Carrasco M., Molino A., Donahue M., Kelson D. D., 2014, ApJ , 795, 126

Bower R. G., Benson A. J., Malbon R., Helly J. C., Frenk C. S., Baugh C. M., Cole S., Lacey C. G., 2006, MNRAS , 370, 645

Buchner J., Bauer F. E., 2017, MNRAS , 465, 4348

Bundy K., Ellis R. S., Conselice C. J., 2005, ApJ , 625, 621

Campbell W. W., Moore J. H., 1918, Publications of Lick Observatory, 13, 75

Capelo P. R., Volonteri M., Dotti M., Bellovary J. M., Mayer L., Governato F., 2015, MNRAS , 447, 2123

Cappelluti N., Ajello M., Burlon D., Krumpe M., Miyaji T., Bonoli S., Greiner J., 2010, ApJ , 716, L209

Chandrasekhar S., 1943, ApJ , 97, 255

Chatterjee S., Degraf C., Richardson J., Zheng Z., Nagai D., Di Matteo T., 2012, MNRAS , 419, 2657

Chelouche D., 2013, ApJ , 772, 9

Choi E., Naab T., Ostriker J. P., Johansson P. H., Moster B. P., 2014, MNRAS , 442, 440

Choi E., Ostriker J. P., Naab T., Johansson P. H., 2012, ApJ , 754, 125

Choi E., Ostriker J. P., Naab T., Oser L., Moster B. P., 2014, ArXiv e-prints: 1403.1257

Choi E., Ostriker J. P., Naab T., Somerville R. S., Hirschmann M., Núñez A., Hu C.-Y., Oser L., 2017, ApJ , 844, 31

Churazov E., Sazonov S., Sunyaev R., Forman W., Jones C., Böhringer H., 2005, MNRAS , 363, L91

Cisternas M., Jahnke K., Inskip K. J., Kartaltepe J., Koekemoer A. M., Lisker T., Robaina A. R., Scodeggio M., Sheth K., Trump J. R., Andrae R., Miyaji T., Lusso E., Brusa M., Capak P., 2011, ApJ , 726, 57

Coe D., Zitrin A., Carrasco M., Shu X., Zheng W., Postman M., Bradley L., Koekemoer A., Bouwens R., Broadhurst T., Monna A., Host O., Moustakas L. A., Ford H., Moustakas J., van der Wel A. a., 2013, ApJ , 762, 32

Coil A. L., Georgakakis A., Newman J. A., Cooper M. C., Croton D., Davis M., Koo D. C., Laird E. S., Nandra K., Weiner B. J., Willmer C. N. A., Yan R., 2009, ApJ , 701, 1484

Coil A. L., Hennawi J. F., Newman J. A., Cooper M. C., Davis M., 2007, ApJ , 654, 115

Cole S., Norberg P., Baugh C. M., Frenk C. S., Bland-Hawthorn J., Bridges T., Cannon R., Colless M., Collins C., Couch W., Cross N., Dalton G., De Propris R., Driver S. P., Efstathiou G., Ellis R. S., Glazebrook K., Jackson 2001, MNRAS , 326, 255

Comerford J. M., Gerke B. F., Newman J. A., Davis M., Yan R., Cooper M. C., Faber S. M., Koo D. C., Coil A. L., Rosario D. J., Dutton A. A., 2009, ApJ , 698, 956

Comerford J. M., Greene J. E., 2014, ApJ , 789, 112

Comerford J. M., Griffith R. L., Gerke B. F., Cooper M. C., Newman J. A., Davis M., Stern D., 2009, ApJ , 702, L82

Comerford J. M., Pooley D., Barrows R. S., Greene J. E., Zakamska N. L., Madejski G. M., Cooper M. C., 2015, ApJ , 806, 219

Comerford J. M., Pooley D., Gerke B. F., Madejski G. M., 2011, ApJ , 737, L19

Comerford J. M., Schluns K., Greene J. E., Cool R. J., 2013, ApJ , 777, 64

Cooray A., Sheth R., 2002, Phys. Rep. , 372, 1

Cotini S., Ripamonti E., Caccianiga A., Colpi M., Della Ceca R., Mapelli M., Severgnini P., Segreto A., 2013, MNRAS , 431, 2661

Croom S. M., Boyle B. J., Shanks T., Smith R. J., Miller L., Outram P. J., Loaring N. S., Hoyle F., da Ângela J., 2005, MNRAS , 356, 415

Croton D. J., Springel V., White S. D. M., De Lucia G., Frenk C. S., Gao L., Jenkins A., Kauffmann G., Navarro J. F., Yoshida N., 2006, MNRAS , 365, 11

Cuadra J., Nayakshin S., Springel V., Di Matteo T., 2006, MNRAS , 366, 358

Daddi E., Dickinson M., Morrison G., Chary R., Cimatti A., Elbaz D., Frayer D., Renzini A., Pope A., Alexander D. M., Bauer F. E., Giavalisco M., Huynh M., Kurk J., Mignoli M., 2007, ApJ , 670, 156

Danielson G. C., Lanczos C., 1942, J. Franklin Inst., 233, 365

Davé R., Oppenheimer B. D., Finlator K., 2011, MNRAS , 415, 11

Davé R., Thompson R., Hopkins P. F., 2016, MNRAS , 462, 3265

Davies R., Burtscher L., Dodds-Eden K., Orban de Xivry G., 2012, in Journal of Physics Conference Series Vol. 372 of Journal of Physics Conference Series, Do stellar winds play a decisive role in feeding AGN?. p. 012046

Davis M., Efstathiou G., Frenk C. S., White S. D. M., 1985, ApJ , 292, 371

Davis S. W., Laor A., 2011, ApJ , 728, 98

Dayal P., Dunlop J. S., Maio U., Ciardi B., 2013, MNRAS , 434, 1486

de la Torre S., Guzzo L., Peacock J. A., Branchini E., Iovino A., Granett B. R., Abbas U., Adami C., Arnouts S., Bel J., Bolzonella M., Bottini D., 2013, A&A , 557, A54

De Lucia G., Blaizot J., 2007, MNRAS , 375, 2

De Lucia G., Springel V., White S. D. M., Croton D., Kauffmann G., 2006, MNRAS , 366, 499

Debuhr J., Quataert E., Ma C.-P., 2011, MNRAS , 412, 1341

Degraf C., Di Matteo T., Springel V., 2011, MNRAS , 413, 1383

Degraf C., Oborski M., Di Matteo T., Chatterjee S., Nagai D., Richardson J., Zheng Z., 2011, MNRAS , 416, 1591

DeGraf C., Sijacki D., 2017, MNRAS , 466, 3331

Dehnen W., Aly H., 2012, MNRAS , 425, 1068

Dekel A., Birnboim Y., Engel G., Freundlich J., Goerdt T., Mumcuoglu M., Neistein E., Pichon C., Teyssier R., Zinger E., 2009, Nature , 457, 451

Del Moro A., Alexander D. M., Bauer F. E., Daddi E., Kocevski D. D., McIntosh D. H., Stanley F., Brandt W. N., Elbaz D., Harrison C. M., Luo B., Mullaney J. R., Xue Y. Q., 2016, MNRAS , 456, 2105

Di Matteo T., Colberg J., Springel V., Hernquist L., Sijacki D., 2008, ApJ , 676, 33

Di Matteo T., Khandai N., DeGraf C., Feng Y., Croft R. A. C., Lopez J., Springel V., 2012, ApJ , 745, L29

Di Matteo T., Springel V., Hernquist L., 2005, Nature , 433, 604

Djorgovski S., Davis M., 1987, ApJ , 313, 59

Dolag K., Borgani S., Murante G., Springel V., 2009, MNRAS , 399, 497

Dolag K., Borgani S., Schindler S., Diaferio A., Bykov A. M., 2008, Space Sci. Rev. , 134, 229

Dolag K., Jubelgas M., Springel V., Borgani S., Rasia E., 2004, ApJ , 606, L97

Dolag K., Komatsu E., Sunyaev R., 2016, MNRAS , 463, 1797

Dolag K., Mevius E., Remus R.-S., 2017, Galaxies, 5, 35

Dolag K., Reinecke M., Gheller C., Imboden S., 2008, New Journal of Physics, 10, 125006

Dolag K., Vazza F., Brunetti G., Tormen G., 2005, MNRAS , 364, 753

Done C., Jin C., Middleton M., Ward M., 2013, MNRAS , 434, 1955

Donnert J., Dolag K., Brunetti G., Cassano R., 2013, MNRAS , 429, 3564

Draper A. R., Ballantyne D. R., 2012, ApJ , 751, 72

Dressler A., 1980, ApJ , 236, 351

Drory N., Bender R., Feulner G., Hopp U., Maraston C., Snigula J., Hill G. J., 2004, ApJ , 608, 742

Dubois Y., Gavazzi R., Peirani S., Silk J., 2013, MNRAS , 433, 3297

Dubois Y., Peirani S., Pichon C., Devriendt J., Gavazzi R., Welker C., Volonteri M., 2016, MNRAS , 463, 3948

Dubois Y., Pichon C., Welker C., Le Borgne D., Devriendt J., Laigle C., Codis S., Pogosyan D., Arnouts S., Benabed K., Bertin E., Blaizot J., Bouchet F., Cardoso J.-F., Colombi S., de Lapparent V., 2014, MNRAS , 444, 1453

Dubois Y., Volonteri M., Silk J., Devriendt J., Slyz A., 2014, MNRAS , 440, 2333

Dunne L., Ivison R. J., Maddox S., Cirasuolo M., Mortier A. M., Foucaud S., Ibar E., Almaini O., Simpson C., McLure R., 2009, MNRAS , 394, 3

Edgar R., 2004, New A Rev. , 48, 843

Efstathiou G., Davis M., White S. D. M., Frenk C. S., 1985, ApJS , 57, 241

Elbaz D., Daddi E., Le Borgne D., Dickinson M., Alexander D. M., Chary R.-R., Starck J.-L., Brandt W. N., Kitzbichler M., MacDonald E., Nonino M., Popesso P., Stern D., Vanzella E., 2007, A&A , 468, 33

Ellison S. L., Mendel J. T., Patton D. R., Scudder J. M., 2013, MNRAS , 435, 3627

Ellison S. L., Patton D. R., Mendel J. T., Scudder J. M., 2011, MNRAS , 418, 2043

Elvis M., Wilkes B. J., McDowell J. C., Green R. F., Bechtold J., Willner S. P., Oey M. S., Polomski E., Cutri R., 1994, ApJS , 95, 1

Evans D. A., Kraft R. P., Worrall D. M., Hardcastle M. J., Jones C., Forman W. R., Murray S. S., 2004, ApJ , 612, 786

Faber S. M., Jackson R. E., 1976, ApJ , 204, 668

Fabjan D., Borgani S., Tornatore L., Saro A., Murante G., Dolag K., 2010, MNRAS , 401, 1670

Fakhouri O., Ma C.-P., 2008, MNRAS , 386, 577

Falcke H., Körding E., Markoff S., 2004, A&A , 414, 895

Fall S. M., 1983, in Athanassoula E., ed., Internal Kinematics and Dynamics of Galaxies Vol. 100 of IAU Symposium, Galaxy formation - Some comparisons between theory and observation. pp 391–398

Fan L., Han Y., Fang G., Gao Y., Zhang D., Jiang X., Wu Q., Yang J., Li Z., 2016, ApJ , 822, L32

Fanaroff B. L., Riley J. M., 1974, MNRAS , 167, 31P

Fanidakis N., Baugh C. M., Benson A. J., Bower R. G., Cole S., Done C., Frenk C. S., 2011, MNRAS , 410, 53

Fanidakis N., Baugh C. M., Benson A. J., Bower R. G., Cole S., Done C., Frenk C. S., Hickox R. C., Lacey C., Del P. Lagos C., 2012, MNRAS , 419, 2797

Fanidakis N., Georgakakis A., Mountrichas G., Krumpe M., Baugh C. M., Lacey C. G., Frenk C. S., Miyaji T., Benson A. J., 2013, MNRAS , 435, 679

Fath E. A., 1909, Lick Observatory Bulletin, 5, 71

Fernández-Ontiveros J. A., López-Sanjuan C., Montes M., Prieto M. A., Acosta-Pulido J. A., 2011, MNRAS , 411, L21

Fernández-Ontiveros J. A., Prieto M. A., Acosta-Pulido J. A., Montes M., 2012, Journal of Physics Conference Series, 372, 012006

Ferrarese L., Merritt D., 2000, ApJ , 539, L9

Ferrari A., 1998, ARA&A , 36, 539

Fiore F., Feruglio C., Shankar F., Bischetti M., Bongiorno A., Brusa M., Carniani S., Cicone C., Duras F., Lamastra A., Mainieri V., Marconi A., Menci N., Maiolino R., Piconcelli E., Vietri G., Zappacosta L., 2017, A&A , 601, A143

Fontana A., Salimbeni S., Grazian A., Giallongo E., Pentericci L., Nonino M., Fontanot F., Menci N., Monaco P., Cristiani S., Vanzella E., de Santis C., Gallozzi S., 2006, A&A , 459, 745

Frank J., King A., Raine D., 1992, Accretion power in astrophysics.. Camb. Astrophys. Ser., Vol. 21,

Franx M., van Dokkum P. G., Schreiber N. M. F., Wuyts S., Labbé I., Toft S., 2008, ApJ , 688, 770

Fu H., Myers A. D., Djorgovski S. G., Yan L., 2011, ApJ , 733, 103

Fu H., Zhang Z.-Y., Assef R. J., Stockton A., Myers A. D., Yan L., Djorgovski S. G., Wrobel J. M., Riechers D. A., 2011, ApJ , 740, L44

Gaspari M., Ruszkowski M., Oh S. P., 2013, MNRAS , 432, 3401

Gatti M., Shankar F., Bouillot V., Menci N., Lamastra A., Hirschmann M., Fiore F., 2016, MNRAS , 456, 1073

Genel S., Genzel R., Bouché N., Naab T., Sternberg A., 2009, ApJ , 701, 2002

Genel S., Vogelsberger M., Springel V., Sijacki D., Nelson D., Snyder G., Rodriguez-Gomez V., Torrey P., Hernquist L., 2014, MNRAS , 445, 175

Georgakakis A., Coil A. L., Laird E. S., Griffith R. L., Nandra K., Lotz J. M., Pierce C. M., Cooper M. C., Newman J. A., Koekemoer A. M., 2009, MNRAS , 397, 623

George I. M., Fabian A. C., 1991, MNRAS , 249, 352

Gingold R. A., Monaghan J. J., 1977, MNRAS , 181, 375

Glikman E., Simmons B., Mailly M., Schawinski K., Urry C. M., Lacy M., 2015, ApJ , 806, 218

González V., Bouwens R. J., Labbé I., Illingworth G., Oesch P., Franx M., Magee D., 2012, ApJ , 755, 148

Goulding A. D., Forman W. R., Hickox R. C., Jones C., Murray S. S., Paggi A., Ashby M. L. N., Coil A. L., Cooper M. C., Huang J.-S., Kraft R., Newman J. A., Weiner B. J., Willner S. P., 2014, ApJ , 783, 40

Graham A. W., Ciambur B. C., Savorgnan G. A. D., 2016, ApJ , 831, 132

Graham A. W., Ciambur B. C., Soria R., 2016, ApJ , 818, 172

Graham A. W., Scott N., 2013, ApJ , 764, 151

Granato G. L., De Zotti G., Silva L., Bressan A., Danese L., 2004, ApJ , 600, 580

Greenstein J. L., Matthews T. A., 1963, AJ , 68, 279

Grogin N. A., Conselice C. J., Chatzichristou E., Alexander D. M., Bauer F. E., Hornschemeier A. E., Jogee S., Koekemoer A. M., Laidler V. G., Livio M., Lucas R. A., Paolillo M., Ravindranath S., Schreier E. J., Simmons B. D., Urry C. M., 2005, ApJ , 627, L97

Gültekin K., Richstone D. O., Gebhardt K., Lauer T. R., Tremaine S., Aller M. C., Bender R., Dressler A., Faber S. M., Filippenko A. V., Green R., Ho L. C., Kormendy J., Magorrian J., Pinkney J., Siopis C., 2009, ApJ , 698, 198

Guo H., Zehavi I., Zheng Z., Weinberg D. H., Berlind A. A., Blanton M., Chen Y., Eisenstein D. J., Ho S., Kazin E., Manera M., Maraston C., 2013, ApJ , 767, 122

Gupta N., Saro A., Mohr J. J., Dolag K., Liu J., 2017, MNRAS , 469, 3069

Haas M. R., Schaye J., Jeeson-Daniel A., 2012, MNRAS , 419, 2133

Hanbury Brown R., Jennison R. C., Gupta M. K. D., 1952, Nature , 170, 1061

Hargrave P. J., Ryle M., 1974, MNRAS , 166, 305

Häring N., Rix H.-W., 2004, ApJ , 604, L89

Harrison C. M., 2014, PhD thesis

Hasinger G., 2008, A&A , 490, 905

Heckman T. M., Best P. N., 2014, ARA&A , 52, 589

Heckman T. M., Kauffmann G., Brinchmann J., Charlot S., Tremonti C., White S. D. M., 2004, ApJ , 613, 109

Henriques B. M. B., White S. D. M., Thomas P. A., Angulo R., Guo Q., Lemson G., Springel V., Overzier R., 2015, MNRAS , 451, 2663

Hernquist L., Katz N., 1989, ApJS , 70, 419

Hewlett T., Villforth C., Wild V., Mendez-Abreu J., Pawlik M., Rowlands K., 2017, MNRAS , 470, 755

Hickox R. C., Jones C., Forman W. R., Murray S. S., Kochanek C. S., Eisenstein D., Jannuzi B. T., Dey A., Brown M. J. I., Stern D., Eisenhardt P. R., Gorjian V., Brodwin M., Narayan R., Cool R. J., Kenter A., Caldwell N., Anderson M. E., 2009, ApJ , 696, 891

Hickox R. C., Mullaney J. R., Alexander D. M., Chen C.-T. J., Civano F. M., Goulding A. D., Hainline K. N., 2014, ApJ , 782, 9

Hirschmann M., De Lucia G., Fontanot F., 2016, MNRAS , 461, 1760

Hirschmann M., Dolag K., Saro A., Bachmann L., Borgani S., Burkert A., 2014, MNRAS , 442, 2304

Hirschmann M., Khochfar S., Burkert A., Naab T., Genel S., Somerville R. S., 2010, MNRAS , 407, 1016

Hirschmann M., Naab T., Davé R., Oppenheimer B. D., Ostriker J. P., Somerville R. S., Oser L., Genzel R., Tacconi L. J., Förster-Schreiber N. M., Burkert A., Genel S., 2013, MNRAS , 436, 2929

Hirschmann M., Somerville R. S., Naab T., Burkert A., 2012, MNRAS , 426, 237

Hlavacek-Larrondo J., Fabian A. C., Edge A. C., Ebeling H., Allen S. W., Sanders J. S., Taylor G. B., 2013, MNRAS , 431, 1638

Hockney R. W., Eastwood J. W., 1981, Computer Simulation Using Particles. McGraw-Hill

Holmberg E., 1941, ApJ , 94, 385

Hong J., Im M., Kim M., Ho L. C., 2015, ApJ , 804, 34

Hopkins A. M., Beacom J. F., 2006, ApJ , 651, 142

Hopkins P. F., 2015, MNRAS , 450, 53

Hopkins P. F., Hernquist L., 2009, ApJ , 694, 599

Hopkins P. F., Hernquist L., Cox T. J., Di Matteo T., Robertson B., Springel V., 2006, ApJS , 163, 1

Hopkins P. F., Hernquist L., Cox T. J., Keres D., Wuyts S., 2009, ApJ , 691, 1424

Hopkins P. F., Hernquist L., Cox T. J., Kereš D., 2008, ApJS , 175, 356

Hopkins P. F., Hernquist L., Cox T. J., Robertson B., Krause E., 2007a, ApJ , 669, 45

Hopkins P. F., Hernquist L., Cox T. J., Robertson B., Krause E., 2007b, ApJ , 669, 67

Hopkins P. F., Kereš D., Oñorbe J., Faucher-Giguère C.-A., Quataert E., Murray N., Bullock J. S., 2014, MNRAS , 445, 581

Hopkins P. F., Quataert E., 2010, MNRAS , 407, 1529

Hopkins P. F., Quataert E., 2011, MNRAS , 415, 1027

Hopkins P. F., Richards G. T., Hernquist L., 2007, ApJ , 654, 731

Hopkins P. F., Torrey P., Faucher-Giguère C.-A., Quataert E., Murray N., 2016, MNRAS , 458, 816

Hoyle F., Lyttleton R. A., 1939, Proceedings of the Cambridge Philosophical Society, 35, 405

Hubble E. P., 1926, ApJ , 64

Hudson M. J., Gillis B. R., Coupon J., Hildebrandt H., Erben T., Heymans C., Hoekstra H., Kitching T. D., Mellier Y., Miller L., Van Waerbeke L., Bonnett C., 2015, MNRAS , 447, 298

Hughes P. A., 1991, Beams and jets in astrophysics. Cambridge University Press

Jahnke K., Macciò A. V., 2011, ApJ , 734, 92

Jennison R. C., Das Gupta M. K., 1953, Nature , 172, 996

Johansson P. H., Naab T., Burkert A., 2009, ApJ , 690, 802

Juneau S., Bournaud F., Charlot S., Daddi E., Elbaz D., Trump J. R., Brinchmann J., Dickinson M., Duc P.-A., Gobat R., Jean-Baptiste I., Le Floc'h É., Lehnert M. D., Pacifici C., Pannella M., Schreiber C., 2014, ApJ , 788, 88

Juneau S., Dickinson M., Bournaud F., Alexander D. M., Daddi E., Mullaney J. R., Magnelli B., Kartaltepe J. S., Hwang H. S., Willner S. P., Coil A. L., Rosario D. J., Trump J. R., Weiner B. J., Willmer C. N. A., 2013, ApJ , 764, 176

Kannan R., Stinson G. S., Macciò A. V., Brook C., Weinmann S. M., Wadsley J., Couchman H. M. P., 2014, MNRAS , 437, 3529

Kartaltepe J. S., Sanders D. B., Le Floc'h E., Frayer D. T., Aussel H., Arnouts S., Ilbert O., Salvato M., Scoville N. Z., Surace J., Yan L., Capak P., Caputi K., Carollo C. M., Cassata P., Civano F., Hasinger G., 2010, ApJ , 721, 98

Kartaltepe J. S., Sanders D. B., Scoville N. Z., Calzetti D., Capak P., Koekemoer A., Mobasher B., Murayama T., Salvato M., Sasaki S. S., Taniguchi Y., 2007, ApJS , 172, 320

Kaviraj S., Laigle C., Kimm T., Devriendt J. E. G., Dubois Y., Pichon C., Slyz A., Chisari E., Peirani S., 2017, MNRAS , 467, 4739

Kayo I., Oguri M., 2012, MNRAS , 424, 1363

Khachikian E. Y., Weedman D. W., 1974, ApJ , 192, 581

Khachikyan É. Y., Weedman D. W., 1971, Astrophysics, 7, 231

Khandai N., Di Matteo T., Croft R., Wilkins S., Feng Y., Tucker E., DeGraf C., Liu M.-S., 2015, MNRAS , 450, 1349

King A. R., Pringle J. E., 2007, MNRAS , 377, L25

Klypin A. A., Shandarin S. F., 1983, MNRAS , 204, 891

Kocevski D. D., Brightman M., Nandra K., Koekemoer A. M., Salvato M., Aird J., Bell E. F., Hsu L.-T., Kartaltepe J. S., Koo D. C., Lotz J. M., McIntosh D. H., Mozena M., Rosario D., Trump J. R., 2015, ApJ , 814, 104

Kocevski D. D., Faber S. M., Mozena M., Koekemoer A. M., Nandra K., Rangel C., Laird E. S., Brusa M., Wuyts S., Trump J. R., Koo D. C., Somerville R. S., Bell E. F., Lotz J. M., Alexander D. M., Bournaud F., 2012, ApJ , 744, 148

Komatsu E., Smith K. M., Dunkley J., Bennett C. L., Gold B., Hinshaw G., Jarosik N., Larson D., Nolta M. R., Page L., Spergel D. N., Halpern M., Hill R. S., Kogut A., Limon M., Meyer S. S., Odegard N., Tucker G. S., Weiland J. L., 2011, ApJS , 192, 18

Komossa S., Burwitz V., Hasinger G., Predehl P., Kaastra J. S., Ikebe Y., 2003, ApJ , 582, L15

Kormendy J., 1993, in Dejonghe H., Habing H. J., eds, Galactic Bulges Vol. 153 of IAU Symposium, Kinematics of extragalactic bulges: evidence that some bulges are really disks. p. 209

Kormendy J., Djorgovski S., 1989, ARA&A , 27, 235

Kormendy J., Ho L. C., 2013, ARA&A , 51, 511

Kormendy J., Kennicutt Jr. R. C., 2004, ARA&A , 42, 603

Koss M., Mushotzky R., Treister E., Veilleux S., Vasudevan R., Miller N., Sanders D. B., Schawinski K., Trippe M., 2011, ApJ , 735, L42

Koss M., Mushotzky R., Treister E., Veilleux S., Vasudevan R., Trippe M., 2012, ApJ , 746, L22

Koss M., Mushotzky R., Veilleux S., Winter L., 2010, ApJ , 716, L125

Kravtsov A. V., Klypin A. A., Khokhlov A. M., 1997, ApJS , 111, 73

Kravtsov A. V., Vikhlinin A. A., Meshcheryakov A. V., 2018, Astronomy Letters, 44, 8

Krumpe M., Lamer G., Schwope A. D., Wagner S., Zamorani G., Mignoli M., Staubert R., Wisotzki L., Hasinger G., 2007, A&A , 466, 41

Krumpe M., Miyaji T., Coil A. L., 2010, ApJ , 713, 558

Krumpe M., Miyaji T., Coil A. L., 2014, in Multifrequency Behaviour of High Energy Cosmic Sources Clustering Measurements of broad-line AGNs: Review and Future. pp 71–78

Krumpe M., Miyaji T., Coil A. L., Aceves H., 2018, MNRAS , 474, 1773

Krumpe M., Miyaji T., Husemann B., Fanidakis N., Coil A. L., Aceves H., 2015, ApJ , 815, 21

Lanzuisi G., Ranalli P., Georgantopoulos I., Georgakakis A., Delvecchio I., Akylas T., Berta S., Bongiorno A., Brusa M., Cappelluti N., Civano F., Comastri A., Gilli R., Gruppioni C., 2015, A&A , 573, A137

Laor A., Davis S., 2011, ArXiv e-prints: 1110.0653

Lapi A., Pantoni L., Zanisi L., Shi J., Mancuso C., Massardi M., Shankar F., Bressan A., Danese L., 2018, ApJ , 857, 22

Lapi A., Shankar F., Mao J., Granato G. L., Silva L., De Zotti G., Danese L., 2006, ApJ , 650, 42

Leslie S. K., Kewley L. J., Sanders D. B., Lee N., 2016, MNRAS , 455, L82

Li C., Kauffmann G., Wang L., White S. D. M., Heckman T. M., Jing Y. P., 2006, MNRAS , 373, 457

Li J., Ostriker J., Sunyaev R., 2013, ApJ , 767, 105

Li Z., Jones C., Forman W. R., Kraft R. P., Lal D. V., Di Stefano R., Spitler L. R., Tang S., Wang Q. D., Gilfanov M., Revnivtsev M., 2011, ApJ , 730, 84

Liu X., Civano F., Shen Y., Green P., Greene J. E., Strauss M. A., 2013, ApJ , 762, 110

Lucy L. B., 1977, AJ , 82, 1013

Lusso E., Comastri A., Simmons B. D., Mignoli M., Zamorani G., Vignali C., Brusa M., Shankar F., Lutz D., Trump J. R., Maiolino R., Gilli R., Bolzonella M., Puccetti S., Salvato M., Impey C. D., 2012, MNRAS , 425, 623

Ma C.-J., McNamara B. R., Nulsen P. E. J., 2013, ApJ , 763, 63

Magorrian J., Tremaine S., Richstone D., Bender R., Bower G., Dressler A., Faber S. M., Gebhardt K., Green R., Grillmair C., Kormendy J., Lauer T., 1998, AJ , 115, 2285

Mandelbaum R., Seljak U., Kauffmann G., Hirata C. M., Brinkmann J., 2006, MNRAS , 368, 715

Marchesini D., van Dokkum P., Quadri R., Rudnick G., Franx M., Lira P., Wuyts S., Gawiser E., Christlein D., Toft S., 2007, ApJ , 656, 42

Marconi A., Risaliti G., Gilli R., Hunt L. K., Maiolino R., Salvati M., 2004, MNRAS , 351, 169

Marinacci F., Pakmor R., Springel V., 2014, MNRAS , 437, 1750

Martin G., Kaviraj S., Volonteri M., Simmons B. D., Devriendt J. E. G., Lintott C. J., Smethurst R. J., Dubois Y., Pichon C., 2018, MNRAS , 476, 2801

Matthews T. A., Sandage A. R., 1963, ApJ , 138, 30

Mazzarella J. M., Iwasawa K., Vavilkin T., Armus L., Kim D.-C., Bothun G., Evans A. S., Spoon H. W. W., Haan S., Howell J. H., Lord S., Marshall J. A., Ishida C. M., Xu C. K., Petric A., Sanders D. B., Surace J. A., Appleton 2012, AJ , 144, 125

McConnell N. J., Ma C.-P., 2013, ApJ , 764, 184

McNamara B. R., Rohanizadegan M., Nulsen P. E. J., 2011, ApJ , 727, 39

Mechtley M., Jahnke K., Windhorst R. A., Andrae R., Cisternas M., Cohen S. H., Hewlett T., Koekemoer A. M., Schramm M., Schulze A., Silverman J. D., Villforth C., van der Wel A., Wisotzki L., 2016, ApJ , 830, 156

Menci N., Cavaliere A., Fontana A., Giallongo E., Poli F., Vittorini V., 2003, ApJ , 587, L63

Menci N., Fiore F., Lamastra A., 2012, MNRAS , 421, 2384

Menci N., Gatti M., Fiore F., Lamastra A., 2014, A&A , 569, A37

Merloni A., Bongiorno A., Brusa M., Iwasawa K., Mainieri V., Magnelli B., Salvato M., Berta S., Cappelluti N., Comastri A., Fiore F., Gilli R., Koekemoer A., Le Floc'h E., Lusso E., Lutz D., 2014, MNRAS , 437, 3550

Merloni A., Heinz S., 2007, MNRAS , 381, 589

Mezcua M., Prieto M. A., 2014, ApJ , 787, 62

Michałowski M., Hjorth J., Watson D., 2010, A&A , 514, A67

Miyaji T., Krumpe M., Coil A. L., Aceves H., 2011, ApJ , 726, 83

Monaco P., Fontanot F., 2005, MNRAS , 359, 283

Monaghan J. J., Lattanzio J. C., 1985, A&A , 149, 135

Moster B. P., Naab T., White S. D. M., 2013, MNRAS , 428, 3121

Mountrichas G., Sawangwit U., Shanks T., Croom S. M., Schneider D. P., Myers A. D., Pimbblet K., 2009, MNRAS , 394, 2050

Muldrew S. I., Croton D. J., Skibba R. A., Pearce F. R., Ann H. B., Baldry I. K., Brough S., Choi Y.-Y., Conselice C. J., Cowan N. B., Gallazzi A., Gray M. E., 2012, MNRAS , 419, 2670

Müller-Sánchez F., Comerford J. M., Nevin R., Barrows R. S., Cooper M. C., Greene J. E., 2015, ApJ , 813, 103

Murray N., Chiang J., Grossman S. A., Voit G. M., 1995, ApJ , 451, 498

Muzzin A., Marchesini D., Stefanon M., Franx M., McCracken H. J., Milvang-Jensen B., Dunlop J. S., Fynbo J. P. U., Brammer G., Labbé I., van Dokkum P. G., 2013, ApJ , 777, 18

Myers A. D., Brunner R. J., Richards G. T., Nichol R. C., Schneider D. P., Vanden Berk D. E., Scranton R., Gray A. G., Brinkmann J., 2006, ApJ , 638, 622

Narayan R., Mahadevan R., Grindlay J. E., Popham R. G., Gammie C., 1998, ApJ , 492, 554

Narayan R., Yi I., 1995, ApJ , 452, 710

Negri A., Volonteri M., 2017, MNRAS , 467, 3475

Nelson D., Genel S., Vogelsberger M., Springel V., Sijacki D., Torrey P., Hernquist L., 2015, MNRAS , 448, 59

Nelson D., Vogelsberger M., Genel S., Sijacki D., Kereš D., Springel V., Hernquist L., 2013, MNRAS , 429, 3353

Noeske K. G., Weiner B. J., Faber S. M., Papovich C., Koo D. C., Somerville R. S., Bundy K., Conselice C. J., Newman J. A., Schiminovich D., Le Floc'h E., Coil A. L., Rieke G. H., Lotz J. M., Primack J. R., 2007, ApJ , 660, L43

Novikov I. D., Thorne K. S., 1973, in Dewitt C., Dewitt B. S., eds, Black Holes (Les Astres Occlus) Astrophysics of black holes.. pp 343–450

Okamoto T., Nemmen R. S., Bower R. G., 2008, MNRAS , 385, 161

Oke J. B., 1963, Nature , 197, 1040

Oogi T., Enoki M., Ishiyama T., Kobayashi M. A. R., Makiya R., Nagashima M., 2016, MNRAS , 456, L30

Osterbrock D. E., 1977, in Jauncey D. L., ed., Radio Astronomy and Cosmology Vol. 74 of IAU Symposium, Physical Conditions in Radio Galaxies and Quasars. p. 183

Ostriker J. P., Choi E., Ciotti L., Novak G. S., Proga D., 2010, ApJ , 722, 642

Owen F. N., O'Dea C. P., Inoue M., Eilek J. A., 1985, ApJ , 294, L85

Padovani P., Alexander D. M., Assef R. J., De Marco B., Giommi P., Hickox R. C., Richards G. T., Smolčić V., Hatziminaoglou E., Mainieri V., Salvato M., 2017, A&AR , 25, 2

Pakmor R., Bauer A., Springel V., 2011, MNRAS , 418, 1392

Pakmor R., Springel V., 2013, MNRAS , 432, 176

Pannella M., Carilli C. L., Daddi E., McCracken H. J., Owen F. N., Renzini A., Strazzullo V., Civano F., Koekemoer A. M., Schinnerer E., Scoville N., Smolčić V., Taniguchi Y., Aussel H., 2009, ApJ , 698, L116

Panter B., Heavens A. F., Jimenez R., 2004, MNRAS , 355, 764

Parzen E., 1962, Ann. Math. Statist., 33, 1065

Peacock J. A., Smith R. E., 2000, MNRAS , 318, 1144

Peebles P. J. E., 1970, AJ , 75, 13

Peebles P. J. E., 1993, Principles of Physical Cosmology. Princeton University Press

Pelupessy F. I., Di Matteo T., Ciardi B., 2007, ApJ , 665, 107

Peng C. Y., 2007, ApJ , 671, 1098

Pérez-González P. G., Rieke G. H., Villar V., Barro G., Blaylock M., Egami E., Gallego J., Gil de Paz A., Pascual S., Zamorano J., Donley J. L., 2008, ApJ , 675, 234

Pillepich A., Springel V., Nelson D., Genel S., Naiman J., Pakmor R., Hernquist L., Torrey P., Vogelsberger M., Weinberger R., Marinacci F., 2018, MNRAS , 473, 4077

Pollina G., Hamaus N., Dolag K., Weller J., Baldi M., Moscardini L., 2017, MNRAS , 469, 787

Porciani C., Magliocchetti M., Norberg P., 2004, MNRAS , 355, 1010

Press W. H., Schechter P., 1974, ApJ , 187, 425

Price D. J., 2012, Journal of Computational Physics, 231, 759

Prieto M. A., Mezcua M., Fernández-Ontiveros J. A., Schartmann M., 2014, MNRAS , 442, 2145

Prieto M. A., Reunanen J., Tristram K. R. W., Neumayer N., Fernandez-Ontiveros J. A., Orienti M., Meisenheimer K., 2010, MNRAS , 402, 724

Quataert E., Gruzinov A., 2000, ApJ , 545, 842

Quataert E., Narayan R., Reid M. J., 1999, ApJ , 517, L101

Ragagnin A., Dolag K., Biffi V., Cadolle Bel M., Hammer N. J., Krukau A., Petkova M., Steinborn D., 2017, Astronomy and Computing, 20, 52

Raimundo S. I., Fabian A. C., Vasudevan R. V., Gandhi P., Wu J., 2012, MNRAS , 419, 2529

Read J. I., Hayfield T., Agertz O., 2010, MNRAS , 405, 1513

Reddy N. A., Pettini M., Steidel C. C., Shapley A. E., Erb D. K., Law D. R., 2012, ApJ , 754, 25

Rees M. J., 1984, ARA&A , 22, 471

Rees M. J., Begelman M. C., Blandford R. D., Phinney E. S., 1982, Nature , 295, 17

Remus R.-S., 2015, PhD thesis

Remus R.-S., Dolag K., Bachmann L. K., Beck A. M., Burkert A., Hirschmann M., Teklu A., 2015, in Ziegler B. L., Combes F., Dannerbauer H., Verdugo M., eds, IAU Symposium Vol. 309 of IAU Symposium, Disk Galaxies in the Magneticum Pathfinder Simulations. pp 145–148

Remus R.-S., Dolag K., Hoffmann T., 2017, Galaxies, 5, 49

Remus R.-S., Dolag K., Naab T., Burkert A., Hirschmann M., Hoffmann T. L., Johansson P. H., 2017, MNRAS , 464, 3742

Renzini A., 1999, in Carollo C. M., Ferguson H. C., Wyse R. F. G., eds, The Formation of Galactic Bulges Origin of Bulges. p. 9

Reyes R., Mandelbaum R., Gunn J. E., Nakajima R., Seljak U., Hirata C. M., 2012, MNRAS , 425, 2610

Ricci C., Bauer F. E., Treister E., Schawinski K., Privon G. C., Blecha L., Arevalo P., Armus L., Harrison F., Ho L. C., Iwasawa K., Sanders D. B., Stern D., 2017, MNRAS , 468, 1273

Richardson J., Zheng Z., Chatterjee S., Nagai D., Shen Y., 2012, ApJ , 755, 30

Robertson B., Bullock J. S., Cox T. J., Di Matteo T., Hernquist L., Springel V., Yoshida N., 2006, ApJ , 645, 986

Robson I., 1996, Active Galactic Nuclei. Wiley

Romanowsky A. J., Fall S. M., 2012, ApJS , 203, 17

Rosario D. J., McGurk R. C., Max C. E., Shields G. A., Smith K. L., Ammons S. M., 2011, ApJ , 739, 44

Rosario D. J., McIntosh D. H., van der Wel A., Kartaltepe J., Lang P., Santini P., Wuyts S., Lutz D., Rafelski M., Villforth C., Alexander D. M., Bauer F. E., 2015, A&A , 573, A85

Rosas-Guevara Y., Bower R. G., Schaye J., McAlpine S., Dalla Vecchia C., Frenk C. S., Schaller M., Theuns T., 2016, MNRAS , 462, 190

Rosas-Guevara Y. M., Bower R. G., Schaye J., Furlong M., Frenk C. S., Booth C. M., Crain R. A., Dalla Vecchia C., Schaller M., Theuns T., 2015, MNRAS , 454, 1038

Rowan-Robinson M., 1977, ApJ , 213, 635

Russell H. R., McNamara B. R., Edge A. C., Hogan M. T., Main R. A., Vantyghem A. N., 2013, MNRAS , 432, 530

Ryle M., Sandage A., 1964, ApJ , 139, 419

Salcido J., Bower R. G., Theuns T., McAlpine S., Schaller M., Crain R. A., Schaye J., Regan J., 2016, MNRAS , 463, 870

Sandage A., 1965, ApJ , 141, 1560

Sandage A., 1973, ApJ , 180, 687

Sanders D. B., Soifer B. T., Elias J. H., Madore B. F., Matthews K., Neugebauer G., Scoville N. Z., 1988, ApJ , 325, 74

Sasaki S., 1994, PASJ , 46, 427

Satyapal S., Ellison S. L., McAlpine W., Hickox R. C., Patton D. R., Mendel J. T., 2014, MNRAS , 441, 1297

Scannapieco E., Oh S. P., 2004, ApJ , 608, 62

Schawinski K., Dowlin N., Thomas D., Urry C. M., Edmondson E., 2010, ApJ , 714, L108

Schawinski K., Simmons B. D., Urry C. M., Treister E., Glikman E., 2012, MNRAS , 425, L61

Schawinski K., Treister E., Urry C. M., Cardamone C. N., Simmons B., Yi S. K., 2011, ApJ , 727, L31

Schaye J., Crain R. A., Bower R. G., Furlong M., Schaller M., Theuns T., Dalla Vecchia C., Frenk C. S., McCarthy I. G., Helly J. C., Jenkins A., Rosas-Guevara Y. M., White S. D. M., 2015, MNRAS , 446, 521

Schaye J., Dalla Vecchia C., 2008, MNRAS , 383, 1210

Scheuer P. A. G., 1974, MNRAS , 166, 513

Schiminovich D., Catinella B., Kauffmann G., Fabello S., Wang J., Hummels C., Lemonias J., Moran S. M., Wu R., Giovanelli R., Haynes M. P., Heckman T. M., Basu-Zych A. R., Blanton M. R., Brinchmann J., Budavári T., 2010, MNRAS , 408, 919

Schmidt M., 1963, Nature , 197, 1040

Schmidt M., 1965, ApJ , 141, 1

Schmidt M., Matthews T. A., 1964, ApJ , 139, 781

Schneider P., 2006, Einführung in die extragalaktische Astronomie und Kosmologie. Springer

Schulze A., Bongiorno A., Gavignaud I., Schramm M., Silverman J., Merloni A., Zamorani G., Hirschmann M., Mainieri V., Wisotzki L., Shankar F., Fiore F., Koekemoer A. M., Temporin G., 2015, MNRAS , 447, 2085

Schulze F., Remus R.-S., Dolag K., Burkert A., Emsellem E., van de Ven G., 2018, ArXiv e-prints: 1802.01583

Scott N., Graham A. W., Schombert J., 2013, ApJ , 768, 76

Seljak U., 2000, MNRAS , 318, 203

Seyfert C. K., 1943, ApJ , 97, 28

Shakura N. I., Sunyaev R. A., 1973, A&A , 24, 337

Shankar F., 2013, Classical and Quantum Gravity, 30, 244001

Shankar F., Guo H., Bouillot V., Rettura A., Meert A., Buchan S., Kravtsov A., Bernardi M., Sheth R., Vikram V., Marchesini D., Behroozi P., 2014, ApJ , 797, L27

Shankar F., Lapi A., Salucci P., De Zotti G., Danese L., 2006, ApJ , 643, 14

Shankar F., Salucci P., Granato G. L., De Zotti G., Danese L., 2004, MNRAS , 354, 1020

Shankar F., Weinberg D. H., Miralda-Escudé J., 2009, ApJ , 690, 20

Shankar F., Weinberg D. H., Miralda-Escudé J., 2013, MNRAS , 428, 421

Shen Y., Hennawi J. F., Shankar F., Myers A. D., Strauss M. A., Djorgovski S. G., Fan X., Giocoli C., Mahabal A., Schneider D. P., Weinberg D. H., 2010, ApJ , 719, 1693

Shen Y., McBride C. K., White M., Zheng Z., Myers A. D., Guo H., Kirkpatrick J. A., Padmanabhan N., Parejko J. K., Ross N. P., Schlegel D. J., Schneider D. P., Streblyanska A., Swanson M. E. C., Zehavi I., Pan K., Bizyaev D., Brewington H., 2013, ApJ , 778, 98

Shen Y., Strauss M. A., Oguri M., Hennawi J. F., Fan X., Richards G. T., Hall P. B., Gunn J. E., Schneider D. P., Szalay A. S., Thakar A. R., Vanden Berk D. E., Anderson S. F., Bahcall N. A., Connolly A. J., Knapp G. R., 2007, AJ , 133, 2222

Shen Y., Strauss M. A., Ross N. P., Hall P. B., Lin Y.-T., Richards G. T., Schneider D. P., Weinberg D. H., Connolly A. J., Fan X., Hennawi J. F., Shankar F., Vanden Berk D. E., Bahcall N. A., Brunner R. J., 2009, ApJ , 697, 1656

Sheth R. K., Mo H. J., Tormen G., 2001, MNRAS , 323, 1

Sheth R. K., Tormen G., 1999, MNRAS , 308, 119

Shields G. A., 1999, PASP , 111, 661

Shields G. A., Rosario D. J., Junkkarinen V., Chapman S. C., Bonning E. W., Chiba T., 2012, ApJ , 744, 151

Shima E., Matsuda T., Takeda H., Sawada K., 1985, MNRAS , 217, 367

Shlosman I., Frank J., Begelman M. C., 1989, Nature , 338, 45

Sijacki D., Springel V., Di Matteo T., Hernquist L., 2007, MNRAS , 380, 877

Sijacki D., Springel V., Haehnelt M. G., 2011, MNRAS , 414, 3656

Sijacki D., Vogelsberger M., Genel S., Springel V., Torrey P., Snyder G. F., Nelson D., Hernquist L., 2015, MNRAS , 452, 575

Silk J., Rees M. J., 1998, A&A , 331, L1

Slipher V. M., 1917, Lowell Observatory Bulletin, 3, 59

Smith F. G., 1951, Nature , 168, 555

Soergel B., Saro A., Giannantonio T., Efstathiou G., Dolag K., 2017, ArXiv e-prints: 1712.05714

Somerville R. S., Hopkins P. F., Cox T. J., Robertson B. E., Hernquist L., 2008, MNRAS , 391, 481

Sparre M., Hayward C. C., Springel V., Vogelsberger M., Genel S., Torrey P., Nelson D., Sijacki D., Hernquist L., 2015, MNRAS , 447, 3548

Springel V., 2005, MNRAS , 364, 1105

Springel V., 2010, MNRAS , 401, 791

Springel V., Di Matteo T., Hernquist L., 2005, MNRAS , 361, 776

Springel V., Hernquist L., 2002, MNRAS , 333, 649

Springel V., Hernquist L., 2003, MNRAS , 339, 289

Springel V., Pakmor R., Pillepich A., Weinberger R., Nelson D., Hernquist L., Vogelsberger M., Genel S., Torrey P., Marinacci F., Naiman J., 2018, MNRAS , 475, 676

Springel V., White S. D. M., Jenkins A., Frenk C. S., Yoshida N., Gao L., Navarro J., Thacker R., Croton D., Helly J., Peacock J. A., Cole S., Thomas P., Couchman H., Evrard A., Colberg J., Pearce F., 2005, Nature , 435, 629

Springel V., White S. D. M., Tormen G., Kauffmann G., 2001, MNRAS , 328, 726

Springel V., Yoshida N., White S. D. M., 2001, New Astron. , 6, 79

Stark D. P., Ellis R. S., Bunker A., Bundy K., Targett T., Benson A., Lacy M., 2009, ApJ , 697, 1493

Stark D. P., Schenker M. A., Ellis R., Robertson B., McLure R., Dunlop J., 2013, ApJ , 763, 129

Steinborn L. K., Dolag K., Comerford J. M., Hirschmann M., Remus R.-S., Teklu A. F., 2016, MNRAS , 458, 1013

Steinborn L. K., Dolag K., Hirschmann M., Prieto M. A., Remus R.-S., 2015, MNRAS , 448, 1504

Steinborn L. K., Hirschmann M., Dolag K., Shankar F., Juneau S., Krumpe M., Remus R.-S., Teklu A. F., 2018, ArXiv e-prints: 1805.06902

Steinhardt C. L., Speagle J. S., Capak P., Silverman J. D., Carollo M., Dunlop J., Hashimoto Y., Hsieh B.-C., Ilbert O., Le Fevre O., Le Floc'h E., Lee N., Lin L., Lin Y.-T., Masters D. a., 2014, ApJ , 791, L25

Steinmetz M., Navarro J. F., 2002, New Astron. , 7, 155

Strauss M. A., Willick J. A., 1995, Phys. Rep. , 261, 271

Teklu A. F., Remus R.-S., Dolag K., Arth A., Burkert A., Obreja A., Schulze F., 2018, ApJ , 854, L28

Teklu A. F., Remus R.-S., Dolag K., Beck A. M., Burkert A., Schmidt A. S., Schulze F., Steinborn L. K., 2015, ApJ , 812, 29

Teklu A. F., Remus R.-S., Dolag K., Burkert A., 2017, MNRAS , 472, 4769

Teyssier R., 2002, A&A , 385, 337

Teyssier R., Moore B., Martizzi D., Dubois Y., Mayer L., 2011, MNRAS , 414, 195

Tinker J. L., Weinberg D. H., Zheng Z., Zehavi I., 2005, ApJ , 631, 41

Toomre A., 1974, in Shakeshaft J. R., ed., The Formation and Dynamics of Galaxies Vol. 58 of IAU Symposium, Gravitational interactions between galaxies. pp 347–363

Tornatore L., Borgani S., Dolag K., Matteucci F., 2007, MNRAS , 382, 1050

Tornatore L., Borgani S., Springel V., Matteucci F., Menci N., Murante G., 2003, MNRAS , 342, 1025

Trakhtenbrot B., 2014, ApJ , 789, L9

Treister E., Schawinski K., Urry C. M., Simmons B. D., 2012, ApJ , 758, L39

Tremaine S., Gebhardt K., Bender R., Bower G., Dressler A., Faber S. M., Filippenko A. V., Green R., Grillmair C., Ho L. C., Kormendy J., Lauer T. R., Magorrian J., Pinkney J., Richstone D., 2002, ApJ , 574, 740

Tremmel M., Governato F., Volonteri M., Quinn T. R., 2015, MNRAS , 451, 1868

Tremmel M., Karcher M., Governato F., Volonteri M., Quinn T. R., Pontzen A., Anderson L., Bellovary J., 2017, MNRAS , 470, 1121

Tristram K. R. W., Burtscher L., Jaffe W., Meisenheimer K., Hönig S. F., Kishimoto M., Schartmann M., Weigelt G., 2014, A&A , 563, A82

Tully R. B., Fisher J. R., 1977, A&A , 54, 661

Tundo E., Bernardi M., Hyde J. B., Sheth R. K., Pizzella A., 2007, ApJ , 663, 53

Urrutia T., Lacy M., Becker R. H., 2008, ApJ , 674, 80

Urry C. M., Padovani P., 1995, PASP , 107, 803

Vale A., Ostriker J. P., 2004, MNRAS , 353, 189

van den Bosch R. C. E., 2016, ApJ , 831, 134

Van Wassenhove S., Capelo P. R., Volonteri M., Dotti M., Bellovary J. M., Mayer L., Governato F., 2014, MNRAS , 439, 474

Van Wassenhove S., Volonteri M., Mayer L., Dotti M., Bellovary J., Callegari S., 2012, ApJ , 748, L7

Vazza F., Dolag K., Ryu D., Brunetti G., Gheller C., Kang H., Pfrommer C., 2011, MNRAS , 418, 960

Villforth C., Hamann F., Rosario D. J., Santini P., McGrath E. J., van der Wel A., Chang Y. Y., Guo Y., Dahlen T., Bell E. F., Conselice C. J., Croton D., Dekel A., Faber S. M., Grogin N., 2014, MNRAS , 439, 3342

Villforth C., Hamilton T., Pawlik M. M., Hewlett T., Rowlands K., Herbst H., Shankar F., Fontana A., Hamann F., Koekemoer A., Pforr J., Trump J., Wuyts S., 2017, MNRAS , 466, 812

Vittorini V., Shankar F., Cavaliere A., 2005, MNRAS , 363, 1376

Vogelsberger M., Genel S., Sijacki D., Torrey P., Springel V., Hernquist L., 2013, MNRAS , 436, 3031

Vogelsberger M., Genel S., Springel V., Torrey P., Sijacki D., Xu D., Snyder G., Bird S., Nelson D., Hernquist L., 2014, Nature , 509, 177

Vogelsberger M., Genel S., Springel V., Torrey P., Sijacki D., Xu D., Snyder G., Nelson D., Hernquist L., 2014, MNRAS , 444, 1518

Volonteri M., Bogdanović T., Dotti M., Colpi M., 2016, IAU Focus Meeting, 29, 285

Volonteri M., Dubois Y., Pichon C., Devriendt J., 2016, MNRAS , 460, 2979

Volonteri M., Madau P., 2008, ApJ , 687, L57

von Hoerner S., 1963, ZAp , 57

Weedman D. W., 1970, ApJ , 159, 405

Weedman D. W., 1977, ARA&A , 15, 69

Weigel A. K., Schawinski K., Treister E., Trakhtenbrot B., Sanders D. B., 2018, MNRAS

Weinberger R., Springel V., Hernquist L., Pillepich A., Marinacci F., Pakmor R., Nelson D., Genel S., Vogelsberger M., Naiman J., Torrey P., 2017, MNRAS , 465, 3291

Weinberger R., Springel V., Pakmor R., Nelson D., Genel S., Pillepich A., Vogelsberger M., Marinacci F., Naiman J., Torrey P., Hernquist L., 2017, ArXiv e-prints: 1710.04659

Weston M. E., McIntosh D. H., Brodwin M., Mann J., Cooper A., McConnell A., Nielsen J. L., 2017, MNRAS , 464, 3882

White S. D. M., Frenk C. S., 1991, ApJ , 379, 52

Wiersma R. P. C., Schaye J., Smith B. D., 2009, MNRAS , 393, 99

Wyithe J. S. B., Loeb A., 2003, ApJ , 595, 614

Wylezalek D., Zakamska N. L., Liu G., Obied G., 2016, MNRAS , 457, 745

Xu C. K., Zhao Y., Scoville N., Capak P., Drory N., Gao Y., 2012, ApJ , 747, 85

Xu G., 1995, ApJS , 98, 355

Yabe K., Ohta K., Iwata I., Sawicki M., Tamura N., Akiyama M., Aoki K., 2009, ApJ , 693, 507

Yu Q., Lu Y., Mohayaee R., Colin J., 2011, ApJ , 738, 92

Yuan F., Narayan R., 2014, ARA&A , 52, 529

Yuan F., Yu Z., Ho L. C., 2009, ApJ , 703, 1034

Yusef-Zadeh F., Arendt R., Bushouse H., Cotton W., Haggard D., Pound M. W., Roberts D. A., Royster M., Wardle M., 2012, ApJ , 758, L11

Zavala J., Avila-Reese V., Firmani C., Boylan-Kolchin M., 2012, MNRAS , 427, 1503

Zehavi I., Zheng Z., Weinberg D. H., Blanton M. R., Bahcall N. A., Berlind A. A., Brinkmann J., Frieman J. A., Gunn J. E., Lupton R. H., Nichol R. C., Percival W. J., Schneider D. P., Skibba R. A., Strauss M. A., Tegmark M., York D. G., 2011, ApJ , 736, 59

Zheng W., Postman M., Zitrin A., Moustakas J., Shu X., Jouvel S., Høst O., Molino A., Bradley L., Coe D., Moustakas L. A., Carrasco M., Ford H., Benítez N., Lauer T. R., Seitz S., Bouwens R., Koekemoer A., 2012, Nature , 489, 406

Zheng X. Z., Bell E. F., Somerville R. S., Rix H.-W., Jahnke K., Fontanot F., Rieke G. H., Schiminovich D., Meisenheimer K., 2009, ApJ , 707, 1566

List of Figures

List of Tables

Acknowledgments

First of all I would like to thank my family, in particular my husband Daniel Steinborn and our daughter Lily Steinborn, who always supported me, gave me enough free space to write this thesis, and always cheered me up in the evenings after long working days. I would also like to thank my sister Jessica Bachmann and my parents Anja Schwab and Udo Bachmann, who supported me from childhood on and teached me the importance of education without putting any pressure on me.

Secondly, I would like to thank my supervisor PD Dr. Klaus Dolag for giving me the opportunity to write this thesis and to work with one of the largest and sophisticated hydrodynamic cosmological simulations to date. I would also like to thank Prof. Dr. Harald Lesch for evaluating this thesis.

Next, I would like to thank my collaborators for many fruitful discussions which strongly impacted my scientific work, in particular Dr. Michaela Hirschmann, Dr. Mirko Krumpe, Dr. Rhea-Silvia Remus, Dr. M. Admudena Prieto, and Dr. Takamitsu Miyaji. I would also like to thank Dr. David Hubber for carefully reading this thesis before submission.

I also would like to thank my co-students not only for the many scientific discussions, but also for the great time we have had at USM. In particular I would like to thank Adelheid F. Teklu, Felix Schulze, Stefan Heigl, Alexander Arth, Marcel Lotz, and many more. Finally, I would like to thank all members of the CAST group for the many discussions and useful feedback, in particular the head of our group, Prof. Dr. Andreas Burkert.

Publications

Accepted Publications

2014 Michaela Hirschmann, Klaus Dolag, Alexandro Saro, **Lisa Bachmann**, Stefano Borgani, Andreas Burkert: *Cosmological simulations of black hole growth: AGN luminosities and downsizing*; MNRAS, 442, 2304

2015 Remus, Rhea-Silvia; Dolag, Klaus; **Bachmann, Lisa K.**; Beck, Alexander M.; Burkert, Andreas; Hirschmann, Michaela; Teklu, Adelheid: *Disk Galaxies in the Magneticum Pathfinder Simulations*; IAU Symposium Vol. 309, IAU Symposium. pp 145–148, doi: 10.1017/S1743921314009491

2015 **Lisa K. Steinborn**, Klaus Dolag, Michaela Hirschmann, M. Almudena Prieto, Rhea-Silvia Remus: *A refined sub-grid model for black hole accretion and AGN feedback in large cosmological simulations*; MNRAS, 448, 1504

2015 Teklu, A. F.; Remus, R.-S.; Dolag, K.; Beck, A. M.; Burkert, A.; Schmidt, A. S.; Schulze, F.; **Steinborn, L. K.**: *Connecting Angular Momentum and Galactic Dynamics: The complex Interplay between Spin, Mass, and Morphology*; ApJ, 812, 29

2015 E. Rasia, S. Borgani, G. Murante, S. Planelles, A. M. Beck, V. Biffi, C. Ragone-Figueroa, G. L. Granato, **L. K. Steinborn**, K. Dolag: *Cool Core Clusters from Cosmological Simulations*; ApJ, 813, L17

2016 Francisco Villaescusa-Navarro, Susana Planelles, Stefano Borgani, Matteo Viel, Elena Rasia, Giuseppe Murante, Klaus Dolag, **Lisa K. Steinborn**,Veronica Biffi, Alexander M. Beck, Cinthia Ragone-Figueroa: *Neutral hydrogen in galaxy clusters: impact of AGN feedback and implications for intensity mapping*; MNRAS, 456, 3553

2016 **Lisa K. Steinborn**, Klaus Dolag, Julia M. Comerford, Michaela Hirschmann, Rhea-Silvia Remus, Adelheid F. Teklu: *Origin and properties of dual and offset AGN in a cosmological simulation at z=2*; MNRAS, 458, 1013

2016 N. Truong, E. Rasia, P. Mazzotta, S. Planelles, V. Biffi, D. Fabjan, A. M. Beck, S. Borgani, K. Dolag, G.L. Granato, G. Murante, C. Ragone-Figueroa, **L. K. Steinborn**: *Hydrodynamic Simulations of Galaxy Clusters: Scaling Relations and Evolution*; MNRAS, 474, 4089

2017 S. Planelles, D. Fabjan, S. Borgani, G. Murante, E. Rasia, V. Biffi, N. Truong, C. Ragone- Figueroa, G.L. Granato, K. Dolag, E. Pierpaoli, A. M. Beck, **L. K. Steinborn**, M. Gaspari: *Pressure of Hot Gas in Simulations of Galaxy Clusters*; MNRAS, 467, 3827

Submitted Publication

2018 **Lisa K. Steinborn**, Michaela Hirschmann, Klaus Dolag, Francesco Shankar, Stephanie Juneau, Mirko Krumpe, Rhea-Silvia Remus, Adelheid F. Teklu: *Cosmological simulations of BH growth II: how (in)significant are merger events for fuelling nuclear activity?*; submitted to MNRAS